



**HAL**  
open science

# Spatial Altimetry, GNSS Reflectometry and Marine Surcotes

Phuong-Lan Vu

► **To cite this version:**

Phuong-Lan Vu. Spatial Altimetry, GNSS Reflectometry and Marine Surcotes. Earth Sciences. Université Toulouse III Paul Sabatier (UT3 Paul Sabatier), 2019. English. NNT: . tel-02167814

**HAL Id: tel-02167814**

**<https://theses.hal.science/tel-02167814>**

Submitted on 28 Jun 2019

**HAL** is a multi-disciplinary open access archive for the deposit and dissemination of scientific research documents, whether they are published or not. The documents may come from teaching and research institutions in France or abroad, or from public or private research centers.

L'archive ouverte pluridisciplinaire **HAL**, est destinée au dépôt et à la diffusion de documents scientifiques de niveau recherche, publiés ou non, émanant des établissements d'enseignement et de recherche français ou étrangers, des laboratoires publics ou privés.



# THÈSE

En vue de l'obtention du

## DOCTORAT DE L'UNIVERSITÉ DE TOULOUSE

Délivré par : *l'Université Toulouse 3 Paul Sabatier (UT3 Paul Sabatier)*

---

---

Présentée et soutenue le *31/05/2019* par :

**PHUONG LAN VU**

---

**Spatial Altimetry, GNSS Reflectometry and Marine Surcotes**  
**Altimétrie Spatiale, Réflectométrie GNSS et Surcotes Marines**

---

---

### JURY

|                        |   |                       |
|------------------------|---|-----------------------|
| GUY WÖPPELMANN         | Université de La Rochelle                 | Rapporteur            |
| ALDO SOTTOLICHIO       | Université de Bordeaux                    | Rapporteur            |
| BENOIT LAIGNEL         | Université de Rouen                       | Examineur             |
| GUILLAUME<br>RAMILLIEN | Université Paul Sabatier                  | Examineur             |
| ANNY CAZENAVE          | LEGOS, OMP                                | Examineur             |
| DONGKAI YANG           | Beihang University, Beijing<br>Shi, Chine | Examineur             |
| JOSÉ DARROZES          | Université Paul Sabatier                  | Directeur de thèse    |
| FRÉDÉRIC FRAPPART      | Université Paul Sabatier                  | Co-directeur de thèse |
| MINH CUONG HA          | IDAT, Vietnam                             | Invité                |

---

#### École doctorale et spécialité :

*SDU2E : Sciences de la Terre et des Planètes Solides*

#### Unité de Recherche :

*Géoscience Environnement Toulouse(UMR 5563)*

#### Directeur(s) de Thèse :

*José DARROZES et Frédéric FRAPPART*

#### Rapporteurs :

*Prénom Nom, Prénom Nom et Prénom Nom*



---

## Résumé:

L'objectif de ce travail a été de développer une méthodologie de télédétection novatrice, s'appuyant sur des plateformes existantes, de suivi des principaux facteurs influençant la dynamique côtière. Lors de mon étude j'ai développé des suivis basés sur un outil classique: l'altimétrie satellitaire. Mon approche s'est appuyée sur les nouvelles missions spatiales dont j'ai évalué l'apport sur la zone côtière qui est la plus critique du point de vue socio-économique. J'ai plus spécifiquement regardé la façade atlantique entre La Rochelle et Bayonne. Je me suis ensuite intéressée à une technique originale basée sur la réflexion des ondes GNSS (GNSS-R). Ces outils nous permettent de surveiller précisément les diverses ondes de marée et de détecter des phénomènes plus singuliers comme la tempête Xynthia (2010) qui a affecté le Sud de l'Europe. Ces outils démontrent qu'il est possible aussi de suivre la dynamique côtière liée aux variations de houle et son impact sur l'érosion côtière, et même les effets de la forte dépression atmosphérique associée à Xynthia et qui a eu un impact visible sur le niveau local de l'océan atlantique. Ma thèse repose sur deux approches complémentaires basées sur deux échelles d'analyse, l'une globale associée à l'altimétrie satellitaire l'autre plus locale, dédiée à la détection des événements extrêmes et basée sur le réflectométrie.

La première étude s'appuie sur différentes missions altimétriques et nous a permis de suivre les variations du niveau de la mer de la côte atlantique française au Sud du golfe de Gascogne durant la période de 1995-2015. Les données SARAL, dont l'empreinte au sol au de l'ordre de 6 km, montrent qu'il est maintenant possible de s'approcher de la bande côtière jusqu'à  $\sim 10$  km avec une grande précision ( $\sim 20$  cm). La seconde application repose sur le GNSS-R que nous avons utilisé pour suivre la partie protégée de la baie de Saint Jean de Luz. Là encore les résultats sont exceptionnels puisqu'ils nous ont permis de suivre l'impact de la tempête Xynthia. J'ai ainsi mis en évidence qu'il était possible avec un seul instrument de suivre les effets des marées, et les effets des surcotes marines qui associées à l'impact de la pression atmosphérique donnent une bonne corrélation ( $R=0.77$  entre la composante RC3 et les surcôtes, et  $R=0.73$  avec la pression atmosphérique) durant la tempête. Enfin nous avons aussi regardé ce qui se passe lors de la transition eaux continentales/océaniques pour les deltas du Fleuve Rouge et du Mékong (Vietnam). Et même si les séries temporelles sont assez courtes, les résultats sont plus qu'encourageant puisqu'ils nous ont permis de suivre les épisodes de crues associées à deux tempêtes tropicales (Mirinae et Nida) et de mesurer le retard entre les chutes de pluies et la propagation de l'onde crue qui montre dans le cas présent un délai de 48h pour Nida.

---

Grâce au déploiement dans de nombreux pays de réseaux GNSS permanents, cette technique peut être appliquée lorsqu'une station GNSS permanente est située près du rivage. L'approche GNSS-R peut être alors utilisée pour le suivi des variations du niveau de la mer mais aussi l'impact d'évènements extrêmes. Pour cela nous avons utilisé 3 mois d'enregistrements (janvier-mars 2010) de la station GNSS de Socoa, pour déterminer les composantes, court terme, de la marée dans les signaux GNSS-R et pour identifier la tempête Xynthia. Cette étude est le premier exemple de l'utilisation du GNSS-R pour détecter les surcôtes, les tempêtes par des techniques de décomposition du signal sous forme d'analyse spectrale singulière (SSA) et de transformation en ondelettes continues. L'un des modes de décomposition du SSA était lié aux variations temporelles de surcotes et des fluctuations atmosphériques à travers le baromètre inversé.

Mes travaux montrent que l'altimétrie satellitaire et GNSS-R constituent une alternative très intéressante aux techniques classiques de mesure *in situ* surtout pour les zones côtières et estuariennes et la surveillance de l'élévation globale du niveau de la mer. Les techniques basées sur l'altimétrie spatiale montrent leur efficacité pour le suivi des niveaux marins en haute mer mais les nouvelles missions montrent qu'il est possible de s'approcher de plus en plus des côtes tout en conservant une très bonne qualité de mesure. Le GNSS-R présente, quant à lui, l'avantage de s'appuyer sur des réseaux nationaux/internationaux et d'avoir de longues chroniques temporelles (>10 ans). Autre point fondamental il peut suivre la dynamique côtière et des deltas.

**Mots clés:** Hauteur de la surface de la mer; GNSS-R; SNR; altimétrie côtière; marégraphe; validation; analyse spectrale singulière; transformation en ondelettes continues; baromètre inversé; onde de tempête.

---

---

## Abstract :

The objective of this PhD thesis was to develop an innovative remote sensing methodology, based on existing platforms, to monitor the main factors influencing coastal dynamics. We propose monitoring based on a classic tool *i.e.* satellite altimetry but with a focus on new space missions (SARAL, Sentinel-3). Whose contributions will be evaluated, particularly in the coastal zone, which is the most critical from a socio-economic point of view. I have focused my attention on the French Atlantic coast between La Rochelle and Bayonne. We will also rely on an original technique based on the reflection of GNSS positioning satellites (technical known as GNSS-R). These tools will allow us to precisely monitor the various tidal waves, but they have also allowed us to detect more unusual phenomena such as the extreme event of 2010: the storm Xynthia that affected the coasts of southern Europe. These tools demonstrate that it is also possible will also be able to seeto monitor the coastal dynamics related to swell variations and its impact on coastal erosion, and even the effects of the strong atmospheric depression associated with Xynthia, which has had a measurable impact on the local sea level of the Atlantic Ocean. My thesis is focused on two complementary approaches based on two scales of study: the first one is global and used satellite altimetry, the second one is more local and focused on the extreme event detection and it is based on the GNSS reflectometry.

The first study, which I carried out, relies on different satellite altimetry missions (ERS-2, Jason- 1/2/3, ENVISAT, SARAL) which allowed us to follow the sea level variations (SSH) from the French Atlantic coast to the south of the Bay of Biscay during the 1995-2015 period. SARAL data, including a footprint of around 6 km, show that it is now possible to approach the coastal fringe up to  $\sim 10$  km with a great precision (RMSE  $\sim 20$  cm). The second application is based on the GNSS-R methodology that we used to track SSH in the inner part of the bay of Saint Jean de Luz – Socoa during the storm Xynthia. Here again the results are exceptional since they allowed us to follow the impact of the storm Xynthia on the local level of the ocean. I thus highlighted that it was possible with only one instrument to follow the effects of the tides, and even the effects of the marine surges which associated to the impact of the atmospheric pressure on the sea level give a good correlation ( $R = 0.77$  between the RC3 component and the surge, and  $R = 0.73$  with the atmospheric pressure) during storm. Finally we also looked at what is happening in the transition between continental and oceanic waters for the deltas of the Red River and Mekong in Vietnam. And, even if the time series are rather short or truncated (Red River) the results are more than encouraging since they allowed us to follow the flooding events associated with two tropical storms (Mirinae and Nida)

---

and to measure the delay between the rain falls and the propagation of the flood wave which shows in this case a delay of 48 h for Nida.

With the deployment of permanent GNSS networks in many countries, this technique can be applied when a permanent GNSS station is located near the shore. The GNSS-R approach can be used to monitor sea level variations but also the effect of extreme events. For that we used 3 months of recordings (January-March 2010) from the Socoa GNSS station to determine the tidal components in the GNSS-R signals and to identify the Xynthia storm. This study is the first example of the use of GNSS-R to detect overcoats and storms using signal decomposition techniques in the form of singular spectral analysis (SSA) and continuous wavelet transformation. One of the modes of decomposition of the SSA was related to temporal variations in surcharges and atmospheric fluctuations across the inverted barometer.

My work shows that new altimetry mission and GNSS-R are a powerful alternative and a significant complement technique for managing water resource and monitoring SLR near the coastal area. The GNSS-R technique have also a great advantage based on an already developed and sustainable GNSS satellite networks which has recorded continuous and large time series shall exceed 15 years. These quite long time series are necessary to have a good estimation of the effects of the global warming on the sea level height.

**Keywords:** Sea Surface Height; GNSS-R; SNR; Coastal altimetry; Tide gauge; validation, Singular Spectrum Analysis; Continuous Wavelet Transform; Inverted barometer; Surge Storm.

---

---

## Acronyms and notations

- **C/A** Coarse Acquisition
- **AMR** Advanced Microwave Radiometer
- **ARGOS-3** Advance Research and Global Observation Satellite
- **BOC** Binary Offset Carrier
- **BPSK** Binary Phase Shift Keying
- **CBOC** Composite BOC
- **CDMA** Code Division Multiple Access
- **CM** Code Moderate
- **CNES** Centre National d'études Spatiales
- **CS** Commercial Service
- **CTOH** Centre de Topographie de l'Océan et de l'Hydrosphère
- **CWT** Continuous Wavelet Transform
- **DDM** Delay-Doppler Map
- **DIODE** Détermination Immédiate d'Orbite par Doris Embarqué
- **DORIS** Doppler Orbitography and Radiopositioning Integrated by Satellite
- **DWT** Discrete Wavelet Transform
- **ECMWF** European Center for Medium-range Weather Forecast
- **EM** Electromagnetic
- **ENVISAT** Environmental Satellite
- **ERS** European Remote Sensing
- **ESA** European Space Agency
- **FDMA** Frequency Division Multiple Access
- **GDR** Geophysical Data Records
- **GIM** Global Ionospheric Maps

- 
- **GIS** Geographic Information System
  - **GLONASS** Globalnaya Navigatsionnaya Sputnikovaya Sistema
  - **GNSS-R** Global Navigation Satellite System-Reflectometry
  - **GPS** Global Positioning System
  - **GRSS** GNSS Reflected Signals Simulations
  - **IB** Inverted Barometer
  - **IGN69** Institut Géographique National 1969
  - **IGS** International GNSS Service
  - **IPT** Interference Pattern Technique
  - **IRNSS** Indian Regional Navigational Satellite System
  - **ISRO** Indian Space Research Organization
  - **LHCP** Left Hand Circularly Polarized
  - **LRA** Laser Reflector Array
  - **LRM** Low Resolution Mode
  - **LRO** Long Repeat Orbit
  - **MAPS** Multi-mission Altimetry Processing Software
  - **MBOC** Multiplexed BOC
  - **MLE** Maximum Likelihood Estimator
  - **MSS** Mean Sea Surface
  - **NASA** National Aeronautics and Space Administration
  - **NIC 09** New Ionospheric Climatology 2009
  - **OCOG** Offset Centre Of Gravity
  - **OS** Open Service
  - **PCA** Principal Component Analysis
  - **POD** Precise Orbit Determination

- 
- **PRN** Pseudo Random Noise
  - **PRS** Public Regulated Service
  - **QPSK** Quadrature Phase Shift Keying
  - **QZSS** Quasi-Zenith Satellite System
  - **RGP** Réseau GNSS Permanent
  - **RHCP** Right Hand Circularly Polarized
  - **RMS** Root Mean Square
  - **RMSE** Root Mean Square Errors
  - **RRD** Red River Delta
  - **SAR** Synthetic Aperture Radar
  - **SARAL** Satellite with ARgos and ALtiKa
  - **SLR** Sea Level Rise
  - **SNR** Signal to Noise Ratio
  - **SRAL** Synthetic aperture Radar Altimeter
  - **SSA** Singular Spectrum Analysis
  - **SSH** Sea Surface Height
  - **SoL** Safety of Life
  - **TMBOC** Time Multiplexed BOC
  - **USO** Ultra Stable Oscillator
  - **UTC** Coordinated Universal Time
  - **WTC** Wet Troposphere Correction
  - **iCWT** inverse Continuous Wavelet Transform

---

## Remerciements

Pour arriver jusqu'ici aujourd'hui, j'ai dû faire beaucoup d'efforts, avec l'aide et le soutien indispensable de ma famille, des amis et des collègues. Je ne suis pas une doctorante particulièrement forte. À certains moments je me suis sentie incapable de poursuivre mon chemin. Pourtant, à l'heure où j'écris ces mots, je suis en train de faire mes derniers pas pour finaliser cette thèse.

Cette thèse, je la dois à mes professeurs qui m'ont soutenue et ont cru en moi, José Darrozes et Frédéric Frappart, qui ont répondu à toutes mes questions, et sans eux, ce travail n'aurait pas été réussi. Ils m'ont particulièrement accompagnée durant quatre années de mon doctorat. Je les remercie sincèrement pour leurs conseils inspirants, leur intérêt constant, leurs suggestions et leurs encouragements tout au long du travail. Leur dire simplement « Je vous remercie beaucoup » est vraiment trop peu par rapport à ce qu'ils ont fait pour moi. Je tiens à remercier le gouvernement vietnamien, qui en m'attribuant une bourse d'étude durant quatre ans, a permis que je me dédie à la recherche.

Je souhaite remercier le laboratoire GET, qui m'a permis de mener ma recherche dans les meilleures conditions.

Je souhaite également remercier sincèrement M. WÖPPELMANN Guy et M. SOTOLICHIO Aldo qui ont accepté d'être les rapporteurs de cette thèse, pour avoir accordé du temps à une lecture attentive et détaillée de mon manuscrit, ainsi que pour leurs remarques encourageantes et constructives, et je leur suis très reconnaissante. Je tiens également à remercier M. LAIGNEL Benoit, M. YANG Dongkai, Mme. CAZENAVE Anny et M. RAMILLIEN Guillaume pour avoir accepté de participer à mon jury de thèse.

Un grand merci à ceux qui m'ont aidé: tous le personnel du GET, particulièrement à M. Étienne Ruellan, le directeur du GET, et Madame Carine Baritaud, la secrétaire du GET, de m'avoir accueilli durant ces années. Je voudrais également remercier la direction de l'école doctorale SDU2E pour son soutien.

Je voudrais adresser un grand merci à tous les membres de l'équipe de la télédétection et GNRR-R du GET pour m'avoir aidée à terminer mon travail.

Je passe ensuite un remerciement spécial à M. Guillaume Ramillien, pour la gentillesse, les analyses, les commentaires et les conseils qu'il a fait à mon égard durant ma thèse.

Je tiens aussi à mentionner le plaisir que j'ai eu à travailler au GET, et j'en remercie ici tous mes collègues doctorants, Yolande Traoke, Yu Chen, Paty Nakhle et Kassem Asfour.

Je voudrais également remercier tous mes amis vietnamiens à Toulouse, qui m'ont soutenue beaucoup pendant mon séjour en France.

Enfin, j'ai la chance d'avoir l'appui de mes amis et de ma famille, en particulier de mon chéri Minh Cuong et ma fille Bao Lam, tous mes remerciements à ma famille bien aimé. Ce fut ma grande motivation pour travailler. Merci pour être toujours à mes côtés

---

pendant ce temps.

*Grand merci!*  
*Thank you so much!*  
*Xin chân thành cảm ơn!*

---

## Acknowledgements

To get here today, I had to make a lot of effort, with the help and support of my family, friends and colleagues. I'm not a particularly strong doctoral student. At times I felt unable to continue on my way. However, as I write these words, I am taking my last steps to finalize this thesis.

This thesis, I owe it to my professors who supported me and believed in me, José Darrozes and Frédéric Frappart, who answered all my questions, supported me very enthusiastically, and without them, this work would not have been successful. They particularly accompanied me during four years of my doctorate. I sincerely thank them for their inspiring advice, constant interest, suggestions and encouragement throughout the work. Just saying "Thank you so much" is really too little compared to what they did for me.

I would like to thank the Vietnamese government which by giving me a scholarship for four years, allowed me to dedicate myself to my research without having to worry about financing it.

I wish to thank the laboratory GET, allowing me to conduct my research in the best conditions.

I would also like to sincerely thank Mr., ..., who have accepted to be the rapporteurs of this thesis, for having given time to a careful and detailed reading of my manuscript as well as for their encouraging and constructive remarks and I am very grateful to them. I would also like to thank Mr.,..., for agreeing to participate in my thesis jury.

I sincerely acknowledge to everyone who helped me: all the members of the GET, especially Mr. Étienne Ruellan, the director of the GET, and Mrs. Carine Baritaud, the secretary of the GET, for welcoming me during these years.

I would also like to thank the management of the SDU2E doctoral school for their support. I would like to extend my sincere thanks to all members of GET's remote sensing and GNR-R team for helping me finish my work.

I would then pass a special thanks to Mr. Guillaume Ramillien for the kindness, analysis, comments and advice that he gave me during my thesis.

I would also like to mention the pleasure I had in working at GET, and I thank all my doctoral colleagues, Yolande Traoke, Yu Chen, Paty Nakhle and Kassem Asfour.

I would also like to thank all my Vietnamese friends in Toulouse, who supported me a lot during my stay in France.

Finally, I am fortunate to have the support of my friends and family, especially my darling Minh Cuong and my daughter Bao Lam, all my thanks to my beloved family. That was my great motivation to work. Thanks for always by my side during this time.

---

*Grand merci!*  
*Thank you so much!*  
*Xin chân thành cảm ơn!*



# Contents

| Contents   | Page No.  |
|--|-----------|
| <b>GENERAL INTRODUCTION</b>  | <b>1</b>  |
| <b>I Radar Altimetry</b>   | <b>13</b> |
| I.1 Introduction . . . . .   | 14        |
| I.2 Principle of the Radar Altimeter . . . . .                                     | 15        |
| I.2.1 Estimation of the water height . . . . .                                     | 15        |
| I.2.2 Corrections to the Range . . . . .   | 18        |
| I.2.3 Precise orbit determination . . . . .  | 22        |
| I.3 Altimeter waveform . . . . .   | 22        |
| I.3.1 Waveforms identification . . . . .   | 22        |
| I.3.2 Altimeter waveforms over inland waters . . . . .                             | 24        |
| I.3.3 Altimeter waveforms over coastal domains . . . . .                           | 26        |
| I.4 Tracking and Retracking . . . . .  | 27        |
| I.4.1 Retracking algorithms for the study over inland water . . . . .              | 29        |
| I.4.2 Retracking algorithms for the study over coastal areas . . . . .             | 32        |
| I.5 SAR altimetry . . . . .  | 35        |
| I.6 The limitations of altimetry in coastal areas . . . . .                        | 37        |
| I.6.1 Waveform retracking problem . . . . .  | 37        |
| I.6.2 The stall of the altimeter . . . . .   | 38        |
| I.6.3 The correction of the wet troposphere in coastal areas . . . . .             | 39        |
| I.6.4 Surface slope effect . . . . .   | 40        |
| I.7 The different satellite altimetry missions . . . . .                           | 41        |
| I.7.1 Topex/Poseidon, Jason-1, Jason-2, Jason-3 . . . . .                          | 41        |
| I.7.2 ERS-1/2 and ENVISAT . . . . .  | 42        |
| I.7.3 SARAL/AltiKa . . . . .   | 42        |
| I.7.4 Sentinel-3A . . . . .  | 44        |
| <b>II GNSS Reflectometry</b>   | <b>45</b> |
| II.1 Introduction . . . . .  | 46        |
| II.2 State of the art . . . . .  | 50        |
| II.2.1 Principle of GNSS . . . . .   | 50        |
| II.2.2 The ancestor still full of youth: Global Positioning System (GPS) . . . . . | 50        |
| II.2.3 Globalnaya Navigatsionnaya Sputnikovaya Sistema (GLONASS) . . . . .         | 57        |
| II.2.4 New GNSS . . . . .  | 58        |

|   |            |
|---|------------|
| II.2.5 The Positioning measurement . . . . .  | 61         |
| II.3 Reflection of GNSS signals . . . . .   | 65         |
| II.3.1 Multipath . . . . .  | 66         |
| II.3.2 Specular and diffuse reflection . . . . .  | 68         |
| II.4 GNSS Reflectometry (GNSS-R) . . . . .  | 72         |
| II.4.1 GNSS-R measurement technique . . . . .   | 72         |
| II.4.2 Reflectometry through opportunity signals . . . . .  | 78         |
| II.4.3 Reflectometer with single antenna . . . . .  | 83         |
| II.4.4 Application of GNSS-R for altimetry . . . . .  | 86         |
| II.5 Conclusions . . . . .  | 87         |
| <br>  |            |
| <b>III Validation altimetry on coastal zone: example of the Bay of Biscay</b>   | <b>89</b>  |
| III.1 Summary of the article published in Remote Sensing . . . . .  | 90         |
| III.2 Article published in Remote Sensing (11 January 2018) . . . . .   | 92         |
| <br>  |            |
| <b>IV GNSS Reflectometry for detection of tide and extreme hydrological events: example of the Socoa (France), Mekong delta and Red River Delta (Vietnam)</b> | <b>121</b> |
| IV.1 Résumé étendu . . . . .  | 123        |
| IV.2 Introduction . . . . .   | 125        |
| IV.3 State of the art . . . . .   | 129        |
| IV.4 Methodology . . . . .  | 131        |
| IV.4.1 Sea surface height (SSH) derived from GNSS-R signals . . . . .   | 131        |
| IV.4.2 Analysis of the GNSS-R-based SSH using SSA and CWT methods   | 137        |
| IV.5 The Socoa experiment . . . . .   | 144        |
| IV.5.1 Characteristics of the Socoa study area . . . . .  | 144        |
| IV.5.2 Datasets . . . . .   | 145        |
| IV.5.3 SNR-based sea surface height variation estimates . . . . .   | 147        |
| IV.5.4 Complementary between SSA and CWT method to extract the<br>tides components in GNSS-R signals . . . . .  | 149        |
| IV.5.5 Detection the Xynthia storm in the GNSS R signals using SSA and<br>XWT method . . . . .  | 151        |
| IV.6 The Mekong delta experiment (Vietnam) . . . . .  | 153        |
| IV.6.1 Characteristics of the Mekong delta area and experimental conditions   | 153        |
| IV.6.2 Parameters for SNR signals analyzing . . . . .   | 155        |
| IV.6.3 Comparison between the water level derived from GNSS-R and in-<br>situ gauge records . . . . .   | 155        |
| IV.7 Red River Delta (RRD) experiment . . . . .   | 156        |
| IV.7.1 The study area and datasets . . . . .  | 156        |
| IV.7.2 Parameters for SNR signals analyzing . . . . .   | 160        |
| IV.7.3 Results . . . . .  | 162        |

## Contents

---

|  |            |
|--|------------|
| IV.8 Conclusions and perspectives . . . . .  | 164        |
| IV.9 Revised version of the article submitted at Remote Sensing, special issue<br>“Remote Sensing of hydrological Extremes”: . . . . . | 166        |
| <b>V Conclusion and perspectives</b>   | <b>183</b> |
| V.1 Conclusion . . . . .   | 184        |
| V.2 Perspectives . . . . .   | 191        |
| <b>Bibliography</b>  | <b>203</b> |



---

INTRODUCTION

**GENERAL INTRODUCTION**

---

---

## Introduction générale (en français)

L'élévation du niveau des mers, causée par le réchauffement climatique de la planète, a et aura un impact considérable sur les terres côtières de faible élévation non seulement en raison de l'accroissement du risque d'inondation/submersion, mais aussi en raison de l'augmentation de la fréquence des événements extrêmes i.e. tempêtes, surcotes marines (Cooper et al., 2008; FitzGerald et al., 2008; Kirshen et al., 2008). Ces changements impactent déjà diverses régions des conditions climatiques font peser une menace majeure pour la part croissante de la population mondiale vivant dans les régions (Bondesan, 1995; Karim and Mimura, 2008; Tebaldi et al., 2012), ce qui constitue une menace majeure pour la part croissante de la population mondiale vivant dans les régions côtières à quelques mètres au-dessus du niveau de la mer (McGranahan et al., 2007). L'eau de mer envahit de plus en plus la zone côtière, provoquant l'érosion des sols et la salinisation des terres agricoles. Les intrusions d'eau de mer dans les zones humides, et l'augmentation des biseaux salés menacent l'écosystème côtier et induisent une salinisation de plus en plus importante des aquifères.

La surveillance des variations du niveau des mers s'est principalement appuyée sur les mesures in situ des marégraphes en zone côtière. Pour cela nombre de marégraphe mondiaux (90 % selon l'UNSECO en 1983) sont basées sur le principe du marégraphe à flotteur placé dans un puit de tranquillisation qui réduit les hautes fréquences et sont souvent étalonnés par une échelle de marée qui est le système le plus ancien et qui préconisé par l'UNSECO, 1985 et le bureau hydrographique international). Lors des périodes récentes de nouveaux types de marégraphe permettent d'avoir une approche plus globale qui intègre non seulement les marées mais aussi d'autres signaux comme l'hydro-isostasie, les surcharges océaniques, les tempêtes, les tsunamis, les charges atmosphériques etc (WOPPELMANN, 1997; Gouriou, 2012). Ces nouvelles familles de marégraphe : sont par ordre chronologique i) le marégraphe à capteur de pression rendus fiables dès 1964 par Eyries ; ii) les marégraphe à sonde aérienne acoustique qui

mesure le temps de parcours aller-retour d'une onde acoustique entre la sonde et la surface de l'eau et qui étaient très en vogue dans les années 80-90 et qui nécessitait aussi un puit de tranquillisation; iii) les marégraphe Radar dont les évolutions récentes sont les capteurs radar à l'air libre qui s'affranchissent du puit de tranquillisation (Woodworth and Smith, 2003). Depuis le début des années 2000 a vu l'avènement des altimètres radar embarqués sur satellite, qui mesurent le temps de trajet aller-retour du satellite à la surface marine, et permettent une cartographie globale des hauteurs océaniques. Autre point important, même si de nombreux marégraphe sont installés près des côtes, il y a encore peu de houlomètres qui permettent d'obtenir des informations sur l'état de mer. Cependant, le coût élevé de ces types d'instruments et les difficultés rencontrées dans la mise en œuvre des mesures en mer ne permettent que des collectes de données spatiales et temporelles limitées.

Cependant au cours du 20ème siècle, les seules mesures régulières de l'environnement côtier sont les séries marégraphe qui constituent la plus longue série d'observation de la mer connue. Ils fournissent des séries chronologiques des variations du niveau des mers. Ces données ne couvrent pas tous les besoins d'observation de la région et se limitent à la côte.

L'augmentation du nombre d'observations apparaît comme le moyen le plus naturel d'améliorer la connaissance de la zone côtière. C'est pour pallier ce manque de données à l'échelle globale qu'à partir des années 2000, s'est développée, une surveillance planétaire grâce à l'altimétrie satellitaire. La nécessité d'observations plus fréquentes et/ou spatialement plus denses est impérative sur la zone côtière où "s'accumule" environ 70% de la population mondiale.

### ***Observation altimétrique spatiale***

Les observations satellitaires se sont fortement développées au cours des années 1990. Le premier altimètre sur Skylab 3 (1973) avait une précision de 0,6 m (Fu et al., 1988; Frappart et al., 2017). Ses données ont été principalement utilisées pour la détermination du géoïde marin. Il a été suivi par les lancements des satellites Geosat (1985-1990) et ERS-

---

1 (1991-2000), puis par le lancement Topex-Poseidon (1992-2005), qui a ouvert l'ère de l'altimétrie de haute précision, et ces satellites ont marqué un tournant dans l'étude des mouvements océaniques. De plus, ces dernières années, les techniques basées sur la télédétection spatiale ont été utilisées pour étudier non seulement les variations des stocks d'eau océaniques mais aussi celles des grands bassins hydrographiques, ce qui a permis d'obtenir des variations spatiotemporelles des stocks d'eaux continentaux. En fournissant des mesures rapides, complètes et répétées de la surface de l'océan, ces données ont véritablement révolutionné l'histoire de l'océanographie physique moderne. Cependant, ces outils, basés sur les outils de la télédétection, présentent une résolution temporelle médiocre et une distance inter-trace généralement assez grande (par exemple, de 315 km à l'équateur pour TOPEX/Poséidon).

### ***Observations du niveau des mers avec le GNSS***

Une méthode qui tend à se développer depuis les quinze dernières années est celle qui consiste à utiliser des bouées GNSS qui ont montré leur utilité pour calibrer et valider les missions d'altimétrie spatiale (M Watson et al., 2004). Un autre avantage de ces bouées c'est qu'elles enregistrent les différentes composantes de la marée, avec une précision centimétrique proche de celle des marégraphes classiques, mais aussi les signaux haute fréquence. Enfin, autre aspect non négligeable elles permettent de s'affranchir de la zone côtière et peuvent être placées en pleine mer ce qui évitera d'inclure les mouvements verticaux de croûte auxquels sont rattachés les marégraphes côtiers (Blewitt et al., 2010). Bien qu'initialement destiné à la navigation et au positionnement, le GPS (Global positioning system), devenu GNSS (Global Navigation Satellite System) avec l'avènement de nouvelles constellations (GLONASS, BEIDOU, GALILEO) a évolué pour être utilisé de manière opportuniste dans de nombreuses autres applications qui utilisent les signaux des satellites GNSS pour déduire d'autres propriétés ou caractéristiques de la Terre, comme l'épaisseur de neige ou l'humidité du sol (Motte et al., 2016). Avec la modernisation et la densification des constellations GNSS on observe une augmentation drastique des signaux

d'opportunité exploitables. La télédétection GNSS, à partir des signaux réfléchis, est un exemple de ces applications qui permettent aussi de regarder les variations du niveau des mers. Bien que la propagation des trajets réfléchis est considérée comme une source d'erreur en positionnement GNSS, elle a aussi pu être utilisée avec succès pour faire de l'altimétrie selon une technique appelée réflectométrie GNSS ou GNSS-R ([Martin-Neira, 1993](#)). Le GNSS-R est un outil de télédétection prometteur qui répond aux exigences de couverture spatiale élevée, d'un temps de revisite temporel court, d'un faible coût et d'un faible poids car les capteurs GNSS-R sont des systèmes passifs simples et économiques. En océanographie, les informations sur la position de l'antenne/récepteur et les propriétés physiques de la surface réfléchissante peuvent être utilisées pour produire divers paramètres tels que : la rugosité de surface, la hauteur de la surface de l'océan, la vitesse et la direction du vent, les variations de salinités et même d'identifier la glace de mer.

Récemment, avec l'augmentation des phénomènes météorologiques extrêmes et l'élévation du niveau des mers, les populations du monde entier vont être fortement impactées, en particulier celles de la frange côtière. Pour cette raison, la densification des capteurs et des observations est cruciale pour établir des systèmes de surveillance et d'alerte bien structurés, afin d'assurer la sécurité des populations. Dans cette thèse, j'ai combiné l'utilisation d'observations *in situ*, de mesures altimétriques satellitaires et de données GNSS-R, qui permettent d'établir une couverture géographique à différentes échelles depuis la mesure locale jusqu'aux données globales ceci pour une répétitivité temporelle élevée, continue dans le temps, qui sont indispensables pour la surveillance des événements extrêmes, de la dynamique côtière et même des marées si l'on peut extraire les hautes fréquences indépendantes du signal de marée.

### ***Structure de la thèse***

Ce manuscrit se compose de 4 chapitres:

- Chapitre 1 : Ce chapitre décrit l'altimétrie par satellite, son principe

---

général et les différents aspects physiques de la mesure océanique. Les principales missions altimétriques en cours (Topex/Poséidon, ERS-1&2, Jason-1, ENVISAT, Jason-2, SARAL, Jason-3 et Sentinel-3) sont aussi présentées. Ce chapitre se concentre sur l'estimation des niveaux d'eau et présente les limites actuelles de l'altimétrie.

- Chapitre 2 : Le deuxième chapitre se concentre sur l'état de l'art de la technique GNSS-R, et se focalisera plus particulièrement sur les applications de la réflectométrie GNSS pour l'estimation des niveaux d'eau à partir du SNR de récepteurs mono-antenne classique.
- Le troisième chapitre montre une analyse réelle de l'évolution des performances des missions altimétriques, ERS-2, SARAL, etc. pour l'estimation du niveau des mers dans le golfe de Gascogne. Les résultats montrent une nette amélioration de la qualité des données altimétriques SSH dans un rayon de 50 km de la côte voir moins pour les missions les plus récemment mises en orbite, ces résultats sous forme d'article publié dans la revue internationale "Remote Sensing" ([Vu et al., 2018](#)).
- Le quatrième chapitre porte sur le traitement des signaux SNR mesurés par une antenne GNSS géodésique pour le suivi des variations des niveaux d'eau sur différents exemple : i) la baie de Socoa (France), ii) delta du Mékong et iii) delta du Fleuve Rouge (Vietnam). Dans ces différents exemples, le signal SNR a été utilisé pour décrypter les signaux des marées et des inondations mais aussi d'évènements extrêmes souvent très rapides.
- Enfin, le cinquième chapitre compile les principaux résultats obtenus dans cette thèse et présente les différentes perspectives offertes par l'altimétrie satellitaire et le GNSS-R.

### General introduction (in english)

Rising sea levels, caused by global warming, have and will have a significant impact on low-lying coastal lands not only because of the increased risk of flooding/submersion, but also because of the increase in the frequency of extreme events i.e. storms, marine surges (Cooper et al., 2008; FitzGerald et al., 2008; Kirshen et al., 2008). These changes impact already various regions (Bondesan, 1995; Karim and Mimura, 2008; Tebaldi et al., 2012), which constitutes a major threat to the growing share of the world population living in coastal areas a few meters above the sea level (McGranahan et al., 2007). Seawater is increasingly invading the coastal zone, causing soil erosion and salinization of agricultural land. Seawater intrusions into wetlands and increased salt wedges threaten the coastal ecosystem and induce increasing salinization of aquifers.

Monitoring sea level variations has historically been achieved using *in situ* measurements of tide gauges in coastal zone. For this purpose, many of global tide gauges (90% according to UNSECO in 1983) are based on the principle of the float tide gauge placed in a stilling well that reduces high frequencies and are often calibrated by a tidal scale, which is the oldest system and advocated by UNSECO, 1985 and the International Hydrographic Bureau. In recent periods, new types of tide gauges made it possible to have a more global approach that includes not only tides but also other signals such as hydro-isostasy, oceanic overloads, storms, tsunamis, atmospheric loads, etc. (WOPPELMANN, 1997; Gouriou, 2012). These new tide gauge families: are in chronological order i) the pressure sensor tide gauge made reliable by Eyries in 1964; ii) the acoustic aerial probe tide gauge which measures the travel time of an acoustic wave between the probe and the water surface, which was very popular in the 1980s and 1990s and which also required a stilling well; iii) Radar tide gauges whose recent developments are the open air radar sensors which do not require a stilling well (Woodworth and Smith, 2003). Since the early 2000s, altimetry radar have been developed, which measure the travel time from the satellite to the sea surface and allow global mapping of ocean heights.

---

Still in modern techniques we can also talk about GNSS buoys which have proven their usefulness in calibrating and validating space altimetry missions (M Watson et al., 2004). Another important point, even though many tide gauges are installed near the coast, there are still few swell that provide information on sea state. However, the high cost of these types of instruments and the difficulties encountered in implementing measurements at sea only allow limited spatial and temporal data collection.

However, during the 20<sup>th</sup> century, the only regular measurements of the coastal environment are the tide gauge series, which constitute the longest known series of observations of the sea. They provide time series of the sea level changes. These data do not cover all the observation needs and are limited to the coast.

Increasing the number of sightings is the most natural way of improving knowledge of the coastal zone. It is to overcome this lack of data on a global scale that from the 2000s, a global monitoring has developed thanks to the satellite altimetry. The need for more frequent and/or spatially dense observations is imperative in the coastal zone where about 70% of the world's population is "accumulating".

### ***Satellite altimetry observation***

Space altimetry observation developed strongly during the 1990s. The first altimeter on Skylab 3 (1973) had an accuracy of 0.6 m (Fu et al., 1988; Frappart et al., 2017). These data were mainly used for the determination of the marine geoid. It was followed by the launches of the satellites Geosat (1985-1990) and ERS-1 (1991-2000), followed by the launch of Topex-Poseidon (1992-2005), which opened the era of high precision altimetry, and these satellites marked a turning point in the study of oceanic displacements. In addition, in recent years, remote sensing-based techniques have been used to study not only changes in oceanic water stocks but also those of large continental watersheds, which have resulted in spatio-temporal changes in water stocks of continental waters. By providing rapid, complete and repeated measurements of the ocean surface, these data have truly revolutionized the history of modern physical oceanography. How-

ever, these tools, based on remote sensing, have a poor temporal resolution and a generally large inter-track distance (*e.g.* from 315 km to the equator for TOPEX/Poseidon).

### ***Sea level observations with GNSS***

One method that has tended to develop over the past fifteen years is the use of GNSS buoys that have proven useful in calibrating and validating space altimetry missions ([M Watson et al., 2004](#)). Another advantage of these buoys is that they record the different components of the tide, with a centimeter accuracy close to that of conventional tide gauges, but also high frequency signals. Finally, another important aspect is that they make it possible to avoid the coastal zone and can be placed in the open sea, which will avoid including the vertical crust movements to which coastal tide gauges are attached ([Blewitt et al., 2010](#)). Although originally intended for navigation and positioning, the GPS (Global positioning system), now GNSS (Global Navigation Satellite System) with the advent of new constellations (GLONASS, BEIDOU, GALILEO) has evolved to be used opportunistically in many other applications that use GNSS satellite signals to infer other properties or characteristics of the Earth, such as snow depth or soil moisture ([Motte et al., 2016](#)). With the modernization and increasing amount of GNSS constellations, there is a drastic growth in usable opportunity signals. GNSS remote sensing, based on reflected signals, is an example of these applications that also allow us to look at sea level variations. Although the propagation of reflected paths, known as GNSS reflectometry (GNSS-R), is considered as a source of error in GNSS positioning, GNSS-R has also been successfully used to make altimetry ([Martin-Neira, 1993](#)). GNSS-R is a promising remote sensing tool that fulfills the requirements of high spatial coverage, short revisit period, low cost/low weight systems because GNSS-R sensors are simple, passive and economic systems. In oceanography, antenna/receiver position information and the physical properties of the reflective surface can be used to produce various parameters such as: surface roughness, ocean surface height, velocity and the direction of the wind, the variations of salinity

---

and even to identify the sea ice.

Recently, with the increase in extreme weather events, and rising sea levels, people around the world will be heavily impacted, especially those on the coastal fringe. For this reason, the growth of the amount of sensors and observations is crucial for establishing well-structured monitoring and warning systems to ensure the safety of populations. In this thesis, I have combined in situ observations, satellite altimetry measurements and GNSS-R data, which allow geographic coverage to be established at different scales (from local measurement to global data) with a high temporal repeatability, continuous over time, which are essential for monitoring extreme events, coastal dynamics and even tides if the high frequencies independent of the tidal signal can be extracted.

### ***Thesis Structure***

This manuscript consists of 4 chapters:

- Chapter 1: This chapter describes satellite altimetry, its general principle and the different physical aspects of ocean measurement. The main current altimetry missions (Topex/Poseidon, ERS-1&2, Jason-1, ENVISAT, Jason-2, SARAL, Jason-3 and Sentinel 3) are also presented. This chapter focuses on estimating water levels and highlights the current limitations of altimetry.
- The second chapter focuses on the state-of-the-art of the GNSS-R technique, and will focus more particularly on the applications of GNSS reflectometry for the estimation of water from the SNR of conventional mono-antenna receivers.
- The third chapter shows a real analysis of the performance of radar altimetry from ERS-2 to SARAL in the Bay of Biscay. Altimetry-based SSH from former missions was compared to tide gauge measurements acquired along the French Atlantic Coast in the Southern Bay of Biscay. The results show a significant improvement in the quality of the altimetry-derived SSH data within 50 km from the coast for the more

recent missions. These results are published in the form of an article in the international journal "Remote Sensing" ([Vu et al., 2018](#)).

- The fourth chapter deals with the processing of GNSS SNR signals measured by a geodesic antenna for the monitoring of the variations of the water levels on various examples: i) Socoa Bay (France), ii) the Mekong Delta; and iii) the Red River Delta (Vietnam). In these different examples, the SNR signal has been used to decrypt tide and flood signals as well as extreme events that are often very fast.
- Finally, the fifth chapter compiles the main results obtained in this thesis and presents the different perspectives offered by satellite altimetry and GNSS-R.



---

CHAPTER I

# Radar Altimetry

---

## Contents

---

|            |  |           |
|------------|--|-----------|
| <b>I.1</b> | <b>Introduction</b> . . . . .                                    | <b>14</b> |
| <b>I.2</b> | <b>Principle of the Radar Altimeter</b> . . . . .                | <b>15</b> |
| I.2.1      | Estimation of the water height . . . . .                         | 15        |
| I.2.2      | Corrections to the Range . . . . .                               | 18        |
| I.2.3      | Precise orbit determination . . . . .                            | 22        |
| <b>I.3</b> | <b>Altimeter waveform</b> . . . . .                              | <b>22</b> |
| I.3.1      | Waveforms identification . . . . .                               | 22        |
| I.3.2      | Altimeter waveforms over inland waters . . . . .                 | 24        |
| I.3.3      | Altimeter waveforms over coastal domains . . . . .               | 26        |
| <b>I.4</b> | <b>Tracking and Retracking</b> . . . . .                         | <b>27</b> |
| I.4.1      | Retracking algorithms for the study over inland water . . . . .  | 29        |
| I.4.2      | Retracking algorithms for the study over coastal areas . . . . . | 32        |
| <b>I.5</b> | <b>SAR altimetry</b> . . . . .                                   | <b>35</b> |
| <b>I.6</b> | <b>The limitations of altimetry in coastal areas</b> . . . . .   | <b>37</b> |
| I.6.1      | Waveform retracking problem . . . . .                            | 37        |
| I.6.2      | The stall of the altimeter . . . . .                             | 38        |
| I.6.3      | The correction of the wet troposphere in coastal areas . . . . . | 39        |
| I.6.4      | Surface slope effect . . . . .                                   | 40        |
| <b>I.7</b> | <b>The different satellite altimetry missions</b> . . . . .      | <b>41</b> |
| I.7.1      | Topex/Poseidon, Jason-1, Jason-2, Jason-3 . . . . .              | 41        |
| I.7.2      | ERS-1/2 and ENVISAT . . . . .                                    | 42        |
| I.7.3      | SARAL/AltiKa . . . . .   | 42        |
| I.7.4      | Sentinel-3A . . . . .  | 44        |

---

## I.1 Introduction

The Earth is a complex ecosystem where millions of living species, including humans, are strongly impacted by the water cycle. This cycle has also an impact on oceans because they cover 71% of our planet. Multiple physical phenomena have a direct impact on our lives and occur on this planet that is constantly evolving. Some these phenomena can rapidly modify its equilibrium such as earthquakes that can cause tsunamis, or on longer time-scale as global warming which has an effect on the increase in the height of the sea surface, ice melting ([Mimura, 2013](#); [Senior et al., 2002](#)), natural hazard like earthquakes that can cause tsunamis and the displacement of warm oceanic masses that lead to El Niño climatic events. Earth climate is also subject to long-term oscillations such as El Niño Southern Oscillation (ENSO) that has a strong effect on the different fluxes and reservoirs of the global hydrological cycle ([Grimm and Tedeschi, 2009](#); [Trenberth and Hoar, 1996](#)). So, in order to study them, we must observe their effects on the ocean surface, which is achieved by the radar altimetry. Indeed, the main goal of radar altimetry is the measurement of the surface topography of the ocean.

An altimeter is a radar instrument that emits electromagnetic (EM) pulse and records the round-trip time, amplitude, and shape of each return signal after reflection on the Earth's surface. This instrument measures the distance between the satellite and the sea surface. In order to obtain sea surface height (SSH), several corrections to the range due to the atmosphere, the environment, and the instrument need to be taken into account. These measurements are of great importance and intervene in various applications such as sea level changes, geostrophic current determination or bathymetry estimates. Since the beginning of the high precision altimetry era, which started in 1991 with the launch of ERS-1, a lot of technical improvements in terms of sensors and orbit determination contributed to higher accuracy of the altimetry-based height estimates.

In the coastal zones, the satellite altimetry data within 20 km from the

coast cannot be used, due to the interaction of the radar signal with land topography, inaccuracy in some of the geophysical adjustments and the rapid changes in sea level. In order to optimize the completeness and the accuracy of the sea surface height information derived from satellite altimetry in coastal ocean areas, the X-TRACK system has been developed by the Center of Topography of the Ocean and Hydrosphere in Toulouse (CTOH - LEGOS) to improve classical altimetry over oceans and land surfaces (Birol et al., 2016; Stammer et al., 2017) (F. Birol, 2017; Stammer, et al., 2017). Similar, MAPS (Multi-mission Altimetry Processing Software) is a software developed to process altimetry data on lakes, rivers and flood zones to calculate water time series (Frappart et al., 2015). Currently, MAPS software has been upgraded to improve the quality of the satellite altimetry data on coastal areas as well as land surfaces. We used the MAPS software to process multi-satellite altimetry data for the Bay of Biscay (see in the chapter III).

This chapter, first of all, presents the principle of the radar altimetry and the processing chain to estimate the SSH from the altimetry measurements. The characteristics of the altimeter waveforms and retracking algorithms are then described over inland waters and coastal domains. Finally, I will present the various altimetry missions used, in this work, to measure sea surface height.

## I.2 Principle of the Radar Altimeter

### I.2.1 Estimation of the water height

The principle of spatial altimetry is illustrated in Fig. I.1. The radar altimeter emits an EM pulse towards the ocean surface and measuring their reflections using the backscattering coefficient well-known as sigma nought ( $\sigma^0$ ). Altimetry satellites determine the distance between the satellite and the reflecting sea surface, is called range (R), thanks to the two-way travel time of the signal ( $\Delta t$ ). The speed of the wave is known ( $c$  is the velocity of

light) and the round-trip time is measured. It is derived from the equation (Chelton et al., 2001):

$$R = \frac{c \cdot \Delta t}{2} \quad (\text{I.1})$$

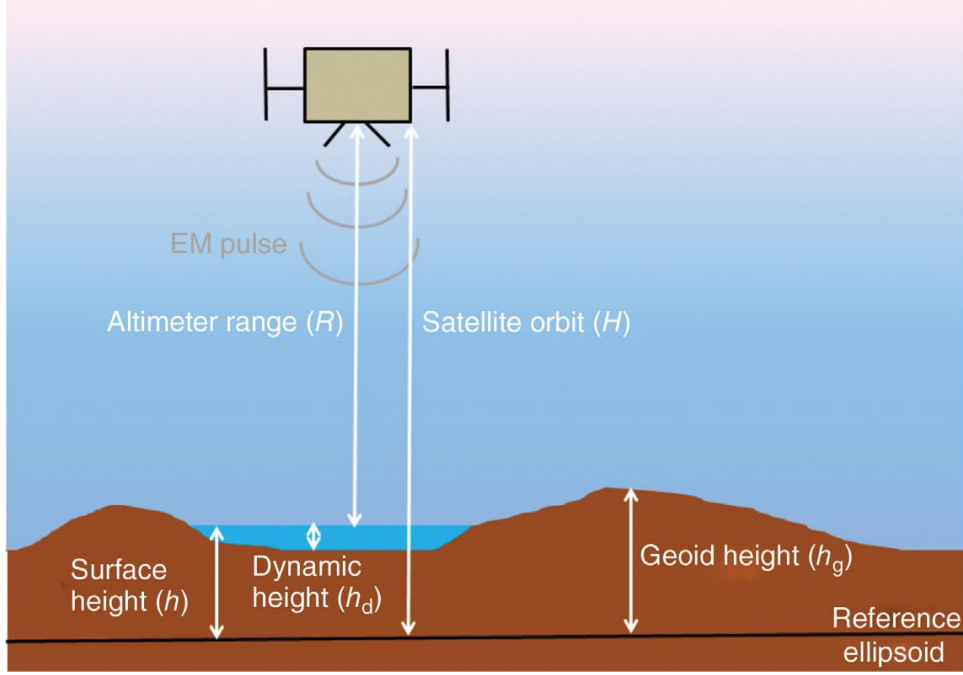


Figure I.1 – Principle of satellite altimetry (Frappart et al., 2017)

The height of the reflecting surface ( $h$ ) relative to the reference ellipsoid is the difference between the orbital height ( $H$ ) and the instantaneous height measurements ( $R$ ):

$$h = H - R + \sum_j \Delta R_j \quad (\text{I.2})$$

where  $\Delta R_j$  is the sum of the instrument corrections, propagation corrections, geophysical corrections and surface corrections, which will be presented detail in § II.2. The height  $h$  is calculated as the sum of two components: the height of the geoid  $h_g$  relative to the reference ellipsoid and the average dynamic topography  $h_d$ . The geoid is a physical equipotential surface of terrestrial gravity which corresponds to the average level of the oceans. The average dynamic topography is due to the large and

medium stationary ripples of the ocean surface. The Range ( $R$ ) is measured from the return echo received by the altimeter. The amplitude and shape of the echoes contain characteristic information of the reflecting surface. The area of the intersection of the sea surface and the wave increases to a constant value. The shape of the return pulse is a function of the roughness of the sea surface. Over the ocean, the waveform transmits important information about the state of the sea, such as wave height or speed surface winds (Stammer et al., 2017).

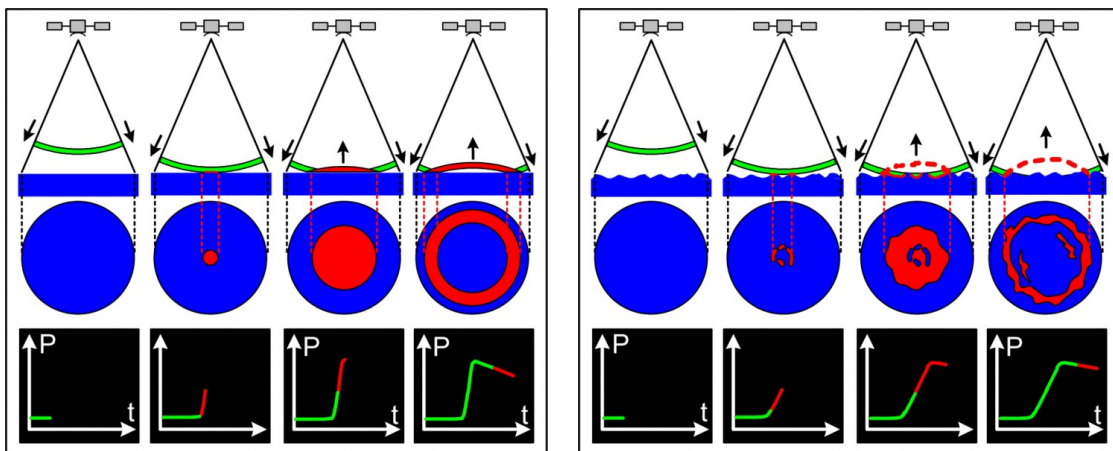


Figure I.2 – Principle of the waveform analysis (CNES)

The diagram in Fig. I.2 shows how the return wave is formed. As the pulse reaches the surface observations, the illuminated surface then increases linearly until a disk-like surface. The power of measurement directly correlated with the illuminated surface. As soon as the impulse enters the ocean, the curvature of the pulses leads to the surface being illuminated in the form of increasingly small surfaces (Fig. I.2 left). The measured power then decreases linearly. In the case of a rough sea surface (Fig. I.2 right), the echo formation mechanism is similar but with weaker ascending and descending slopes. Indeed, the first illuminated surfaces correspond to the peaks of the waves. Gradually, as the pulse illuminates more and more waves, the measured power increases linearly reaching a maximum when the hollows of the waves at nadir (shortest distance between the satellite and the ocean) are illuminated.

In addition to the measurement of the distance between the satellite

and the ocean, the altimetry echoes make it possible to determine the average height of the waves taking into account this correlation.

### I.2.2 Corrections to the Range

The signals emitted and picked up by the radar cross an environment that is not empty. During its round trip through the atmosphere, some elements such as electrons present, the dry area of the atmosphere and the water vapor, slow down the speed of propagation of the wave and increase the wave path. These phenomena can lead to an overestimation of the range up to 2.5 m. It is, therefore, necessary to apply propagation corrections to obtain a correct determination of the range. In addition, the deformation of the solid Earth is the effect of the attraction of the Moon and the Sun and the variation in the orientation of its axis of rotation, also modify in the precise estimate of the range with an error of the length  $\sim 20$  cm. These are well-known as geophysical corrections. Some of these corrections are considered directly by the satellite thanks to specific instruments installed on board, other corrections are deduced on the ground using climatological models (Chelton et al., 2001). On the other hand, changes in sea level due to tides or the response to atmospheric pressure must be removed from the altimeter measurement.

#### I.2.2.1 Propagation corrections

The propagation time of the signal by the altimeter must be best known. However, the radar echo crosses the ionosphere and the troposphere which have a delaying effect on the speed of propagation and lead to systematic errors on the calculated sea level. It is, therefore, necessary to correct the measures of raw distances.

**Ionosphere correction:** The refraction of EM waves in the Earth's ionosphere is caused by the presence of free electrons and ions at altitude above 100 km. These electrons and ions delay the propagation of the EM wave proportionally to the electron density (referred as total electron content or

TEC) in the ionosphere. The diffusion of the radar signal by the electrons contained in the ionosphere can prolong the distance from 2 to 30 mm (Frappart et al., 2006b) depending on the satellite elevation. The ionosphere range correction is also inversely proportional to the square of the radar frequency (Imel, 1995)

$$\Delta R_{ion} = -\frac{kTEC}{f^2} \quad (I.3)$$

where  $k = 0.04025m \text{ GHz}^2 \text{ TECU}^{-1}$ , with the TEC Unit or TECU equals to  $10^6$  electrons  $m^{-2}$ . This correction can be determined from measurements carried out by dual-frequency positioning systems aboard satellites, using the difference in the range at the two frequencies provides a noisy estimate of the TEC. This dual-frequency method is used to correct the range for the refraction of the ionosphere over the ocean. Over land and ice sheets, the EM wave can penetrate the surface. The penetration depth is function of the nature of the surface and can reach several meters (Chelton et al., 2001). The penetration is also different in the two frequency bands. So, over these surfaces, the difference in range of the two frequencies cannot be used to correct the delay introduced by the ionosphere. Therefore, the ionosphere corrections to the range are estimated using Global Ionospheric Map model (GIM). These GPS-derived global ionosphere maps (GIM) can be interpolated in space and time to the altimeter ground track and come close to the accuracy of the dual-frequency altimeters.

The NIC09 ionosphere climatological model is based on the GIMs for 1998–2008 and can also be applied to all single frequency altimeter data prior to 1998 (Scharroo and Smith, 2010)

Another way of estimating TEC is using the Doppler Orbitography and Radiopositioning Integrated by Satellite (DORIS) system, used a mono-free combination of the measurements (pseudo-range or phase) to remove the first order ionospheric effect. However, this method lacks accuracy compared to GIM mode, the production of DORIS ionosphere maps has

ceased ([Chelton et al., 2001](#))

**Dry troposphere correction:** Below the ionosphere, altitude from 0 to 15 km is the troposphere. The permanent gases of the atmosphere (oxygen, nitrogen), modify the atmospheric reflective index and slow down the electromagnetic radiation emitted by the altimeter, causing an error on the altimeter measurement of the order of 2.30 m at sea level. This correction calculated on the ground from meteorological models such as the ECMWF model (European Center for Medium-range Weather Forecast) ([Trenberth and Olson, 1988](#)).

**Wet troposphere correction:** Water vapor content in the atmosphere also causes a slowing down of the radar wave. This effect cause errors of  $\sim 15$  cm on the altimeter measurement ([Chelton et al., 2001](#)). The value of the correction is determined using the measurements of the radiometer present on board the satellite. Nevertheless, this correction is effective only on the oceans. In fact, on the inland waters and the coastal zones ( $< 50$  km), radiometric data are “polluted” when flying over the land. Consequently, the corrections given by the radiometer are useless for calculating the correction of wet troposphere on inland waters and coastal zones. The wet troposphere corrections are therefore deduced from the meteorological models such as the model ECMWF.

### I.2.2.2 Instrumental corrections

The quality of the altimeter measurement will also depend on the reliability and the precise determination of the radar measurement. The altimeter range instrumental correction is the sum of the following instrumental corrections ([Chelton et al., 2001](#)):

- Doppler correction
- USO (Ultra Stable Oscillator) drift correction
- Internal path delay correction
- Distance from antenna to center of gravity

- Modelled instrumental errors correction
- System bias

### I.2.2.3 Geophysical corrections

Geophysical corrections must be added to the range measurement to correct this range due to the tides (ocean, solid earth, polar tides and loading effects).

**Solid earth tide:** is the response of the solid Earth to gravitational attractions of the Moon and the Sun, this phenomena is known as the solid earth tide. The magnitude of the solid earth tide ranges up to  $\pm 20$  cm when using closed formulas as described in ([Wahr and et al., 1981](#); [Edden et al., 1973](#); [Cartwright and Tayler, 1971](#)).

**Pole tides:** The variation of both the solid Earth and the oceans to the centrifugal potential that is generated by small perturbations to the Earth's rotation axis, produce a signal in sea surface height at the same frequency, called the pole tide ([Wahr, 1985](#)). The pole tide has an amplitude of 2 cm over a few months.

**Rapid fluctuations of the atmosphere:** The range is also affected by the load of the atmospheric pressure. For low pressure conditions, the sea level rises, whereas for high pressure conditions, the sea level decreases. This is called inverted barometer effects (IB), any change of atmospheric pressure deforms the sea water/air interface an increase in barometric pressure of 1 mbar corresponds to a fall in sea level of 0.01 m ([Wunsch and Stammer, 1997](#)).

### I.2.2.4 Sea Surface corrections

The Sea State Bias (SSB) is an altimeter ranging error due to the time-varying physical effect of the sea surface to corresponding wave height and wind speed differences ([Chelton et al., 2001](#); [Frappart et al., 2017](#)). This bias consists of three interrelated effects: an electromagnetic bias or radar scattering bias (EMB), a range tracking bias and a skewness

bias. The EMB is physically related to the distribution of the specular facets (Vignudelli et al., 2011). The range tracking bias is related to the tracker used to estimate the significant wave height (SWH) derived from the waveform (Brown, 1977). The elevation skewness bias is the difference between median sea level used median tracker and the real mean sea level.

#### I.2.3 Precise orbit determination

Satellite orbits reference to an ellipsoid need to be accurately determined using the Precise Orbit Determination (POD) technique based on the force perturbation models on the satellite and tracking systems such as the DORIS tracking system and supplemented by different services of satellite constellations such as GNSS (Frappart et al., 2017). It is an orbitography and localization system based on a network of 52 beacons distributed around the world and using Doppler measurements related to the movement of the satellite in its orbit. The DORIS system is installed on Spot satellites as well as the JASON-1/2, Envisat, Cryosat, AltiKa and the new missions like JASON-3 and Sentinel 3. In addition, GPS and laser positioning systems are also used. The GPS measurements obtained are integrated into an orbit calculation model that restores the distance between the satellite and the reference ellipsoid with an accuracy of a few centimeters (approximately 2 cm for T/P and JASON-1). It is truly thanks to the considerable reduction in orbit error that altimetry satellites can now measure centimeter variations in ocean or inland water levels (Fig. I.3).

## I.3 Altimeter waveform

### I.3.1 Waveforms identification

The raw data of altimetry satellites is in the form of wave, it is called a waveform. The magnitude and shape of the waveforms contain information about the characteristics of the surface are described in the Fig. I.4 (Brown, 1977; Hayne, 1980). From this shape, six parameters can be

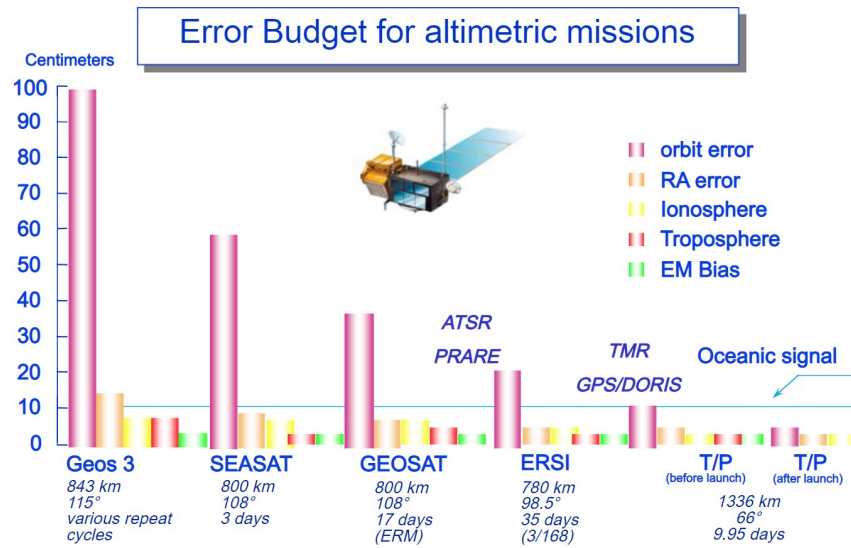


Figure I.3 – Error budget for altimeter missions (©LEGOS/CNRS)

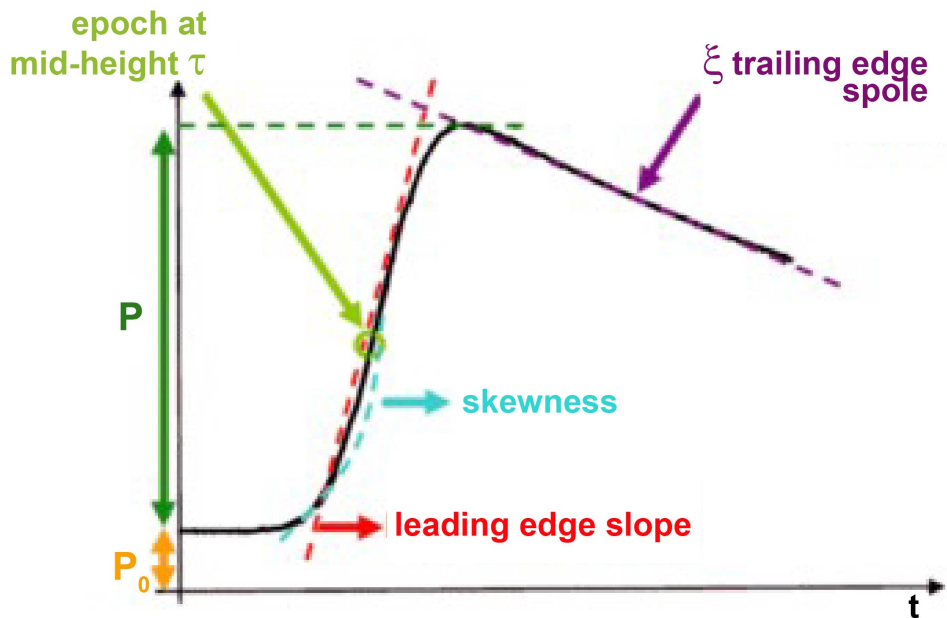


Figure I.4 – Theoretical ocean waveform from the Brown model (Brown, 1977) and its characteristics (©AVISO/CNES)

deduced:

- Epoch at the mid-height ( $\tau$ ): the position of the mid-power point (knee point) of the waveform at the middle of the analysis window.
- The power of the echo (P): the amplitude of the useful signal.
- Thermal noise power ( $P_o$ ): is followed by a rapid rise of returned power called "leading edge", and a gentle and sloping plateau known as "trailing edge".
- Leading edge slope: significant wave height (SWH).
- Skewness: the leading edge curvature
- Trailing edge slope ( $\xi$ ): related to the deviation from the nadir of the radar pointing.

The shape of the return radar waveform depends on the surface roughness function, which can be described as a function of the delay time. Over the ocean, most return waveforms are Quasi-Brown waveform with a shape and stable narrow peak. The treatment of the echoes based on the theoretical waveform given by the Brown model ([Brown, 1977](#); [Hayne, 1980](#); [Rodriguez and Martin, 1995](#); [Callahan et al., 2004](#); [Chelton et al., 2001](#)).

#### I.3.2 Altimeter waveforms over inland waters

Over the inland water, the waveforms are more complex related to slope and roughness surface within footprint, which are classified in 4 categories ([MAJ et al., 1986](#); [Guzkowska et al., 1990](#); [Berry et al., 2005](#)): Oceanic (Quasi-Brown model), Quasi-Specular, Broad-Peak and multiple-peak (Fig. I.5a,b,c,d, respectively).

- Oceanic (Quasi-Brown) waveforms (Fig. I.5a) are characterized by leading edge with wide noisy plateau descending. They correspond to reflections on flat surfaces of uniform diffusion and are observed

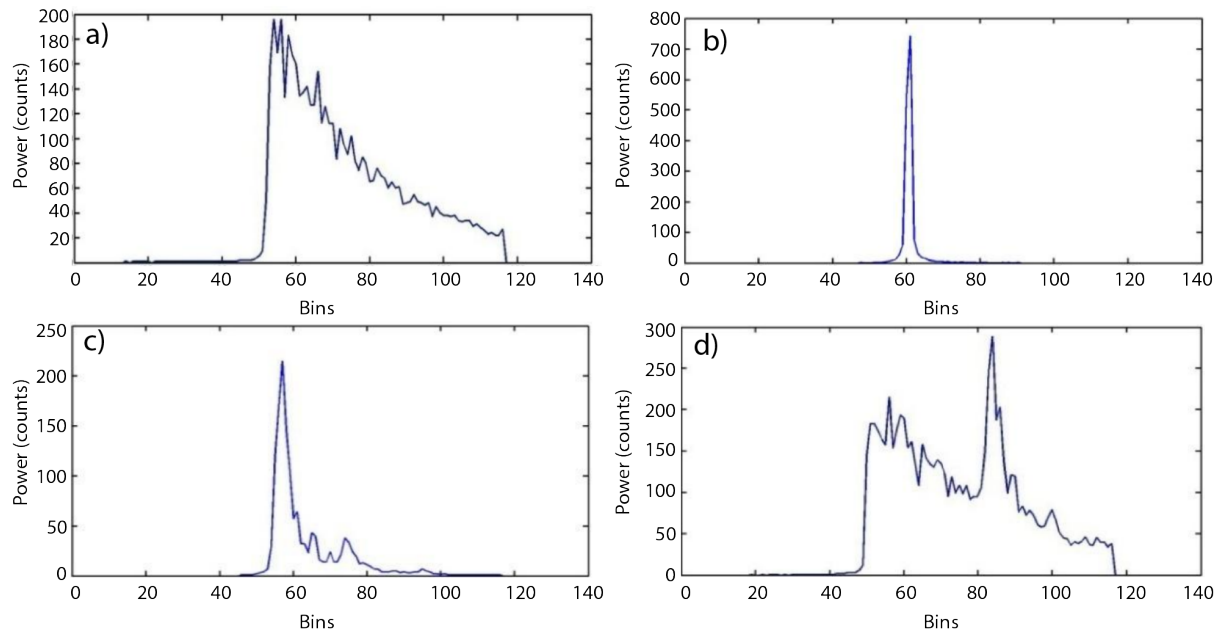


Figure I.5 – Typical waveform shapes over inland water (modified from (Berry et al., 2005)).

over the large lakes, wide rivers or flood plains that the echo is not disturbed by contamination.

- Quasi-Specular waveforms (Fig. I.5b) have a shape vertical leading edge and a rapid decrease of trailing edge. This kind of the waveforms are found on smooth surfaces such as marshes, rivers, or small water bodies.
- Broad peak waveforms (Fig. I.5c) are characterized by slower descending trailing edge than quasi-specular waveforms. This category is formed by the water bodies surrounded by low reflecting surfaces (rivers or small lakes).
- Multiple peak waveform (Fig. I.5d): the echoes with several peaks, where each peak corresponds to the reflection from respective areas covered with water (riverbanks, small lakes...).
- Contamination by land also exists but we discuss about these interferences in the following section.

### I.3.3 Altimeter waveforms over coastal domains

The altimeter waveform in the coastal areas extremely diverse due to the contamination by the vicinity of land (Vignudelli et al., 2011; Gommenginger et al., 2011). In the cases of land/sea or sea/land transitions, the number of gates depends on the height and areal extent of the land within the altimeter footprint (Fig I.6).

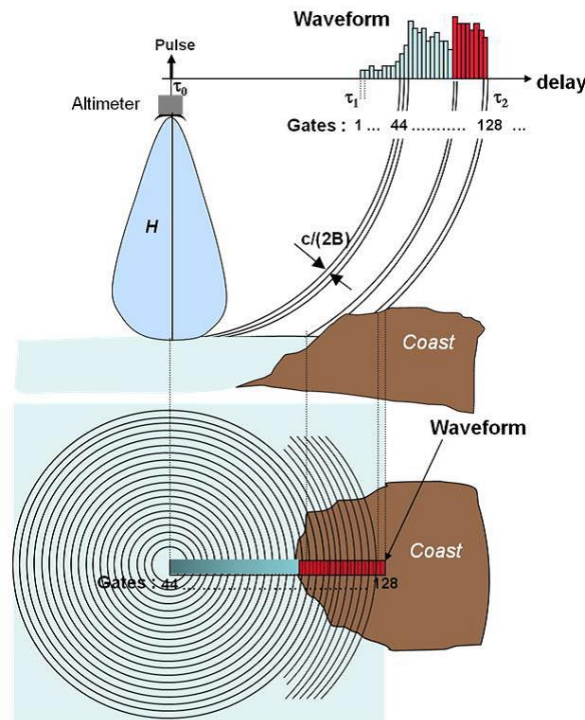


Figure I.6 – Perturbation of the radar waveform by the emerged lands within the altimeter footprint (© CLS).

Over coastal areas, the altimeter waveforms deviate from the Brown model echo about 10 km from the coast. The waveforms are classified according to their shapes (Fig. I.7). Over 15 km from the coast, between 90% and 95% of waveforms are "Brown" echoes (blue curve). This percentage rapidly decreases onshore of 15 km from the coastline. Conversely, the percentage of “peak” echoes rises rapidly onshore off 5 km from the coast (pink curve for peak echoes and red curve for the peak with noise in Fig. I.7). Within 10 km from the coast, the waveform shape classes corresponding to waveforms with a rise in the trailing edge (yellow curve) (Vignudelli

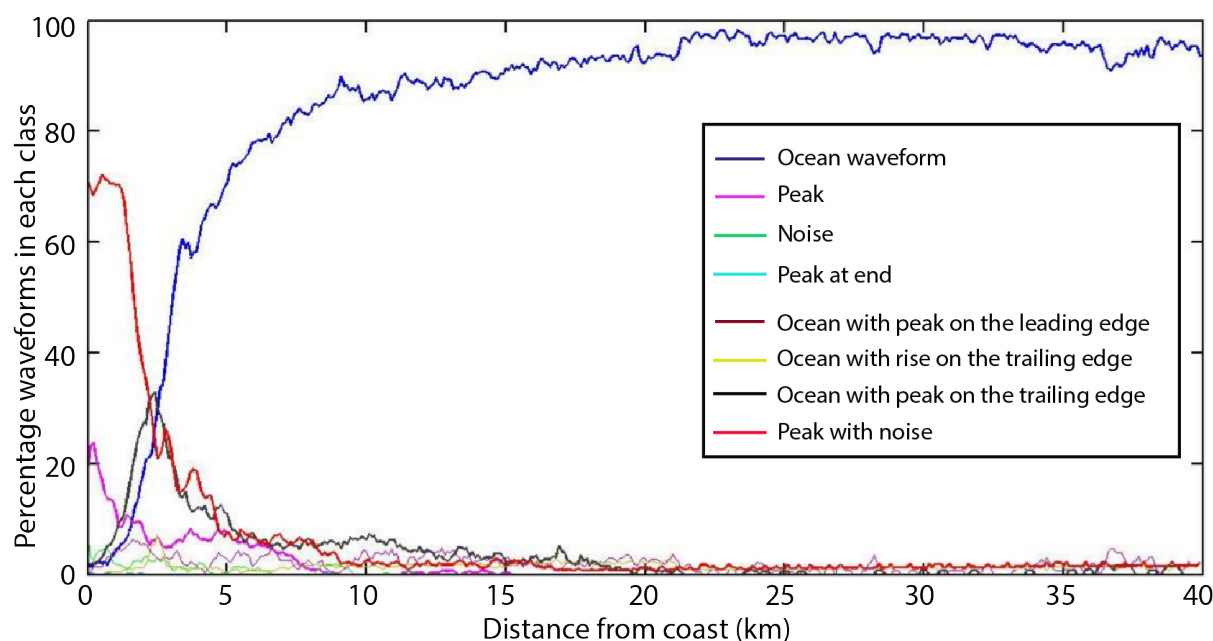


Figure I.7 – Percentage of types echoes encountered in offshore environment (modified from (Thibaut, 2008)).

et al., 2011).

## I.4 Tracking and Retracking

The waveforms are acquired thanks to a tracking system placed on-board the satellite (Chelton et al., 2001). The purpose of the on-board tracker is to keep the position of the middle of the leading edge points to ensure that the echo remains in the reception window. The anticipation system of the measurement makes it possible to minimize the errors. The tracking system is based on the analysis of the parameters of the previous measurement points, this system is effective in a homogeneous medium such as the ocean (Brown, 1977). But echo waveforms on others surface such as continental surface include a lot of configurations which are difficult to process, the altimeter is not able to adapt, in real time, these reception parameters. A few seconds are needed for the altimeter to find a surface where measurements can resume (Chelton et al., 2001). These few seconds are sufficient to no measurement points are recorded over several kilometers.

Since JASON-2, tracking systems have evolved and use a digital elevation model (DEM) to open the reception window depending on the altitude of the nadir point over pre-determined zones.

In order to obtain the highest possible accuracy on range measurements, the final retrieval of geophysical parameters from the waveforms is performed on the ground, called “waveform retracking”. This reprocessing is based on different algorithms developed according to the nature of the surface overflown (*i.e.* ice, sea ice). The final range measurement is obtained by combining the range of the analysis window (the tracker range) with the retrieved epoch obtained by retracking (the position of the leading edge with respect to the fixed nominal tracking point in the analysis window) (Vignudelli et al., 2011). According to Brown’s theoretical model (Brown, 1977), the altimetry waveform can be represented by the double convolution between the radar pulse, the response function of a reflective surface element (comprising the antenna gain) and the distribution function of these surface elements. The power received by the altimeter can be represented by (Rodriguez and Chapman, 1989):

$$P_r(t) = P_e(t) * f_{ptr}(t) * g_{gdf}(z) \quad (\text{I.4})$$

where  $P_r(t)$  is the power received by the altimeter,  $P_e(t)$  is the transmitted power,  $f_{ptr}(t)$  is the function of response of a reflective surface element (including antenna gain),  $g_{gdf}(z)$  is the distribution function of these surface elements. This model is based on the following 5 assumptions (Brown, 1977):

- 1) The diffusing surface is formed of a large number of small independent elements.
- 2) The statistical distribution of the surface heights is assumed constant over the entire illuminated surface.
- 3) Diffusion is a scalar process, without polarization effect and independent of frequency.
- 4) The variation of the diffusion process with the angle of incidence

depends only on the backscattering cross section and the antenna gain.

5) The Doppler effect is negligible compared to the frequency width of the envelope of the transmitted pulse.

Brown's model, which theoretically reconstructs the oceanic echo, is the basis of the algorithm used for the treatment of ocean waveforms. After performing the convolution based on the first order Bessel function, the altimeter received power can be expressed as (Deng and Featherstone, 2006):

$$P(t) = P_N + \frac{1}{2}A\left[\operatorname{erf}\left(\frac{\tau}{\sqrt{2}}\right) + 1\right] \exp\left[-d\left(\tau + \frac{d}{2}\right)\right] \quad (\text{I.5})$$

where  $P_N$  is the altimeter's thermal noise,  $A$  is the amplitude,  $t$  is the time measured, such that  $t = t_0$  corresponds to the time arrival of the half power point of the radar return, and  $\sigma$  is the rise time.  $\tau$  is given as  $\tau = \frac{t - t_0}{\sigma} - d$ , where  $d = \left(\delta - \frac{\beta^2}{4}\right)\sigma$ , and  $\delta = \frac{4c}{\gamma h} \cos(2\xi)$ ;  $\beta = \frac{4}{\gamma} \left(\frac{c}{h}\right)^{\frac{1}{2}} \sin(2\xi)$ ,  $h$  is the modified satellite altitude,  $\gamma$  is an antenna beam width parameter,  $\xi$  is off-nadir angle.

The analytical expression shown in Eq. I.5 is called the 'Ocean Model' which contains five parameters:  $P_N$  is thermal noise,  $A$  is amplitude,  $\sigma$  is rise time, and  $\xi$  is off-nadir angle.

#### I.4.1 Retracking algorithms for the study over inland water

As shown by the results presented in § I.3.2 on the nature of waveforms recorded on inland waters, the radar echoes encountered in the continental domain are very different from those on the ocean. Different reprocessing solutions of waveforms have been developed according to the surface roughness function considered. The main methods used for the study in the continental domain: the threshold methods, the analytical methods and the pattern recognition methods (Frappart et al., 2006a).

I.4.1.1 The threshold methods

- *The Ice-1 algorithm:* The ice-1 waveform reprocessing algorithm has been developed for the study of polar ice caps, and more generally, continental surfaces. This method based on the principle of thresholding, which necessaries the estimation of the amplitude of the waveform. This technique is known as the OCOG (Offset Centre Of Gravity) method developed by Wingham in 1986 (Wingham et al., 1986) should be estimated with the numerical method (Fig. I.8) and is described as follows:

$$COG = \frac{\sum_{n=1+aln}^{n=N-aln} ny^2(n)}{\sum_{n=1+aln}^{n=N-aln} y^2(n)} \quad (I.6)$$

$$A = \sqrt{\frac{\sum_{n=1+aln}^{n=N-aln} y^4(n)}{\sum_{n=1+aln}^{n=N-aln} y^2(n)}} \quad (I.7)$$

$$W = \frac{(\sum_{n=1+aln}^{n=N-aln} y^2(n))^2}{\sum_{n=1+aln}^{n=N-aln} y^4(n)} \quad (I.8)$$

$$Lep = COG - 0.5.W \quad (I.9)$$

where  $N$  is the total gate number;  $aln$  is the number of estimated gate in the starting and ending of waveform;  $y(n)$  is the value of the  $n$ th gate;  $A$  is the amplitude;  $W$  is the width; COG is the center of gravity of waveform;  $Lep$  is the middle point of leading edge.

- *The Sea Ice algorithm:* is a threshold retracker intended for reprocess the nature of waveforms from sea ice. The amplitude of the waveform is identified: this is the maximum value of the waveform provided by (Kurtz et al., 2014). No model describing the nature of waveforms from sea ice, only a simple method can be used to reprocess this type of radar echoes. The amplitude of the waveform is firstly identified: it is the maximum value of the waveform (Eq. I.10):

$$amplitude = max_{n \in N}(y(n)) \quad (I.10)$$

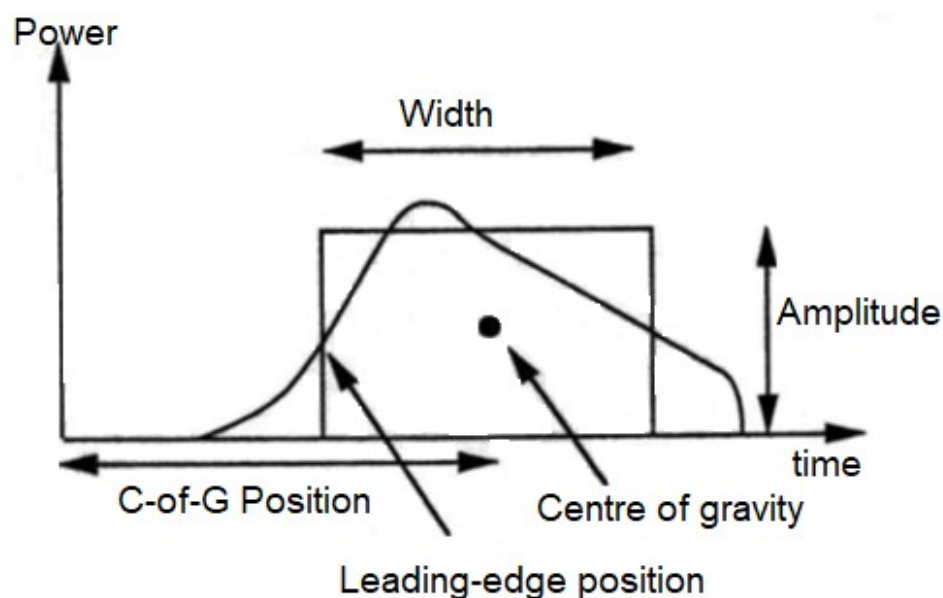


Figure I.8 – Schematic diagram of the OCOG algorithm (Wingham et al., 1986).

where  $y$  is the value of the  $n^{\text{th}}$  sample of the waveform and  $N$  is the number of sample of the waveform.

#### I.4.1.2 The analytical methods

- *The Ice-2 algorithm:* is based on the Brown model (Brown, 1977) to process altimeter waveforms obtained over most of the non-ocean surfaces, intended for ice caps studies, consist in detecting the leading edge width, the trailing edge slope and the backscatter coefficient (Fig. I.9) (Rémy et al., 1997).
- *The Ocean algorithm:* used to fit a model to measured waveform with a return power model. The waveform shape of an echo is assumed to follow the functional form Brown (Brown, 1977; Hayne, 1980). The ocean retracking algorithm objectives is to retrack the waveforms of conventional altimeters by fitting a mathematical model, according an unweighted Least Square Estimator derived from a Maximum Likelihood Estimator (MLE) method or least squares estimators (Amarouche et al., 2004; Thibaut et al., 2010; Vignudelli et al.,

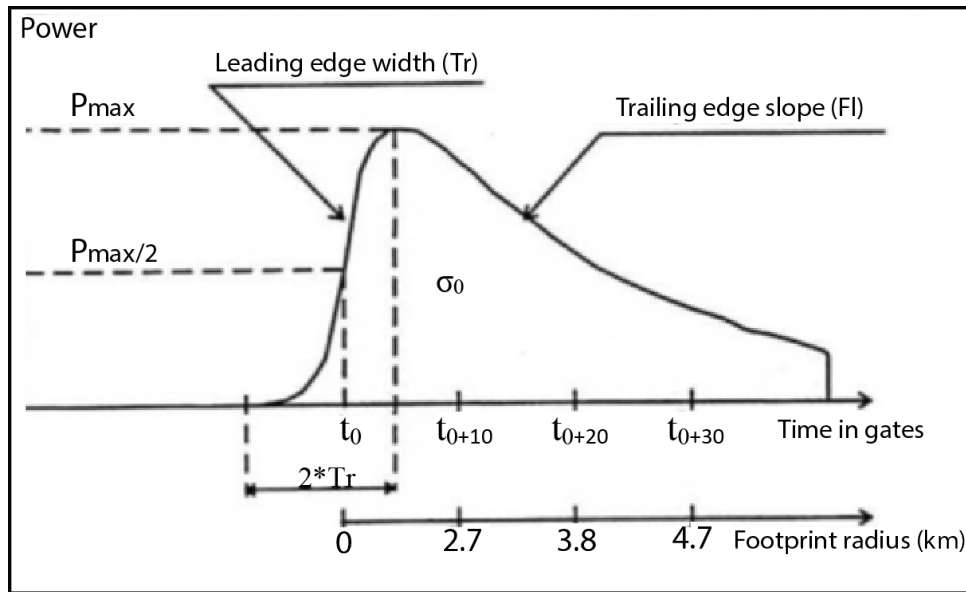


Figure I.9 – Theoretical waveform sought by the Ice-2 algorithm (Rémy et al., 1997)

2011).

#### I.4.1.3 The pattern recognition methods

An alternative technique has been developed to process the waveform observed over inland domain. It includes the classification of waveforms based on their appearance, and then applies a reprocessing algorithm that is appropriate for each type of identification (Berry, 2000).

### I.4.2 Retracking algorithms for the study over coastal areas

As mentioned in § I.3, most of the return waveform was found in coastal areas deviate from the Brown model echo, especially at a distance of 0-10 km from the coastline (Vignudelli et al., 2011). The main retracking algorithms used for the coastal domain:

- **The Offset Centre of Gravity (OCOG) algorithm:** this approach does not depend on a functional form (Vignudelli et al., 2011). The COG, the amplitude (A) and the width (W) of waveform are estimated from the waveform data using Eq. I.6, I.7, and I.8.

- **The Threshold algorithm:** developed by [Davis \(1995\)](#) based on the rectangle about the effective COG of the waveform computed using the OCOG method. The Threshold retracking method with 10%, 25% and 50% threshold level are used for the return waveform from coastal domain ([Vignudelli et al., 2011](#)).
- **$\beta$  parameter fitting algorithm:** is an alternative technique, was developed by Martin in 1983 from the National Aeronautics and Space Administration, USA (NASA) ([Martin et al., 1983](#)). This method fits a theoretical model based on an ocean-like waveform to find the tracker point ([Bamber, 1994](#)). The parameters can be estimated by the iterative calculation with the least squares adjustment or the MLE method. The 5- $\beta$  parameters is used to fit signal-ramp return waveform as shown in (Fig I.10). The general expression for the 5 –  $\beta$  parameters functional form of the returned power  $y(t)$  is:

$$y(t) = \beta_1 + \beta_2(1 + \beta_5 Q(t))P\left(\frac{t - \beta_3}{\beta_4}\right) \quad (\text{I.11})$$

$$P(z) = \frac{1}{\sqrt{2\pi}} \int_{-\infty}^z e^{-\frac{q^2}{2}} dq = \frac{1}{2} + \frac{1}{2} \text{erf}\left(\frac{z}{\sqrt{2}}\right), \quad z = \frac{t - \beta_3}{\beta_4} \quad (\text{I.12})$$

$$Q(t) = \begin{cases} 0 & t < \beta_3 + 0.5\beta_4 \\ t - (\beta_3 + 0.5\beta_4) & t \geq \beta_3 + 0.5\beta_4 \end{cases} \quad (\text{I.13})$$

where  $y(t)$  is the sampling power at time;  $\beta_1$  is the thermal noise level of return waveform;  $\beta_2$  is the return signal amplitude;  $\beta_3$  is the middle point of leading edge;  $\beta_4$  is the rise time parameter of return waveform;  $\beta_5$  is the slope of trailing edge;  $P(z)$  is the error function;  $Q(t)$  is a linear function to fit the gradual attenuation waveform in the trailing edge [Bamber \(1994\)](#). However, the empirical parameters remain simple parameters, not related to physical properties, the slope of the trailing edge of the parameter model can be greater than that of the Brown model (1977), which makes the parameter model able to fit more complex waveform over coastal areas.

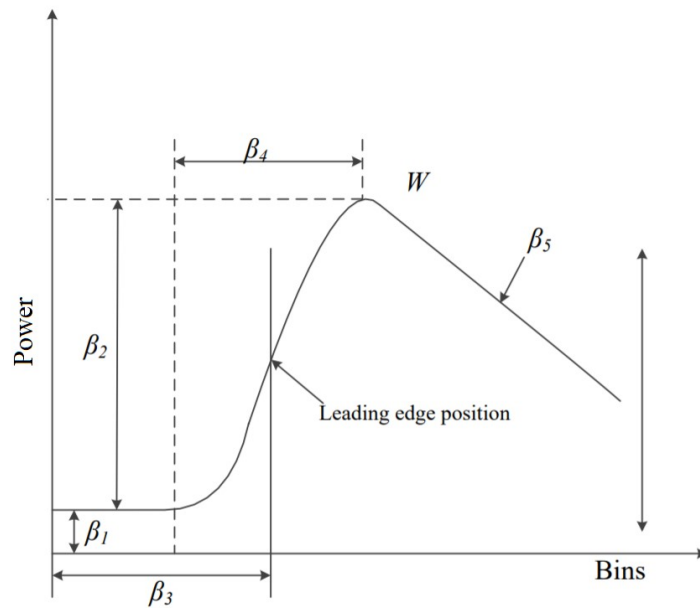


Figure I.10 – Schematic diagram of 5- $\beta$  parameter fitting method (Martin et al., 1983)

- **Maximum Likelihood Estimator (MLE):** is based on the Brown retracking method (Brown, 1977), which is developed to fit return waveform to the Brown model (Gommenginger et al., 2011; Vignudelli et al., 2011; Rodriguez, 1988). The MLE retracker estimates the geophysical parameters by determining the value that maximizes the probability of obtaining the recorded waveform shape in the presence of noise of a given statistical distribution. From the Brown model, the time series of mean return power  $P(t)$  measured by the satellite can be expressed in the time domain as shown in Eq. I.5 (Deng and Featherstone, 2006). The MLE3 algorithm based on the same least square principle to estimates three parameters (range, significant wave height, and power) whereas the MLE4 estimates four parameters (the three previous ones and the slope of the waveform trailing edge). The MLE-4 retracker is an optimal way to adapt the noisy altimeter waveform data. It gives an unbiased estimate with the lowest variance.

## I.5 SAR altimetry

The development of SAR nadir altimeter has a close relationship with the better known as SAR images. Their main interest is that they provide a greatly reduced footprint with respect to the one associated with conventional altimetry LRM measurements. This gain in spatial resolution is in the direction of displacement of the satellite (along track) (Frappart et al., 2017).

While the processing of SAR data is a rather complex process, one can explain simply how this gain can be obtained. Consider the frequency shift caused by the Doppler effect that affects the signal coming from a given scattering point on the ground. This shift is caused by the projection of the speed of the satellite along the line of sight.

If the satellite flies horizontally, the Doppler shift is zero for a scattering point at the subsatellite point. And it increases in absolute value almost linearly with the along-track distance between the scatterer and the subsatellite point.

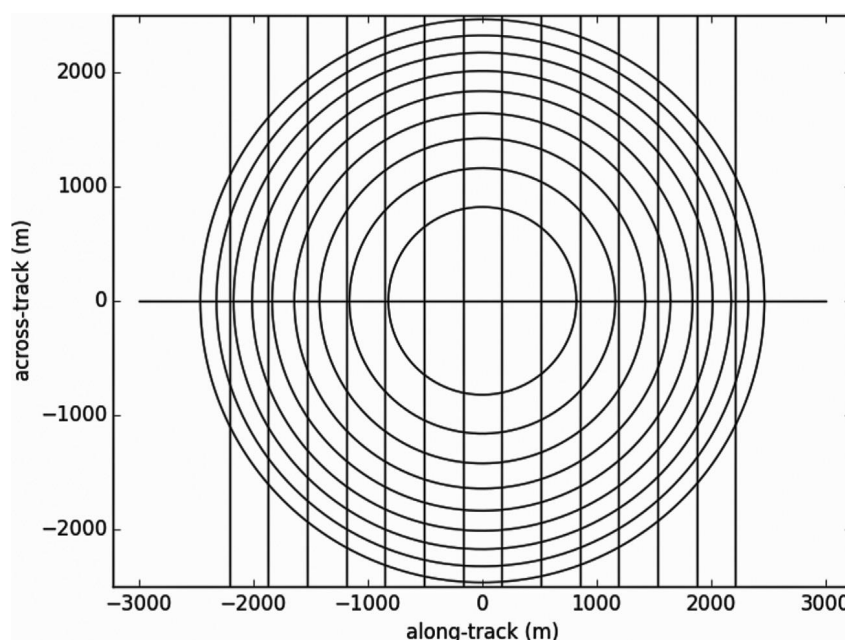


Figure I.11 – Delay-doppler isocontours on the ground supposed to be a perfect spherical surface (9 first isorange contours, and 14 isodoppler contours). The horizontal line is the trajectory of the satellite (Frappart et al., 2017)

Figure I.11 shows two families of curves plotted on the ground surface that is supposed to be spherical. The first one (straight lines) corresponds to the contours of equal Doppler shift. The second family (circles) is a selection of the contours of equal range seen from the radar corresponding to the nine first bins of the waveforms after the leading edge (see § I.2). The horizontal line is the subsatellite trajectory on the ground.

In essence, the SAR processing removes the power coming from all the vertical bands shown on Fig. I.11 except the central one (called the zero Doppler band) its width is typically 340 m. This is repeated for the adjacent Doppler bands to form a stack of waveforms. This builds a SAR waveform that spans the same range window as the conventional LRM processing but with a shape that is definitely different (more peaky). Of course, this is a very simplified view presented here, and the SAR processing is more complex and nuanced. Indeed, the processing produces an azimuth impulse response function that induces some power leakage between the Doppler bands. The effect of this leakage can be observed easily in the real data whenever there are strong discontinuities in the backscattering coefficient, for example when the satellite flies over a river or a lead between sea ice ([Wingham et al., 2006](#)). Classical altimetry retracking algorithms cannot be applied to this new type of waveform and dedicated ones have to be developed for different target types. Cryosat-2 and Sentinel-3 SAR data are reprocessed using the SAMOSA Echo Model ([Ray et al., 2015](#)) using a curve-fitting scheme based on the Levenberg–Marquardt least-square minimization algorithm. The SAMOSA model is physically based and provides a complete description of the SAR altimeter return waveform for an ocean surface. The waveform is given in the form of maps of reflected power in delay-Doppler space (or delay-Doppler Maps – DDM) or expressed as multilook echoes ([Dinardo et al., 2015](#)). SAR altimetry retracking algorithms for rivers and ice sheets do not exist yet and need to be developed. The improvement of the spatial resolution with SAR processing clearly appears on Fig. I.11 when considering the intersection of the rings and the central zero Doppler band. It has many benefits, such as reducing the sea-level

perturbations when approaching the coast (particularly when the satellite ground-track crosses the coast orthogonally) or in reducing the impact of off nadir backscattering in hydrology. In addition, the along-track slope has no impact on the height retrieval (although it does have an impact on the level of signal received with the current design of CryoSat-2 and Sentinel-3). This advantage is counterbalanced by the sensitivity to the across-track slope with the SAR processing, which is often not accurately known over ice sheets and land surfaces. SAR altimetry allows both an increased resolution and a better speckle reduction owing to the multilook processing ([Keith Raney, 1998](#)).

## I.6 The limitations of altimetry in coastal areas

### I.6.1 Waveform retracking problem

In coastal areas, the classic description of the Brown waveform ([Brown, 1977](#)) is no longer suitable. The height measured by the altimeter may depend on the shoreline distance, slope and reflectivity of the radar altimeter on the continental surface ([Brooks et al., 1997](#)). The function of the retracking system is to locate the midpoint of the rising edge of the radar echo. This determination depends on the width of the time window over which the waveforms are averaged (from 2 to 16 first gates of the altimetry waveform). For an altimeter signal sampled at 20 Hz ( $\sim 350$  m) along the altimeter tracks, related to sea state ([Chelton et al., 2001](#)). As the footprint of the altimeter beam approaches the shoreline, part of the transmitted signal can be reflected from an emerged land surface, including the distance (obliquely) from the satellite may be less than the height measured at nadir. When the illuminated surface includes both marine and continental surfaces, the return echo comes from facets at different heights and with inhomogeneous reflectivity, so that the recorded waveform becomes "multi-peaked" (Fig. I.5d), or complex enough (Fig. I.5b and I.5c) not to be analyzed by traditional retracking algorithms. As a result, most

oceanographers do not use altimetry data in a coastal strip between 20 km and 50 km from the coast (Strub and James, 2002) depending mainly on the footprint of the altimetry satellite.

The waveform can also be affected by coastal sea states whose spatial and temporal variability is generally more chaotic. For example, for coastal areas marked by low ocean surface roughness, such as estuarine areas, the echo returned to the altimeter has maximum power. It called "peak effect" (Fig. I.5b) or "specular surface reflection". In the latter case, Brown's classic model is also unsuitable.

In this thesis, we will present a treatment methodology to valid sea levels that can be used for altimetry measurements within 50 km from the coast in chapter 3.

### I.6.2 The stall of the altimeter

A retracking system on board the satellite will perform a first summary analysis of the waveform in order to anticipate the adjustment of the return echo recording window. Indeed, this window must be well positioned with respect to the moment when the return echo is sent back to the satellite following its reflection on a terrestrial surface (ice, ocean, land...). At the land-ocean transition, the anticipation procedure is no longer suitable since the window is calibrated for a continental surface measurement with a low backscatter coefficient, while the echo from the ocean surface is powerful. As the retracking algorithm is not adapted, the parameters resulting from the waveform analysis cannot be determined. In this case, the measurement acquisition device is reset, referred to as an "altimeter stall". This stall is accompanied by a loss of data over a distance of between 6 and 20 km from the coast (Chelton et al., 2001), which corresponds to the distance traveled by the satellite before the measurement system becomes active again.

In order to avoid altimeter stalls, the DIODE On-Board Orbit Determination software was used for the altimetry mission SARAL/AltiKa (Jayles

et al., 2015) and Jason-2. It is a calculation program which, coupled with a DORIS receiver, provide new information on the satellite's position (latitude, longitude and altitude) with an accuracy  $\sim 2.5$  cm (Jayles et al., 2015). This real-time location system, combined with a DEM, should allow a better understanding of land-ocean transitions during the return echo acquisition phases. Indeed, the geodetic information from DIODE is transmitted to the altimeter, which was then be able to optimally adjust the size of the return echo acquisition window and thus significantly reduce the problems of dropping out in coastal areas.

### **I.6.3 The correction of the wet troposphere in coastal areas**

Altimeter measurements must be corrected for the propagation delay of the electromagnetic wave through the different atmospheric layers. Among the corrections to be applied, the "wet troposphere" correction, a correction related to the interaction of the wave radar with the water vapor content of the lower atmospheric layers, is particularly critical in coastal areas.

In the open ocean, the wet troposphere correction is usually deduced from measurements acquired by a radiometer on board the satellite. The combination of altimeter and radiometer is satisfactory for the study of surface topographic variability in the offshore ocean.

However, this is no longer the case in coastal areas where radiometric measurement faces two main difficulties.

First of all, the radiometer has a larger ground spot than the altimeter. Thus, the spatial variability of the water vapor content in the atmosphere is under-sampled by radiometric measurement because the scales of variability in coastal areas are finer.

In addition, the presence of soil in the radiometer's ground spot (as with the altimeter) disrupts the measurement of the troposphere's water content, which assumes a marine surface. The high and variable emissivity of the soil leads to an error in the correction of a few cm. Gloss temperatures are calculated over an ocean radius of 21.7 km around nadir for the

18 GHz channel (Ruf et al., 1995), so radiometric corrections within 21.7 km of the coast are unreliable.

It is therefore necessary to define relevant strategies for wet troposphere correction in coastal areas where altimetry measurements may be present but where corrections are required radiometric are absent or unusable. To do this, three strategies can be used envisaged:

- Develop and use a wet troposphere correction model.
- Select, filter and extrapolate the radiometric measurement to the coast.
- Develop high-resolution coastal weather models.

### I.6.4 Surface slope effect

These errors are related to land topography and are known as slope errors (Brenner et al., 1983). Above flat surfaces, the altimeter measurement represents the distance between the satellite and the surface located at nadir, while above a sloping surface, the measurement represents the distance to the nearest point of the sloping surface area contained in the altimeter ground track (Figure I.12).

This point is at a higher altitude than the point directly at nadir (Brenner et al., 1983). The error on the Earth-satellite distance is worth (Eq. I.14):

$$\Delta H = H(1 - \cos(\alpha)) \sim \frac{H\alpha^2}{2} \quad (\text{I.14})$$

with  $\Delta H$  the error on the altimeter measurement,  $H$  the altimeter measurement at nadir,  $\alpha$  the slope of the surface.

The error in this correction can be significant. If we consider realistic values of the satellite's altitude and slope, the error related to topography can reach several tens of meters.

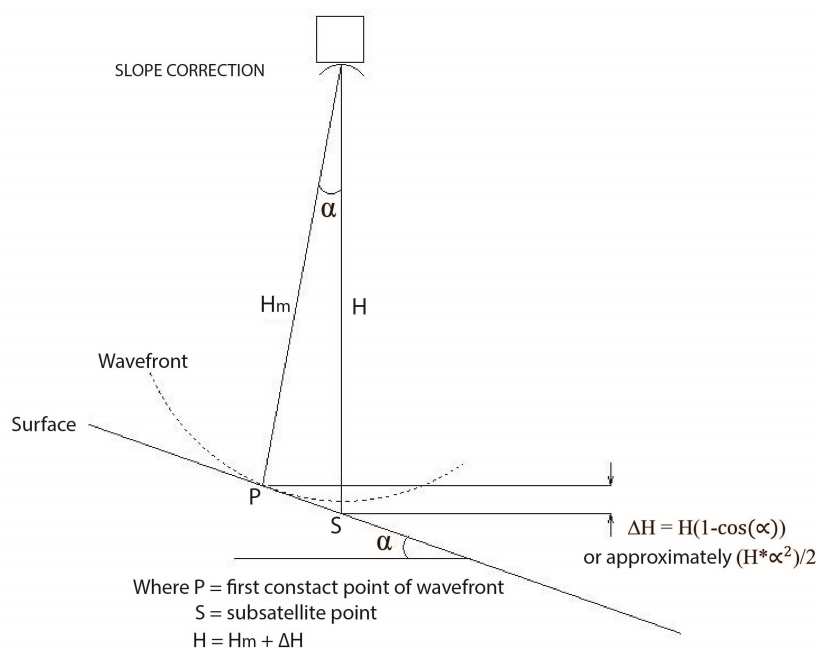


Figure I.12 – Schematic description of the slope error for an incline surface  $\alpha$  (NASA).

## I.7 The different satellite altimetry missions

### I.7.1 Topex/Poseidon, Jason-1, Jason-2, Jason-3

From this generation of four satellites created as part of a collaboration between CNES and NASA, the Jason-3 has just been launched in January 2016 is a collaboration between CNES, NASA, Eumetsat and NOAA. The orbit is common to this series of four satellites (in Tab. I.1). Launched in 1992, Topex/Poseidon (T/P) is measured ocean surface topography with an accuracy better than 5 cm. This satellite was still in operation at the launch of its successor Jason-1 in December 2001, allowing a phase of calibration and validation of Jason-1 data. In the first phase, the Jason-1 satellite was placed behind T/P with a slight time shift. Once the calibration phase was completed, the two satellites were placed in spatially spaced orbits to interpose the tracks on the ground for better spatial resolution. An effort has been made on the miniaturization of devices, Jason-1 has a mass of 500 kg is five times lighter than its predecessor. The Jason-2

mission began in June 2008. The altimeter Poseidon-3 has the same general characteristics as Poseidon-2, with a decrease in instrumental noise and has, in addition, an algorithm coupled with DORIS allowing a better observation on the coastal zones, continental domain and the ice. The accuracy on the orbit is  $\sim 1$  cm (against 2 cm for Jason-1) and  $\sim 2.5$  cm on the altimeter measurement. From October 2016, the Jason-2 orbit is shifted, to join the intercalated orbit previously by T/P and Jason-1. In July 2017 (from Cycle 500), Jason-2 was placed in a lower orbit at about 1309.5 km, named LRO for Long Repeat Orbit, also known as geodetic orbit. After the success of predecessors, Jason-3 ensures the continuity of high precision ocean altimetry measurements for climate monitoring, operational oceanography and seasonal forecasting. Jason-3 will be an essential part of the constellation of altimetry satellites in the coming years.

### I.7.2 ERS-1/2 and ENVISAT

Unlike the other series of missions mentioned above, the ERS-1, ERS-2, and ENVISAT missions are not only dedicated to altimetry. The ERS-1 satellite was launched in 1991 by ESA for observing the oceans, polar ice caps, coastal areas and measuring marine geoid. The ERS-2 satellite, launched in 1995 on the same orbit as ERS-1 on a time-shift day (see in Tab. I.1). After 22 June 2003, the dataset coverage is limited to ground station visibility. The ENVISAT mission was launched in March 2002 on the same orbit with ERS-1 and ERS-2. The goal was to collect radar altimetry data over ocean, land, and ice caps. The ENVISAT remained on its nominal orbit until October 2010 and its mission ended 8 April 2012.

### I.7.3 SARAL/AltiKa

The SARAL mission was launched on 25 February 2013 (see in Tab. I.1). SARAL is a collaboration between CNES and Indian Space Research Organization (ISRO). Its payload included the AltiKa radar altimeter and

TABLE I.1 – Main characteristics of the altimetry missions (Adapted from AVISO/CNES).

| Missions                       | ERS-1      | Topex/Poseidon                    | ERS-2      | JASON-1        | ENVISAT        | JASON-2                   | SARAL      | JASON-3                   | Sentinel-3A                    |
|--------------------------------|------------|-----------------------------------|------------|----------------|----------------|---------------------------|------------|---------------------------|--------------------------------|
| Agency                         | ESA        | NASA/CNES                         | ESA        | NASA/CNES      | ESA            | CNES/EUMESAT<br>NASA/NOAA | CNES/ISRO  | CNES/EUMESAT<br>NASA/NOAA | ESA                            |
| Launch on                      | 17/07/1991 | 10/08/1992                        | 21/04/1995 | 07/12/2001     | 01/03/2002     | 20/06/2008                | 25/02/2013 | 17/01/2016                | 16/02/2016                     |
| End date                       | 31/03/2000 | 18/01/2006                        | 06/07/2011 | 01/07/2013     | 08/06/2012     | 2016                      | Present    | Present                   | Present                        |
| Altimeter name                 | RA         | Topex-A/B                         | RA         | Poseidon-2     | RA-2           | Poseidon-3                | AltiKa     | Poseidon-3B               | SRAL                           |
| Radar frequency                | Ku-band    | Ku and C-bands                    | Ku-band    | Ku and C-bands | Ku and S-bands | Ku and C-bands            | Ka-band    | Ku and C-bands            | Ku and C-bands                 |
| Altitude                       | 785 km     | 1136 km                           | 785 km     | 1136 km        | 790 km         | 1136 km                   | 790 km     | 1336 km                   | 814.5 km                       |
| Orbit inclination              | 98.52°     | 66°                               | 98.52°     | 66°            | 98.54°         | 66°                       | 98.54°     | 66°                       | 98.645589°                     |
| Repetitivity                   | 35 days    | 9.9156 days                       | 35 days    | 9.9156 days    | 35 days        | 9.9156 days               | 35 days    | 9.9156 days               | 27 days                        |
| Altimeter Footprint Dimensions | ~18 km     | ~5.5 - 11.7 km<br>(Chelton, 1989) | ~18 km     | ~10 km         | ~18 km         | ~10 km                    | ~6 km      | ~10 km                    | >2km (SRAL)<br>~18 km<br>(MWR) |

bi-frequency radiometer, and a triple system for precise orbit determination: the real-time tracking system DIODE of DORIS instrument, a Laser Reflector Array (LRA), and the Advance Research and Global Observation Satellite (ARGOS-3). ARGOS-3 will provide geopositioning and data collection services to nearly 20,000 active Argos Platform Transmitter Terminals (PTT) deployed worldwide. These miniaturized transmitters relay precious data about the world's oceans, atmosphere and animal life from anywhere on the globe. The AltiKa radar altimeter is a solid-state mono-frequency altimeter that provides accurate range measurements and is the first altimeter to operate Ka-band (35.75 GHz). Formerly, the SARAL orbit was used by ERS-1 and 2 and ENVISAT, with an equatorial ground-track spacing of about 85 km, and a 35-day repeating cycle. It was placed on a drifting orbit as of 7 April 2016 (Verron et al., 2015). The use of the Ka-band cause reduces the size of altimetry footprint ( $\sim 6$  km for SARAL in Tab. I.1), thus enabling a better observation of ocean mesoscale, coastal areas, continental water bodies as well as the waves height.

### I.7.4 Sentinel-3A

Launched in 2016, the new Sentinel-3A mission is operating in Synthetic Aperture Radar (SAR) mode (Table I.1). The Sentinel-3 satellite, dedicated to the monitoring of the Earth and Oceans, is part of the Copernicus program, founded in cooperation between ESA and the European Commission. This program is the European response to the ever-growing needs of environmental management. SRAL altimeter is derived from the Cryosat Sival Doppler altimeter. The main frequency used for measuring the satellite-to-surface distance is the Ku band (13.575 GHz, 350 MHz bandwidth), but unlike Cryosat, a second frequency is used. Band C (5.41 GHz, 320 MHz bandwidth) is used for ionospheric correction. Sentinel-3A S-3 measurements will also be used to determine sea, ice and land surface topography, temperature, ocean and atmospheric measurements with high accuracy (Donlon et al., 2012).

---

CHAPTER II

# GNSS Reflectometry

---

## Contents

---

|  |           |
|--|-----------|
| <b>II.1 Introduction</b> . . . . .                                       | <b>46</b> |
| <b>II.2 State of the art</b> . . . . .                                   | <b>50</b> |
| II.2.1 Principle of GNSS . . . . .                                       | 50        |
| II.2.2 The ancestor still full of youth: Global Positioning System (GPS) | 50        |
| II.2.3 Globalnaya Navigatsionnaya Sputnikovaya Sistema (GLONASS) .       | 57        |
| II.2.4 New GNSS . . . . .  | 58        |
| II.2.5 The Positioning measurement . . . . .                             | 61        |
| <b>II.3 Reflection of GNSS signals</b> . . . . .                         | <b>65</b> |
| II.3.1 Multipath . . . . .   | 66        |
| II.3.2 Specular and diffuse reflection . . . . .                         | 68        |
| <b>II.4 GNSS Reflectometry (GNSS-R)</b> . . . . .                        | <b>72</b> |
| II.4.1 GNSS-R measurement technique . . . . .                            | 72        |
| II.4.2 Reflectometry through opportunity signals . . . . .               | 78        |
| II.4.3 Reflectometer with single antenna . . . . .                       | 83        |
| II.4.4 Application of GNSS-R for altimetry . . . . .                     | 86        |
| <b>II.5 Conclusions</b> . . . . .  | <b>87</b> |

---

## II.1 Introduction

### En français:

Le développement du système mondial de navigation par satellite a débuté dans les années 1970 et reposait sur deux constellations pionnières (GPS et GLONASS) qui ont permis de faire un positionnement et une navigation précis à des fins aussi bien militaires que civiles. Cependant, le GNSS a évolué et est utilisé pour de nombreuses autres applications qui utilisent des signaux GNSS pour étudier et suivre d'autres propriétés de la Terre *e.g.* la surveillance de l'environnement, les prévisions météorologiques, la recherche climatologique ([Hofmann-Wellenhof et al., 2001](#)). Ce système a démontré des performances de haute qualité en géodésie, en météorologie et dans de nombreux domaines de la géophysique ([Hofmann-Wellenhof et al., 2001](#)). Avec la modernisation et la densification des anciennes (GPS, GLONASS) et l'apparition de nouvelles constellations GNSS (GALILEO, BEIDOU/COMPASS), davantage de signaux d'opportunité peuvent être envisagés et utilisés. Alors que les signaux réfléchis sont souvent considérés comme une source d'erreur pour le positionnement GNSS traditionnel, la réflexion des ondes électromagnétiques peut être exploitée avec succès pour détecter à distance les propriétés de la surface de la Terre grâce à une technique opportuniste appelée réflectométrie GNSS (GNSS-R).

La technique GNSS-R offre de nombreux avantages, à commencer par sa pérennité et la continuité des mesures, ainsi qu'une couverture dense du globe. Les applications envisagées sont variées: détermination de l'épaisseur de la neige, de l'humidité du sol, de la biomasse, de la surveillance des eaux océaniques, des zones côtières, des eaux continentales ([Darrozes et al., 2016](#)), etc. Les questions scientifiques sont donc très importantes. Les premières études expérimentales utilisant la technique GNSS-R pour la surveillance du niveau de la mer ont été proposées par Martín-Neira en 1993 ([Martin-Neira, 1993](#)). Le concept de la réflectométrie GNSS, développé durant cette période, reposait sur l'analyse de la différence de

trajet entre les signaux directs émis par les satellites et ceux réfléchis à la surface de l'océan, ce qui permettait de déduire un certain nombre de paramètres e. g. hauteur de l'océan, vitesse du vent, etc. Ce premier exemple d'applications GNSS-R utilisait un récepteur spécifique à deux antennes (direct/réfléchi) et enregistrait l'intégralité des formes d'onde GNSS. (Kavak et al., 1998) ont mis en évidence le potentiel d'une technique GNSS-R basée sur l'analyse du rapport signal sur bruit (SNR) mesuré par un récepteur GNSS classique à une antenne. Cette nouvelle approche est utilisée pour la surveillance du niveau de la mer (Anderson, 2000; Cardellach, 2001; Martin-neira et al., 2002; Marchan-Hernandez et al., 2010; Larson et al., 2013b,a; Löfgren and Haas, 2014; Roussel et al., 2015b; Lestarcquit et al., 2016), la mesure du niveau de l'eau à l'intérieur des terres (Treuhaft et al., 2001; Motte et al., 2016), l'humidité du sol (Larson et al., 2008b, 2010; Roussel et al., 2015a, 2016; Chew et al., 2016), épaisseur de la neige (Larson et al., 2009; Cardellach et al., 2012), surveillance de la contamination minière (Dufrechou, 2017) et même de la biomasse (Egido et al., 2014).

Ainsi, les techniques de télédétection GNSS-R se divisent en deux principales familles:

- La première famille utilise un radar à faisceaux multiples bistatique et analyse directement la forme d'onde GNSS à l'aide d'un récepteur GNSS spécifique doté de deux antennes ou plus. Cette technique est très prometteuse en raison de sa flexibilité: elle peut être utilisée pour des applications in situ, aéronautiques et satellitaires. Cette méthodologie peut être mise aux avions/RPAS/satellite pour développer des services de cartographie de l'humidité du sol et des zones inondées;
- Le second utilise un récepteur GNSS classique et une seule antenne, et peut aussi utiliser un récepteur "low cost". C'est également une technique prometteuse, mais pour le domaine de l'in situ et à basse altitude (drone, hauteur de vol  $< 300$  m). Cependant, la grande

quantité des réseaux GNSS qui existent à travers le monde entier, il est possible de réutiliser certaines de ces stations pour surveiller les systèmes environnementaux (humidité du sol, biomasse, zone inondée, *etc.*). Cette méthodologie peut être utilisée pour valider des missions aéroportées/drones/ satellites par des mesures au sol multi-échelles appropriées.

Dans ce chapitre, nous présenterons le principe du GNSS et ses différentes constellations. Ensuite, nous nous concentrerons sur les signaux "d'opportunité" du GNSS-R. Nous présenterons ensuite les techniques de mesure GNSS-R et leur application pour l'altimétrie.

**In English:**

The development of Global Navigation Satellite System began in the 1970s and was based on two pioneer constellations (GPS and GLONASS) for accurate positioning and navigation in military purposes. However, GNSS has evolved to serve many other applications that GNSS signals to infer other properties of the Earth, such as environmental monitoring, weather forecasting, climatology research ([Hofmann-Wellenhof et al., 2001](#)). This system has shown a high quality of performance in geodesy, meteorology and many fields of geophysics ([Hofmann-Wellenhof et al., 2001](#)). With the modernization and the densification of the old (GPS, GLONASS) and new GNSS constellations (GALILEO, BEIDOU/COMPASS), more opportunity signals can be considered and improved. While reflected signals are often considered a source of error for traditional GNSS positioning, reflection of electromagnetic waves can be successfully exploited to remotely detect the Earth's surface properties in an opportunistic technique called GNSS reflectometry (GNSS-R).

GNSS-R technique offers many advantages, starting with the durability and continuity of GNSS satellite measurements as well as dense and continuous coverage around the world. The applications envisaged are varied: depth of snow, soil moisture, biomass or monitoring of ocean waters, coastal zones, inland water, *etc.* ([Darrozes et al., 2016](#)). The scientific issues are therefore very important. The first experimental studies using

GNSS-R technique for sea level monitoring was proposed by (Martin-Neira, 1993), the concept of GNSS reflectometry is based on the analysis of the difference of paths between the direct signals emitted by the satellites of the GNSS systems and those reflected on the ocean surface, which allows us to deduce a number of parameters *e.g.* height of the ocean, wind speed etc. These first example of GNSS-R applications used a specific two antenna (direct/reflected) receiver and record the complete GNSS waveforms. (Kavak et al., 1998) have demonstrated a strong potential of GNSS-R based on the analysis of the SNR (Signal-to-Noise Ratio) estimated by a classical one antenna GNSS receiver. This new approach is used for sea level monitoring (Anderson, 2000; Cardellach, 2001; Martin-neira et al., 2002; Marchan-Hernandez et al., 2010; Larson et al., 2013b,a; Löfgren and Haas, 2014; Roussel et al., 2015b; Lestarquit et al., 2016), measuring the water level on inland (Treuhaft et al., 2001; Motte et al., 2016), soil moisture (Larson et al., 2008b, 2010; Roussel et al., 2015a, 2016; Chew et al., 2016), snow depth (Larson et al., 2009; Cardellach et al., 2012), monitoring of mining contamination (Dufréchou, 2017) and even biomass (Egido et al., 2014). Thus, GNSS-R remote sensing techniques are divide into two main families:

- The first family used a GNSS Bistatic Multi-Beam Radar and will analyses directly the GNSS waveform using specific receiver with two or more antennas. This technique is very promising due to is flexibility: it can be used for in-situ, aircraft and satellite applications. This methodology can be associated to aircraft/RPAS to develop mapping services for soil moisture and flooded area;
- The second one uses a classical GNSS receiver and only one antenna, and could use low-cost receiver, it is also a promising technique but for in-situ and low elevation fly (RPAS, flight height < 300 m). However due to the large amount of GNSS network existing worldwide it is possible to re-use some of these stations to make environmental system monitoring (soil moisture, biomass, flooded area etc.). This

methodology can be used to validate aircraft and/or RPAS and/or satellite missions by appropriated multi-scale ground measurements.

This chapter, we will present the principle of GNSS and the various GNSS constellations. Then, we will focus on opportunistic signals from the GNSS-R. We will then present the GNSS-R measurement techniques and its application for altimetry.

## II.2 State of the art

### II.2.1 Principle of GNSS

In general, a GNSS consists of three segments corresponding to those of the first one *i.e.* GPS constellation ([Duquenne et al., 2005](#)) used herein as example:

- *The space segment:* including the satellite constellation and the broadcasted signals.
- *The ground segment that controls the system:* It consists of 5 ground stations located in Hawaii, Ascension Island, Diego Garcia, Kwajalein (Marshall Islands) and Colorado Springs. These stations continuously record the GPS signals, conduct meteorological measurements and send the data to the Master Control Station: Colorado Spring station.
- *The user segment:* consisting of the users (both military and civilian). An important part of the user segment is the national and international organizations that maintain their own permanent GNSS networks, consisting of ground-based receivers and antenna, providing data and products to the users.

### II.2.2 The ancestor still full of youth: Global Positioning System (GPS)

The Global Positioning System (GPS) is the most well-known and successful GNSS constellation, was initially proposed under a collaboration

within NATO but funded by the United States Army in 1973, the first satellites were launched in 1978 ([Hofmann-Wellenhof et al., 2001](#)).

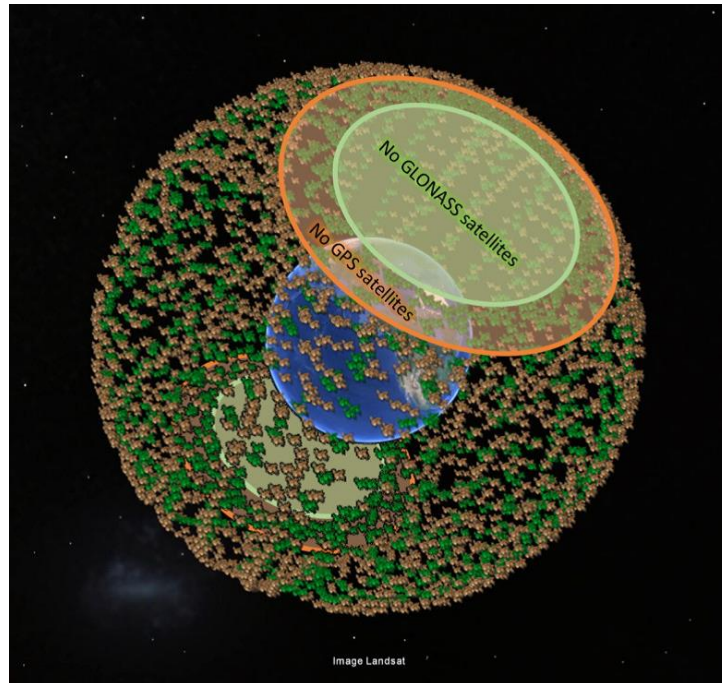


Figure II.1 – Coverage density of the two oldest GNSS constellations: the US GPS system (orange) and the Soviet GLONASS system (green). However, there is a lack of coverage at the poles, this hole is more important for the GPS system than for the GLONASS system. On this representation are represented the different positions, during a day, of the set of satellites of each constellation, the time step between two positions is fifteen minutes. N.B.: the distance from Earth (blue sphere) to satellite is not to scale.

Initially, the GPS system consisted of 24 satellites (Fig. II.1) spread over 6 orbital planes  $\approx 55^\circ$ /equator. Each satellite is in an almost circular orbit at an altitude of 20,200 km above the Earth's surface, with a revolution period of  $\sim 12$  sidereal hours. They are evenly distributed around the Earth in six planar orbits inclined  $66^\circ$  to the equatorial plane, offset by  $60^\circ$  in longitude. The current constellation consists of 31 fully operational satellites ([GPS-WORLD, 2012](#)).

### II.2.2.1 Transmitted signals

The main principle of GNSS positioning is to measure the distance to several satellites with known positions based on the signal propagation time

from each satellite to the receiver (Hofmann-Wellenhof et al., 2001). Each GNSS satellite continuously transmits an L-type microwave (1.1 GHz to 1.7 GHz frequency range,  $\sim 1$  cm to  $\sim 25$  cm wavelength) whose fundamental frequency is modulated. This phase modulation allows the satellite to send:

- Pseudo Random Noise (PRN) codes or “Gold codes” (Groves, 2008): the *C/A* code (Fig. II.2) allows each satellite to be identified and the *P* code is reserved for military applications. These codes are based on the “Code Division Multiple Access” (CDMA) technique, for sending information by spectrum diffusion, which is an effective response to the multipath problems that are specific to mobile signals. More generally, this type of communications is particularly suitable for the GNSS signals with a low signal-to-noise ratio (SNR).
- A navigation message giving the satellite’s condition, the GNSS time, the gap between the GNSS time and Coordinated Universal Time (UTC), the satellite ephemeris, the almanacs of different satellites (accuracy of orbital parameters is less than the ephemeris), weather information and other relevant parameters for calculation of the final position of the receiver; A total of 25 frames, 1500 bits each, are transmitted at a rate of 50 bits per second (bps).

### II.2.2.2 PRN codes

Let us consider a Pseudo-Random Noise code (PRN) as a random sequence of  $n$  pulses generated at a given frequency, with an amplitude of  $a_n$ , equal to +1 or -1 with equal probability. For a pulse duration  $T_c$  which corresponds to the inverse of the frequency, the signal sequence is written:

$$S(t) = \sum_{n=-\infty}^{+\infty} a_n \Pi\left(\frac{t - nT_c}{T_c}\right) \quad (\text{II.1})$$

The individual pulse of the random sequence is called a chip. The auto-correlation function  $R_p$  of this infinite sequence can be represented by a

triangle  $\Lambda_{\tau_c}$ :

$$R_p(\tau) \approx \Lambda_{\tau_c} = \begin{cases} -\frac{|\tau|}{\tau_c} & \text{when } |\tau| < \tau_c \\ 0 & \text{otherwise} \end{cases} \quad (\text{II.2})$$

with  $\tau$  is the time interval.

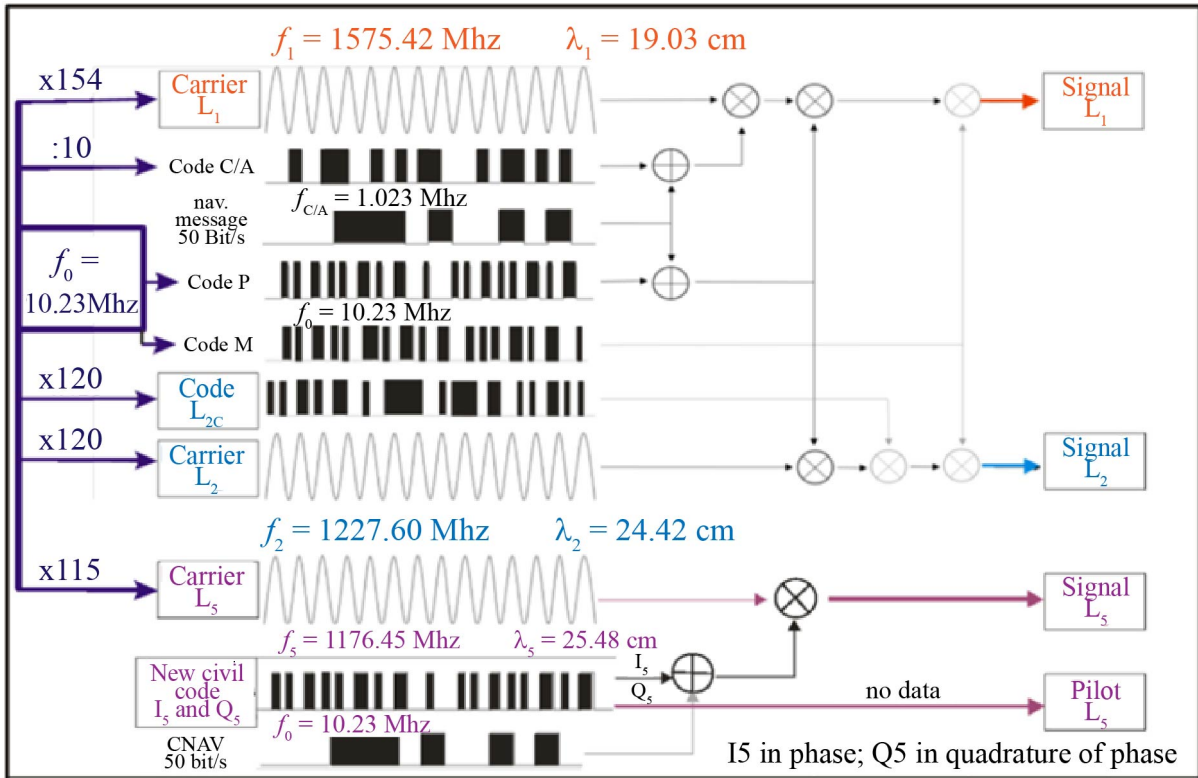


Figure II.2 – Structure of the modernized L-band GPS signals, the M-code is a new version of previous military P(Y) code. For Block IIR-M, IIF, and subsequent blocks, the  $L_{2C}$  signal, scheduled to be the first of the modernized civil GPS signals. It will provide greater accuracy and robustness and faster signal acquisition than the current  $L_1$  C/A-code signal. It is combination of C/A and two additional PRN ranging codes will be transmitted:  $L_2$  Civil Moderate ( $L_2$  CM) code and the  $L_2$  Civil Long ( $L_2$  CL) code.

As illustrated in Eq. II.2, increasing the frequency of chips induces a final triangle correlation for which the base is narrower and therefore the final correlation is more accurate. Two types of the PRN code are used for the distributions of GPS signals: the Coarse Acquisition (C/A) and code P (precise). The C/A code is used for civil applications, it has a frequency of 1,023 MHz and is “Open Access”. The length of this code is 1.023 chips, generated with a 1,023 MHz clock and a spectral bandwidth of

2,046 MHz. The C/A code is unique for each GPS satellite, this PRN code correlation has similar properties to the white Gaussian noise. That is to say a high auto-correlation to uniquely identifying each of the satellites and low cross-correlation that, because of the finite length of the C/A code, is not zero but is low enough for the proposed navigation applications, thus enabling a single receiver to receive the GPS satellite signals that are simultaneously different and without significant interference between them. It only modulates on the  $L_1$  carrier, which has a frequency equal to 154 times the fundamental frequency  $f_0$  at 1,575.42 MHz.

Code P, which is reserved for the military, has a frequency that is equal to the fundamental frequency at 10.23 MHz. It has a period of 7 days ( $\sim 720$  Gbytes). It modulates the carrier frequencies  $L_1$  and  $L_2$  ( $120 \times f_0$  at 1,227.60 MHz). When it is encrypted by the military code W (in wartime), it gives a new code called code P(Y).

The GPS signals are generated synchronous to each other in order to have a common reference time for solving positioning equations. The signals are transmitted in Right Hand Circularly Polarized (RHCP), therefore the polarization rotation caused by the ionosphere does not affect signal reception. Circular polarization means that the end of the electric field vector is a circle with a clockwise rotation in a plane perpendicular to the wave propagation direction, one can note that when we have a reflection of these signals, the polarization direction is inverted and we obtain a Left Hand Circularly Polarized (LHCP).

### II.2.2.3 $L_1$ band signals

The  $S_1$  signal equation (Eq. II.3) of the  $L_1$  carrier is modulated by the C/A and P(Y) codes, respectively in phase (I) and quadrature of phase (Q). The navigation message is superimposed on the two codes. The analytical expression of the  $S_1$  signal transmitted on  $L_1$  with the carrier frequency

$f_1$  for a given satellite is:

$$S_1(t) = \sqrt{2P_{C/A,L_1}} D(t)C/A(t) \cos(2\pi f_1 t + \Phi_{L_1}) + \sqrt{2P_{P(Y),L_1}} D(t)P(t) \sin(2\pi f_1 t + \Phi_{L_1}) \quad (\text{II.3})$$

where  $P_{C/A,L_1}$  and  $P_{P(Y),L_1}$  are the powers transmitted in  $L_1$  for both  $C/A$  and  $P(Y)$  codes,  $D(t)$  is the transmission message,  $C/A(t)$  and  $P(t)$  are the binary sequences of codes  $C/A(t)$  and  $P(Y)$ . The PRN codes and navigation messages are synchronized as they are based on the same reference clock.

#### **II.2.2.4 $L_2$ band signals**

The  $S_2$  signal equation (Eq. II.4) of the  $L_2$  carrier is only modulated by the  $P(Y)$  code. It is written:

$$S_2(t) = \sqrt{2P_{P(Y),L_2}} P(t) \cos(2\pi f_2 t + \Phi_{L_2}) \quad (\text{II.4})$$

where  $P_{P(Y),L_2}$  is the transmission power for  $L_2$ ,  $P(t)$  is the sequence of the code  $P(Y)$ . There is no data transmitted on the  $L_2$  frequency ( $D(t)$  is absent, figure II.2).

#### **II.2.2.5 Modernization of the GPS system**

The GPS system is seeking to perpetuate, so it is essential to make it evolve according to technological progress, the appearance of new constellations and/or new applications. In the early time, developments were guided by technological progress, as evidenced by the various blocs that have been launched. The emergence of new applications for civil aviation for example and the arrival of competing constellations (for example GLONASS, GALILEO, BEIDOU) have led to deeper changes such as the emergence of new civil codes and (IIR-M block) and a new carrier. In addition, so-called augmentation systems, which seek to improve the accuracy of the system (§ II.5), rely on ground stations and a few satellites to provide corrections to reduce the GNSS system errors.

- *The new  $L_{2C}$  Civil code:* The new civil signal (in Fig. II.2), which modulates the  $L_2$  carrier, makes it possible to correct the ionospheric effects by combining the measurements of pseudo-distances obtained on  $L_{2C}$  with the measurements of the C/A code obtained on  $L_1$ . The main difference between the  $L_{2C}$  code and the C/A code, except for a different carrier frequency, is that for the civil part of the  $L_{2C}$  signal, there are two codes multiplexed between them (the military part of the signal is close to that of  $L_1$ ). One of these codes, called “Code Moderate” (CM clocked at 511 kHz), which is multiplexed with the navigation message while the other code known as "Code Long" (CL clocked at 511 kHz), is not. These codes have a longer period than the C/A code, with a period of 1ms. The CL code has a period of 1.5 seconds and the CM code of 20 ms. The  $S_{2C}$  signal (Eq. II.5) that transmits at frequency  $f_2$  for the  $L_2$  band for a given satellite is:

$$\begin{aligned}
 S_{2C}(t) = & \sqrt{2P_{P,L_2}}D(t)P(t) \cos(2\pi f_2 t + \Phi_{L_2}) \\
 & + \sqrt{2P_{C/A,L_2}}[D(t)CM(t) \oplus CL(t)] \cos(2\pi f_2 t + \Phi_{L_2})
 \end{aligned} \tag{II.5}$$

with  $\oplus$  modulo-2 addition, which corresponds to the multiplexing operator of civil codes ([Azmani, 2010](#)).

- *The new carrier  $L_5$  and its civil code:* In addition to having a different carrier frequency (Fig. II.2), the  $S_5$  signal of the  $L_5$  carrier (1,176.45MHz) (Eq. II.6) is modulated by a third civil code ([Azmani, 2010](#)). This code was designed for “life safety” applications in civil aviation. The  $S_5$  signal is modulated by a Quadrature Phase Shift Keying modulation (QPSK) with a component in phase  $I_5 = NH_{10}I$ , which contains the navigation information and the quadrature component  $Q_5 = NH_{20}Q$  (period of 20 ms) that contains no data and is called the “pilot signal” in Fig. II.2:

$$\begin{aligned}
 S_5(t) = & \sqrt{2P_{C/A,L_5}}D(t)NH_{10}I_5(t) \cos(2\pi f_5 t + \Phi_{L_5}) \\
 & + \sqrt{2P_{P,L_5}}NH_{20}Q_5 \sin(2\pi f_5 t + \Phi_{L_5})
 \end{aligned} \tag{II.6}$$

where  $NH_{10}$  and  $NH_{20}$  are the Neumann-Hoffman multiplexing codes of  $I_5$  and  $Q_5$  at 10 ms and 20 ms, respectively.

### **II.2.3 Globalnaya Navigatsionnaya Sputnikovaya Sistema (GLONASS)**

The other fully operational constellation, GLONASS (Globalnaya Navigatsionnaya Sputnikovaya Sistema), started in 1976 by the former Soviet Union. It began to finally achieve its goals in 2001. Since 2001, many new satellites have been launched and the constellation has provided global geo-positioning since 2007. The constellation is currently nominal with 24 satellites in three orbital planes inclined at  $64.8^\circ$ . The inclination of orbits, which are higher than the GPS orbits, allows us to better “see” polar regions (Fig. II.1). The near circular orbits are on an altitude of 19,100 km above the Earth’s surface and the orbital period is 11 h 15 min with a repeatability of 8 sidereal days (one sidereal day = 23 h 56 min). The Russian system uses multiple access the CDMA in the  $L_3$  band (first satellite launched in 2010) like other constellation but one of the peculiarities, for  $L_1$  and  $L_2$  bands, is that GLONASS used the Frequency Division Multiple Access (FDMA, Tab. II.1) access for the satellite identification and the PRN code is the same for all satellites which in theory allows GLONASS system to be more resilient to interference signals. Frequencies  $L_1$  and  $L_2$  can be defined as follows:

$$f_1 = 1,601MHz + k0.5625Mhz \quad (\text{II.7})$$

$$f_2 = 1,246MHz + k0.4375Mhz \quad (\text{II.8})$$

where  $k$  is the used channel number. This number has changed over time: until 1998,  $k$  ranged from 0 to 12, then from 1998 to 2005 it was changed to vary between  $-7$  and 12 and finally from 2005, its final configuration only uses 12 values between  $-7$  and 4 and two channels are reserves: 5 and 6 can be used exceptionally (Tab. II.2). The  $f_1/f_2$  ratio, for each satellite, is constant and equal to  $9/7$ .

Recent developments in the GLONASS system saw the emergence of a

new  $L_5$  carrier of frequency  $f_5 = 1176.45$  MHz.

TABLE II.1 – Characteristics of operational or most advanced GNSS constellations. The arrow indicates future developments. The set of GNSS frequency modulation codes is also presented: Binary Phase Shift Keying (BPSK: the most classic); Binary Offset Carrier (BOC); Multiplexed BOC (MBOC); Time Multiplexed BOC (TMBOC); Composite BOC (CBOC); Alternate BOC (AltBOC); Quadrature Phase Shift Keying (QPSK). Done on March 28, 2018, this table may therefore have evolved following the launches of the different satellites of the various constellations.

| Constellation GNSS  | GPS (USA)                                 | GLONASS (RUSSIAN)  | GALILEO (EUROPE)   | COMPASS/BeiDou (CHINA)                                     |
|---|---|--|--|--|
| Operational satellites  | 32 MEO                                    | 24 MEO   | 4 IOV<br>30 MEO  | 5 GEO<br>30 MEO<br>3 IGSO                                  |
| Altitude (km)   | 20,200                                    | 19,100   | IOV: 23,222<br>MEO: 23,616                                 | 21,150   |
| Orbital Plans   | 6   | 3  | 3  | 3  |
| Orbital period  | 11 h 58 min                               | 11 h 58 min  | 14 h 21 min  | 12 h 53 min  |
| Angle   | 55°                                       | 64.8°  | 56°  | 55°  |
| Multiple Access   | CDMA                                      | FDMA/CDMA  | CDMA   | CDMA   |
| Carriers and Frequencies (MHz)  | L1: 1575.42<br>L2: 1227.60<br>L5: 1176.45 | L1: 1598.06-1605.38<br>L2: 1242.94-1248.63<br>L3: 1207.14<br>L5: 1176.45 | E1: 1575.42<br>E5a: 1176.45<br>E5b: 1207.14<br>E6: 1278.75 | B1: 1561.10<br>B1-2: 1589.74<br>B2: 1207.14<br>B3: 1268.52 |
| Modulation  | BPSK, BOC, TMBOC                          | BPSK, BOC  | BPSK, BOC, CBOC, AltBOC                                    | QPSK, BOC, MBOC, TMBOC                                     |
| Status  | OP  | OP   | VAL  | -OP  |
| <p>OP: operational, -OP: Quasi-operational, VAL: Validation phase<br/>           Code Division Multiple Access: CDMA, Frequency DMA: FDMA<br/>           MEO: Medium Earth Orbit, GEO: Geostationary, IOV: In Orbit Validation, IGSO: Inclined GeoSynchronous Orbit</p> |   |  |  |  |

## II.2.4 New GNSS

### II.2.4.1 Galileo

Galileo is Europe’s Global Satellite Navigation System (GNSS), was designed and developed on a civilian basis, while integrating the necessary security protections. Started in the 1990s, the project really began to grow from March 26, 2002, when the Council of Ministers of the European

## Chapter II. GNSS Reflectometry

---

TABLE II.2 – Correspondence between channel number and sub-band for GLONASS  $L_1$  and  $L_2$  carriers of different satellites of the various constellations.

| Channel number | Nominal frequency of sub-band $L_1$ (MHz) | Nominal frequency of sub-band $L_2$ (MHz) |
|----------------|---|---|
| 6              | 1605.3750                                 | 1248.6250                                 |
| 5              | 1604.8125                                 | 1248.1875                                 |
| 4              | 1604.2500                                 | 1247.7500                                 |
| 3              | 1603.6875                                 | 1247.3125                                 |
| 2              | 1603.1250                                 | 1246.8750                                 |
| 1              | 1602.5625                                 | 1246.4375                                 |
| 0              | 1602.0000                                 | 1246.0000                                 |
| -1             | 1601.4375                                 | 1245.5625                                 |
| -2             | 1600.8750                                 | 1245.1250                                 |
| -3             | 1600.3125                                 | 1244.6875                                 |
| -4             | 1599.7500                                 | 1244.2500                                 |
| -5             | 1599.1875                                 | 1243.8125                                 |
| -6             | 1598.6250                                 | 1243.3750                                 |
| -7             | 1598.0625                                 | 1242.9375                                 |

Union Transport validated the Galileo program's development phase. The first validation satellite IOVE-A (Galileo In Orbit Validation Element, Tab. II.1) was launched at the end of 2005, before being joined by a second IOVE-B in April 2008. These two satellites (IOVE-A and IOVE-B on a near-operational orbit of 23,222 km) allowed us to demonstrate the interoperability of Galileo and GPS systems that is the possibility of substitution, transparent to the user, of one system over the other. The first four operational Galileo satellites were then launched in October 2011 and 2012. Galileo is being developed by the European Space Agency (ESA) and will consist of a constellation of 30 satellites placed in three orbital planes spaced at  $120^\circ$  and inclined at  $56^\circ$  relative to the equator at an altitude of 23,616 km and a satellite orbital period of 14 h 21 min. As shown in Tab. II.1, compatibility is maintained between both the GPS and Galileo systems through the existence of common carriers (for example,  $L_1 = E_1 = 1575.42$  MHz).

In the operational phase, the Galileo system will offer 5 services with more or less restricted access to:

- Open Service (OS), completely open, free service, for the standard modes of maritime and land navigation systems, has the standard and precise working mode. Guaranteed accuracy in horizontal plane is 4m, while in vertical plane it is 8 m;
- Commercial Service (CS), commercial approach, the introduction of two additional encrypted signals, the level of accuracy is sufficient for precision agriculture, surveying measurements, *etc.* Continuity of service is guaranteed. Accuracy of spatial coordinate's determination in the CS mode is at centimeter level;
- Safety of Life (SoL) has all the functionality of OS services, users are authorized, and the continuity of service is guaranteed, suitable for navigation in air, land and maritime transport. Guaranteed accuracy in horizontal plane is 4m, while in vertical plane it is 8 m;
- Public Regulated Service (PRS), authorized access, encryption signals for PVT, with high priority of continuous service use, strategic and secure infrastructure. Guaranteed accuracy in horizontal plane is 6.5 m, while in vertical plane it is 12 m;
- Search and Rescue (SAR), the current localization of emergency calls, rescue operations, *etc.* Authorized services have the access.

### II.2.4.2 COMPASS-BeiDou

Wishing also to overcome the dependence on the US GPS, the Chinese authorities began very quickly establish a regional free system: BeiDou-1. This system, initiated in the early 1990s, was realized by the launch of two first BeiDou-1A and BeiDou-1B satellites in 2000. This system has recently evolved into a comprehensive system known as BEIDOU-2 or COMPASS. The constellation consists of three types of orbit: 5 satellites in geostationary orbit, 3 in inclined geosynchronous orbit ( $55^\circ$ ) and 27 in medium Earth orbit. BEIDOU-2 has been operational since late 2012 with coverage including China and the surrounding countries. In early

2015, over a dozen satellites were in orbit. The BEIDOU system offers two services:

- authorized service (AS): a public service with an accuracy of less than 10 m, operational since January 14, 2013;
- reserved service of unknown accuracy.

The structure of the signal (Tab. II.1) is close enough to the other systems with the CDMA transmission with the correlation function BOC, but also more complex ones like MBOC and AltBOC that improve mainly altimetry accuracy and the new QKSP modulations.

### II.2.4.3 Regional Systems QZSS and IRNSS

The Quasi-Zenith Satellite System (QZSS) is a regional satellite positioning system (the Tundra orbit flying over Japan and Australia), which is under development by the Japanese space agency JAXA. It will contain six signals: conventional  $L_{1C}$  frequencies using the  $C/A$  code (1,575.42 MHz),  $L_{2C}$  (1,227.6 MHz),  $L_5$  (1,176.45 MHz) as well as the  $L_{1-SAIF}$  frequency (1,575.42 MHz), which is used by the augmentation system (SBAS) for real-time, sub-meter accuracy. The  $L_{EX}$  carrier (1,278.75 MHz) is a high-precision signal (3 cm) that is compatible with the Galileo  $E_6$  signal.

The Indian Regional Navigation Satellite System (IRNSS) is also a regional satellite navigation system that is being developed. Its regional coverage focuses on India and its periphery up to a distance of  $\sim 2,000$  km from its borders.

### II.2.5 The Positioning measurement

It is possible with the GNSS system to position itself in two different ways according to the capacities of the receivers. Cheaper mono-frequency receivers ( $L_1$ ) use positioning by measuring the code; the more sophisticated receivers, more expensive acquire bi- or tri-frequencies use the measurement of the phase much more accurate for positioning.

### II.2.5.1 Code measurement

The fundamental principle of positioning by measuring the code is based on the observation of distances between satellites and the unknown position of the receiver, which could be on the ground, on a boat or on an airplane (Hofmann-Wellenhof et al., 2001). The position of satellites is roughly determined by the control segment (ephemeris and almanacs). The precise orbits are recalculated by the International GNSS Service (IGS) after satellite overpass. The distance measured between the receiver and a satellite is represented by a wavefront located at a distance  $d$  from the satellite. This wavefront appears in space through a sphere where the center is satellite  $j$  and on which is located receiver  $i$ . Theoretically, three satellites are needed to obtain the intersection point of three spheres (actually, two points exist but one of them is not on Earth). To get distance  $D_i^j$  that separates receiver  $i$  and satellite  $j$ , which must be visible, we multiply the wave propagation time  $\Delta t_i^j$  by the wave propagation speed  $c$  ( $\sim$  speed of light). Thus we get:

$$D_i^j = c\Delta t_i^j \quad (\text{II.9})$$

while in theory it is simple to measure, it does raise certain issues: how can the propagation delay be measured? Which satellite is sending the signal? This is why the GPS receivers have a satellite tracking function that identifies the satellites by the PRN code (by reading the  $C/A$  code on the  $L_1$ ) from the transmitter satellite, generates the replica of the identified the GPS satellite and delays this replica until it is aligned/correlates with the satellite signal; this aligned delay corresponds to the propagation time  $\Delta t_i^j$  with the synchronization error, which is actually why we speak of measuring “pseudo-distance”. Indeed, in practice, all the times are in absolute the GPS time, which corresponds to January 6, 1980 at 00 h UTC. Therefore, for proper positioning, it is necessary to calculate this satellite/receiver offset:

$$\Delta t_i^j = t_{Ri} - t_E^j \quad (\text{II.10})$$

where:

- $t_R = t_{Ri} + \delta t_i$  is the arrival time of the wave at receiver  $i$  in receiver time and which depends on the absolute arrival time  $t_R$  and the clock offset of the receiver with respect to the absolute time  $\delta t_i$ ;
- $t_E = t_E^j + \delta t^j$  is the time of transmission by the satellite  $j$  in satellite time which depends on the absolute transmission time  $t_E$  and the satellite clock offset relative to the absolute time  $\delta t^j$ .

The equation II.10 expressed in absolute is:

$$\Delta t_i^j = t_R - t_E + (\delta t^j - \delta t_i) \quad (\text{II.11})$$

The measurement of the pseudo-distance (PSD), derived from equation II.9 and II.11, is therefore:

$$PSD_i^j = c(t_R - t_E) + c(\delta t^j - \delta t_i) = \rho_i^j + c(\delta t^j - \delta t_i) \quad (\text{II.12})$$

where  $\rho_i^j = \sqrt{(X^j - X_i)^2 + (Y^j - Y_i)^2 + (Z^j - Z_i)^2}$ , is the geometric distance between satellite  $j$  and receiver  $i$ , we can see that there are four unknowns in Eq. II.12. The first unknown is time ( $t_{Ri}$ ) then we look at coordinates (X, Y and Z). This relation underlies a propagation in the vacuum of the wave. It is no longer true when it comes into the atmosphere. In order to achieve geodetic accuracy, other corrections should also be taken into account. For example, the apparent extension of the satellite receiver distance due to the troposphere crossing ( $\delta_{tropo}$ ) should be corrected and the perturbation of signal due to the dispersion nature of the ionosphere (ionospheric delay  $\delta_{iono}$ , depending on the frequency  $f$  of the signal). It is also necessary to take into account an term containing all the other factors that can disturb the signal (relativistic effect, multiple reflections of the electromagnetic signal before reception, etc.). The measurement of the pseudo-distance is then written:

$$PSD_i^j = \rho_i^j + c(\delta t^j - \delta t_i) + \delta_{tropo} + \delta_{iono} + \varepsilon \quad (\text{II.13})$$

All these errors allow the accuracy of pseudo-distance measurements to

be around a few meters and can be reduced to meter using augmentation systems like WAAS (USA) or EGNOS (Europe). In order to get accurate determination, phase measurement is preferred. It corresponds to the determination of the number of cycles performed by the carrier since its emission.

### II.2.5.2 Phase measurement

Here again, we go through a satellite identification phase. The modulation (code and navigation message) is removed from the main frequency of the considered carrier. The phase of the signal at time  $t$  is compared with a copy/replica generated by the receiver, which can generate a replica of the modulation codes of any satellite. The phase shift between the carrier and its replica is measured, meaning that we measure the cycle fraction that represents the offset between the two, rather than the total number of cycles that the carrier has achieved from its issuance from the satellite until it reaches the receiver.

The phase at time  $t$  is defined as:

$$\Phi(t) = \Delta\Phi(t) + n(t) + N \quad (\text{II.14})$$

$\Delta\Phi(t)$  is the decimal fraction of the phase (phase shift),  $n(t)$  is the integer number of cycles elapsed since the first correlation/measurement counted by the receiver's cycle counter and  $N$  is the integer ambiguity (satellite-receiver distance divided by the signal wavelength and from which we extract the integer part) that corresponds to the integer number of cycles from the satellite to the receiver. It is therefore understandable that observing distance between the receiver and the satellite is ambiguous of what is called integer ambiguity  $N$ . To get distance  $\rho_i^j$  (Eq. II.15) that separates the satellite  $j$  from receiver  $i$  will require subtracting the integer ambiguity  $N_i^j$ , the clock biases  $\delta t^j$  and satellite and receiver biases  $\delta t_i$ , and tropospheric  $\delta_{tropo}$  and ionospheric  $\delta_{iono}(f)$  effects (multi-frequencies reduce drastically this effect) from the phase shift  $\Delta\Phi_i^j$ . For this phase

difference in meters and not in cycles, we will have to multiply the result by the wavelength  $\lambda$ :

$$\Delta\Phi_i^j = \rho_i^j + \lambda N_i^j + c(\delta t^j - \delta t_i) + \delta_{iono}(f) + \delta_{tropo} + \varepsilon \quad (\text{II.15})$$

Once it has been determined, the integer ambiguity  $N_i^j$  remains constant for satellite  $j$  throughout the continuous observation of  $j$ . This is what is called phase tracking. A simple cycle counter will show the number of cycles  $n(t)$  since the first measurement. As a result, we do not create a new integer ambiguity at each observation, but the initial value is simply incremented. However, it may be that we lose the signal because of a receiver malfunction or under the effect of ionospheric scintillation, or even because of the presence of a mask (tree, wall) between the satellite and receiver: this is called a cycle slip. In this case, a new integer ambiguity must be determined (Duquenne et al., 2005).

### II.3 Reflection of GNSS signals

Natural elements (mountains, trees, *etc.*) and artificial (various constructions) on the surface of the Earth may impede electromagnetic signals transmitted by the satellites of different GNSS constellations. Depending on the nature of the obstacles encountered, they will then be absorbed, attenuated, reflected or refracted (Andréani, 2001). In the latter two cases, the reflected signals will change propagating direction (thus being reflected several times), creating well-known multipath. The signal thus takes longer to reach the antenna and be noisy and mitigated. In classical cases of GNSS positioning, the delay in the transmission time will result automatically by an error on the receiver-satellite distance and hence the position deduced from observations. So, in classical positioning, multipath are a source of error to remove.

GNSS reflectometry (GNSS-R) offers an alternative vision: Reflected GNSS signals contain crucial information on reflective backgrounds. By isolating and analyzing these reflected signals, one can therefore trace back

to the properties of the surroundings of the receiver. This opportunistic application in remote sensing is becoming more promising since the GNSS constellations are constantly developing with the sustainability and stability of the assured network.

This sector presents the process of reflection and analysis of electromagnetic waves in order to extract the characteristics of the reflective backgrounds.

### II.3.1 Multipath

The multipath phenomenon occurs when the signal from the GNSS satellite arrives at the receiver after following another path than the direct path. This is the case of at least one reflection on a close surface (Fig. II.3). This phenomenon is particularly present in urban areas, and can occur more than one time (many reflections = multipath) due to the presence of buildings known as urban corridor. The reflected signals will then disrupt the total signal received by the antenna and in particular modify the pseudo-distance and phase measurements performed by the receiver. The perturbation associated with the multiple paths is both correlated with time and with respect to the various satellite signals. For this reason, we cannot associate this contribution with a simple white noise (random), which distorts the algorithms commonly used in classical positioning (Sutour et al., 2012).

Considering to the direct signal of amplitude  $A_d$  and phase  $\phi_d$  in the form  $A_d \cos(\phi_d)$ , the reflected signal will be:

$$\alpha A_d \cos(\phi_d + \Delta\phi_r) \tag{II.16}$$

where:

- $\alpha$ : an attenuation factor ( $0 \leq \alpha \leq 1$ );
- $\Delta\phi_r$ : the phase shift due to the elongation of the path (Duquenne et al., 2005).

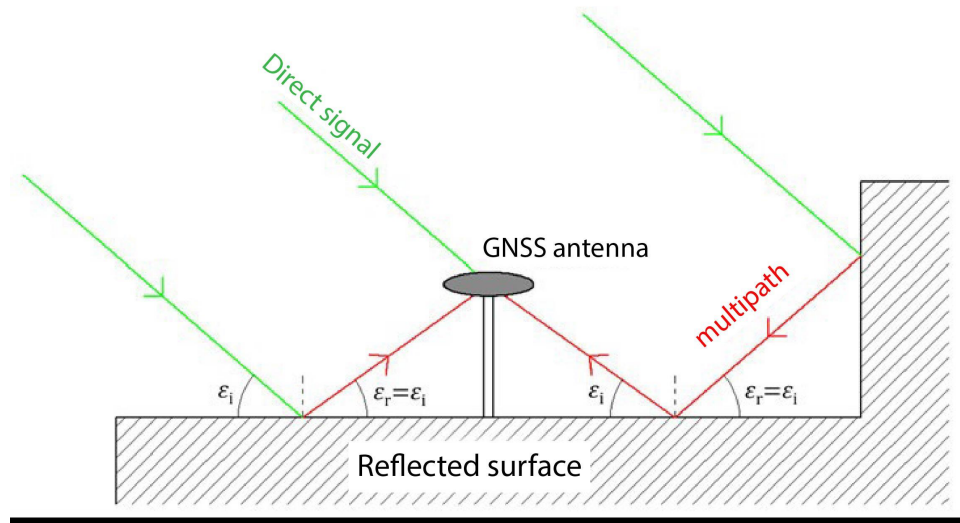


Figure II.3 – Multipath phenomenon on GNSS signals.  $\varepsilon_i$ : angle of incidence.  $\varepsilon_r$ : angle of reflection. Here we can see three different paths one with one reflection (left path) and the second one with 2 reflections (right path) and the last one, the center path corresponds to the direct path. To estimate SSH from GNSS signal, only one reflection (left path) is used.

Regarding the measurement of pseudo-distance based on the code, lengthening the path can cause an error of up to 20 m (depends on the distance between the antenna and the point of reflection). In order to minimize the impact of the multipath, it is understood that in geodetic positioning where precision is required, we have to minimize the maximum influence of the multipath. This can be done in several solutions:

- First, the measurement site solutions, take care to choose a more isolated measurement site possible, avoiding close reflective surfaces.
- Hardware solutions, it's possible to equip antennas with an absorbing system like ground plane, Choke ring *etc.* This device equips most geodetic antennas, we have to avoid this kind of antenna for GNSS-R.
- Solutions in the processing of observations including the possibility of filtering the waves received at the receiver to eliminate the waves of low incidence at the time of treatment ([Andréani, 2001](#)). For example, the multipath will be less effects if the acquisition time is long. In other words, the most sensitive techniques to multipath are those

based on rapid observations; the extreme case being when a position is determined by time (kinematic) (Duquenne et al., 2005).

### II.3.2 Specular and diffuse reflection

Multipath are the GNSS signals arriving at the antenna after reflection on nearby surfaces. Conceptually, it is possible to distinguish two contributions: the specular or coherent component and the diffuse or non-coherent component (Cardellach, 2001), as illustrated in Fig. II.4. The specular component comes from a reflection at a particular point (called the specular point SP in the remainder of this manuscript). This is the point of the reflective surface for which the reflected wave travels the shortest distance. This point obeys to physical optics *i.e.* the Snell-Descartes law of reflection which stipulates that the angle of reflection  $r$  and the angle of incidence  $i$  are equal in absolute value.

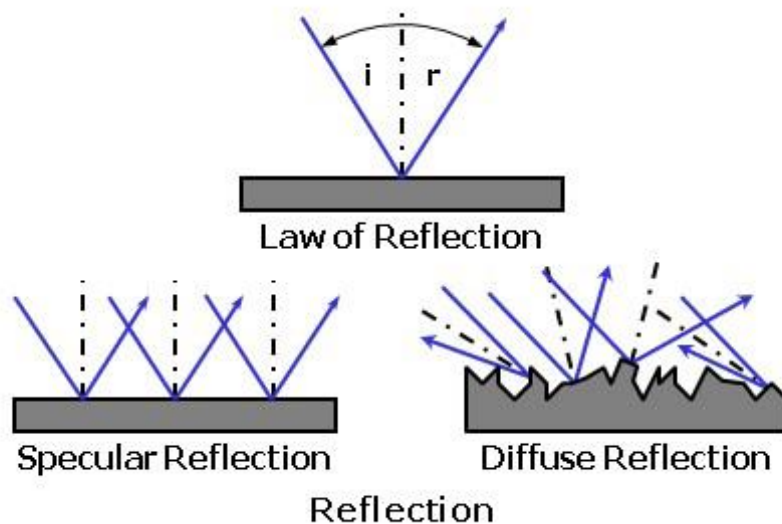


Figure II.4 – Specular and diffuse reflection

The specular term is characterized by high orientation whereas the diffuse contribution spreads the signal over a wide range of reflected signals. In a purely specular reflection, it is possible to receive the signal only in one preferred direction, which is not the case for the diffuse component.

In practice, a reflected signal contains both a specular component and a diffuse component, in proportions depending on the angle of incidence and the roughness of the reflection surface.

### II.3.2.1 Specular reflection

Specular reflection is generally described in geometrical optics, the electromagnetic propagation being modeled as a simple ray. A radius arriving on a perfectly flat surface with a certain angle of incidence generates another ray with an opposite azimuth and incidence angle in the plane defined by the incident ray and the normal to the surface at the point of incidence. Using this simple model, the specular point is the intersection of the two rays (incident and reflected) on the surface.

It is also possible to model specular reflection with a more realistic model using wave optics. Following the Huygens-Fresnel principles, each point of the incident wave front acts as a potential source of a secondary spherical wave. The reflected signal will then be the sum of all these secondary spherical waves and the major part of the energy will come from source points located on a surface surrounding the SP: all these sources define the 2-D **glistering zone** or **Fresnel surface**.

Each point inside the Fresnel surface is at the origin of a signal whose phase shift is less than a certain proportion of the wavelength of the incident signal.

For specular reflections, which occur at low surface roughness (ice, water, flat ground), it is generally assumed that most of the reflected signal power comes from the 1<sup>st</sup> Fresnel zone. This zone is defined by all the points for which the difference of trajectory (with respect to the SP) is less than  $\lambda/2$ .

The 1<sup>st</sup> Fresnel zone corresponds to a semi-major axis ellipse ( $r_a$ ) and semi-small axis ellipse ( $r_b$ ) which can be defined by ([Larson and Nievinski, 2013](#)):

$$r_b = \sqrt{\frac{\lambda h}{\sin(\theta)} + \left(\frac{\lambda}{2 \sin(\theta)}\right)^2} \quad (\text{II.17})$$

$$r_a = \frac{r_b}{\sin(\theta)} \quad (\text{II.18})$$

where  $\lambda(\text{m})$  the wavelength ;  $h(\text{m})$  the height of the antenna;  $\theta(^{\circ})$  the elevation angle of the satellite.

### II.3.2.2 Diffusion reflection

A flat reflection surface is a purely theoretical case. When the reflecting surface has a non-zero roughness (real case), the reflection is no longer solely specular, but a diffuse component appears.

Like specular reflection, diffuse reflection can also be modelled in two ways: simple modelling in geometric optics, and a somewhat more complex modeling done in wave optics. In geometric optics, the reflective surface is constituted by a concatenation of small facets (scattering) of different sizes and orientations. Each of these facets acts as a mirror for the incident ray. Under these conditions, a receiver R receives reflections of each facet having an ideal orientation, namely an orientation such as the normal to the facet to the point of impact S of the incident ray is the bisector of the incident ray and the right (SR): in Fig. II.5. It is therefore understandable that for a wave incident on a surface modeled by facets, reflections no longer come only from the nominal SP, but from multiple SP, provided that the facets are well oriented.

We then define the flickering surface or glistening zone which is the zone in which it is possible to have well-oriented facets, respecting a defined probability threshold. More roughness of the reflecting surface, more the probability of having oriented facets and the nominal SP, and consequently this area corresponds to the glistening zone.

In an optical wave, the diffuse component reflected by the surface is equal to the sum of the spherical wave re-emitted by each point of the surface. A diffusion beam is thus defined. The signal received after a diffuse

reflection can then be considered as the cumulative multiple individual contributions, each introducing a different shift of phase.

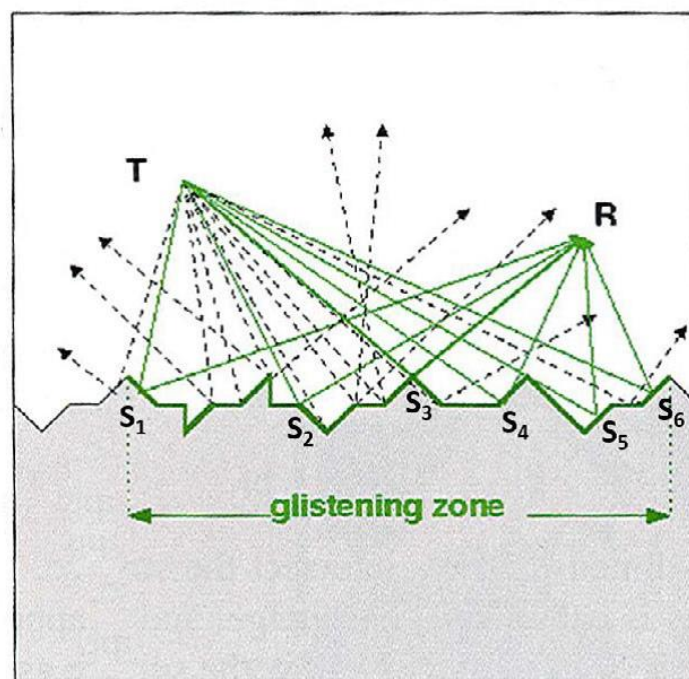


Figure II.5 – Glistening zone, decomposition of the reflective surface into multiple reflective facets. (Adapted from (Shuanggen Jin, 2014)).

### II.3.2.3 Roughness of the reflective surface (The Rayleigh criterion)

As we have seen, if the surface of reflection were perfectly plane, there would be only specular reflection: diffuse reflection is due to the roughness of the surface (Beckmann and Spizzichino, 1987). The specular component dominates the signal when the reflecting surface is sufficiently smooth. In this case, the reflection process can be modelled by multiplying the incident wave by the Fresnel reflection coefficient and by an attenuation factor that depends on the surface roughness. Conversely, the diffuse (or incoherent) component dominates the signal when the reflective surface is sufficiently rough. When the diffuse component dominates, the diffusion coefficient and the phase are different for each facet. The total reflected power is the power of the sum of the electric fields coming from each facet (Alonso-

Arroyo et al., 2015). This total power is less than that obtained when the coherent component dominates.

The **Rayleigh criterion** is generally used to distinguish a smooth surface from a rough surface (Beckmann and Spizzichino, 1987). A surface is considered smooth if:

$$\sigma_{rms} = \frac{\lambda}{8 \sin(\theta)} \quad (\text{II.19})$$

where  $\lambda$  is the wavelength of the signal;  $\theta$  is the elevation angle of the satellite;  $\sigma_{rms}$  is the Root Mean Square (RMS) roughness, which is the mean of the geometric deviation of the topographic surface the mean line of the roughness.

This criterion is equivalent to the condition that the phase difference between each facet is less than  $\pi/2$ . It is possible to apply a more restrictive criterion by replacing the factor 8 in Eq. II.19 by 16 or 32 (Beckmann and Spizzichino, 1987), which respectively means the maximum phase difference between each facet will be  $\pi/4$ , or  $\pi/8$ . It is important to emphasize here that the roughness is therefore not a defined quantity from the point of the diffraction view, since the same surface can be judged to be very smooth a given frequency and angle, and very rough for different frequency and angle.

## II.4 GNSS Reflectometry (GNSS-R)

### II.4.1 GNSS-R measurement technique

The first example of this type measurement was created in 1988 when Hall and Cordy (Hall and Cordy, 1988) proposed the concept of a “multi-static scatterometer” in order to estimate surface winds using a space radiometer that measured signals from the GPS constellation reflected by the oceans. In 1992, the French military detected, from an airplane, the GPS interference caused by reflections on ocean surfaces (Auber et al., 1994). Since then, many acquisition systems for the GNSS-R have emerged. These re-

ceivers can acquire GNSS waveforms (Fig. II.6 and II.7) and are quite different from conventional GNSS systems because they require a specific receiver that is capable of collecting the direct signal from the satellite and the reflected signal from a reflective surface (sea, lakes, vegetation, soil, car park, *etc.*). This is therefore a double antenna device (Fig. II.8). Equation II.20 with correlation amplitude  $Y^c$  between the received signal and the replica of the carrier is given by the following expression:

$$Y^c(t_0, \tau, f_d) = \frac{1}{T_c} \int_{t_0}^{t_0+T_c} S_R(t) a^*(t - \tau) e^{-j2\pi(f_c+f_d)t} dt \quad (\text{II.20})$$

where  $t_0$  is the time that marks the beginning of the integration, which is of duration  $T_c$ .

For the acquisition, there are two main families of receivers that carry out the complete acquisition of the waveform  $I$  and  $Q$  signals (see § II.2.2.3); these receivers are said to be “conventional” and “interferometric”.

“Conventional” waveform receptors or cGNSS-R (Fig. II.6) seek to coherently correlate, throughout a time interval  $T_c$  (generally  $1/f_c$ ,  $\sim 1$  ms or even up to 19 ms), the reflected signal  $S_R(t)$  with a replica  $a^*(t - \tau)$  of the  $C/A$  code generated locally by the receiver with a time lag  $\tau$  and after Doppler frequency shift compensation  $f_d$ . However, as the correlation amplitude  $Y^c$  (Eq. II.21) has a low amplitude and suffers from significant noise known as speckle, in order to reduce it, it is essential to have an incoherent average ( $N_i$ ) to improve the  $Y^c$  signal:

$$\langle |Y^c(\tau, f_d)|^2 \rangle \approx \frac{1}{N_i} \sum_{n=1}^{N_i} |Y^c(t_n, \tau, f_d)|^2 \quad (\text{II.21})$$

The width of the auto-correlation function is particularly important for applications in altimetry, which assumes that the overall noise is the sum of the thermal noise and speckle, both being totally uncorrelated. These receivers require a high bandwidth to achieve the root mean square of  $Y^c$  and to have a good range resolution. This bandwidth is limited by the

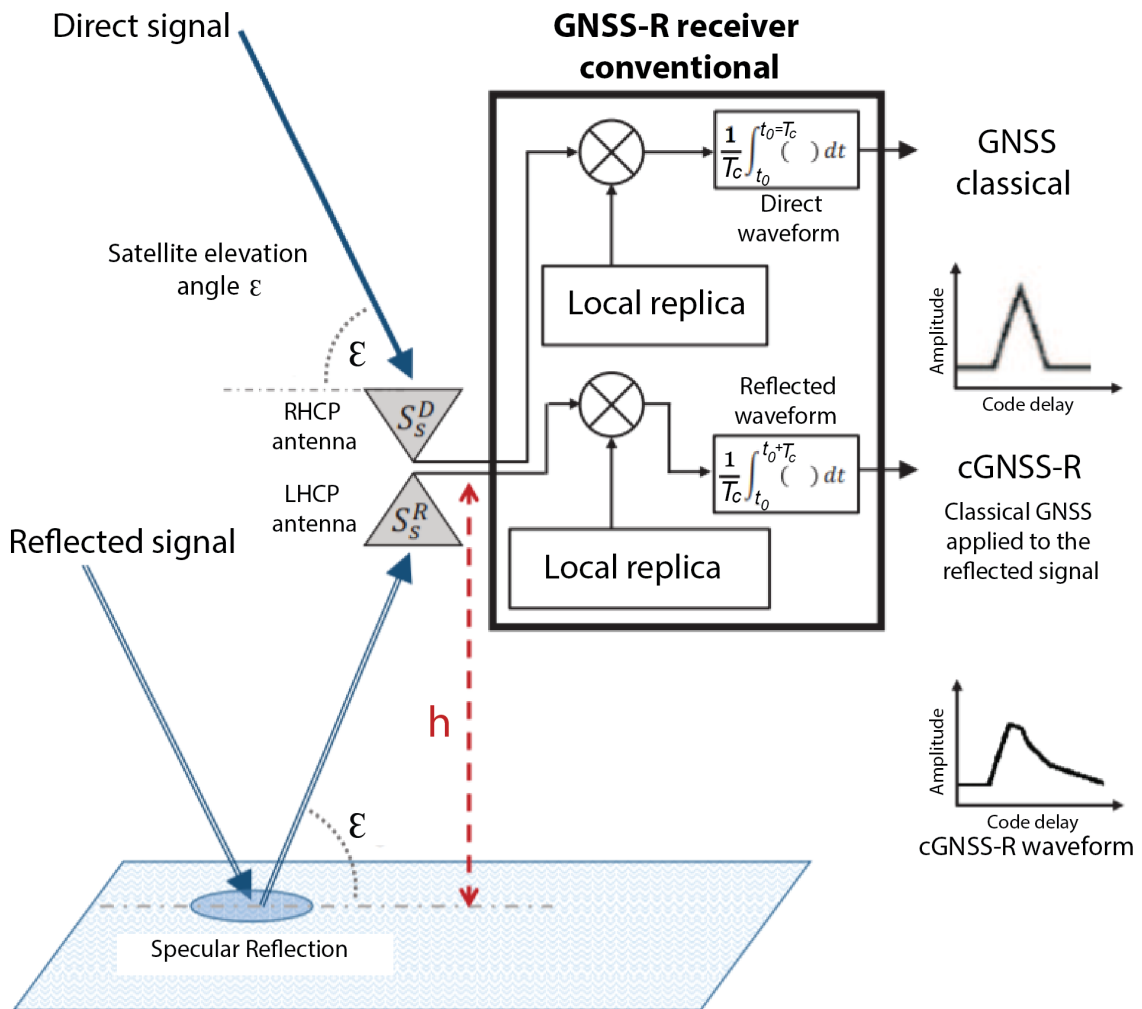


Figure II.6 – Principle of the cGNSS-R. The receiver records the waveform of the direct and reflected signals and correlate them with local replicas generated by the receivers (modified from (Kucwaj, 2016)).

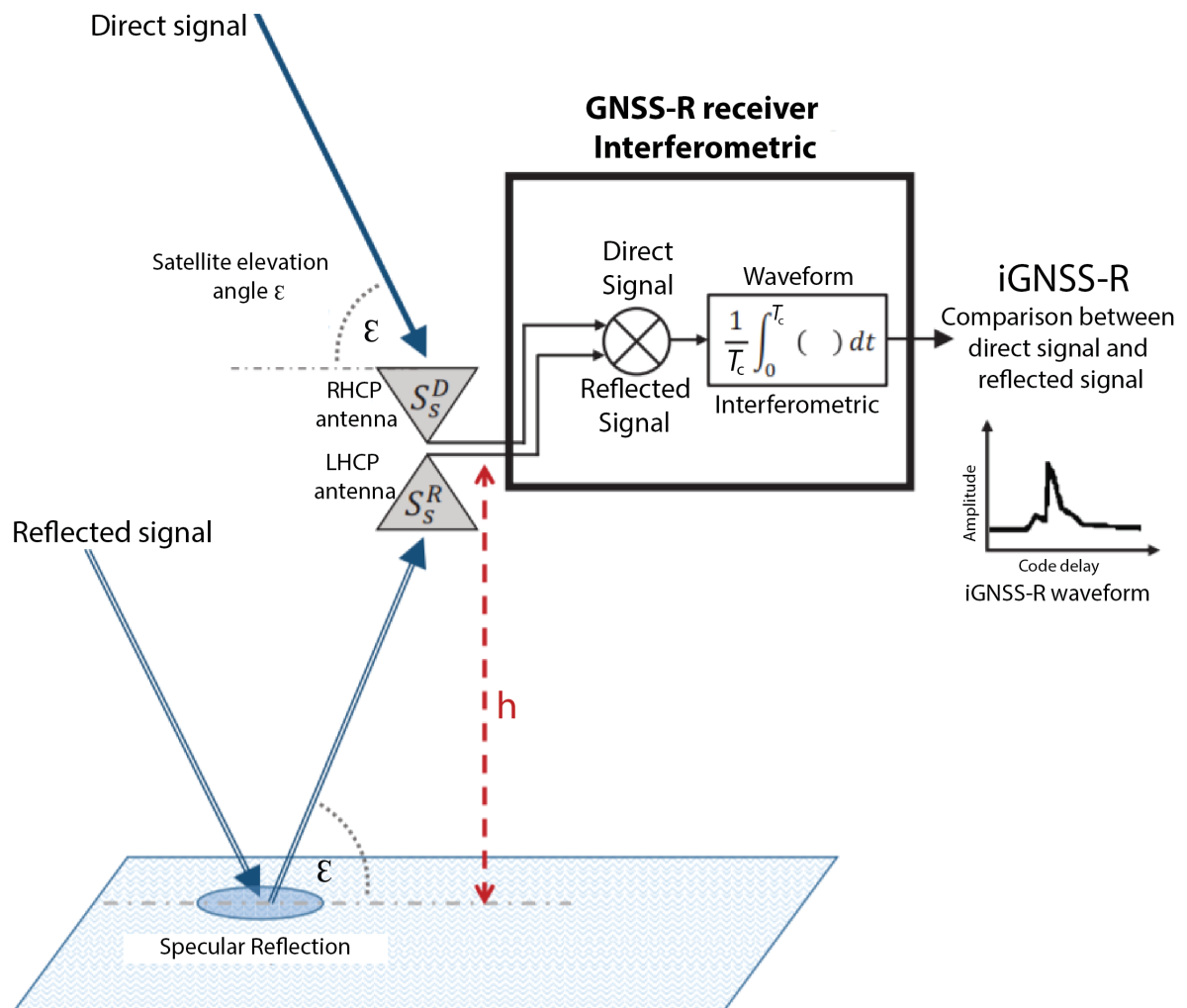


Figure II.7 – Principle of iGNSS-R. The receiver records the reflected signal and correlates it with the direct signal by the receiver. D and R mean direct and reflected paths (modified from (Kucwaj, 2016)).

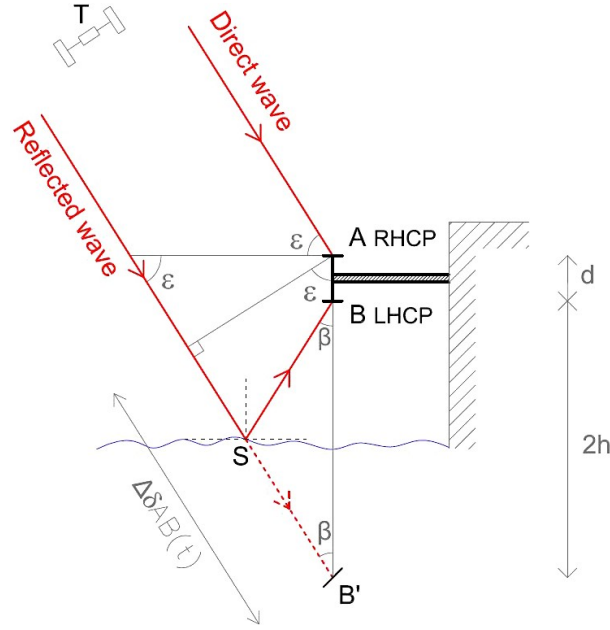


Figure II.8 – Principle of GNSS reflectometry with double antenna.  $T$ : satellite/transmitter;  $S$ : specular reflection point;  $\varepsilon$ : satellite elevation;  $\Delta\delta_{AB}(t)$ : additional path covered by the reflected wave;  $d$ : interdistance between the LHCP and RHCP antennas; and  $h$ : height of the receiver above the reflecting surface (Roussel et al., 2014).

modulation required to code the GNSS signal, and may be insufficient for certain applications. To solve this problem, recent receivers (since 2010) use the interferometric technique.

Interferometric waveform receivers iGNSS-R or PARIS (name of the first receiver of this type (Camps et al., 2012) are receivers in which (Fig. II.7) the reflected signal (recorded by the LHCP antenna) is not correlated with a replica, but with the direct signal (recorded by the RHCP antenna equations II.20, II.21). If we take the equations II.22, II.23 and we replace the replica  $a^*(t)$  with the direct signal  $S_d$ , we get:

$$Y^i(t_0, \tau, f_d) = \frac{1}{T_c} \int_{t_0}^{t_0+T_c} S_R(t) S_d^*(t - \tau) e^{-j2\pi(f_c + f_d)t} dt \quad (\text{II.22})$$

$$\langle |Y^i(\tau, f_d)|^2 \rangle \approx \frac{1}{N_i} \sum_{n=1}^{N_i} |Y^i(t_n, \tau, f_d)|^2 \quad (\text{II.23})$$

The inter-comparison between cGNSS-R and iGNSS-R is not simple since there are advantages and disadvantages in both approaches. From

the perspective of the installation geometry of cGNSS-R or iGNSS-R waveform receivers, it is identical and requires two opposite polarization antennas: the RHCP for the direct signal from the antenna to the zenith and the LHCP for the reflected antenna looking downward (Fig. II.8). For the cGNSS-R, the code replica is generated locally and it allows us to distinguish between different satellites by their codes. It has an intrinsic SNR and infinite small antennas can be used to monitor the reflected signals. The use of the  $C/A$  code for altimetry is not precise enough because of the width of the bandwidth. In addition, the Doppler dynamics for these codes are wider, requiring more frequent adjustment during operational measurements.

For iGNSS-R, this technique allows us to use not only the GNSS satellites, but also other types of satellite (radio, television, *etc.*). Moreover, processing cross-correlation produces Dopplers with smaller dynamics, which improves satellite tracking. However, the RHCP antenna must be with high gain and directive in order to target a satellite.

For my PhD work, I used another technic based on conventional receivers and the interference pattern technique (IPT), which gives good results for ground or low altitude applications.

This technique of reflectometry by interference pattern (IPT) of GNSS signals is also, like that of the waveforms, based on bi-static scattering since the transmitter and receiver are physically separated. The L-band signals from GNSS constellations are received by the omni-directional GNSS antennas located at varying heights above the ground/sea and defined by the user depending on the phenomena being studied. Let us note, however, that this technique does not tolerate antennas that are too high above the reflecting surface, unlike waveform receivers that can also be embedded on aircraft or satellites. In IPT, the majority of the signal goes directly to the antenna and the surrounding terrain also reflects part of the incident signal. This reflectometry technique requires standard GNSS receivers, meaning those for which the receiver outputs are no longer the raw waveforms, but the results of a correlation between the “direct/reflected” signal and a lo-

cal replica generated by the receiver. The processing result is stored in a standard RINEX file (as defined by the International GNSS Service). In this case, we consider the total signal to noise ratio ( $\text{SNR}_t$ ) which is a complex function of the direct SNR ( $\text{SNR}_d$  acquired in RHCP polarization) and the reflected SNR ( $\text{SNR}_r$  acquired in LHCP polarization), which are recorded by the single omni-directional antenna (Fig. II.9).

### II.4.2 Reflectometry through opportunity signals

#### II.4.2.1 Geometry of multi-static systems

There are therefore two types of geometry for multi-static systems: those with dual antennas with specific receivers capable of acquiring the waveforms (cGNSS-R or iGNSS-R) and those with a single antenna using standard receivers and omnidirectional antennas that are able to acquire direct and reflected waves.

- *Dual antenna device:* To acquire a direct signal, we use an antenna pointing toward the zenith (facing the sky) and for which the polarization is RHCP. For a reflected signal, because of the change in polarization linked to reflection, we use a LHCP antenna oriented toward the reflective surface. The path difference between the direct and the reflected signals can be retrieved by simple geometrical construction (Fig. II.8).
- *Standard antenna device:* In the geometry with a standard antenna (Fig. II.9), the single antenna combines direct and indirect signals, producing constructive and destructive interference oscillations that are observable in the SNR. The SNR data exhibits a quasi-sinusoidal pattern in which the predominant modulation frequency is correlated with the antenna height relative to the reflective surface (Larson et al., 2009).

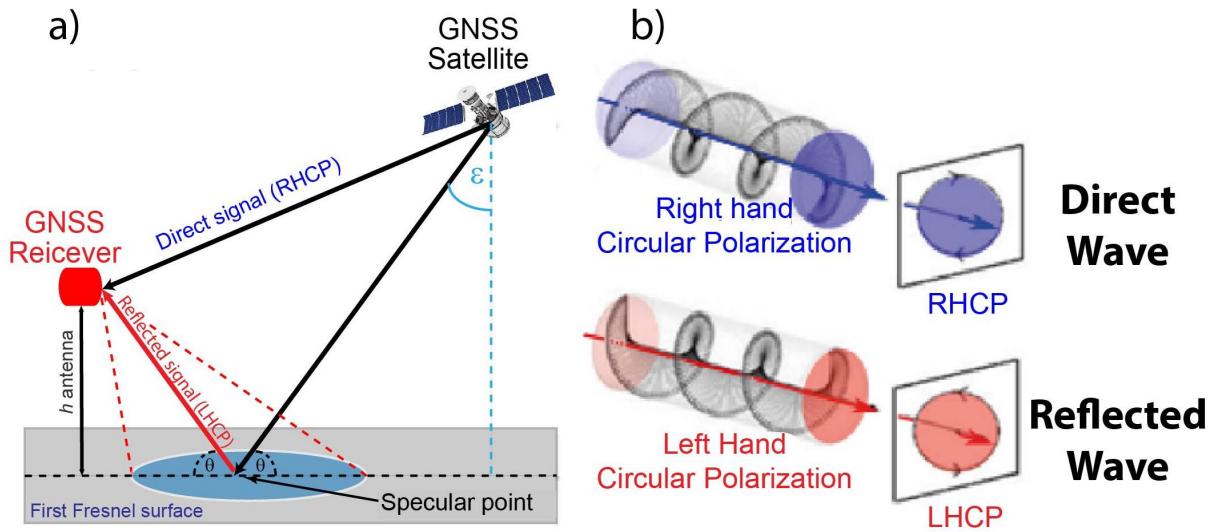


Figure II.9 – *In-situ* measurement scheme by the IPT method; a) geometry of the reflected multipath, position of the specular point that corresponds to the center of the first Fresnel surface (in blue); b) representation of the different polarizations recorded by an antenna "classic".

#### II.4.2.2 Observables

##### a) Delay-Doppler Map (DDM)

Figure II.10 shows the reflected waveform profiles for different surface conditions. There is a significant decrease in reflected signal power, which is accompanied by a strong asymmetry of the waveform with increasing surface roughness because the individual contributions are low and for some, very far from the specular point.

The shifts observed (Figure II.10a and II.10b compared with II.10c) between reflected and direct signals are linked to the extension of the path of the reflected signal, which passes through the reflective surface before reaching the receiver. The map that shows power versus delay and the Doppler is the DDM and it is the fundamental reflectometry observable. It reflects contributions of different pairs  $(\tau, f)$  from different cells of the observed surface. These cells are the intersections of iso-Delay and iso-Doppler at any point on the surface, with a delay size determined by the satellite PRN code and the Doppler coherent integration time.

By measurement this delay, the height (Eq. II.24) of the receiver can

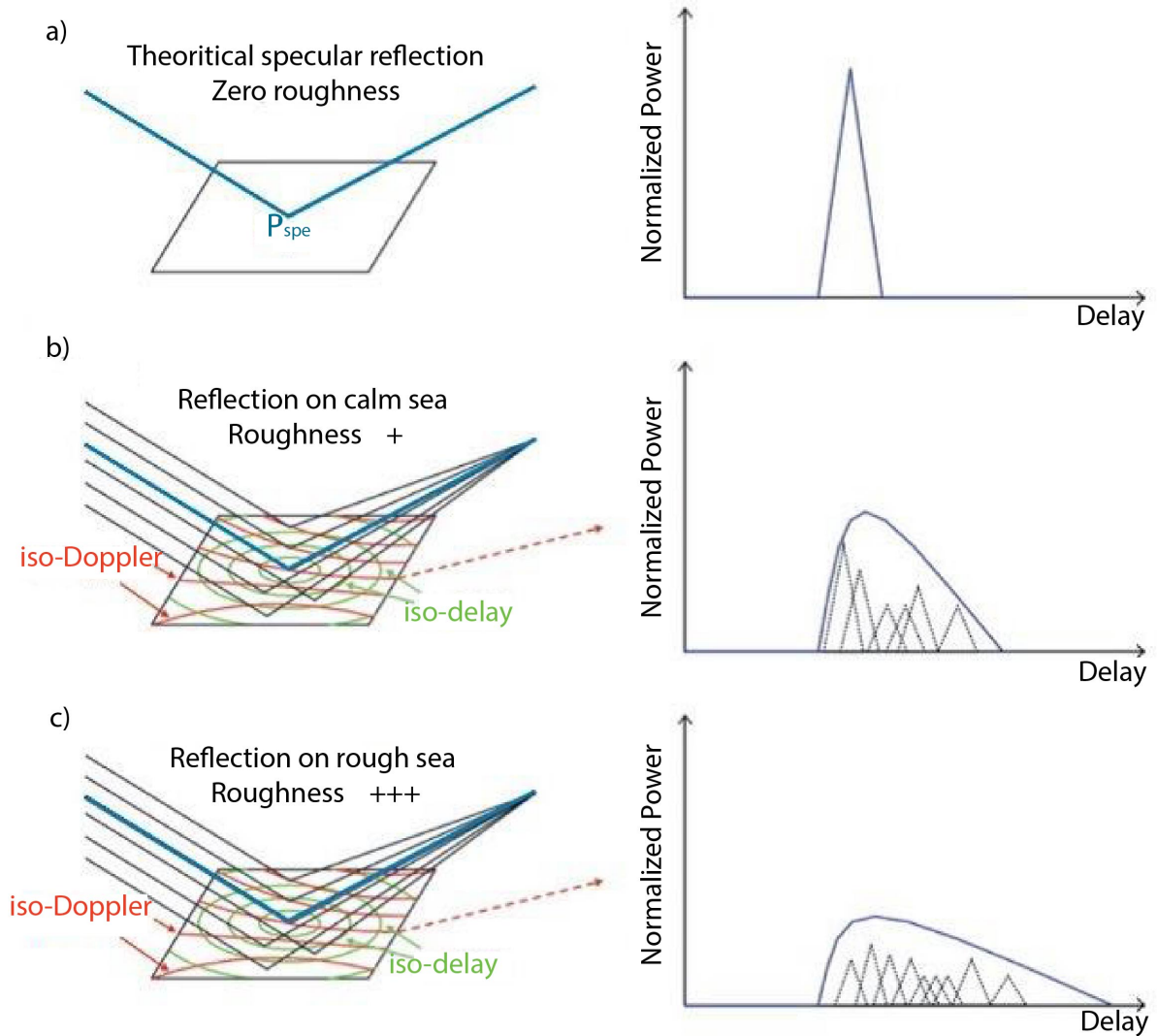


Figure II.10 – Waveforms depending on the type of scatter applied to a perfectly flat land surface (lake) and more or less rough ocean. For each profile, the blue curve shows the total waveform and the black curves show the individual reflections near the specular points, which are involved in the construction of the waveform. With  $P_{spe}$ : specular point. On the maps, the path in blue corresponds to the path of the specular point.

be estimated relative to the surface, and thus information related to the altimetry surface can be derived. For example, for a receiver installed *in situ* on a mast, with the approximation of a flat surface, the convention equation of GNSS-R altimetry is written as:

$$c\tau_i = 2h \sin(\varepsilon_i) + SB \quad (\text{II.24})$$

where  $\tau_i$  is the measured delay between the direct and reflected waveforms for satellite  $i$ ,  $\varepsilon_i$  is the elevation of the satellite and  $h$  is the receiver height relative to the surface.  $SB$  is the system bias linked to the path difference between direct and reflected and which must also be considered.

For airborne or space receivers, the above equation cannot be used because of the non-applicability of the flat surface approximation and other disruptive effects on the delay that are linked to the troposphere and ionosphere.

The additional length of the reflected signal path can also be ascertained through the phase difference between direct and reflected electromagnetic fields, which can be measured through the complex cross-correlation waveform. This phase difference provides an estimate for surface altimetry, with increased accuracy that is theoretically around a centimeter. Finally, the waveform's downwards slope can be used to get information on the surface roughness.

### *b) The bi-static scattering coefficient*

The bi-static scattering coefficient is particularly well analyzed for applications on ocean surfaces (roughness, surface wind) but here, we especially focus on land surfaces (soil moisture, plant cover biomass, *etc.*). To do this, we specifically look at the transmitter and receiver polarizations, the GNSS signal transmitted by the satellites is in RHCP. Following its reflection on the earth's surface, the electromagnetic wave generally undergoes a reversal of the polarization sign and thus the majority of the scattered power passes in LHCP. However, the combined effects of the roughness, and geophysical parameters of the surface, means that the sig-

nal from the right polarization may be significant and thus be used for the determination of geophysical parameters of the surface. We thus obtain a more complex response which is dependent on the RHCP component called co-polar  $\tau_0$  and the LHCP component called cross-polar  $\tau_x$ :

$$\tau_0 = \frac{\tau_h + \tau_v}{2}, \quad \tau_x = \frac{\tau_h - \tau_v}{2} \quad (\text{II.25})$$

These components are based on vertical reflection coefficients  $\tau_v$  and horizontal  $\tau_h$  reflection coefficients, which are dependent on the surface reflection parameters:

$$\tau_h = \frac{\sin(\theta) - \sqrt{\varepsilon - \cos^2(\theta)}}{\sin(\theta) + \sqrt{\varepsilon - \cos^2(\theta)}}, \quad \tau_v = \frac{\varepsilon \sin(\theta) - \sqrt{\varepsilon - \cos^2(\theta)}}{\varepsilon \sin(\theta) + \sqrt{\varepsilon - \cos^2(\theta)}} \quad (\text{II.26})$$

with the complex dielectric constant  $\varepsilon = \varepsilon_r - j(\sigma/(\omega\varepsilon_0))$ , where  $\varepsilon_r$  is the relative permittivity,  $\sigma$  is the electrical conductivity of the reflection surface and  $\varepsilon_0$  is the vacuum permittivity.

### *c) Surface reflectivity*

The surface reflectivity can be quantified using the ratio of direct and reflected waveforms, in the case of signals that are not affected by thermal noise. To do this, we consider that frequency  $f$  is aligned with the Doppler shift of the direct signal, by applying a change of variable:  $\tau' = \tau - R_d$ , where  $R_d$  is the direct path. The reflectivity of the surface is described by the equation:

$$\Gamma'_{pq} = \left| \left\langle \frac{Y_{r,q}(\Delta\tau, f)}{Y_{d,p}(0, f)} \right\rangle \right|^2 \quad (\text{II.27})$$

where  $\langle \rangle$  is the operator of the average,  $\Delta\tau$  is the delay between the direct and reflected paths;  $Y_{d,p}$  corresponds to the correlation function of the direct signal of incident polarization  $p$  and  $Y_{r,q}$  is that of the reflected signal of reflected polarization  $q$ .

## II.4.3 Reflectometer with single antenna

### II.4.3.1 Geometry of the multi-static system

If one considers a single geodetic RHCP antenna. The direct signal is received by the upper hemisphere of the antenna, as in conventional GNSS reception, while the reflected signal is received by the lower hemisphere: see Fig. II.11.

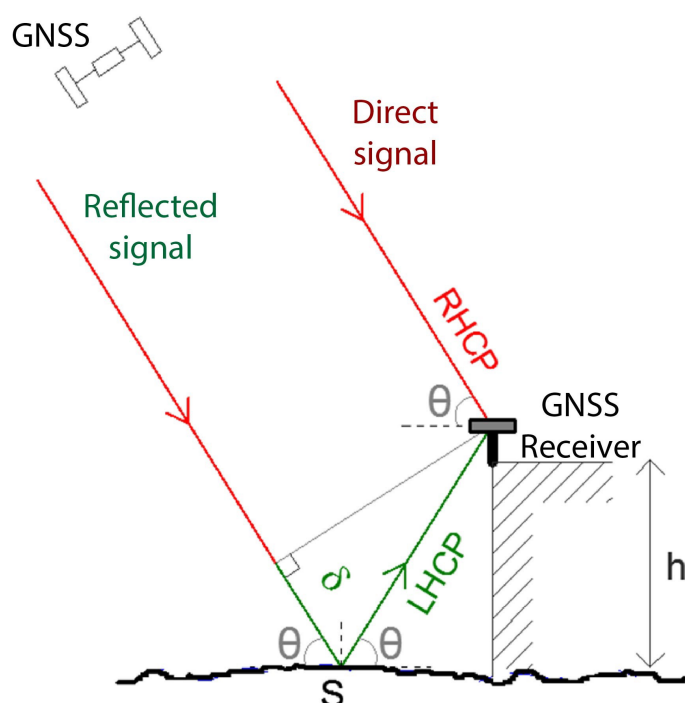


Figure II.11 – Geometry of a GNSS reflectometer with single antenna.

The reflected signal will therefore interfere with the direct signal at the antenna and affect the measurements made by the receiver. These interferences have a negative effect on the measurements carried out for positioning, and generally sought to be removed in classical geodesy (see § II.3.1). In GNSS reflectometry, on the contrary, the analysis of these interferences will provide useful information about the reflected signal, and therefore about the characteristics of the reflection surface.

### II.4.3.2 Interference pattern technique (IPT)

This technique, called Interferometric Pattern Technique (IPT), uses a single antenna: one in the RHCP for the direct path, the other in the LHCP for the reflected signals (Fig. II.11). Direct and reflected signals are combined to get the interference pattern that is visible on the total SNR ( $SNR_t$ ), resulting from the addition of direct SNR ( $SNR_d$ ) and reflected SNR ( $SNR_r$ ). This information is linked to various geophysical parameters such as ground surface moisture level or if the plant density is too high, vegetation moisture. One can also get information about the electrical conductivity  $\sigma$ , the relative permittivity  $\varepsilon_r$  or the surface altimetry  $h$ .

### II.4.3.3 Observable: Signal-to-Noise Ratio (SNR)

The SNR, is one of the classic observables of a GNSS receiver and is mainly used to quantify the quality of the GNSS measurements performed. The SNR is generally recorded at each measuring step and for each frequency measured by the receiver. Some instruments record it in binary form (1 when the quality of the measurements is sufficient to establish a position calculation, and 0 when the noise is too large), but most current receivers record it in its decimal form. The SNR therefore quantifies the amplitude of the received signal and is generally derived from the carrier tracking loop of the GNSS signal at the receiver. The tracking loop can be described (Georgiadou and Kleusberg, 1988; Ward, 2005; Bilich and Larson, 2007) as the relationship between the  $I$  (in phase) and  $Q$  (in quadrature) components of the received signal (see Fig. II.12). If we consider a theoretical case free of any multipath, the phase diagram in Fig. II.11) would contain only the contribution of the direct signal, *i.e.* only the amplitude phasor  $A_d$ , which is equivalent to the SNR. The carrier phase corresponds to the angle  $\phi_d$ .

On the other hand, in the presence of multipath, one (or more) phasors of amplitude  $A_r$  in Fig. II.12 are added to the diagram. This phasor has a relative phase  $\psi$  in relation to phase  $Q$  of the direct path. The tracking

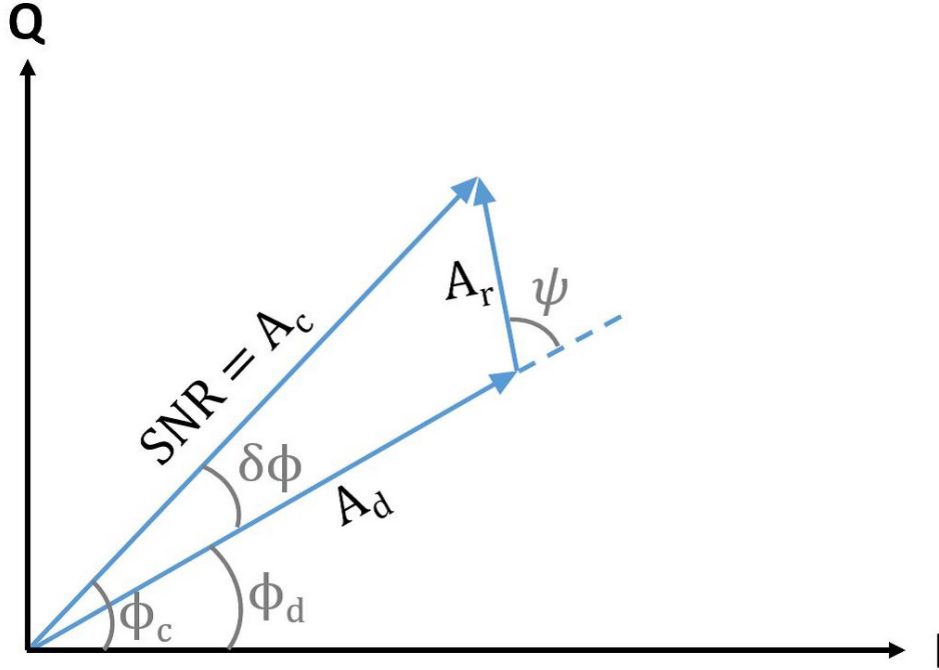


Figure II.12 – Phase diagram of the received GNSS signal illustrating the relationships between the phase (I) and quadrature (Q) components of the signal.

loop of the receiver will therefore lock on the signal composite of amplitude  $A_c$  and phase  $\phi_c$ , which is the sum vector of all phasers, containing both the direct and reflected signal. This implies that the SNR is equivalent to the amplitude of the composite signal. Considering the model in Fig. II.12, the phase error  $\delta\phi = \phi_c - \phi_c$  will be equal by (Larson et al., 2008a):

$$\tan(\delta\phi) = \frac{A_r \sin(\psi)}{A_d + A_r \cos(\psi)} \quad (\text{II.28})$$

And we'll have:

$$SNR^2 = A_c^2 = A_d^2 + A_r^2 + 2A_d A_r \cos(\psi) \quad (\text{II.29})$$

with  $A_r$  and  $A_d$  are the amplitudes of the multipath and direct signal, respectively, and  $\psi$  is the phase difference between the two signals. We can assume that  $A_r \ll A_d$ , SNR can be approximated by:

$$SNR^2 \approx A_d^2 + 2A_d A_r \cos(\psi) \quad (\text{II.30})$$

Equation II.30 shows that the general appearance of the SNR will be mainly dictated by the direct signal, which exhibits variations only related to the elevation angle of the satellite. On the other hand, the reflected signal produces an additional signal at high frequency and small amplitude in relation to the direct signal. The reflected signal perturbations will mainly be visible for low satellite elevation angles (Löfgren et al., 2011). Assuming a planar reflector which corresponds to sea surface, the relative phase angle can be derived geometrically from the path delay  $\delta$  of the reflected signal (Bishop et al., 1985):

$$\psi = \frac{2\pi}{\lambda}\delta = \frac{4\pi h}{\lambda} \sin(\theta) \quad (\text{II.31})$$

where  $\lambda$  the signal wavelength,  $\theta$  the satellite elevation and  $h$  the distance between the antenna phase center and the reflecting surface (Fig. II.11).

Equation II.31 it is possible to derive the frequency of the multipath oscillations (Roussel et al., 2015b):

$$f_\psi = \frac{d\psi}{dt} = \frac{4\pi\dot{h}}{\lambda} \sin(\theta) + \frac{4\pi h}{\lambda} \cos(\theta)\dot{\theta} \quad (\text{II.32})$$

$\dot{h}$  ( $= dh/dt$ ) defines the vertical velocity and  $\dot{\theta}$  ( $= d\theta/dt$ ) defines the elevation angle velocity. Equation II.32 can be simplified by making a change of variable  $x = \sin(\theta)$ :

$$\tilde{f} = \frac{d\psi}{dx} = \frac{4\pi}{\lambda} \left( \dot{h} \frac{\tan(\theta)}{\dot{\theta}} + h \right) \quad (\text{II.33})$$

where  $\tilde{f}$  is the frequency of the multipath oscillation.

#### II.4.4 Application of GNSS-R for altimetry

Equation II.33 shows that if we consider a reflection surface and a static antenna ( $\dot{h} \approx 0$ , in the static case), we will have  $\tilde{f} = 2h/\lambda$  is constant and therefore the frequency of oscillations due to the multipath will be directly proportional to the height of the antenna above the reflecting surface. This

altimetry method based on SNR analysis by using IPT technique has been the subject of numerous studies, mainly American (Larson et al., 2008a).

In the dynamic case (surface of the sea for example),  $\dot{h}$  cannot be neglected, and the frequency  $\tilde{f}$  therefore also depends on the elevation angle of the satellite  $\theta$ , its variation speed  $\dot{\theta}$  and the rate of variation of the height of the reflection surface  $\dot{h}$ . Considering Eq. II.33 only two unknowns have to be solve:  $h$  and  $\dot{h}$ .

### II.5 Conclusions

The scientific issues and implications of the development of GNSS reflectometry are very important. Altimetry measurements are made by estimating the delay between direct and reflected signals, and can reach an accuracy to the centimeter level. The range of potential applications of this opportunistic remote sensing technique is impressive in the altimetry domain:

- Altimetry monitoring of oceanic and continental waters;
- Determination of sea surface properties: roughness, wave height, currents and surface winds, salinity (Camps et al., 2006), *etc.*;
- Monitoring of flooded areas.

We have seen that the GNSS-R, along with the recent development of different GNSS constellations, is and will be a fundamental tool for monitoring environmental phenomena. Some studies even demonstrate the potential of GNSS-R for detection of meteorological event such as tsunami (Stosius et al., 2010), changes in droughts, rivers and ice, *etc.*

In chapter IV, I will focus mainly on the technique using a classical GNSS receiver with the single-antenna system and the "SNR" method to estimate the water level and detect the extreme events. We have performed in two different study areas: the Bay of Saint de Luz, located in the south western part of the Bay of Biscay, along the French Atlantic coast, the Red River and the Mekong River Delta, in Vietnam.



---

CHAPTER III

**Validation altimetry on coastal zone:  
example of the Bay of Biscay**

---

**Contents**

---

|   |    |
|---|----|
| III.1 Summary of the article published in Remote Sensing . . . . .    | 90 |
| III.2 Article published in Remote Sensing (11 January 2018) . . . . . | 92 |

---

## III.1 Summary of the article published in Remote Sensing

### En français:

Au chapitre I, j'ai présenté un bref état de l'art de l'altimétrie côtière à la fois d'un point de vue technique et à la fois au travers différentes limitations de l'altimétrie dans les zones côtières. L'article ci-dessous décrit les techniques mises en œuvre au cours de cette thèse pour tirer la quintessence des données altimétriques et ainsi démontrer qu'elles sont exploitables dans les zones côtières. Après avoir présenté le contexte de cette étude et les problèmes qu'elle couvre, nous en décrivons les principales avancées et les résultats les plus représentatifs. L'objectif majeur de ce travail était de décrire, valider et évaluer la précision des données altimétriques, en utilisant différent type de correction à moins de 5 km de la côte. Pour ce faire, ces données altimétriques ont été extraites à l'aide du logiciel MAPS (Multi-mission Altimetry Processing Software) (Frappart et al., 2015). Les SSH ont ensuite été déduites et comparées aux marégraphes situés sur le littoral de la côte atlantique française, dans le sud du golfe de Gascogne. En termes de corrections, nous avons corrigé les effets de propagation ionosphérique, troposphérique que ce soit la troposphère sèche ou humide et les effets géophysiques très sensibles près de la côte i.e. les effets des marées solides, marées polaires. On doit aussi prendre en compte la différence de hauteur entre le marégraphe et l'altimètre et le biais liés à l'état de la mer. Un traitement similaire a été appliqué à sept marégraphes sur notre zone d'étude. Ce traitement nous a permis d'augmenter le nombre de mesures altimétriques valides proches du littoral, notamment pour une distance assez faible  $\sim 5$  km. Cette étude a montré que le modèle de correction ionosphérique GIM et ceux de la troposphère humide obtenue grâce au données ECMWF donnent des corrections plus réalistes près des côtes que celles obtenues par des acquisitions bi-fréquences pour la ionosphère et celles liées aux mesures des radiomètres pour la troposphère humide. En milieu marin ouvert, les deux méthodes donnent des mesures comparables. La meilleure RMSE  $\sim 20$  cm est obtenue par le satellite SARAL

qui présente la plus petite tâche au sol et il est donc particulièrement adapté à la zone côtière. Enfin les satellites récents Jason-3 et Sentinel 3 doivent améliorer notre compréhension de la frange côtière en augmentant drastiquement le nombre d'observations sur ce domaine.

#### **In English:**

In Chapter I, I presented a state of the art of coastal altimetry both from a technical point of view and through different limitations of altimetry in coastal areas. The following article describes the techniques implemented during this thesis to generate improved and exploitable altimetry data in the coastal zones. After introducing the context of this study and the issues it covers, we describe the main features and results. The primary goal of this work was to describe, validate and evaluate the accuracy of the corrected altimetry data within 5 km from the coast. To do this, altimetry SSH was computed using the Multi-mission Altimetry Processing Software (MAPS) (Frappart et al., 2015). The SSH were then compared with tide gauges located on the coastal along the French Atlantic Coast in the Southern Bay of Biscay. Altimetry data from all satellites were corrected for the classical propagation and geophysical corrections needed from the coast, including instrumental, ionosphere, wet and dry troposphere, sea state bias, solid earth, pole tide corrections and the difference in geoid heights between the tide gauge and the altimeter. A similar processing was applied to seven tide gauges on our study zone. This processing can increase the number of valid altimetry measurements within 5 km from the coastline. This study showed that the GIM ionospheric correction model and those of the wet troposphere obtained from the ECMWF data provide more realistic corrections near the coasts than those obtained by bi-frequency acquisitions for the ionosphere and those related to radiometer measurements for the wet troposphere. In open marine environments, both methods provide comparable measurements. The best RMSE  $\sim 20$  cm is obtained by the SARAL satellite which has the smallest ground track and is therefore particularly suitable for the coastal zone. Finally, the recent Jason-3 and Sentinel-3 satellites should improve our understanding of

### **III.2. Article published in Remote Sensing (11 January 2018)**

---

the coastal fringe by drastically increasing the number of observations in this field.

### **III.2 Article published in Remote Sensing (11 January 2018)**

Article

# Multi-Satellite Altimeter Validation along the French Atlantic Coast in the Southern Bay of Biscay from ERS-2 to SARAL

Phuong Lan Vu <sup>1,\*</sup> , Frédéric Frappart <sup>1,2</sup>, José Darrozes <sup>1</sup>, Vincent Marieu <sup>3</sup>, Fabien Blarel <sup>2</sup>, Guillaume Ramillien <sup>1</sup>, Pascal Bonnefond <sup>4</sup> and Florence Birol <sup>2</sup>

<sup>1</sup> GET-GRGS, UMR 5563, CNRS/IRD/UPS, Observatoire Midi-Pyrénées, 14 Avenue Edouard Belin, 31400 Toulouse, France; frederic.frappart@get.omp.eu (F.F.); jose.darrozes@get.omp.eu (J.D.); Guillaume.Ramillien@get.omp.eu (G.R.)

<sup>2</sup> LEGOS-GRGS, UMR 5566, CNES/CNRS/IRD/UPS, Observatoire Midi-Pyrénées, 14 Avenue Edouard Belin, 31400 Toulouse, France; florence.biol@legos.obs-mip.fr (F.B.); fabien.blarel@legos.obs-mip.fr (F.B.)

<sup>3</sup> UMR CNRS 5805 EPOC—OASU—Université de Bordeaux, Allée Geoffroy Saint-Hilaire CS 50023, 33615 Pessac CEDEX, France; vincent.marieu@u-bordeaux.fr

<sup>4</sup> SYRTE, Observatoire de Paris, PSL Research University, CNRS, Sorbonne Universités, UPMC Univ. Paris 06, LNE, 75014 Paris, France; pascal.bonnefond@obspm.fr

\* Correspondence: phuonglan.vu@get.omp.eu; Tel.: +33-7-8232-1136

Received: 5 November 2017; Accepted: 28 December 2017; Published: 11 January 2018

**Abstract:** Monitoring changes in coastal sea levels is necessary given the impacts of climate change. Information on the sea level and its changes are important parameters in connection to climate change processes. In this study, radar altimetry data from successive satellite missions, European Remote Sensing-2 (ERS-2), Jason-1, Envisat, Jason-2, and Satellite with ARGOS and ALtiKa (SARAL), were used to measure sea surface heights (SSH). Altimetry-derived SSH was validated for the southern Bay of Biscay, using records from seven tide gauges located along the French Atlantic coast. More detailed comparisons were performed at La Rochelle, as this was the only tide gauge whose records covered the entire observation period for the different radar altimetry missions. The results of the comparison between the altimetry-based and in-situ SSH, recorded from zero to five kilometers away from the coast, had root mean square errors (RMSE) ranging from 0.08 m to 0.21 m, 0.17 m to 0.34 m, 0.1 m to 0.29 m, 0.18 m to 0.9 m, and 0.22 m to 0.89 m for SARAL, Jason-2, Jason-1, ENVISAT, and ERS-2, respectively. Comparing the missions on the same orbit, ENVISAT had better results than ERS-2, which can be accounted for by the improvements in the sensor mode of operation, whereas the better results obtained using SARAL are related to the first-time use of the Ka-band for an altimetry sensor. For Jason-1 and Jason-2, improvements were found in the ocean retracking algorithm (MLE-4 against MLE-3), and also in the bi-frequency ionosphere and radiometer wet troposphere corrections. Close to the shore, the use of model-based ionosphere (GIM) and wet troposphere (ECMWF) corrections, as applied to land surfaces, reduced the error on the SSH estimates.

**Keywords:** sea surface height; coastal altimetry; validation; tide gauge

## 1. Introduction

Satellite altimetry is a radar technique detailing the topography of the earth's surface based on the measurement of the distance between the satellite and the surface, derived from the two-way travel time of an electromagnetic wave emitted by the altimeter, or altimeter range and the precise knowledge of the satellite orbit [1,2]. The primary objectives of satellite radar altimetry are to measure the marine geoid, ocean currents, and sea level variability. In the coastal zones, sea level data retrieval and interpretation is particularly complex. This is due to the interaction of the radar signal with

land topography [3–6], geophysical corrections becoming inaccurate or incorrect when land surfaces are encompassed by the footprint of altimeters and radiometers [7], and to the short time scales and small spatial scales of the coastal dynamics [8] that are only partly sampled by the different altimeter missions, even when used in conjunction. Advances were made in altimeter instrument design with the development and launch of the Ka-band AltiKa instrument with on-board Satellite with ARgos and ALtiKa (SARAL). The use of this higher frequency reduces noise and has a smaller radar footprint in the images than in those obtained with the classical Ku-band instruments [9]. As a result, the coastal band is reduced where echoes are impacted by the presence of land. The launches of the first altimeters using the Synthetic Aperture Radar (SAR) technique [10], SIRAL on-board Cryosat-2 and SRAL on-board Sentinel-3, allowed more reliable observations in coastal areas. In parallel, advances were made in the development of new processing algorithms, corrections, and products for coastal applications of radar altimetry [11–14].

In this study, a comparison was completed of the most-used altimetry missions for monitoring the dynamic topography of the ocean surface, Jason-1, Jason-2, ERS-2, Envisat, and SARAL on their nominal tracks, operating in Low Resolution Mode (LRM) along the Atlantic coast of the Bay of Biscay (42–48°N, 0–10°W) from 1993 to 2015. Compared to the permanent calibration facilities or Calibration/Validation (Cal/Val) sites, parts of the ESA Earth Observation ground segment are located in Corsica, the Western Mediterranean Sea at the Harvest platform [15], the Eastern Pacific Ocean in Gavdos [16], the Eastern Mediterranean Sea [17], and the Bass Strait, between Australia and Tasmania [18]. Our goal was to evaluate the quality of altimeter-based sea surface heights (SSH). Our study had two main interests: to be well-instrumented with the presence of seven tide gauges in close proximity to eight altimeter tracks from five altimetry missions (Figure 1), and to investigate different tidal conditions than the classical altimetry Cal/Val sites. In contrast to the Corsica and Gavdos Mediterranean sites that are in semi-diurnal micro-tidal environments, the Harvest platform on the Pacific coast of California and the Bass Strait site between Australia and Tasmania are in mixed semi-diurnal macro and micro-tidal environments, respectively. The Bay of Biscay study area is in a semi-diurnal macro-tidal environment [19–21].

The error in the SSH retrieval from radar altimetry is caused by two main components: the ionosphere and wet troposphere corrections. For all satellites, the Ionosphere Correction (IC), due to electron content in the ionosphere, is obtained either by the bi-frequency altimeters, in Ku and C bands for T/P, Jason-1/2, and in Ku and S bands for Envisat, or from the electronic content of the ionosphere, such as the Global Ionospheric Maps (GIM) [22], available after 1998, or the New Ionospheric Climatology 2009 (NIC 09) [23] for mono-frequency altimeters such as ERS-2 or SARAL. The Wet Troposphere Correction (WTC), due to liquid water in the atmosphere, is derived either from radiometer measurements present on altimetry satellites or from meteorological model outputs, such as the ones made available by the European Center for Medium Range Weather Forecasting (ECMWF). Bi-frequency and radiometer-based corrections are used over the ocean even in coastal areas.

This study assessed the altimetry-based SSH in terms of number of observations, bias, root mean square error (RMSE), and correlation coefficient, for almost all the missions that were in orbit between 1993 and 2015, using records from seven tide gauges located along the French Atlantic coast in the southern Bay of Biscay. Contrary to what is commonly performed when using radar altimetry in coastal areas, the performance was assessed for different combinations of corrections applied to the altimeter range available in the Geophysical Data Records (GDR). A detailed analysis of the impact of these corrections on the accuracy of the altimetry-based SSH was performed at the La Rochelle tide gauge because this tide gauge is the only one that covers the entire observation period for the different radar altimetry missions.

## 2. Datasets and Study Area

### 2.1. Radar Altimetry Data

The radar altimetry data used in this study was obtained from the high precision altimetry missions launched after 1992 with the exception of Topex/Poseidon and Geosat Follow-On. Figure 1 shows a timeline of the different missions. The data were made available by the Centre de Topographie de l'Océan et de l'Hydrosphère (CTOH [24]). Altimetry data from all satellites were corrected for the classical propagation and geophysical corrections needed from the coast, including instrumental, ionosphere, wet and dry troposphere, sea state bias, solid earth, and pole tide corrections.

### Timeline for RADAR Altimeters with short periods used in our study

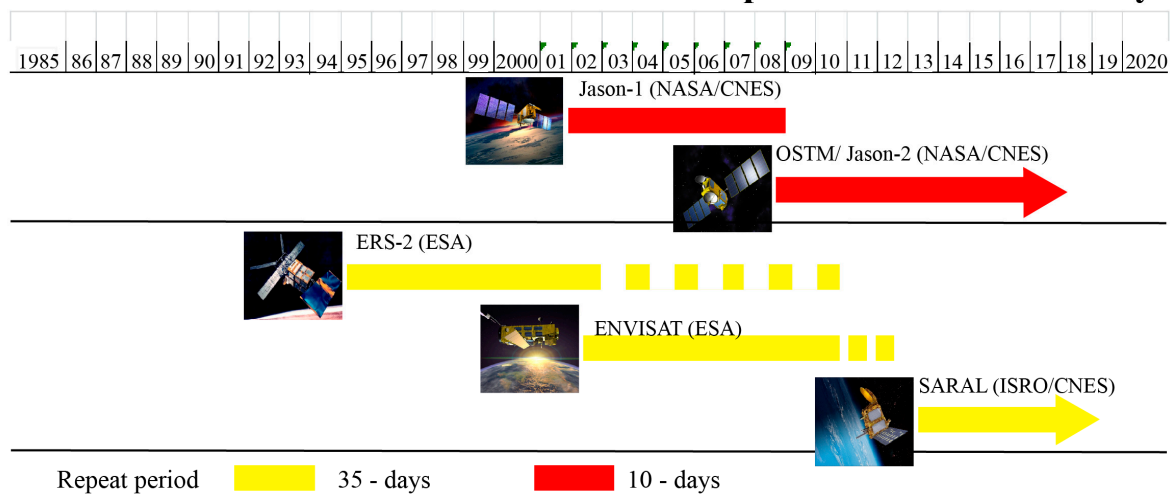


**Figure 1.** Timeline for radar altimeters used in our study (modified from [25]).

#### 2.1.1. Jason-1

This mission was launched in December 2001 by the National Aeronautics and Space Administration (NASA) and the Centre national d'études spatiales (CNES) to ensure continuity of the oceanographic observations provided by the Topex/Poseidon mission. The Jason-1 payload is composed of the Poseidon-2 altimeter operating at Ku (13.575 GHz) and C (5.3 GHz) bands, a microwave radiometer, and a triple system for precise orbit determination [26]. Jason-1 orbits at an average altitude of 1336 km, with an inclination of  $66^\circ$ , on a 10-day repeating cycle. Observations along the ground track of all ocean and continental surfaces from these altimeters are collected from  $66^\circ\text{N}$  to  $66^\circ\text{S}$ .

#### 2.1.2. Jason-2

The Jason-2 mission was launched on 20 June 2008 as a co-operation between CNES, EUMESAT, NASA, and The National Oceanic and Atmospheric Administration (NOAA). Its payload is mostly composed of the Poseidon-3 radar altimeter from CNES, the Advanced Microwave Radiometer (AMR) from JPL/NASA, and a triple system for precise orbit determination: the real-time tracking system Détermination Immédiate d'Orbite par Doris Embarqué (DIODE) of the Doppler Orbitography by Radiopositioning Integrated on Satellite (DORIS) instrument from CNES, a Global Positioning System (GPS) receiver and a Laser Reflector Array (LRA) from NASA. Jason-1 and Jason-2 share the same orbit of 1336 km above the earth, with a cycle time of 10 days. Poseidon-3 radar altimeter is a two-frequency solid-state altimeter that accurately measures the distance between the satellite and the surface (range). It also provides ionospheric delay corrections over the ocean with a precision of about 2 cm, operating at Ku (13.575 GHz) and C (5.3 GHz) bands [25,27].

### 2.1.3. ERS-2

European Remote Sensing-2 (ERS-2) was launched in 1995 by the European Space Agency (ESA) as an ERS-1 follow-up mission, designed to study the earth's environment. The satellite carries, among other instruments, a radar altimeter (RA) operating at Ku-band (13.8 GHz), developed for measuring the height of the ocean, land, and ice caps. ERS-2 orbits at an average altitude of 790 km, with an inclination of  $98.54^\circ$ , on a sun-synchronous orbit with a 35-day repeating cycle. It provides observations of the earth's surface, including ocean, land, and ice caps, from  $82.4^\circ\text{N}$  to  $82.4^\circ\text{S}$ . This orbit was formerly used by the ERS-1 mission, with an equatorial ground-track spacing of about 85 km. ERS-2 data are available from 17 May 1995 to 9 August 2010. After 22 June 2003, the dataset coverage is limited to ground station visibility.

### 2.1.4. Envisat

The Envisat mission was launched on 1 March 2002 by ESA, carrying 10 instruments including the advanced radar altimeter (RA-2). Envisat was based on the on-board sensor on the ERS-1 and 2 satellites. RA-2 was a nadir-looking pulse-limited radar altimeter operating at two frequencies at the Ku (13.575 GHz), as ERS-1 and 2, and S (3.2 GHz) bands. The goal was to collect radar altimetry data over ocean, land, and ice caps [26,28] Envisat remained on its nominal orbit until October 2010 and its mission ended 8 April 2012. RA-2 stopped operating correctly at S-band in January 2008. Its initial orbital characteristics were the same as for ERS-2.

### 2.1.5. SARAL/AltiKa

The SARAL mission was launched on 25 February 2013. SARAL is collaboration between CNES and Indian Space Research Organization (ISRO). Its payload included the AltiKa radar altimeter and bi-frequency radiometer, and a triple system for precise orbit determination: the real-time tracking system DIODE of DORIS instrument, a Laser Reflector Array (LRA), and the Advance Research and Global Observation Satellite (ARGOS-3). The AltiKa radar altimeter is a solid-state mono-frequency altimeter that provides accurate range measurements and is the first altimeter to operate Ka-band (35.75 GHz). Formerly, the SARAL orbit was used by ERS-1 and 2 and Envisat, with an equatorial ground-track spacing of about 85 km [9], and a 35-day repeating cycle. It was placed on a drifting orbit as of 7 April 2016.

## 2.2. Tide Gauge Records

The tidal data used in this study was obtained from records of tide gauges SSH from the French Réseaux de référence des observations marégraphiques (REFMAR) networks [29]. We used data from 7 tide gauge stations located along the southwestern coast of France (Table 1; Figure 1). The SSH data were provided at 10-min intervals and were referenced to the Institut Géographique National 1969 (IGN69) ellipsoid. For comparison with the altimetry data, the difference between the two reference systems (ZH/GRS80 in Table 1) was calibrated at the 7 station tide gauges. We used daily Mean Sea Surface (MSS) from 1995 to 2016, available on Système d'Observation du Niveau des Eaux Littorales (SONEL) networks ([www.sonel.org](http://www.sonel.org)), obtained from different tidal filters (e.g., Doodson filter and Demerliac filter) to reduce the tidal effects. Several such linear filters compute the daily mean sea levels [27,30].

## 2.3. Study Area

The study area is located along the Atlantic coast in the Bay of Biscay ( $42\text{--}48^\circ\text{N}$ ,  $0\text{--}10^\circ\text{W}$ ), an extension of the Atlantic Ocean, off the western coast of Europe, bordered by France and Spain. In this area, the continental shelf is narrow in the south ( $\sim 30$  km) and extends to 180 km in the north [31]. The oceanic circulation is characterized by the presence of a large-scale gyre, the Iberian Poleward Current (IPC) [29,32] These characteristics, combined with a seasonal wind regime [30,33] and a

large amount of fresh water from river discharges [31,34], drive a complex system of coastal currents, mesoscale eddies, local upwellings, and internal tide [33,35].

In the study area, five passes of ERS-2/Envisat/SARAL were available (Figure 2a), three descending passes (#0360, #0818, #0274), and two ascending passes (#0945, #0859). Three Jason-1 and Jason-2 passes, two descending (#70, #248), and an ascending pass (#213) were available.

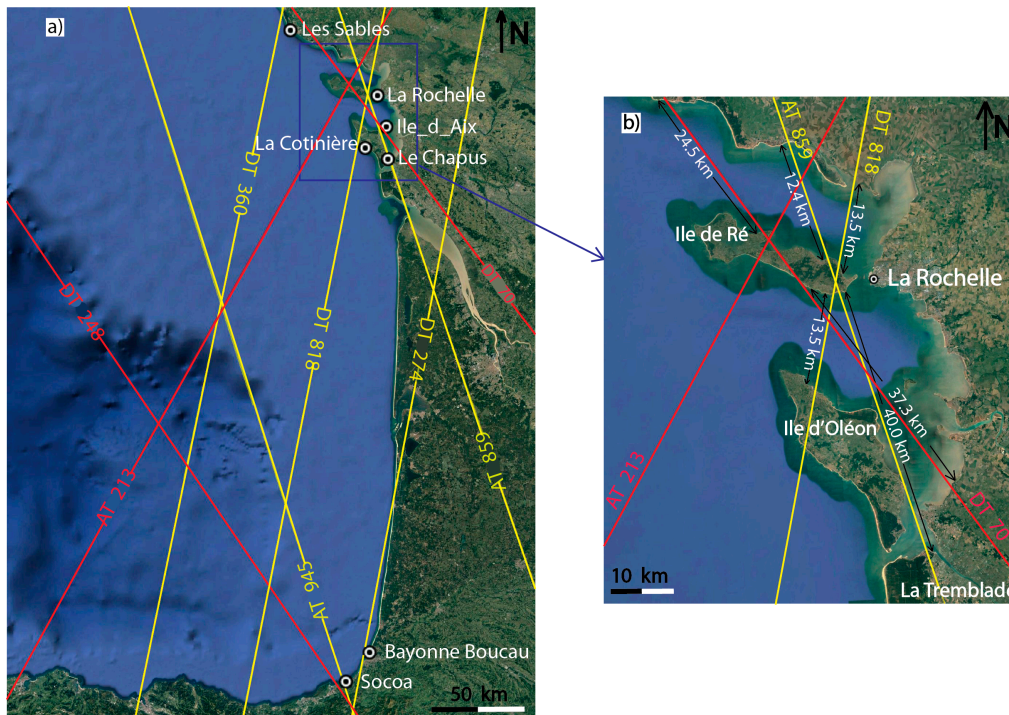


**Figure 2.** Google Earth image of the study area (a) with superposition of theoretical traces altimetry. Jason-1 and Jason-2 tracks are represented with red lines and ERS-2, Envisat, and SARAL tracks with yellow lines; (b) detail near La Rochelle tide gauge with Jason-1 and Jason-2 tracks in red lines and ERS-2, Envisat, and SARAL tracks in yellow.

Envisat and ERS-2 altimetry heights are referenced to the WGS 84 ellipsoid, and Jason-1 and 2 and SARAL are relative to the Topex/Poseidon ellipsoid. The corrections applied to the different sensors, contained in the Envisat, ERS-2, Jason-1 and 2, and SARAL GDR standard data products are listed in Table 2.

**Table 1.** Locations of the tide gauge stations and the available time period in the study area. Columns 6 and 7 show the satellite track number and the distance track–tide gauge. The green highlights the tracks close to the coastline (<15 km). The yellow tracks are located in a mixed domain between the coastal area and open ocean (15–25 km), and the red tracks the open ocean (>25 km).

| Tide Gauge Station      | Longitude (°) | Latitude (°) | Validation Period | ZH/GRS80 (m) | Jason-1 and 2 |               | ERS-2, Envisat, SARAL |               |
|-------------------------|---------------|--------------|-------------------|--------------|---------------|---------------|-----------------------|---------------|
|                         |               |              |                   |              | Track         | Distance (km) | Track                 | Distance (km) |
| Bayonne Boucau          | 43.5273       | −1.5148      | 1999–2015         | 46.41        | 248           | 24.3          | 274, 945              | 3.0, 18.6     |
| Bourceranc le Chapus    | 45.8534       | −1.1778      | 2012–2013         | 43.49        | 70            | 7.0           | 818, 859              | 17.8, <1      |
| Ile d’Aix               | 46.0074       | −1.1743      | 2011–2015         | 43.49        | 70, 213       | 2.88, 29.0    | 818, 859              | 13.7, 4.7     |
| La Rochelle la Pallice  | 46.1585       | −1.2206      | 1996–2015         | 43.46        | 70, 213       | 8.8, 16.8     | 818, 859              | 5.8, 5.4      |
| Les Sables d’Olonne     | 46.4974       | −1.7935      | 1995–2015         | 44.54        | 70            | 7.0           | 360                   | 6.6           |
| La Cotinière            | 45.9136       | −1.3278      | 2006–2015         | 43.45        | 213           | 24.8          | 818                   | 4.7           |
| Saint Jean de Luz Socoa | 43.3952       | −1.6816      | 2002–2015         | 46.64        | 248           | 5.4           | 274, 945              | 6.2, 2.1      |

**Table 2.** Ocean ranges available and corrections for each altimetry mission.

| Altimetry Mission | Period   | Format     | Ocean Retracking Algorithm | Corrections to the Range          |                             |  |   |
|-------------------|--|------------|----------------------------|-----------------------------------|-----------------------------|--|---|
|                   |  |            |                            | Ionosphere                        | Dry Troposphere             | Wet Troposphere                            | Sea State Bias                            |
| ERS-2             | Cycle 1 (May 1995) to cycle 085 (July 2003)          | REAPER GDR | MLE-3                      | NIC 09 GIM                        | ECMWF                       | Radiometer ECMWF                           | Empirical                                 |
| Jason-1           | Cycle 001 (January 2002) to cycle 259 (January 2009) | GDR E      | MLE-3                      | Bi-frequency (C-Ku) GIM model     | ECMWF model derived         | Jason-1 radiometer (JMR) and ECMWF model   | Empirical model derived                   |
| Envisat           | Cycle 006 (May 2002) to cycle 094 (October 2010)     | GDR C v2.1 | MLE-3                      | Bi-frequency (C-Ku) GIM model     | ECMWF model derived         | Microwave Radiometer (MWR) and ECMWF model | Empirical model derived                   |
| Jason-2           | Cycle 001 (July 2008) to cycle 250 (April 2015)      | GDR D      | MLE-4 MLE-3                | Bi-frequency (C-Ku) and GIM model | ECMWF atmospheric pressures | Jason-2 radiometer (AMR) and ECMWF model   | Empirical model derived from Jason-2 data |
| SARAL             | Cycle 001 (March 2013) to cycle 028 (November 2015)  | GDR T      | MLE-4                      | GIM- derived                      | ECMWF model derived         | Radiometer and ECMWF model                 | Empirical model derived                   |

### 3. Methods

#### 3.1. SSH from Altimetry

The absolute calibration technique is required in the determination of the absolute altimeter bias. This technique requires simultaneous measurements of  $SSH_{in\ situ}$  by an altimeter in the same terrestrial reference frame at the exact same location or comparison point. The absolute altimeter bias ( $Bias_{altimeter}$ ) is estimated as follows [33,36]:

$$Bias_{altimeter} = SSH_{altimeter} - SSH_{in\ situ} - \Delta h_{geoid} \quad (1)$$

where  $SSH_{altimeter}$  and  $SSH_{in\ situ}$  are the SSH estimated from the altimeter and in situ measurements, respectively, and  $\Delta h_{geoid}$  represents the difference in geoid heights between the tide gauge and the altimeter measurement locations. A negative bias indicates that the measure of the SSH by the altimeter is underestimated; either the altimeter range is being overestimated, or the orbit is biased downwards [6]. The SSH from the altimeter is given as [2,37]:

$$SSH_{altimeter} = H - \left( R + \sum \Delta R_{environmental} + \sum \Delta R_{geophysical} \right) \quad (2)$$

where  $H$  is the height of the center of the mass of the satellite above the ellipsoid, estimated using the Precise Orbit Determination (POD) technique;  $R$  is the nadir altimeter range from the center of the mass of the satellite to the sea surface while considering instrumental corrections; and  $\sum \Delta R_{environmental}$  and  $\sum \Delta R_{geophysical}$  are the sum of the environmental and geophysical corrections applied to the range, respectively. The environmental corrections are composed of the following contributions:

$$\sum \Delta R_{environmental} = \Delta R_{ion} + \Delta R_{dry} + \Delta R_{wet} + \Delta R_{SSB} \quad (3)$$

where  $\Delta R_{ion}$  is the atmospheric refraction range delay due to the free electron content associated with the dielectric properties of the ionosphere,  $\Delta R_{dry}$  is the atmospheric refraction range delay due to the dry gas component of the troposphere,  $\Delta R_{wet}$  is the atmospheric refraction range delay due to the water vapor and the cloud liquid water content of the troposphere, and  $\Delta R_{SSB}$  is the range correction caused by the various effects of the sea surface roughness within the radar footprint. This is known as sea state bias (SSB) and is the sum of electromagnetic (EM), skew, and tracker biases. The geophysical corrections are composed of the following contributions:

$$\sum \Delta R_{geophysical} = \Delta R_{load} + \Delta R_{solid\ Earth} + \Delta R_{pole} + \Delta R_{atm} \quad (4)$$

where  $\Delta R_{load}$ ,  $\Delta R_{solid\ Earth}$ ,  $\Delta R_{pole}$ , and  $\Delta R_{atm}$  are the corrections accounting for crustal vertical motions due to the solid earth, pole tides, and rapid fluctuations of the atmosphere, respectively.

The leveling of the tide gauge precisely determines the ellipsoidal height ( $H_0$ ) of the gauge zero as:

$$SSH_{in\ situ} = h + H_0 \quad (5)$$

where  $h$  is the instantaneous stage value in the gauge record at time  $t$ .  $H_0$  values are provided by REFMAR (Table 1).

#### 3.2. SSH Processing and Editing

Altimetry SSH was obtained using the Multi-mission Altimetry Processing Software (MAPS) [35,38]. This software computes high frequency SSH referenced to the WGS84 ellipsoid along the altimeter tracks from the altimeter range and a set of corrections chosen by the user. The range can be any of the ranges available in the GDR from different retracking algorithms. MAPS allows a refined selection of the valid altimetry data to build several virtual stations where a SSH time series over the

ocean [39] or water levels over rivers and estuaries [38,40,41] can be constructed. The altimetry-based SSH were automatically computed along the track by MAPS at a 20-Hz frequency rate (i.e., ~0.35 km along the track) for Envisat, ERS-2, Jason-1, and Jason-2, and at 40 Hz (i.e., ~0.18 km along the track) for SARAL. Many different retracking algorithms are used to measure the waveforms applied to the Brown model. Range values suitable for deriving SSH were retracked using the Maximum Likelihood Estimator (MLE) retracking algorithm for all altimeters [42]. The MLE3 algorithm [43] estimates with three degrees of freedom: range, significant wave height, and power, whereas the MLE4 algorithm [41,44] estimates four degrees of freedom including the three previous plus the slope of the waveform trailing edge. We used both algorithms and compared them in this study. Data processing involved three main steps: a coarse delineation of the study area using Google Earth, a refined selection of the valid altimetry data through visual inspection, and the computation of the SSH time series using all the valid points selected by the user. The average altimetry-based SSH was computed for each cycle using the median and the mean of the selected altimetry heights, along with their respective deviation, meaning their mean absolute and standard deviations, respectively.

### 3.3. Comparisons between Altimetry-Based and In Situ-Based SSH

Based on the availability of the altimetry data, the comparison with in-situ SSH, including number of cycles, bias, root means square errors (RMSE), and correlation coefficient (R), was performed using satellite data with open ocean conditions at distances between 5 km and 50 km from the coast. Depending on the frequency of sampling of each tide gauge, the maximum time-lag between in situ records and altimetry data was lower than 10 min for any measurement considered (Section 2.2).

### 3.4. Comparisons of the Atmosphere Delays over the Open Ocean

Bias and RMSE were compared between model-based and bi-frequency ionosphere corrections. Model-based and radiometer-derived wet troposphere corrections were performed over the entire Bay of Biscay. According to a prior study [42,45] the comparisons were performed in along-track cells 7 km in length (i.e., 1-Hz). More details about their definition during the complete observation period of each altimetry mission, whose data were used in this study, are available in previous reports [40,46].

## 4. Results

Comparisons between altimetry-based SSH and tide gauge records were performed at seven locations (Table 1) along the French Atlantic coast between La Rochelle and Bayonne under eight altimetry tracks (Figure 2). We will present the results for the La Rochelle tide gauge as the in situ data records exhibit a longer period of common availability with the altimetry missions than the other tide gauges, and two altimeter tracks, ascending and descending, were available for each altimetry mission. Similar results were obtained from the other tide gauges.

### 4.1. Multi-Missions Comparisons over the French Southern Part of the Bay of Biscay

The metrics compared between the altimetry-based SSH, estimated zero and five kilometers from the coast, and SSH measured by the tide gauge were: number of cycle observations (N), bias, standard deviation (SD), root mean square error (RMSE), and correlation coefficient (R) for the different SSH values. The results are outlined in Table 3 for all the tide gauges present along the French Atlantic coast of the southern part of the Bay of Biscay. The best results were obtained with SARAL ( $R > 0.99$  and  $RMSE < 0.20$  m) among all the tide gauges. Excellent agreement was found using Jason-1 ( $R > 0.9$  and  $RMSE < 0.15$  m for the majority of the time) and Jason-2 ( $R > 0.9$  and  $RMSE < 0.20$  m for the majority of the time). Lower but good agreement was found using Envisat ( $R > 0.7$  for the majority of the time and  $RMSE < 0.21$  m). For ERS-2, the quality of the SSH retrieval was variable.

**Table 3.** Comparisons of distance to the gauge, number of cycle observations (N), bias, root mean square error (RMSE), SD, and the correlation coefficient (R) from zero to five kilometers away from the coast for all tide gauge stations present along the French Atlantic coast of the southern part of the Bay of Biscay for ERS-2, Jason-1, Envisat, Jason-2, and SARAL. The ionosphere and wet troposphere corrections were derived from the Global Ionospheric Maps (GIM) and European Center for Medium Range Weather Forecasting (ECMWF) models, respectively.

| Altimeter | Station                 | Altimetry Track | Distance Alt/Gauge (km) | N   | Bias (m) | RMSE (m) | SD (m) | R     |
|-----------|-------------------------|-----------------|-------------------------|-----|----------|----------|--------|-------|
| ERS-2     | La Rochelle             | 818             | 5.8                     | 13  | −0.6     | 1.4      | 1.05   | 0.41  |
|           | La Rochelle             | 859             | 5.4                     | 25  | −0.65    | 0.22     | 1.45   | 0.99  |
|           | Bayonne Boucau          | 274             | 3.0                     | 21  | −1.00    | 0.89     | 1.05   | 0.51  |
| Jason-1   | La Rochelle             | 70              | 8.8                     | 97  | −0.81    | 0.29     | 0.98   | 0.93  |
|           | La Rochelle             | 213             | 16.8                    | 61  | −0.73    | 0.21     | 0.71   | 0.97  |
|           | Bayonne Boucau          | 248             | 24.3                    | 25  | −0.94    | 0.15     | 1.00   | 0.99  |
|           | Saint Jean de Luz Socoa | 248             | 5.4                     | 35  | −0.77    | 0.10     | 1.00   | 0.996 |
| Envisat   | La Rochelle             | 818             | 5.8                     | 77  | 0.37     | 0.90     | 1.00   | 0.73  |
|           | La Rochelle             | 859             | 5.4                     | 76  | 0.49     | 0.18     | 1.15   | 0.99  |
|           | Bayonne Boucau          | 274             | 3.0                     | 42  | −0.07    | 0.77     | 0.99   | 0.67  |
|           | Saint Jean de Luz Socoa | 274             | 6.2                     | 51  | −0.17    | 0.63     | 0.99   | 0.8   |
|           | Les Sables d’Olonne     | 360             | 6.6                     | 38  | 0.25     | 0.84     | 0.97   | 0.7   |
| Jason-2   | La Rochelle             | 70              | 8.8                     | 150 | −0.30    | 0.19     | 0.99   | 0.99  |
|           | La Rochelle             | 213             | 16.8                    | 37  | −1.20    | 0.21     | 1.27   | 0.91  |
|           | Bayonne Boucau          | 248             | 24.3                    | 118 | −0.65    | 0.34     | 1.03   | 0.93  |
|           | Saint Jean de Luz Socoa | 248             | 5.4                     | 84  | −0.78    | 0.33     | 1.03   | 0.92  |
|           | Les Sables d’Olonne     | 70              | 7.0                     | 111 | −0.67    | 0.17     | 0.99   | 0.98  |
|           | Ile d’Aix               | 213             | 29.0                    | 14  | −1.1     | 0.27     | 1.27   | 0.83  |
|           | Ile d’Aix               | 70              | 2.88                    | 58  | −0.37    | 0.21     | 1.44   | 0.98  |
| SARAL     | La Rochelle             | 818             | 5.8                     | 25  | −0.29    | 0.19     | 0.98   | 0.99  |
|           | La Rochelle             | 859             | 5.4                     | 26  | −0.28    | 0.13     | 1.22   | 0.99  |
|           | Bayonne Boucau          | 274             | 3.0                     | 26  | −0.83    | 0.12     | 0.94   | 0.99  |
|           | Saint Jean de Luz Socoa | 274             | 6.2                     | 14  | −0.80    | 0.12     | 0.94   | 0.996 |
|           | Les Sables d’Olonne     | 360             | 6.6                     | 14  | −0.35    | 0.08     | 1.12   | 0.998 |
|           | Ile d’Aix               | 818             | 13.7                    | 22  | −0.37    | 0.21     | 0.98   | 0.995 |
|           | Ile d’Aix               | 859             | 4.7                     | 22  | −0.47    | 0.14     | 1.22   | 0.99  |

#### 4.2. Multi-Mission Comparisons at La Rochelle Tide Gauge

The site of La Rochelle was chosen for comparisons between tide gauge records and altimetry-based SSH because the tide gauge records cover the entire observation period for the different radar altimetry missions. For all missions in this study, we considered one ascending track and one descending track. These data were compared with the La Rochelle data in terms of N, bias, SD, RMSE, and R for the different SSH values computed using all possible combinations of ocean ranges varying from zero to five kilometers to the coast (Table 4). The considerable bias between altimetry and the tide gauge five kilometers from the coast is explained, in Section 3.1, by the slope of the geoid relative to the ellipsoid. To highlight the differences between the sensors, we present the results for the SSH estimates obtained from the GIM model for the ionosphere correction and the model-based wet troposphere correction. Therefore, the complete ERS-2 record was not used; only the data acquired from 30 November 1998 (cycle 37) to 11 August 2003 (cycle 85) was used since the release of the GIM-based ionosphere correction.

The comparison results between the tide gauge records and the altimetry-based SSH from five kilometers from the coast are presented in Figure 3 for Jason-1 and Jason-2 data, and in Figure 4 for ERS-2, Envisat, and SARAL data. The quality of the results is strongly impacted by the direction of the satellite groundtrack. The results differ between the tracks where the acquisitions were performed first on the ocean and then on the land and the opposite situation. Descending track 70 passes over the Bay of Biscay for 24.5 km between the mainland and Ré Island, and then for another 37.3 km between Ré Island and the mainland, whereas ascending track 213 passes from the ocean to Ré Island and then for 12.4 km from Ré Island to the mainland (Figure 2b). For the Jason-2 data, the number of valid cycles is higher along the descending track, with 60% of 250, cycles than along the ascending track with only 15%. Therefore, even though the descending track 70 passes from land to ocean, the results obtained for this track, the RMSE of 0.19 m and R of 0.99, are better than those of the ascending track with a RMSE of 0.21 m and a R of 0.91

(Figure 3a,b). For the Jason-1 data, the number of valid cycles is higher along the descending track, with 37% of 259 cycles, than along the ascending track with only 24% valid. Accurate results were obtained for the ascending track with a RMSE of 0.21 m and a R of 0.97, which are better than those of the descending track, with a RMSE of 0.29 m and a R value of 0.93. Both were statistically representative with more than 50 samples or cycles (Figure 3c,d). The differences between the satellites (Figure 3) could account for the disparity in tracking mode between the closed-loop Poseidon-2 tracker onboard Jason-1 and the open loop (DIODE/digital elevation model) Poseidon-3 tracker mode onboard Jason-2 [44,47].

The impact of the retracking algorithm was also analyzed. The results of the comparisons between the tide gauge records and the Jason-2 track 213 altimetry-based SSH at La Rochelle, with the two available ocean retracking algorithms (MLE-4 and MLE-3), are presented in Figure S1 for distances varying from 0 to 50 km from the coast. The results show that within the zero to five kilometer zone, only 15% of cycles are valid. Furthermore, the SSH derived from altimetry over five kilometers from the coast is affected not only by less reliable geophysical and environmental corrections, but it is also influenced by the land. The RMSE and R obtained were 0.33 m and 0.8, respectively, using MLE-3, and 0.21 m and 0.91, respectively, using MLE-4.

Figure 4 shows the comparison results for ERS-2, Envisat, and SARAL virtual stations at La Rochelle. Large differences were observed between ascending track 859 and descending track 818 for all missions. As seen in Figure 1b, descending track 818 passes over the Bay of Biscay for 13.5 km between the mainland and Ré Island, and then for another 13.5 km between Ré Island and Oléron Island. Ascending track 859 passes over the Bay of Biscay for 40 km from la Tremblade over the mainland to Ré Island. For ERS-2 data, more valid cycles were found along the ascending track with 51% of 49 cycles, compared to the descending track with only 27% (Figure 4a,b). These results indicate that many cycles are affected by tracking loss effects. Much better results were obtained for the ascending track, with a RMSE of 0.22 m and a R of 0.99, than for the descending track with a RMSE of 1.4 m and a R of 0.41. This poor result can be accounted for by the low cycle number (N = 13), which is not statistically representative.

**Table 4.** Comparisons between altimetry-based SSH and in-situ SSH in La Rochelle from zero to five kilometers away from the coast (N, bias, RMSE, SD, and R) for ascending and descending tracks of ERS-2, Jason-1, Jason-2, Envisat, and SARAL satellites, and for various ionospheric and tropospheric corrections including GIM, bi-frequency, and model-based wet troposphere.

| Altimeter       | Correction | Descending Track |          |          |        |      | Ascending Track |          |          |        |      |
|-----------------|------------|------------------|----------|----------|--------|------|-----------------|----------|----------|--------|------|
|                 |            | N                | Bias (m) | RMSE (m) | SD (m) | R    | N               | Bias (m) | RMSE (m) | SD (m) | R    |
| ERS-2           | Nic09-Rad  | 9                | 0.32     | 1.3      | 1.12   | 0.54 | 33              | −0.40    | 0.21     | 1.41   | 0.99 |
|                 | GIM-Rad    | 8                | 0.25     | 1.3      | 1.08   | 0.52 | 25              | −0.42    | 0.24     | 1.43   | 0.99 |
|                 | Nic09-Mod  | 14               | −0.53    | 1.4      | 1.11   | 0.42 | 37              | −0.68    | 0.22     | 1.40   | 0.99 |
|                 | GIM-Mod    | 13               | −0.6     | 1.4      | 1.05   | 0.41 | 25              | −0.65    | 0.22     | 1.45   | 0.99 |
| Jason-1         | Bi-Rad     | 144              | −0.36    | 0.46     | 0.98   | 0.92 | 56              | −0.78    | 0.29     | 1.01   | 0.94 |
|                 | Bi-Mod     | 97               | −0.81    | 0.46     | 1.01   | 0.82 | 54              | −0.75    | 0.28     | 1.05   | 0.94 |
|                 | GIM-Rad    | 154              | −0.28    | 0.37     | 1.00   | 0.95 | 84              | −0.73    | 0.18     | 0.70   | 0.98 |
|                 | GIM-Mod    | 97               | −0.81    | 0.29     | 0.98   | 0.93 | 61              | −0.73    | 0.21     | 0.71   | 0.97 |
| Envisat         | Bi-Rad     | 77               | 0.6      | 0.9      | 1.00   | 0.73 | 76              | 0.63     | 0.19     | 1.17   | 0.99 |
|                 | Bi-Mod     | 77               | 0.49     | 0.9      | 1.00   | 0.73 | 76              | 0.58     | 0.18     | 1.14   | 0.99 |
|                 | GIM-Rad    | 77               | 0.59     | 0.9      | 0.99   | 0.73 | 76              | 0.63     | 0.19     | 1.19   | 0.99 |
|                 | GIM-Mod    | 77               | 0.37     | 0.9      | 1.00   | 0.73 | 76              | 0.49     | 0.18     | 1.15   | 0.99 |
| Jason-2 (MLE-3) | Bi-Rad     | 119              | −0.61    | 0.2      | 1.02   | 0.97 | 22              | −1.20    | 0.26     | 0.75   | 0.86 |
|                 | Bi-Mod     | 119              | −0.61    | 0.2      | 1.01   | 0.97 | 22              | −1.20    | 0.26     | 0.75   | 0.85 |
|                 | GIM-Rad    | 132              | −0.54    | 0.22     | 0.99   | 0.98 | 42              | −1.30    | 0.33     | 0.91   | 0.81 |
|                 | GIM-Mod    | 132              | −0.54    | 0.21     | 0.99   | 0.98 | 42              | −1.30    | 0.33     | 0.91   | 0.80 |
| Jason-2 (MLE-4) | Bi-Rad     | 142              | −0.31    | 0.36     | 0.99   | 0.95 | 31              | −1.20    | 0.23     | 0.90   | 0.89 |
|                 | Bi-Mod     | 142              | −0.31    | 0.36     | 0.99   | 0.95 | 31              | −1.20    | 0.23     | 0.90   | 0.89 |
|                 | GIM-Rad    | 150              | −0.30    | 0.19     | 0.99   | 0.99 | 37              | −1.20    | 0.2      | 1.27   | 0.91 |
|                 | GIM-Mod    | 150              | −0.30    | 0.19     | 0.99   | 0.99 | 37              | −1.20    | 0.21     | 1.27   | 0.91 |
| SARAL           | GIM-Rad    | 25               | −0.29    | 0.19     | 0.99   | 0.99 | 26              | −0.28    | 0.13     | 1.22   | 0.99 |
|                 | GIM-Mod    | 25               | −0.29    | 0.19     | 0.98   | 0.99 | 26              | −0.28    | 0.13     | 1.22   | 0.99 |

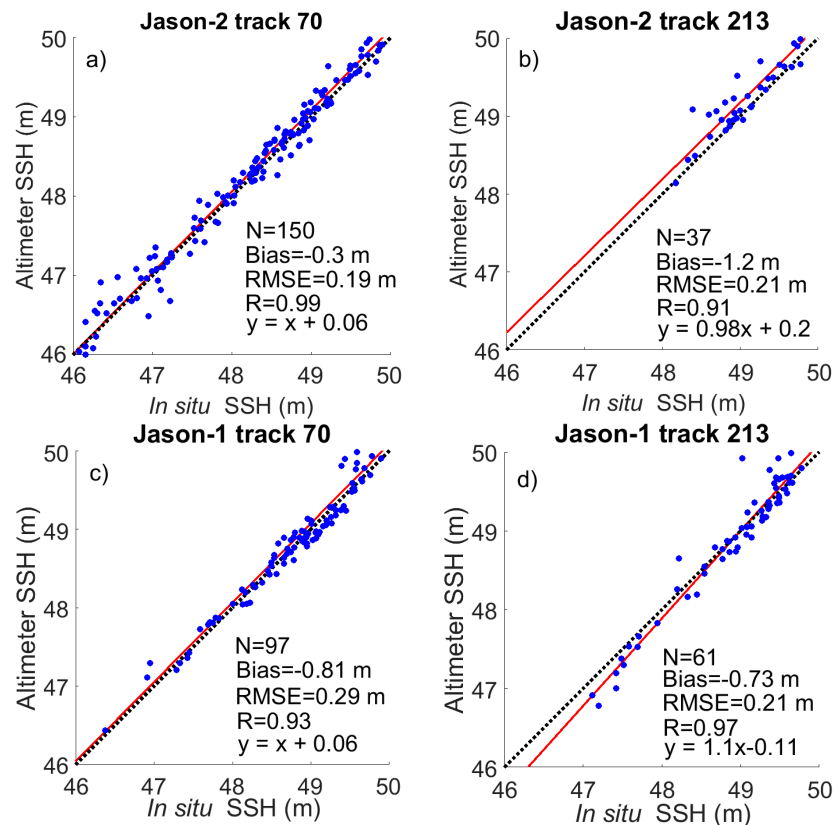


**Figure 3.** Comparisons between in situ and altimeter-based sea level anomalies in La Rochelle for (a,b) Jason-2 and (c,d) Jason-1 for descending track 70 and ascending track 213. The ionosphere and wet troposphere corrections were derived from GIM and ECMWF models, respectively.

More data were acquired in the 330 MHz Ku chirp bandwidth acquisition mode (ocean mode with a 30-m window size) than in the 82.5 MHz Ku chirp bandwidth acquisition mode (ice mode with a 116-m window size) along the 818 ERS-2 descending track and the 859 ERS-2 ascending track. This could account for the low accuracy of the ERS-2 SSH measurement and the considerable loss of data. The number of valid cycles obtained for Envisat on the ascending and descending tracks were close to 77 cycles accounting for 82% of the total. However, the results obtained for the 859 Envisat ascending track, with a RMSE of 0.18 m and a R of 0.99, were better than those for the 818 Envisat descending track, with a RMSE of 0.9 m and a R of 0.73 (Figure 4c,d). Along the 859 Envisat ascending track, the data were acquired in the 320 MHz Ku chirp bandwidth acquisition mode with a 64-m window size. Along the 818 Envisat descending track, the data were acquired in both the 320 and 80 MHz Ku chirp bandwidth acquisition modes with 64- and 256-m window sizes, respectively, over land, and in the 320 MHz bandwidth over open ocean. Over the study area, the altimeter switched between these two modes, accounting for both the data loss and the decrease in accuracy. Similar results were found in the Gironde Estuary [38,41]. Better results were obtained using SARAL data, with a RMSE of 0.19 m and a R value of 0.99 for the 818 descending track, and a RMSE of 0.13 m and a R of 0.99 for the 859 ascending track. The number of valid cycles obtained for SARAL was 92% of the total for both the ascending and descending tracks (Figure 4e,f). This result can be accounted for by the larger effective footprint radius of ERS-2 and Envisat at Ku-band than the one of SARAL at Ka-band, and the surrounding lands along the track are encompassed in the scene observed by the altimeter. Therefore, the number of valid cycles for the SARAL altimeter are greater than the number of valid cycles with ERS-2 and Envisat. If these results are confirmed, we can attribute this accuracy to the smaller effective footprint at Ka-band. Radar echoes are less affected by the presence of land surrounding the study area.

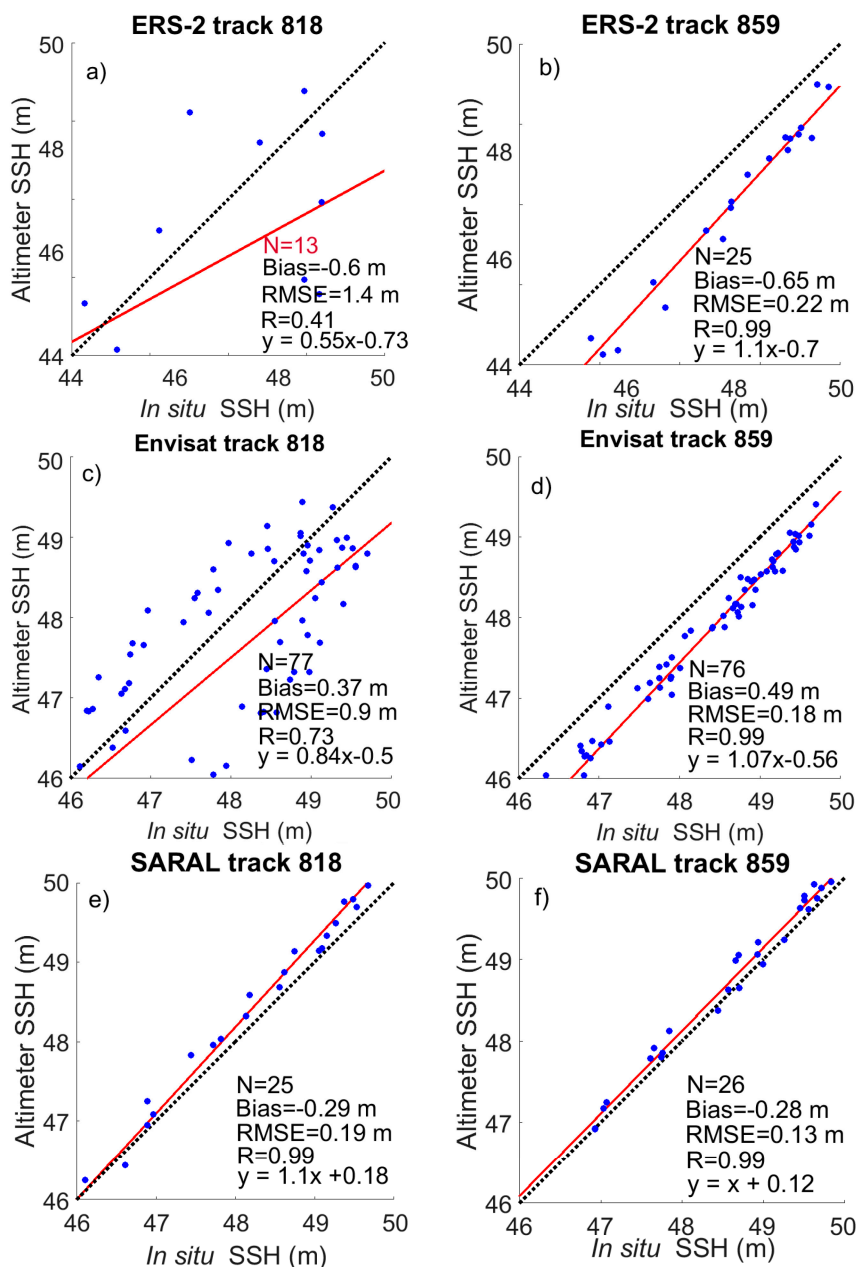


**Figure 4.** Comparisons between in situ and altimeter-based sea level anomalies in La Rochelle for (a,b) ERS-2; (c,d) Envisat; and (e,f) SARAL for descending track 0818 and ascending track 0859. The ionosphere and wet troposphere corrections were derived from GIM and ECMWF models, respectively.

#### 4.3. Comparisons of Atmosphere Corrections over the Open Ocean

##### 4.3.1. Comparisons of Bi-Frequency and Model-Based Ionospheric Corrections

The bias and RMSE for the ionosphere corrections from bi-frequency measurements and GIM model for Jason-1, Envisat, and Jason-2 using the MLE-3 and MLE-4 retracking algorithms are presented in Table 4 and Figures 5 and 6, Figures S2 and S3, respectively, over the entire southern Bay of Biscay. Low biases and RMSE, lower than 0.03 m and 0.05 m, respectively, are found when the distance to the coast is more than 25 km, except for a limited number of locations along the track where the bias reaches 0.1 to 0.2 m, and RMSE reaches up to 0.3 to 0.5 m for Envisat. The Jason-1 and Jason-2 missions exhibit very low variation differences in the ionosphere corrections along the tracks far from the shore. To reduce this variability, ionosphere corrections were smoothed on distances of several

tenths of kilometers. Conversely, a larger variability was observed along the Envisat tracks. Biases and RMSE increased when closer to the shore, reaching several tenths of centimeters. Envisat stopped operating properly at S-band in January 2008, meaning that only the GIM-based ionosphere correction was available until the end of Envisat's scientific mission in October 2010 along the nominal orbit and April 2012 on the drifting orbit.

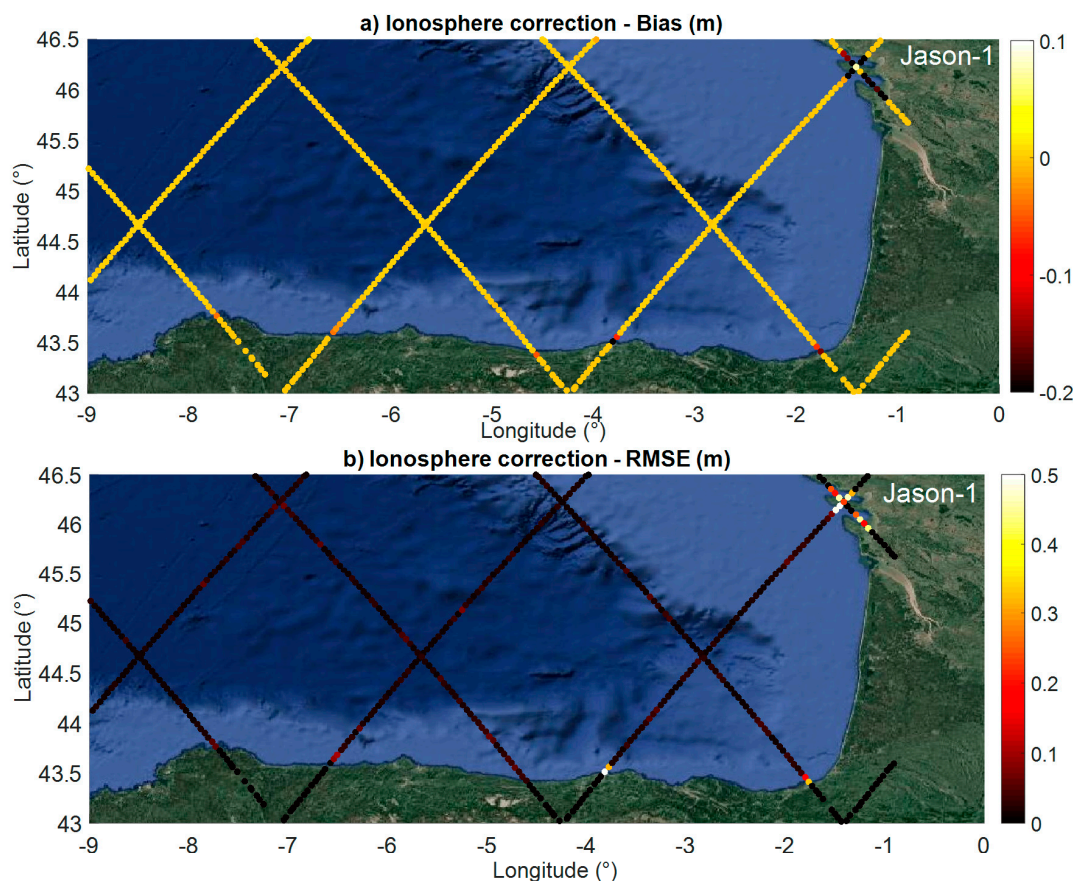


**Figure 5.** Comparison between ionosphere corrections from bi-frequency measurements and the GIM model for Jason-1: (a) bias and (b) RMSE.

Bi-frequency along-track profiles and model-based ionospheric corrections (GIM for all the missions and NIC09 for ERS-2) within 50 km of the coast are presented in Figure 7 for Jason-2 and Jason-1 (track 70), and Envisat and ERS-2 (track 859). Larger discrepancies were observed closer to the coast, reaching 0.25 m for Jason-1 when averaged over the entire observation period. Lower differences, less than 0.10 m, were observed using Jason-2 and less than 0.03 m for Envisat on average. Nevertheless, individual differences up to one meter were observed for distances from the coast, to less than 10 km between model-based and bi-frequency ionosphere corrections. Minute differences were observed between the two ionosphere correction models when compared over their common period of availability.

Due to the footprint size of the altimeter and the different frequencies used, land areas were encompassed in the image. As the radar electromagnetic wave can penetrate land surfaces with a different penetration depth, depending on the frequency and other parameters such as soil type, moisture, and roughness. For Jason-2, Jason-1 (track 213), and Envisat (track 818), within 50 km of the coast near La Rochelle, the bi-frequency-based ionospheric correction cannot be used within five kilometers of the coast, due to land contamination [45,48] (Figure 7). On the contrary, the model-based ionosphere correction presents quite stable values, in the range of a few centimeters, for the entire

observation period. For ERS-2, both GIM- and NIC09-based ionospheric corrections can be used within five kilometers of the coast (Figure 7).

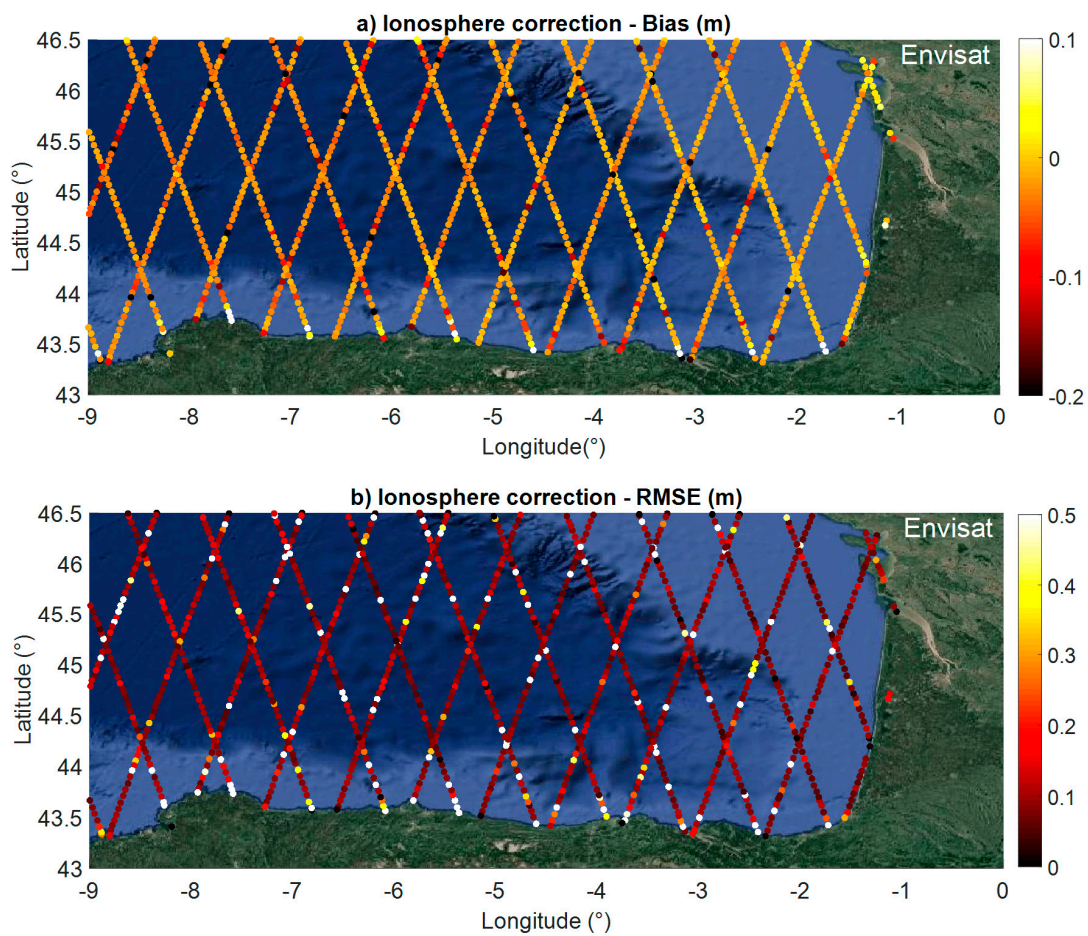


**Figure 6.** Comparison between the ionosphere corrections from bi-frequency measurements and the GIM model for Envisat: (a) bias and (b) RMSE.

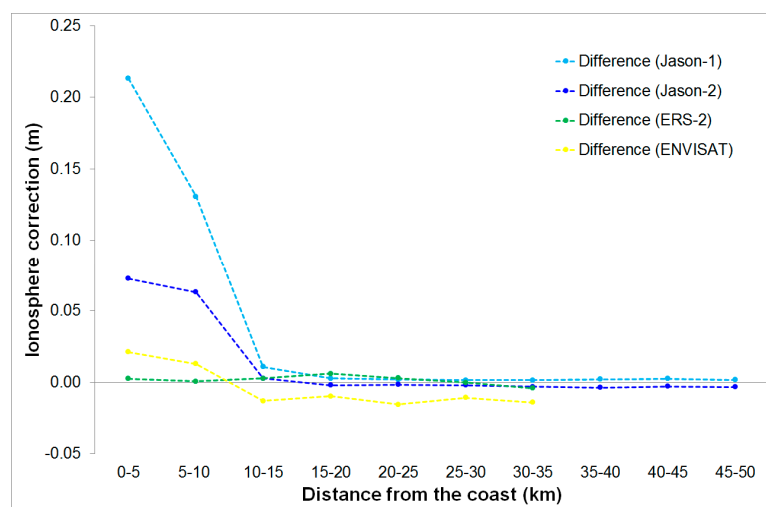


**Figure 7.** Difference between the ionosphere corrections from GIM and bi-frequency measurements for Jason-1 (light blue), Jason-2 (blue), and Envisat (yellow), and between GIM and Nic09 for ERS-2 (green) over La Rochelle within 50 km of the coast.

#### 4.3.2. Wet Tropospheric Correction Comparison between Radiometers and ECMWF Model

Bias and RMSE for the wet troposphere corrections from radiometer measurements and the ECMWF model for Jason-1, Envisat, Jason-2, and SARAL are presented in Figures 8 and 9 and Figures S4–S6, respectively, for the entire southern Bay of Biscay. Over the open ocean, the difference between WTC derived from the ECMWF model and radiometers is negligible. Within a short distance from the coast (<25 km), both bias and RMSE increase. They remain quite small for Jason-1 (Figure 8) and Jason-2 (Figure S5) missions (lower than 0.05 m), and increase up to  $-0.4$  m and  $0.2$  m for ERS-2 (Figure S4),  $-0.3$  m and  $0.2$  m for Envisat (Figure 9), and  $-0.15$  m and  $0.05$  m for SARAL (Figure S6), respectively.

As mentioned previously, due to the footprint size in the different frequencies used by the radiometers, land areas are encompassed in the tracks. The brightness temperatures measured in the different frequencies are affected by the presence of land in the footprint of the radiometer [11]. Corrections based on the deconvolution technique have allowed the removal of the land contribution from the signal measured by the radiometer [46,49] to provide reliable corrections up to five kilometers from the coast, as with Jason-2 (Figure S5).

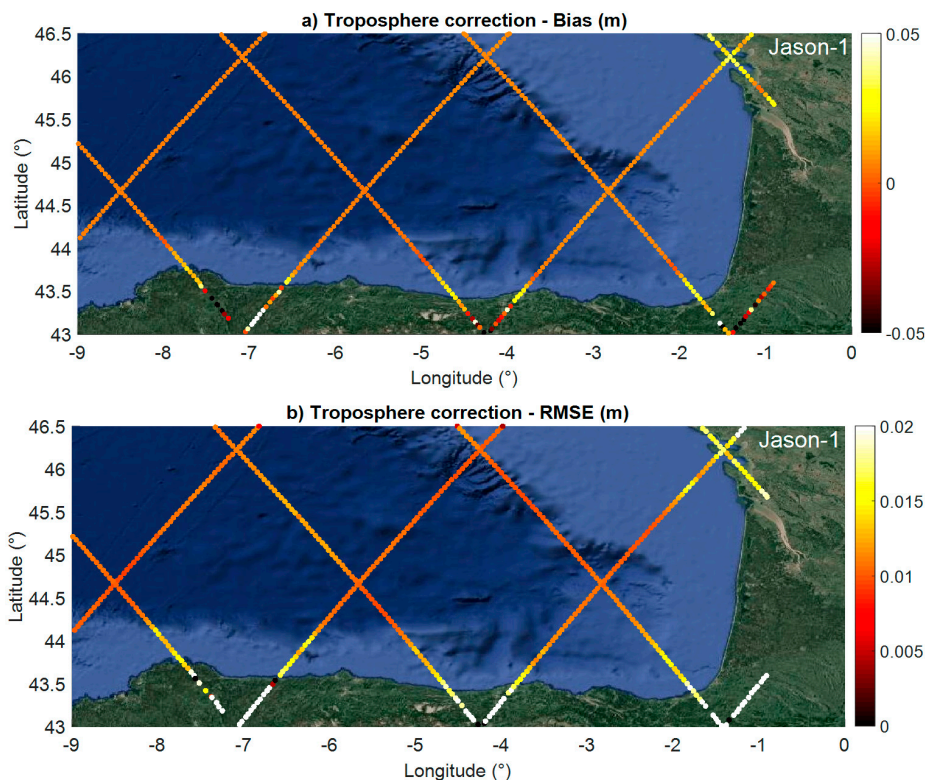


**Figure 8.** Comparison between wet troposphere corrections from radiometer measurements and the CMWF model for Jason-1b (a) Bias and (b) RMSE.

Considering the tracks of Jason-1 and Jason-2 (track 213), and ERS-2, Envisat, and SARAL (track 818) are within 50 km of the coast near La Rochelle, the improvement in the quality of the wet troposphere correction is visible (Figure 10). The wet troposphere correction derived from the ECMWF model output, considered as a reference, is quite stable against time and along the tracks. A clear improvement is observed between Jason-1, with an almost constant bias of five centimeters along the 50 km stretch, and Jason-2, with almost no bias up to 10–15 km from the coast that reaches 0.03 m at the coast, and also between ERS-2 with a small negative bias that increases from 20–25 km from the coast to reach  $-0.20$  m at the coast, Envisat with almost no bias up to 10–15 km from the coast that reaches  $-0.13$  m at the coast, and SARAL with almost no bias up to 10–15 km from the coast that reaches  $-0.06$  m at the coast.

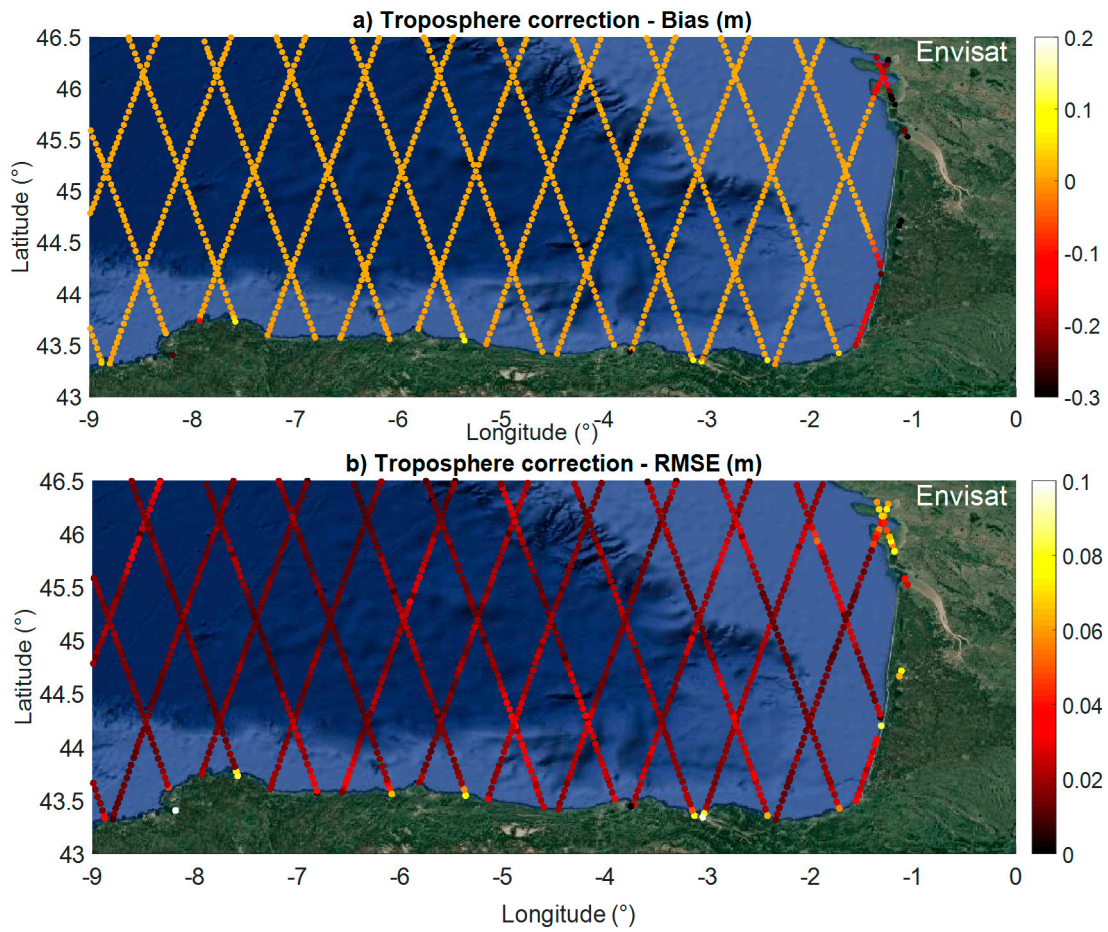


**Figure 9.** Comparison between wet troposphere corrections from radiometer measurements and the ECMWF model for Envisat: (a) bias and (b) RMSE.

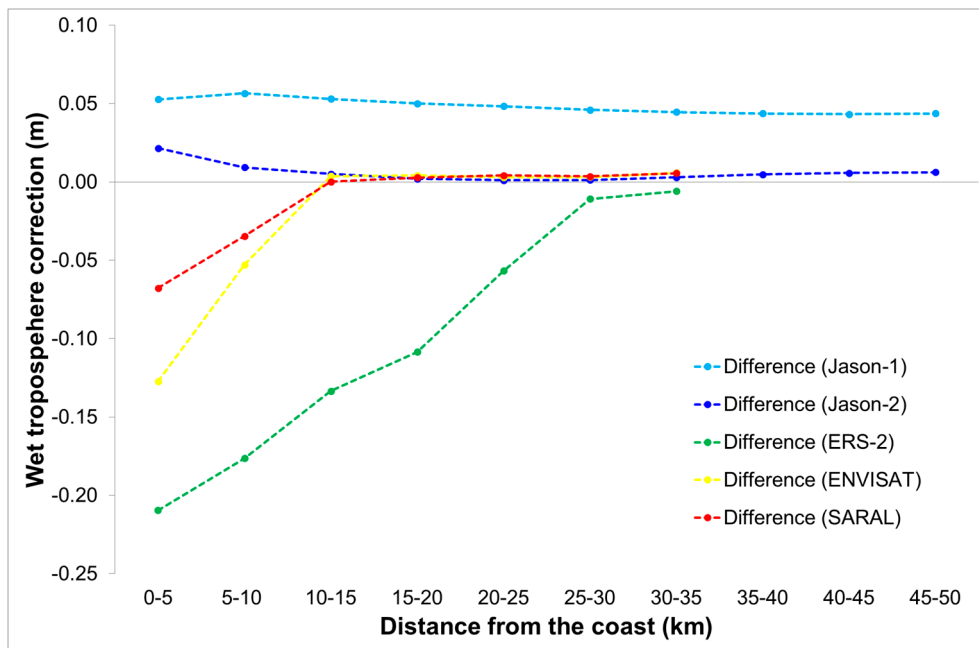


**Figure 10.** Difference between wet troposphere corrections from ECMWF and radiometer measurements for Jason-1 (light blue), Jason-2 (blue), ERS-2 (green), Envisat (yellow), and SARAL (red).

## 5. Discussion

Despite a decrease in the accuracy when approaching the coast, radar altimetry measurements can be used for monitoring the sea surface height close to the shore. The comparisons made with tide gauge records from stations located along the French Atlantic coast in the southern Bay of Biscay showed that the accuracy of the SSH estimates increased for the more recent missions on the 35-day repeating orbit from ERS-2 to SARAL, whereas similar results were observed between Jason-1 and Jason-2 on the 10-day repeating period orbit (Tables 3 and 4). Compared to ERS-2, Envisat benefits from having more acquisitions in ocean mode, at a higher bandwidth frequency mode, that allows a more accurate determination for the middle of the leading edge, and therefore for the altimeter range. SARAL, the first mission to operate at Ka-band, benefits from its smaller footprint (~8 km) [9,50] compared to all the previous altimetry missions (i.e., ~20 km for Jason-2 and ~15 km for Envisat) to obtain better estimates in terms of R (higher than 0.99), and the majority of the time, in terms of RMSE (generally lower than 0.2 m) (Table 3). In this study, if the RMSE values were large, the results presented here were obtained very close to the coast in a macro-tidal environment where the standard deviation of the SSH was generally higher than one meter (Tables 3 and 4). As seen in Figure S1, for a distance more than 10 km from the coast, the results obtained were similar to what was found at the Cal/Val sites. Better results in terms of R and RMSE were obtained when the altimeter ground-track passed from the ocean to land (e.g., track 859 of ERS-2, Envisat, and SARAL). Due to the complexity of the environment under the Jason-1 and Jason-2 tracks around the La Rochelle tide gauge, with the presence of Ré and Oléron islands, no similar conclusion was obtained. Comparisons were performed not only using classical bi-frequency-based ionosphere corrections and radiometer-derived wet troposphere corrections, as measurements were performed over open ocean, but also using corrections derived from model outputs over land, including GIM for the ionosphere and ECMWF for the wet troposphere. The analysis of these different types of corrections showed very good agreement over open ocean but more discrepancies for distances less than 25 km from the coast. However, these results were variable depending on the mission. This latter result shows that model-based ionosphere and wet troposphere corrections could be used for homogeneous long-term altimetry-based SSH from multiple missions, especially given the loss of the secondary frequency, as for Envisat. The deconvolution technique used to filter out the land contribution in the radiometer measurements enables the use of this correction up to the coast in the case of Jason-2 (Figure 10). Efforts to homogenize the corrections are needed to build long term records of altimetry-based SSH. In the near future, the Pertuis Charentais region, encompassed in a few tenths of kilometers by four tide gauge stations (La Rochelle, l'Île d'Aix, La Cotinière, and Le Chapus) could be the first Cal/Val site located along the Atlantic coast. This group of stations benefit from numerous ascending and descending tracks from all the high-precision altimetry missions including Cryosat-2, Sentinel-3A, and the future Sentinel-3B. These stations also have a large diversity in their sea state due to their configuration in the open ocean, away from Ré and Oléron islands and the coastal part between these islands and the shore.

## 6. Conclusions

This study provides a thorough assessment of the performance of radar altimetry-based SSH for all the missions in orbit from ERS-2 to SARAL with the exception of Geosat Follow-On. From all the retracking algorithms, MLE-4 provided the most accurate estimates, especially for distances less than 10 km from the coast. The most recent missions, whose data were considered in this study, showed a clear improvement in the quality of the altimetry-derived SSH data. Results of the comparisons between in situ and Jason-2-based SSH within five kilometers of the coast had a good RMSE, lower than 0.34 m. As the descending track of ERS-2 and Envisat passes from land to ocean, the RMSE obtained was higher compared to the same in situ tide gauges, 1.4 m and 0.9 m, respectively. Due to the large footprint size of Envisat and ERS-2 (18 km), land areas were encompassed, thereby reducing accuracy. The best RMSE was less than 0.21 m for the SSH derived from the SARAL altimeter and the in situ tide gauge at the same nine locations. The comparison statistics showed that the SARAL altimeter

provides better results than other missions over the coastal area. This is due to both improvements in the processing algorithms (MLE-4 vs. MLE-3) and the use of the Ka-band for AltiKa onboard SARAL that is characterized by a smaller footprint that enables obtaining valid range estimates closer to the shore than when using the classical Ku-band.

This study showed that model-based corrections of the ionosphere (GIM) and wet troposphere (ECMWF) delays provide more realistic estimates close to the shore than the bi-frequency-based ionosphere and radiometer-based wet troposphere corrections that are generally used. Besides, these model-based corrections provide very similar values as the instrumental corrections over the open ocean, demonstrating their potential for building homogenous long term datasets.

Better estimates of SSH are likely to be provided by Jason-3, launched 17 January 2016, which can operate in open-loop mode, taking into account a priori ranges from a digital elevation model (DEM) and Sentinel-3, launched 16 February 2016. Sentinel-3 is the first altimeter with a high-resolution mode, also known as Synthetic Aperture Radar mode (SAR), on a repetitive orbit and that can also operate in open-loop. This can increase the number of independent measurements over coastal areas, ice sheet margins, land, and inland waters. The new-era coastal altimetry satellites are becoming an important part of coastal ocean observing systems [47,51].

**Supplementary Materials:** The following are available online at [www.mdpi.com/2072-4292/10/1/93/s1](http://www.mdpi.com/2072-4292/10/1/93/s1). Figure S1: Comparisons between in situ and SSH Jason-2 trace 213 in La Rochelle as a function of the distance from the coast with method MLE-3 and MLE-4. (a) Bias, (b) RMSE, (c) Number of observations, (d) Correlation coefficients R, Figure S2: Comparison between ionosphere corrections from bi-frequency measurements using MLE-4 retracking algorithm and GIM model for Jason-2 (a) Bias, (b) RMSE, Figure S3: Comparison between ionosphere corrections from bi-frequency measurements using MLE-3 retracking algorithm and GIM model for Jason-2 (a) Bias, (b) RMSE, Figure S4: Comparison between wet troposphere corrections from radiometer measurements and ECMWF model for ERS-2 (a) Bias, (b) RMSE, Figure S5: Comparison between wet troposphere corrections from radiometer measurements and ECMWF model for Jason-2 (a) Bias, (b) RMSE, Figure S6: Comparison between wet troposphere corrections from radiometer measurements and ECMWF model for SARAL (a) Bias, (b) RMSE.

**Acknowledgments:** This study was supported by Centre National de la Recherche Scientifique (CNRS) through the framework of MISTRAL project, Centre National d'Etudes Spatiales through OSTST project "FOAM" and TOSCA project "CTOH". PLV gratefully acknowledge the Vietnamese Government's 911 project for funding during my thesis, without which the present study could not have been completed. We thank three anonymous Reviewers for their very helpful comments that helped us in improving the quality of the manuscript.

**Author Contributions:** All of the authors of the present work contributed to the discussion of the results, as well as the writing of the manuscript. Phuong Lan Vu and Frédéric Frappart designed the study. Phuong Lan Vu, Frédéric Frappart and José Darrozes analyzed and discussed the preliminary results. Frédéric Frappart, Vincent Marieu and Fabien Blarel provided the altimetry from Multi—satellite dataset and MAPS software.

**Conflicts of Interest:** The authors declare no conflicts of interest.

## References

1. Fu, L.L.; Cazenave, A. *Satellite Altimetry and Earth Sciences: A Handbook of Techniques and Applications*; International Geophysics Series; Academic Press: San Diego, CA, USA, 2001; Volume 69, 463p.
2. Frappart, F.; Blumstein, D.; Cazenave, A.; Ramillien, G.; Birol, F.; Morrow, R.; Rémy, F. Satellite Altimetry: Principles and Applications in Earth Sciences. In *Wiley Encyclopedia of Electrical and Electronics Engineering*; Webster, J., Ed.; John Wiley & Sons: Hoboken, NJ, USA, 2017; pp. 1–25.
3. Deng, X.; Featherstone, W.E.; Hwang, C.; Berry, P.A.M. Estimation of contamination of ERS-2 and POSEIDON satellite radar altimetry close to the coasts of Australia. *Mar. Geodesy* **2002**, *25*, 249–271. [[CrossRef](#)]
4. Deng, X.; Featherstone, W.E. A coastal retracking system for satellite radar altimeter waveforms: Application to ERS-2 around Australia. *J. Geophys. Res.* **2006**, *111*. [[CrossRef](#)]
5. Gommenginger, C.; Thibaut, P.; Fenoglio-Marc, L.; Qyartly, G.; Deng, X.; Gomez-Enri, J.; Challenor, P.; Gao, Y. Retracking altimeter waveforms near the coasts: A review of retracking methods and some applications to coastal waveforms. In *Coastal Altimetry*; Vignudelli, S., Kostianoy, A., Cipollini, P., Benveniste, J., Eds.; Springer: Berlin/Heidelberg, Germany, 2011; pp. 61–101.
6. Bonnefond, P.; Exertier, P.; Laurain, O.; Thibaut, P.; Mercier, F. GPS-based sea level measurements to help the characterization of land contamination in coastal areas. *Adv. Space Res.* **2013**, *51*, 1383–1399. [[CrossRef](#)]

7. Andersen, O.B.; Scharroo, R. Range and geophysical corrections in coastal regions: And implications for mean sea surface determination. In *Coastal Altimetry*; Vignudelli, S., Kostianoy, A., Cipollini, P., Benveniste, J., Eds.; Springer: Berlin/Heidelberg, Germany, 2011; pp. 103–146.
8. Robinson, A.R.; Brink, K.H. The Global Coastal Ocean: Multiscale Interdisciplinary Processes. In *The Sea*; Harvard University Press: Cambridge, UK, 2005; Volume 13, p. 1062.
9. Verron, J.; Sengenès, P.; Lambin, J.; Noubel, J.; Steunou, N.; Guillot, A.; Picot, N.; Coutin-Faye, S.; Gairola, R.; Raghava Murthy, D.V.A.; et al. The SARAL/AltiKa altimetry satellite mission. *Mar. Geodesy* **2015**, *38*, 2–21. [[CrossRef](#)]
10. Wingham, D.J.; Francis, C.R.; Baker, S.; Bouzinac, C.; Brockley, D.; Cullen, R.; de Chateau-Thierry, P.; Laxon, S.W.; Mallow, U.; Mavrocordatos, C.; et al. CryoSat: A mission to determine the fluctuations in Earth's land and marine ice fields. *Adv. Space Res.* **2006**, *37*, 841–871. [[CrossRef](#)]
11. Obligis, E.; Desportes, C.; Eymard, L.; Fernandes, M.J.; Lázaro, C.; Nunes, A. Tropospheric Corrections for Coastal Altimetry. In *Coastal Altimetry*; Vignudelli, S., Kostianoy, A., Cipollini, P., Benveniste, J., Eds.; Springer: Berlin/Heidelberg, Germany, 2011; pp. 147–176.
12. Passaro, M.; Cipollini, P.; Vignudelli, S.; Quartly, G.D.; Snaith, H.M. ALES: A multi-mission subwaveform retracker for coastal and open ocean altimetry. *Remote Sens. Environ.* **2014**, *145*, 173–189. [[CrossRef](#)]
13. Fernandes, M.J.; Lázaro, C.; Nunes, A.L.; Scharroo, R. Atmospheric Corrections for Altimetry Studies over Inland Water. *Remote Sens.* **2014**, *6*, 4952–4997. [[CrossRef](#)]
14. Birol, F.; Fuller, N.; Lyard, F.; Cancet, M.; Niño, F.; Delebecque, C.; Fleury, S.; Toublanc, F.; Melet, A.; Saraceno, M. Coastal applications from nadir altimetry: Example of the X-TRACK regional products. *Adv. Space Res.* **2017**, *59*, 936–953. [[CrossRef](#)]
15. Bonnefond, P.; Exertier, P.; Laurain, O.; Ménard, Y.; Orsoni, A.; Jan, G.; Jeansou, E. Absolute Calibration of Jason-1 and TOPEX/Poseidon Altimeters in Corsica. *Mar. Geodesy* **2003**, *26*, 261–284. [[CrossRef](#)]
16. Haines, B.J.; Desai, S.D.; Born, G.H. The Harvest experiment of the climate data record from TOPEX/Poseidon, Jason-1 and the ocean surface topography mission. *Mar. Geodesy* **2010**, *33*, 91–113. [[CrossRef](#)]
17. Mertikas, S.P.; Ioannides, R.T.; Tziavos, I.N.; Vergos, G.S.; Hausleitner, W.; Frantzis, X.; Tripolitsiotis, A.; Partsinevelos, P.; Andrikopoulos, D. Statistical models and latest results in the determination of the absolute bias for the radar altimeters of Jason satellites using the Gavdos facility. *Mar. Geodesy* **2010**, *33*, 114–149. [[CrossRef](#)]
18. Watson, C.S.; White, N.C.; Church, J.A.; Burgette, R.J.; Tregoning, P.; Coleman, R. Absolute calibration in Bass Strait, Australia: TOPEX, Jason-1 and OSTM/Jason-2. *Mar. Geodesy* **2011**, *34*, 242–260. [[CrossRef](#)]
19. Pingree, R.D.; Mardell, G.T.; New, A.L. Propagation of internal tides from the upper slopes of the Bay of Biscay. *Nature* **1986**, *321*, 154–158. [[CrossRef](#)]
20. New, A.L. Internal tidal mixing in the Bay of Biscay. *Deep Sea Res. Part A Oceanogr. Res. Pap.* **1988**, *35*, 691–709. [[CrossRef](#)]
21. Pairaud, I.L.; Lyard, F.; Auclair, F.; Letellier, T.; Marsaleix, P. Dynamics of the semi-diurnal and quarter-diurnal internal tides in the Bay of Biscay. Part 1: Barotropic tides. *Cont. Shelf Res.* **2008**, *28*, 1294–1315. [[CrossRef](#)]
22. Iijima, B.A.; Harris, I.L.; Ho, C.M.; Lindqwister, U.J.; Mannucci, A.J.; Pi, X.; Reyes, M.J.; Sparks, L.C.; Wilson, B.D. Automated daily process for global ionospheric total electron content maps and satellite ocean altimeter ionospheric calibration based on Global Positioning System data. *J. Atmos. Sol.-Terr. Phys.* **1999**, *61*, 1205–1218. [[CrossRef](#)]
23. Scharroo, R.; Smith, W.H.F. Global positioning system-based climatology for the total electron content in the ionosphere. *J. Geophys. Res.* **2010**, *115*. [[CrossRef](#)]
24. CTOH: Centre for Topographic Studies of the Oceans and Hydrosphere. Available online: <http://ctoh.legos.obs-mip.fr> (accessed on 4 December 2017).
25. United States Department of Agriculture. Available online: [https://ipad.fas.usda.gov/cropexplorer/global\\_reservoir](https://ipad.fas.usda.gov/cropexplorer/global_reservoir) (accessed on 4 December 2017).
26. Carayon, G.; Steunou, N.; Courrière, J.; Thibaut, P. Poseidon-2 radar altimeter design and results of in-flight performances. *Mar. Geodesy* **2003**, *26*, 159–165. [[CrossRef](#)]
27. Desjonquères, J.-D.; Carayon, G.; Steunou, N.; Lambin, J. Poseidon-3 Radar Altimeter: New Modes and In-Flight Performances. *Mar. Geodesy* **2010**, *33*, 53–79. [[CrossRef](#)]

28. Zelli, C. ENVISAT RA-2 advanced radar altimeter: Instrument design and prelaunch performance assessment review. *Acta Astronaut.* **1999**, *44*, 323–333. [[CrossRef](#)]
29. Service Hydrographique et Océanographique de la Marine. Available online: <http://data.shom.fr/donnes/refmar> (accessed on 4 December 2017).
30. Besser, G. *Marées*; Service Hydrographique et Océanographique de la Marine: Paris, France, 1985.
31. Charria, G.; Lazure, P.; le Cann, B.; Serpette, A.; Reverdin, G.; Louazel, S.; Batifoulier, F.; Dumas, F.; Pichon, A.; Morele, Y. Surface layer circulation derived from Lagrangian drifters in the Bay of Biscay. *J. Mar. Syst.* **2013**, *109*, 60–76. [[CrossRef](#)]
32. Frouin, R.; Fiúza, A.F.G.; Ambar, I.; Boyd, T.J. Observations of a Poleward Surface Current off the Coasts of Portugal and Spain During Winter. *J. Geophys. Res.* **1990**, *95*, 679–691. [[CrossRef](#)]
33. Le Cann, B.; Pingree, R.D. Structure, strength, and seasonality of the slope current in the Bay of Biscay region. *J. Mar. Biol. Assoc.* **1990**, *70*, 857–885.
34. Lazune, P.; Jegou, A.-M.; Kerdreux, M. Analysis of salinity measurements near islands on the French continental shelf of the Bay of Biscay. *Sci. Mar.* **2006**, *70*, 7–14.
35. Pichon, A.; Correard, S. Internal tides modelling in the Bay of Biscay. Comparisons with observations. *Sci. Mar.* **2006**, *70*, 65–88. [[CrossRef](#)]
36. Ménard, Y.; Jeansou, E.; Vincent, P. Calibration of the TOPEX/POSEIDON Altimeters Additional Results at Harvest. *J. Geophys. Res.* **1994**, *99*, 24487–24504. [[CrossRef](#)]
37. Chelton, D.B.; Ries, J.C.; Haines, B.J.; Fu, L.-L.; Callahan, P.S. Satellite Altimetry. In *Satellite Altimetry and Earth Sciences*; Fu, L.-L., Cazenave, A., Eds.; Academic Press: San Diego, CA, USA, 2001; pp. 1–131.
38. Frappart, F.; Papa, F.; Marieu, V.; Malbêteau, Y.; Jordy, F.; Calmant, S.; Durand, F.; Bala, S. Preliminary assessment of SARAL/AltiKa observations over the Ganges-Brahmaputra and Irrawaddy Rivers. *Mar. Geodesy* **2015**, *38*, 568–580. [[CrossRef](#)]
39. Frappart, F.; Roussel, N.; Biancale, R.; Martinez Benjamin, J.J.; Mercier, F.; Pérosanz, F.; Garate Pasquin, J.; Martin Davila, J.; Perez Gomez, B.; Gracia Gomez, C.; et al. The 2013 Ibiza calibration campaign of Jason-2 and SARAL altimeters. *Mar. Geodesy* **2015**, *38*, 219–232. [[CrossRef](#)]
40. Frappart, F.; Legrésy, B.; Niño, F.; Blarel, F.; Fuller, N.; Fleury, S.; Birol, F.; Calmant, S. An ERS-2 altimetry reprocessing compatible with ENVISAT for long-term land and ice sheets studies. *Remote Sens. Environ.* **2016**, *184*, 558–581. [[CrossRef](#)]
41. Biancamaria, S.; Frappart, F.; Leleu, A.S.; Marieu, V.; Blumstein, D.; Boy, F.; Sottolichio, A.; Valle-Levinson, A. Satellite radar altimetry water elevations performance over a hundred meter wide river: Evaluation over the Garonne River. *Adv. Space Res.* **2017**, *59*, 128–146. [[CrossRef](#)]
42. Amarouche, L.; Thibaut, P.; Zanife, O.Z.; Dumont, J.-P.; Vincent, P.; Steunou, N. Improving the Jason-1 ground retracking to better account for attitude effects. *Mar. Geodesy* **2004**, *27*, 171–197. [[CrossRef](#)]
43. Rodríguez, E. Altimetry for non-Gaussian oceans: Height biases and estimation of parameters. *J. Geophys. Res.* **1988**, *93*, 14107–14120. [[CrossRef](#)]
44. Brown, G. The average impulse response of a rough surface and its applications. *IEEE Trans. Antennas Propag.* **1977**, *25*, 67–74. [[CrossRef](#)]
45. Astudillo, O.; Dewitte, B.; Mallet, M.; Frappart, F.; Rutllant, J.; Ramos, M.; Bravo, L.; Goubanova, K.; Illig, S. Surface winds off Peru-Chile: Observing closer to the coast from radar altimetry. *Remote Sens. Environ.* **2017**, *191*, 179–196. [[CrossRef](#)]
46. Blarel, F.; Frappart, F.; Legrésy, B.; Blumstein, D.; Rémy, F.; Fatras, C.; Mougín, E.; Papa, F.; Prigent, C.; Niño, F.; et al. Altimetry backscattering signatures at Ku and S bands over land and ice sheets. In *Remote Sensing for Agriculture, Ecosystems, and Hydrology XVII*; Neale, C.M.U., Maltese, A., Eds.; Society of Photo-Optical Instrumentation Engineers (SPIE): Bellingham, WA, USA, 2015.
47. Martin-Puig, C.; Leuliette, E.; Lillibrige, J.; Roca, M. Evaluating the Performance of Jason-2 Open-Loop and Closed-Loop Tracker Modes. *Am. Meteorol. Soc.* **2016**. [[CrossRef](#)]
48. Vignudelli, S.; Kostianoy, A.G.; Cipollini, P.; Benveniste, J. *Coastal Altimetry*; Springer-Verlag: Berlin/Heidelberg, Germany, 2011; p. 578.
49. Brown, S. A Novel Near-Land Radiometer Wet Path-Delay Retrieval Algorithm: Application to the Jason-2/OSTM Advanced Microwave Radiometer. *Geosci. Remote Sens.* **2010**, *48*, 1986–1992. [[CrossRef](#)]

50. Bonnefond, P.; Verron, J.; Aublanc, J.; Babu, K.N.; Bergé-Nguyen, M.; Cancet, M.; Chaudhary, A.; Crétaux, J.-F.; Frappart, F.; Haines, B.J.; et al. The Benefits of the Ka-Band as Evidenced from the SARAL/AltiKa Altimetric Mission: Quality Assessment and Unique Characteristics of AltiKa Data. *Remote Sens.* **2018**, *10*, 83. [[CrossRef](#)]
51. Liu, Y.; Kerkering, H.; Weisberg, R.H. *Coastal Ocean Observing Systems*; Elsevier: Amsterdam, The Netherlands, 2015; p. 461. ISBN 978-0-12-802022-7.



© 2018 by the authors. Licensee MDPI, Basel, Switzerland. This article is an open access article distributed under the terms and conditions of the Creative Commons Attribution (CC BY) license (<http://creativecommons.org/licenses/by/4.0/>).

# Supplementary Information to

## Multi-satellite altimeter validation along the French Atlantic coast in the southern Bay of Biscay from ERS-2 to SARAL

Phuong-Lan Vu<sup>1,\*</sup>, Frédéric Frappart<sup>1,2</sup>, José Darrozes<sup>1</sup>, Vincent Marieu<sup>3</sup>, Fabien Blarel<sup>2</sup>, Guillaume Ramillien<sup>1</sup>, Pascal Bonnefond<sup>4</sup>, Florence Birol<sup>2</sup>

<sup>1</sup> GET-GRGS, UMR 5563, CNRS/IRD/UPS, Observatoire Midi-Pyrénées, 14 Avenue Edouard Belin, 31400 Toulouse, France ; Emails : [frederic.frappart@get.obs-mip.fr](mailto:frederic.frappart@get.obs-mip.fr); [jose.darrozes@get.obs-mip.fr](mailto:jose.darrozes@get.obs-mip.fr); [guillaume.ramillien@get.obs-mip.fr](mailto:guillaume.ramillien@get.obs-mip.fr)

<sup>2</sup> LEGOS-GRGS, UMR 5566, CNES/CNRS/IRD/UPS, Observatoire Midi-Pyrénées, 14 Avenue Edouard Belin, 31400 Toulouse, France ; Emails : [florence.biol@legos.obs-mip.fr](mailto:florence.biol@legos.obs-mip.fr); [fabien.blarel@legos.obs-mip.fr](mailto:fabien.blarel@legos.obs-mip.fr)

<sup>3</sup> UMR CNRS 5805 EPOC - OASU - Université de Bordeaux Allée Geoffroy Saint-Hilaire - CS 50023 - 33615 PESSAC CEDEX – France ; Email : [vincent.marieu@u-bordeaux.fr](mailto:vincent.marieu@u-bordeaux.fr)

<sup>4</sup> SYRTE - Observatoire de Paris, 61 avenue de l'Observatoire, 75014 Paris – France ; Email : [pascal.bonnefond@obspm.fr](mailto:pascal.bonnefond@obspm.fr)

\* Correspondence: [phuonglan.vu@get.omp.eu](mailto:phuonglan.vu@get.omp.eu); Tel.: +33-7-82-32-11-36.

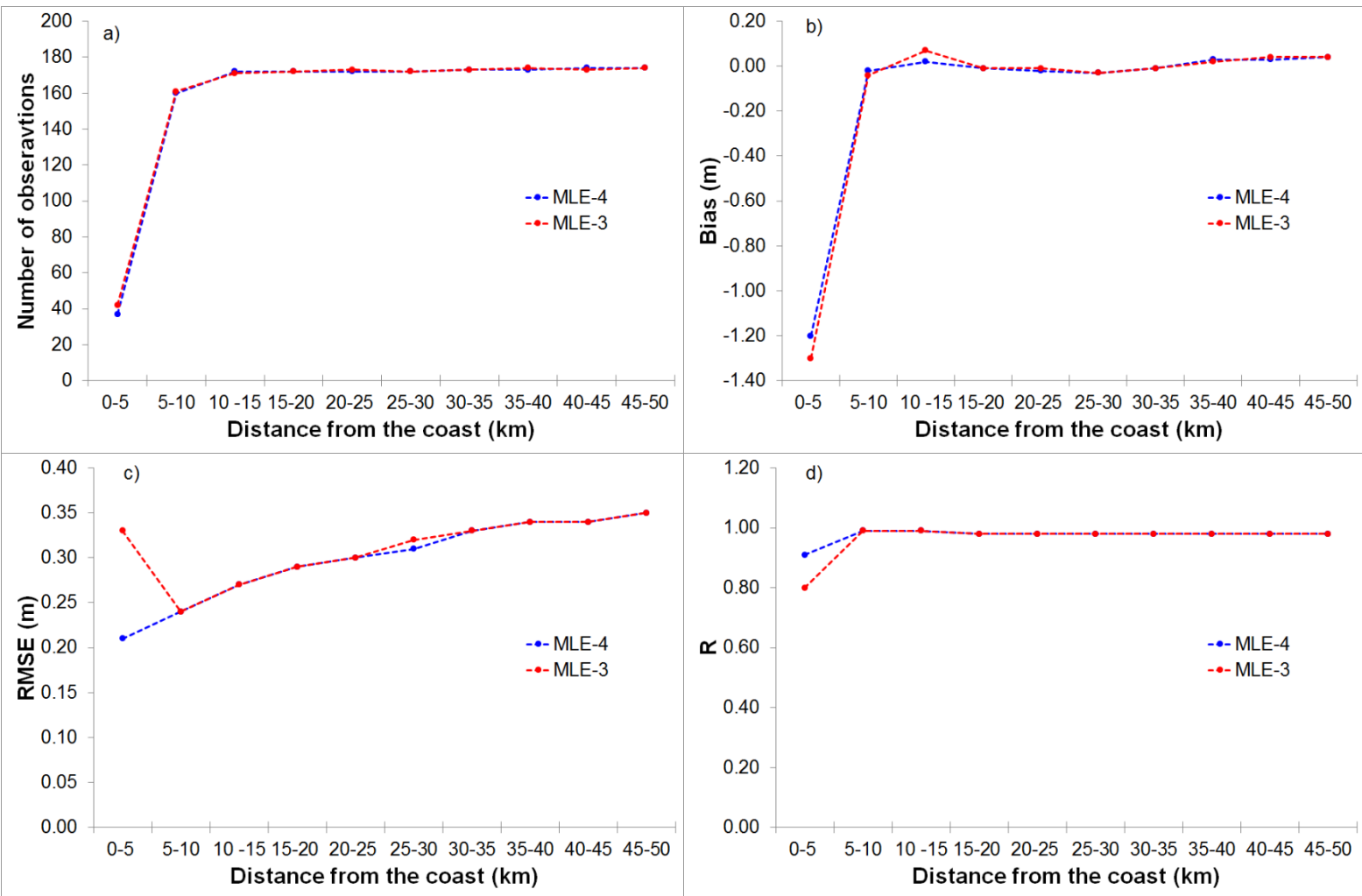


**Figure S1.** Comparisons between *in situ* and SSH Jason-2 trace 213 in La Rochelle as a function of the distance from the coast with method MLE-3 and MLE-4. **(a)** Bias, **(b)** RMSE, **(c)** Number of observations, **(d)** Correlation coefficients R.

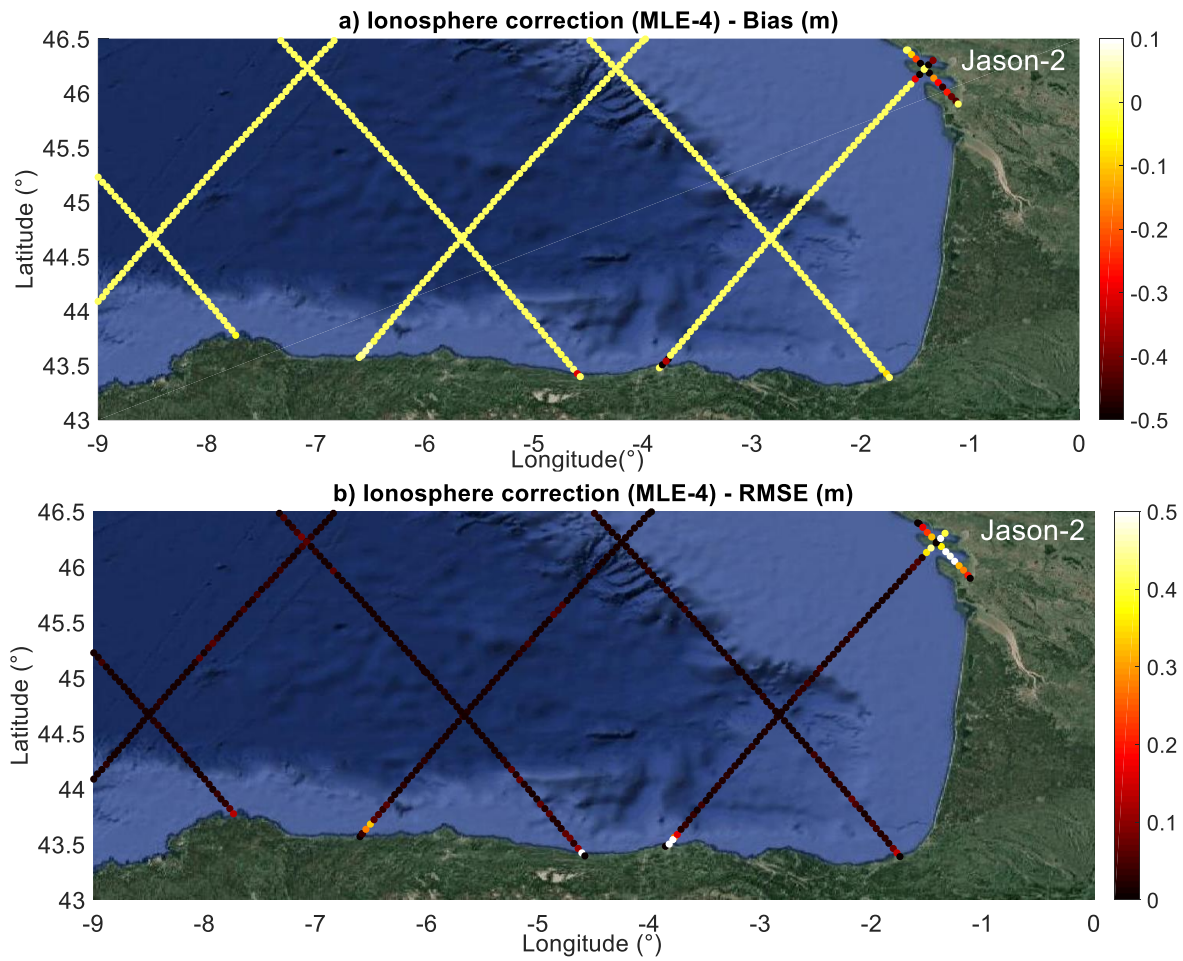


**Figure S2.** Comparison between ionosphere corrections from bi-frequency measurements using MLE-4 retracking algorithm and GIM model for Jason-2 **(a)** Bias, **(b)** RMSE.

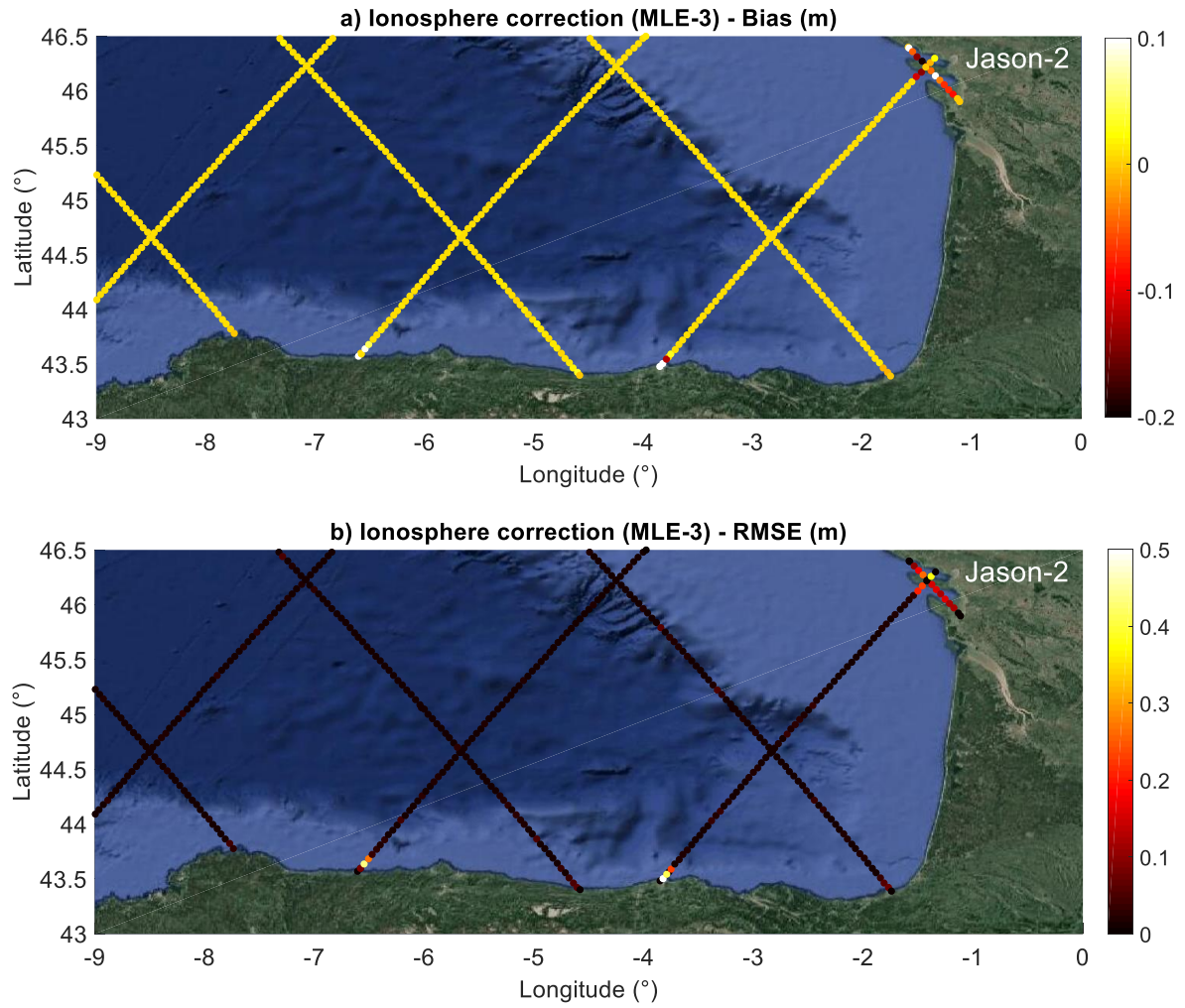


**Figure S3.** Comparison between ionosphere corrections from bi-frequency measurements using MLE-3 retracking algorithm and GIM model for Jason-2 **(a)** Bias, **(b)** RMSE.

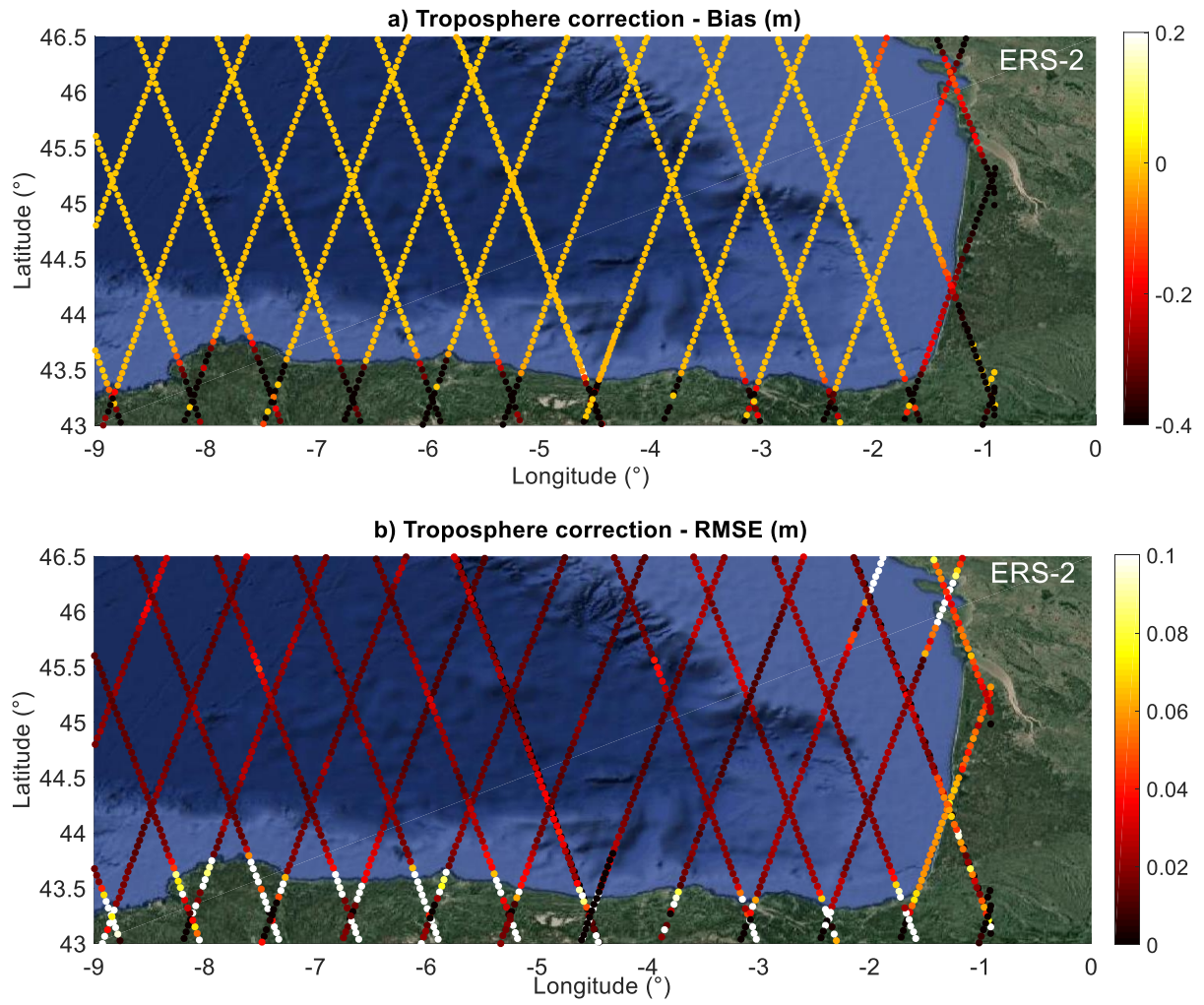


**Figure S4.** Comparison between wet troposphere corrections from radiometer measurements and ECMWF model for ERS-2 **(a)** Bias, **(b)** RMSE.

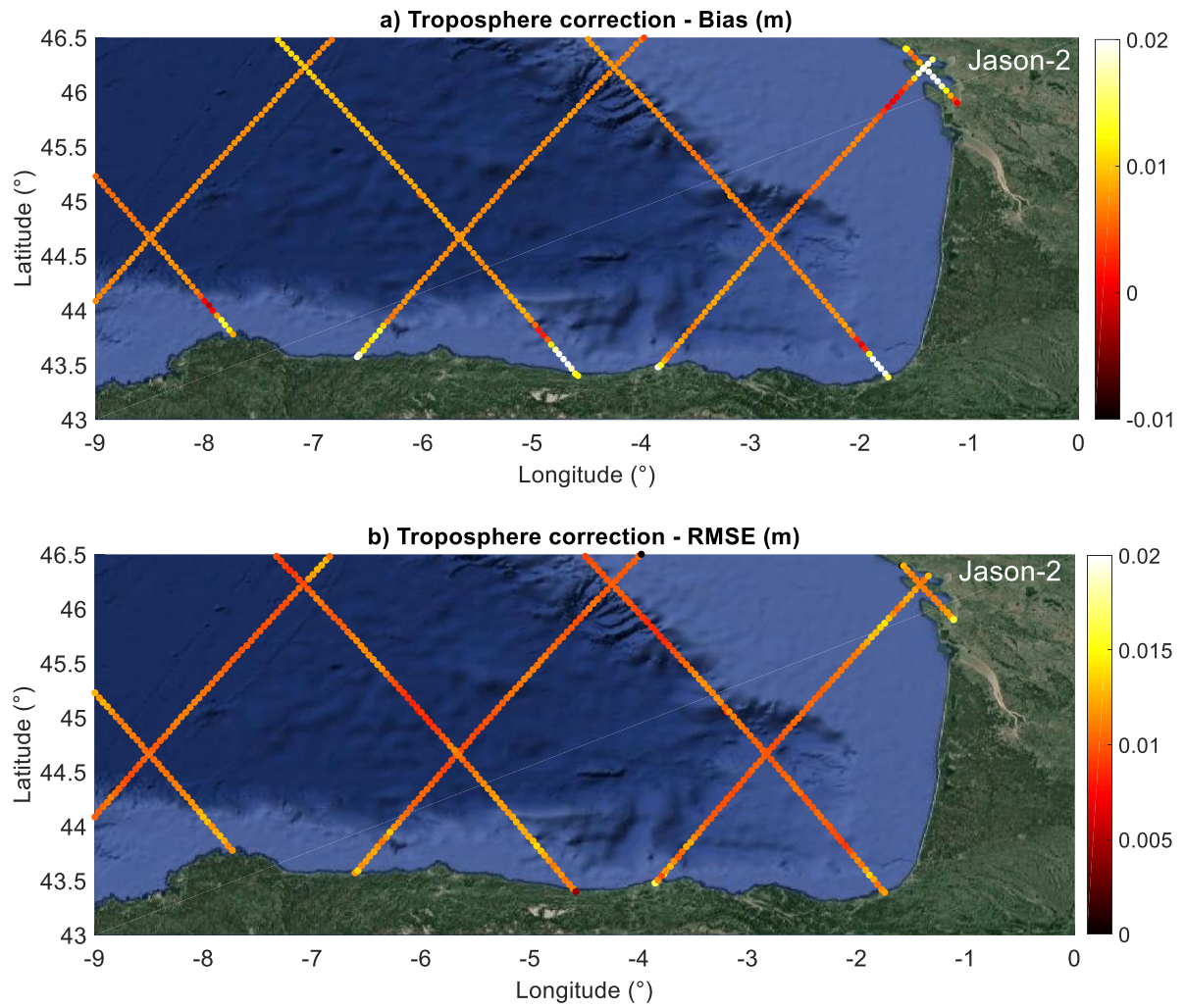


**Figure S5.** Comparison between wet troposphere corrections from radiometer measurements and ECMWF model for Jason-2 **(a)** Bias, **(b)** RMSE.

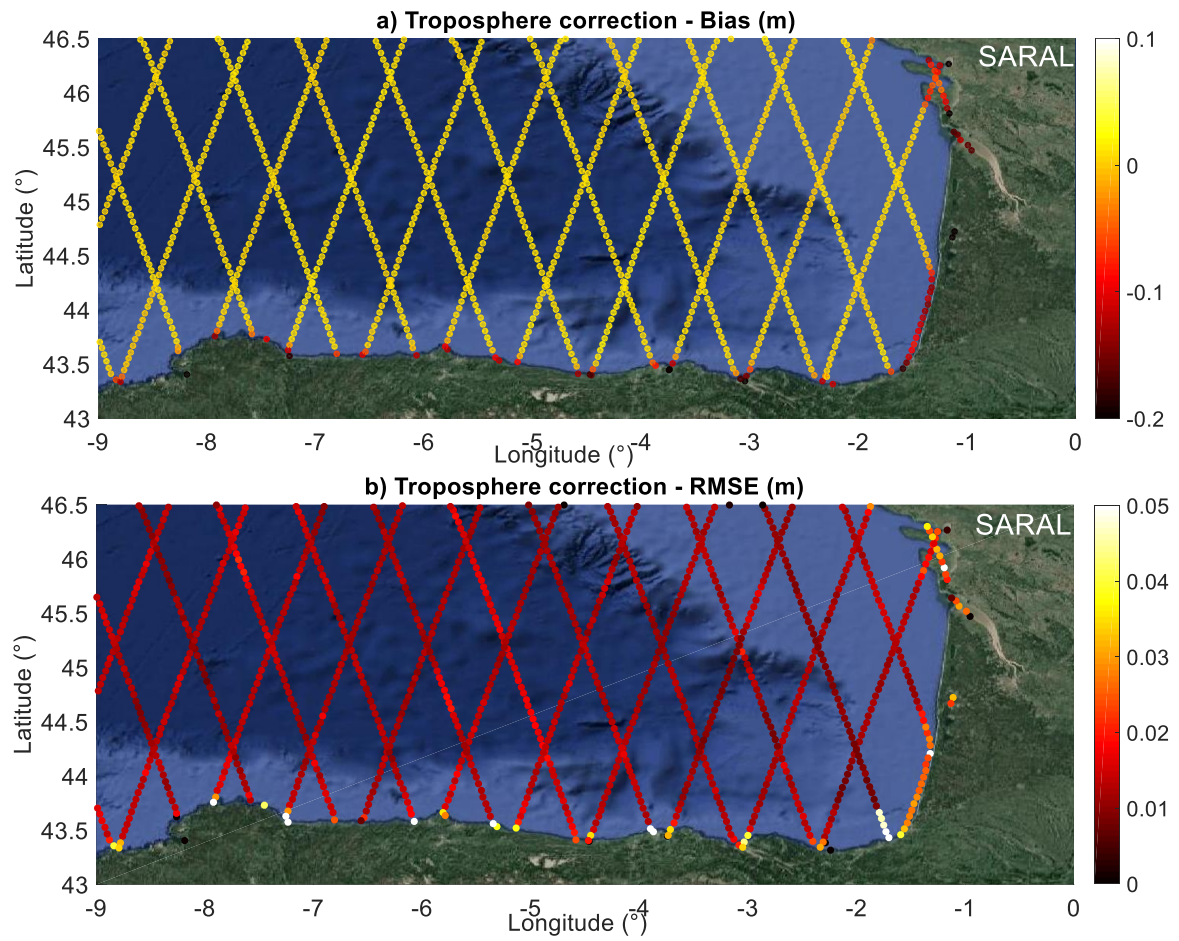


**Figure S6.** Comparison between wet troposphere corrections from radiometer measurements and ECMWF model for SARAL (a) Bias, (b) RMSE.

---

CHAPTER IV

**GNSS Reflectometry for detection of  
tide and extreme hydrological events:  
example of the Socoa (France), Mekong  
delta and Red River Delta (Vietnam)**

---

**Contents**

---

|  |            |
|--|------------|
| <b>IV.1 Résumé étendu . . . . .</b>  | <b>123</b> |
| <b>IV.2 Introduction . . . . .</b>   | <b>125</b> |
| <b>IV.3 State of the art . . . . .</b>   | <b>129</b> |
| <b>IV.4 Methodology . . . . .</b>  | <b>131</b> |
| IV.4.1 Sea surface height (SSH) derived from GNSS-R signals . . . . .  | 131        |
| IV.4.2 Analysis of the GNSS-R-based SSH using SSA and CWT methods  | 137        |
| <b>IV.5 The Socoa experiment . . . . .</b>   | <b>144</b> |
| IV.5.1 Characteristics of the Socoa study area . . . . .   | 144        |
| IV.5.2 Datasets . . . . .  | 145        |
| IV.5.3 SNR-based sea surface height variation estimates . . . . .  | 147        |
| IV.5.4 Complementary between SSA and CWT method to extract the<br>tides components in GNSS-R signals . . . . . | 149        |
| IV.5.5 Detection the Xynthia storm in the GNSS R signals using SSA and<br>XWT method . . . . .                 | 151        |
| <b>IV.6 The Mekong delta experiment (Vietnam) . . . . .</b>  | <b>153</b> |
| IV.6.1 Characteristics of the Mekong delta area and experimental conditions                                    | 153        |
| IV.6.2 Parameters for SNR signals analyzing . . . . .  | 155        |
| IV.6.3 Comparison between the water level derived from GNSS-R and in-<br>situ gauge records . . . . .          | 155        |
| <b>IV.7 Red River Delta (RRD) experiment . . . . .</b>   | <b>156</b> |

---

|  |            |
|--|------------|
| IV.7.1 The study area and datasets . . . . .   | 156        |
| IV.7.2 Parameters for SNR signals analyzing . . . . .  | 160        |
| IV.7.3 Results . . . . .   | 162        |
| <b>IV.8 Conclusions and perspectives . . . . .</b>   | <b>164</b> |
| <b>IV.9 Revised version of the article submitted at Remote Sensing, special issue</b><br><b>“Remote Sensing of hydrological Extremes”:</b> . . . . . | <b>166</b> |

---

## **IV.1 Résumé étendu**

Dans ce chapitre, il a été montré qu'il était possible d'estimer les variations SSH à l'aide d'une seule antenne géodésique en analysant simplement les oscillations du SNR enregistré quotidiennement dans des environnements complexes tels que les estuaires et les zones côtières. Le niveau d'eau dérivé du signal SNR des différentes constellations GNSS fournit des résultats comparables à ceux des marégraphes et des jauges hydrologiques classiques. Cette étude a permis d'évaluer les performances du GNSS-R pour la surveillance des changements climatiques ainsi que les événements extrêmes qu'ils sont associées au niveau des mers ou des cours d'eau. Par conséquent, la réflectométrie GNSS constitue une alternative puissante et un complément significatif aux techniques de mesure actuelles, car elle autorise différentes résolutions spatiales et temporelles ce qui est un vrai plus par rapport aux outils classiques (mesures ponctuelles et continues pour un marégraphe, ou couvrant une vaste zone mais avec une faible répétabilité pour les altimètres conventionnels).

Dans l'expérience de Socoa, la tempête Xynthia a été détectée à l'aide de la méthode SSA et CWT de la station de Socoa. Les comparaisons effectuées avec les relevés de marégraphes de la station de Socoa ont montré que la méthode SSA extrait les marées et les contributions majeures avec une grande précision en supprimant la composante associée au bruit. La précision des estimations de la marée est maximale pour une taille de la fenêtre  $M$  supérieure à 6 h, ce qui correspond au cycle de montée et de descente de la marée. L'analyse des marées avec  $M=12h$  donne deux composantes de marée (RC1+RC2) dont les périodes correspondent aux marées de la baie de Saint Jean de Luz (marées semi-diurnes de 6h et diurnes de 12h). La troisième composante de reconstruction (RC3) utilisant la méthode SSA enregistre, quant à elle, les effets de la pression atmosphérique dans les signaux GNSS on obtient un coefficient de corrélation  $R=0,7$  par rapport aux données de pression atmosphérique mesurées dans la station de Socoa. Cette corrélation grimpe à 0,76 lorsqu'on utilise à

la fois les résidus du SNR associés aux surcotes et de la variation de la pression atmosphérique (voir détail dans l'article au paragraphe IV.9).

Dans le cadre de l'expérience sur le fleuve Mékong, une antenne GNSS a été installée dans le château d'eau de Tran De ( $H=30$  m), à 100 m du fleuve. Les comparaisons avec les données des jauges in situ donnent un coefficient de corrélation de 0,92 avec la méthode de Larson et de 0,85 avec la méthode de LSM. Les résultats de la méthode Larson sont meilleurs que la méthode LSM. Cela peut s'expliquer par la mesure pendant les périodes les plus statiques (maximum ou minimum de marée), moins affectée par les vagues. Le niveau d'eau dérivé du signal SNR fournit des résultats de qualité similaire à ceux des jauges classiques pour les constellations GPS et GLONASS. Cette étude nous a donc permis d'évaluer les performances du GNSS-R pour la surveillance des crues affectant les cours d'eau lors d'évènements extrêmes comme les tempêtes. Nous avons aussi montré la possibilité d'utiliser cette technique pour l'étalonnage/la validation des données altimétriques (SARAL, Jason-2, 3, Sentinel-3A, etc.). Ainsi, l'analyse SNR réfléchi est un outil prometteur pour obtenir des mesures continues et spatialisés des hauteurs d'eau pour les rivières/fleuves. Nous obtenons non seulement le niveau d'eau de la rivière, mais nous pouvons également récupérer la pente locale de la surface de l'eau et les zones inondées.

Ainsi, il peut être utilisé pour détecter des événements hydrologiques extrêmes. À partir des deux études réalisées dans le fleuve rouge et le delta du Mékong, nous avons démontré que le rapport SNR tirés des données GNSS-R permettait d'estimer le niveau de l'eau avec une précision d'environ 10 cm. Les méthodes de Larson ([Larson et al., 2013a](#)) et de Roussel ([Roussel et al., 2015b](#)) peuvent être appliquées non seulement dans la zone côtière, mais également dans les eaux continentales (rivière, lac, etc.) et même dans les zones estuariennes où l'on a des combinaisons complexes entre le régime hydrologique, les marées océaniques les effets des vagues etc. Les deux méthodes donnent de bons résultats mais pour un nombre limité de points pour Larson, tandis que la méthode Roussel donne un

grand nombre de solutions précises. La multi-constellation augmente la précision des solutions et le nombre de points calculés. Sur le fleuve rouge la tempête principale, à savoir Mirinae, n'a pas été complètement enregistrée à cause de problèmes techniques par contre pour Nida les résultats sont plus que concluants. Dans les deux cas on a pu estimer les décalages entre l'onde de crue et l'évènement climatique qui l'a générée. On peut ainsi voir un retard de 48 heures pour Nida en raison du temps de transit des eaux du bassin versant.

## **IV.2 Introduction**

Coastal areas concentrate the majority of the world's economic and urban activities. In recent years, population density has been increasing in the coastal area and demographic projections predict that more than 75% of the global population will live there by 2035 (Haslett, 2008). Coastal areas are strongly affected by human activity, which is responsible for major structural damage by threatening the plant and animal biodiversity that has supported coastal regions for centuries (Creel, 2003; Raven et al., 1992; Harvey, 2015). Global climate change causes extreme events such as storm surges, earthquake and tsunamis have devastating effects along the coasts (Keon et al., 2015; EPA, 2017). Monitoring the evolution of these environments is, therefore, more necessary than ever. Many tools based on observation techniques have been developed for this purpose (tide gauge stations, buoy sensors (Sešek and Trontelj, 2013; Hannah, 2010), satellite radar altimetry (Wolters, 2017). Over the past twenty years, new remote sensing instruments have made it possible to approach these goals, with the appearance of scatter-meters, synthetic aperture radars, or on-board radar altimeters. The new-era coastal altimetry satellites are becoming an important part of coastal ocean observing systems (Liu et al., 2015). Although it has been greatly improved to suit the coastal area, however, spatial and temporal resolutions are inadequate to observe the complex and rapid variations in ocean dynamics in these environments.

Nowadays, sea surface height variations are measured by tide gauges along the coasts. These sensors are dampened to minimize the effects of the wave on the measurements of the tide. Recently, Global Navigation Satellite System-Reflectometry (GNSS-R) demonstrated a strong potential for the monitoring changes in the Earth surface. Thanks to the deployment in many countries of permanent GNSS stations, this technique can be applied when a permanent geodetic GNSS station is located on the shore (in Fig. IV.1). An approach, based on the analysis of the reflected component of the signal to noise ratio (SNR) measured by the geodetic antenna can be used for the monitoring of the level variations of the sea surface.

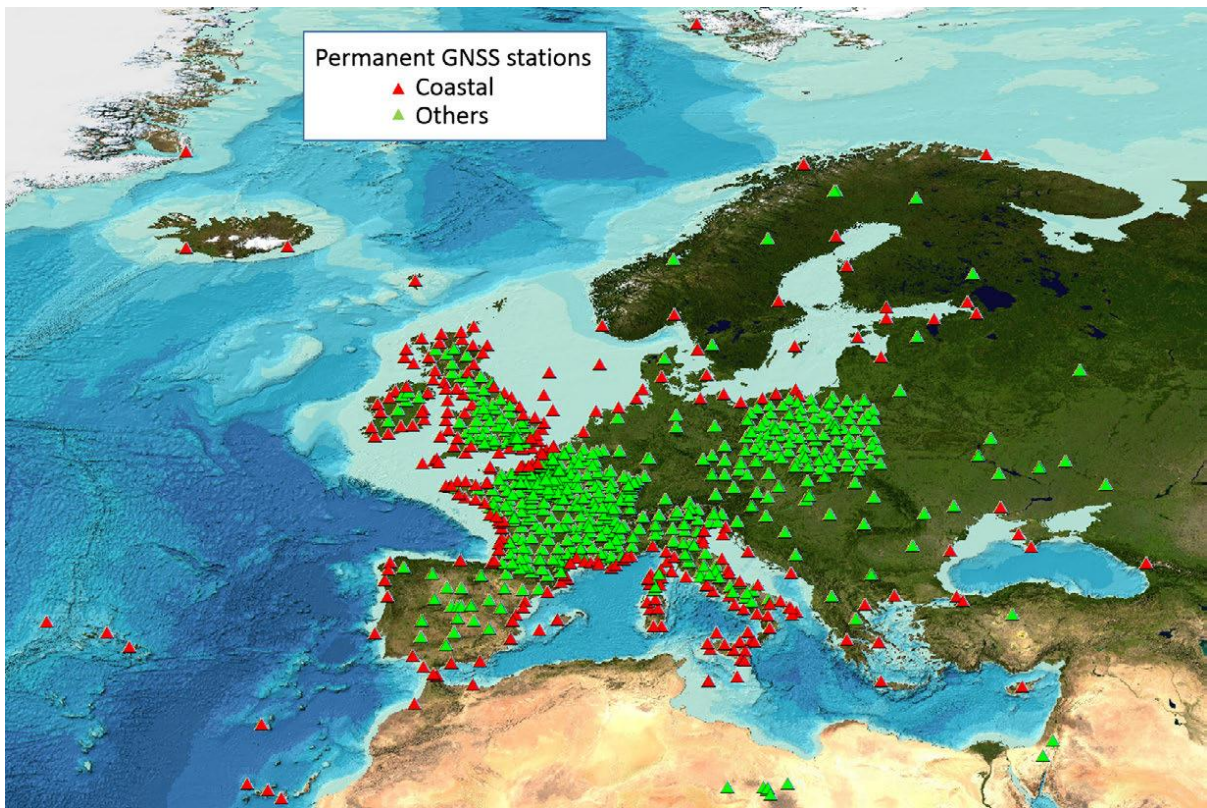


Figure IV.1 – Main permanent GNSS stations in Europe. With GNSS-R altimetry, coastal GNSS station are potential tide gauges (EUREF Permanent GNSS Network).

However, to monitor the sea level variations using these station, some criteria need to be considered: the receiver height, satellite elevation and antenna location. Figure IV.2 shows the variation in the distance between the antenna and the reflection points and the area of the first Fresnel

**Chapter IV. GNSS Reflectometry for detection of tide and extreme hydrological events: example of the Socoa (France), Mekong delta and Red River Delta (Vietnam)**

surface (see § II.3.2) as a function of the satellite elevation angle and the antenna height above the reflection surface.

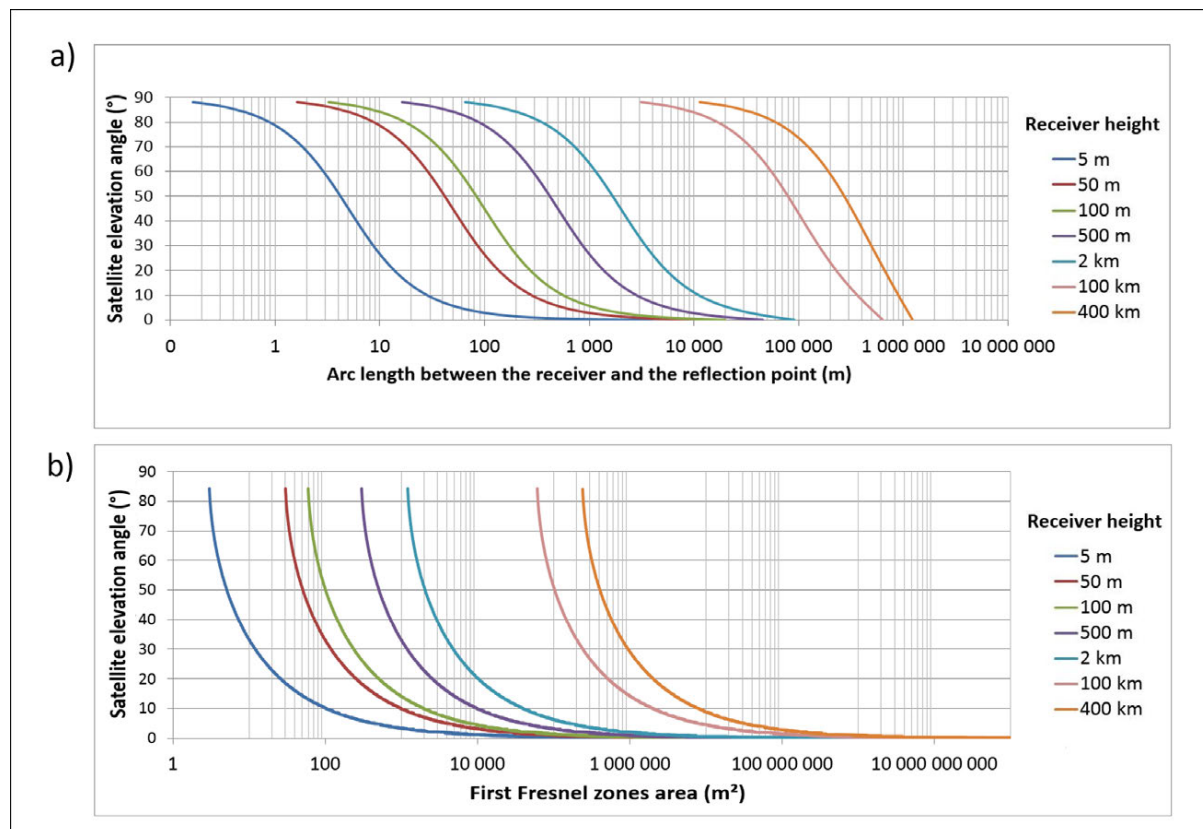


Figure IV.2 – Variations in the distance between the antenna and the specular reflection points (a) and the surface area of the first Fresnel surfaces (b) as a function of the elevation angle of the satellites and for different antenna heights. (Roussel et al., 2016)

For example, if we consider the specular point of a satellite with an elevation angle of 50° and an antenna height of 5 m, the distance antenna – specular point will be about 4 m, while, if we change the antenna height to 400 km, the distance will be about 300 km away from the antenna. In that case the receiver will be a waveform receiver due to the strong increase of the multipath frequency. Considering an antenna height of 50 m and a satellite elevation close to 80°, the first Fresnel surface associated to the specular point will be close to 30 m<sup>2</sup>, and it will be more than 200 km<sup>2</sup> if the satellite elevation is around 10 degrees. Thus, higher antenna increased the area covered but the 1<sup>st</sup> Fresnel surface.

Therefore, assessed the potential of GNSS-R for altimetry in coastal

environments, and particularly the GNSS system with a single antenna at the GNSS tide gauge stations. In the framework of my thesis, I was mainly interested in this promising technique to estimate sea surface height and detect the tide and the extreme events from the GNSS-R signals using Singular Spectrum Analysis (SSA) and Continuous Wavelet Transform (CWT) algorithms. We have also used SSA algorithm for recover missing data in non-periodic time series.

This chapter presented two experiments: the result of the Socoa experiment which are the subject of an article currently under revision in Remote Sensing and the result of the Mekong River and Red River experiment which was presented in the IGARSS international conference July 22-27, 2018 at Valencia, Spain. This article on the Socoa is inserted in § IV.9. This chapter is therefore divided into five main parts which will be a synthesis of the main points of this article. The first part is a brief overview of the state of the art, already discussed in § II.2 of the chapter II. The second part presents the method I used to reverse the measurements of SNR to estimate sea level variations, the SSA and CWT methods to detect the tide and the extreme events from GNSS R signals. The third part presents the application of this approach on the GNSS station from RGP located in the Socoa acquired during 3 months (from January to March, 2010). During this period, the Xynthia storm hit the French Atlantic coast the 28<sup>th</sup> of February 2010, causing large floods from the Gironde to the Loire estuaries and around 50 casualties. The datasets used to validate, characteristics of the Socoa study area and some of main results will be described in the third section. For more details, please refer to the article itself. The fourth and fifth part present the Mekong River and the Red River Delta experiments, respectively, two experiments achieved in the framework of the MISTRAL H2020 project and a funding from the University of Toulouse (ATUPS 2016). The Mekong River experiment, achieved between 23<sup>th</sup> and 31<sup>th</sup> August 2016, is located close to the mouth of the Mekong River where continental water interacts with oceanic water. The antenna/GNSS receiver was installed on the top of

## **Chapter IV. GNSS Reflectometry for detection of tide and extreme hydrological events: example of the Socoa (France), Mekong delta and Red River Delta (Vietnam)**

---

Tran De water tower, Soctrang province, Vietnam. The Red River Delta experiment, from 27<sup>th</sup> July to 12<sup>th</sup> August 2016, during the period of the Mirinae and Nida storms, we installed the antenna/GNSS receiver couple of the Red river (21° 2'44.04"N, 105°51'48.86"E) to identify flood events and morphological changes associated to these hydrological events.

### **IV.3 State of the art**

As explained in § II.4.3 of chapter II, the direct and reflected signals interfere with the antenna. This interference is particularly visible in the SNR measured by the antenna. The quasi-sinusoidal aspect of the SNR time series consists of a low frequency due to the direct signal, and a high frequency due to the reflected signal, which is noted as  $SNR_m$  (in § II.4.3.3 of chapter II).

In these sections, I will explain that the direct and reflected waves interact at the antenna level and give constructive interferences which are particularly visible in the SNR time series. It is possible to isolate the contribution of the reflected signal (noted as  $SNR_m$ ) by correcting the dominant parabolic component, due to the direct signal, to correct this parabolic component we used a polynomial function (see § II.4.1). The high frequency  $\tilde{f}$  of the SNR oscillations due to the multi-path ( $SNR_m$ ) as a function of the sinus of the elevation angle is expressed in (Eq. II.33). The measurement and subsequent inversion of this frequency " $\tilde{f}$ " therefore makes it possible to deduce the variations in distance between the antenna and the reflecting surface.

Most of the studies conducted so far have been carried out under such conditions that  $\dot{h}$  could be neglected. For example, Löfgren and Haas (Löfgren and Haas, 2014) compared the water level estimates obtained by SNR analysis or phase, the variations in antenna height were in the order of a few tens centimeters maximum during 3 days of observations, and  $\dot{h}$  was therefore negligible of a moment to another. However, in very many cases, this assumption is not valid, in waves whose significant height

correspond to a significant value of  $\dot{h}$ .

Some proposals have been made to take into account. (Löfgren and Haas, 2014) suggested for example to do two iterations: the first approximate  $h(t)$  neglecting  $\dot{h}(t)$ , and the second iteration incorporates an estimate of  $\dot{h}(t)$  based on a theoretical sinusoidal function adjusted to the  $h(t)$  values from the first iteration. The underlying idea is that, during a day, the change in water level is mainly due to diurnal and semi-diurnal tides, of known frequencies, and therefore a theoretical sinusoidal function can be predicted. This two-step method improves the accuracy of the results but requires prior knowledge of the phenomena that may influence the antenna height in the study area. In 2013, Larson and Nievinski proposed a similar method, also based on two iterations (Larson and Nievinski, 2013). The first iteration determines an approximate value of  $h(t)$  by neglecting  $\dot{h}(t)$ . Thus, the time series obtained is derived to calculate the time series  $\dot{h}(t)$ . The second iteration will incorporate these values of  $\dot{h}(t)$  to determine more accurate values of  $h(t)$ . Unfortunately, this method only works for small values of  $\dot{h}$  and cannot be used on measurement sites with high waves. In 2015, Roussel et al proposed another method in dynamic case, allowing to determine simultaneously  $h$  and  $\dot{h}$  (Roussel et al., 2015b). This method have been tested *in-situ* under extreme conditions where  $\dot{h}$  cannot be neglected.

In this chapter, I have tested the method in three experiments. The first one is located in a complex environment located in Socoa, in the south of the Bay of Biscay, Basque Country. We used 3 months of records (January-March 2010) from a acquired by a GNSS geodetic station from the GNSS permanent network (RGP for Réseau GNSS Permanent), deployed by the French Geographic Institute (IGN for Institut de l'Information Géographique et Forestière), located in Socoa, in the south of the Bay of Biscay, Basque Country, to determine the SSH variations. In particular, we used SSA and CWT analysis methods to extract tidal information and detect the Xynthia storm as well as recover missing data. The second and third experiments, I have applied Larson

and Roussel methods to obtain SSH from SNR multipath on two cases located in Vietnam (Mekong River experiment and Red River Delta experiment). For the Mekong River experiment, during 23<sup>th</sup>-31<sup>th</sup> August 2016, we installed the antenna/GNSS receiver close to the mouth of the Mekong River (9°31'38.63"N, 106°12'2.01"E) where continental water interacts with oceanic water. For the Red River experiment, is located a couple of the Red River Delta (21°2'44.04"N, 105°51'48.86"E) to identify flood events and morphological changes associated to these hydrological events. This measurements was done since the 27<sup>th</sup> July until 12<sup>th</sup> August 2016, during the period of the Mirinae and Nida storms.

## **IV.4 Methodology**

### **IV.4.1 Sea surface height (SSH) derived from GNSS-R signals**

In order to estimate SSH derived from GNSS-R signals, our method is based on the determination of the time series  $\tilde{f}(t)$  of the frequency of oscillations due to the multipath. By combining the time series  $\tilde{f}_i(t)$  measured for each satellite  $i$  visible simultaneously, it is possible to construct an over-determined linear equation system based on Eq. II.33 for a time period  $\delta t$ , with only two unknowns:  $h$  and  $\dot{h}$ . Such a system of equations can be solved by applying material formalism based on the least squares criterion.

The main points of this method are presented in this section, and is composed of four main steps presented in a flow chart in the Fig. IV.3.

#### **IV.4.1.1 Deleting the contribution of the direct signal**

As explained in § II.4.3, the direct signal dominates the reflected signal, and corresponds to the low main frequency of  $SNR(t)$ , while the reflected signal causes low amplitude but high frequency disturbances. To isolate these high frequencies  $\tilde{f}$  from multipath oscillations, the contribution of the direct signal to the SNR must first be removed to obtain the  $SNR_m$

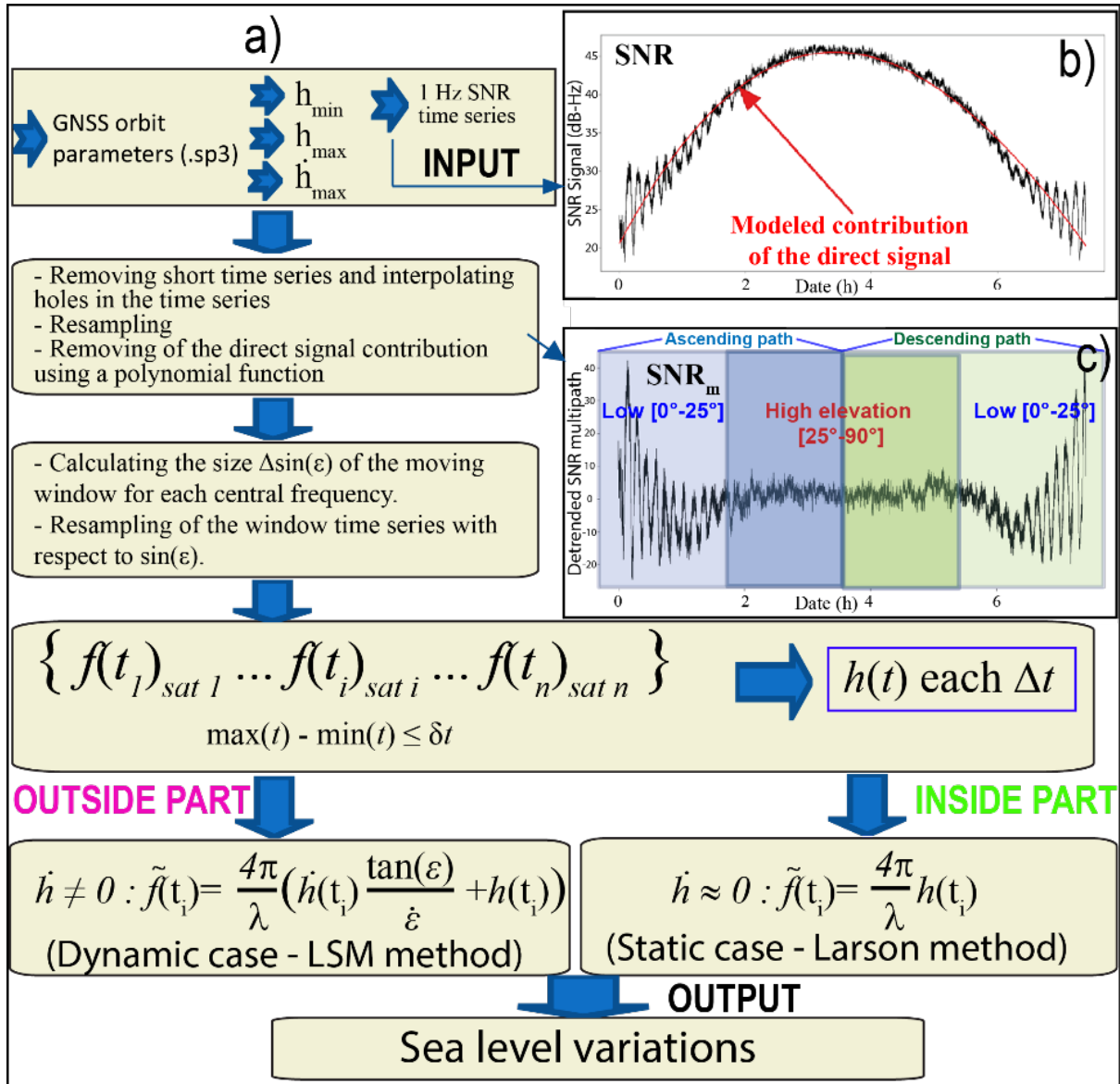


Figure IV.3 – a) Processing flow chart of the data presenting the successive steps of the processing of SNR data to sea level variation time series: the input, the different steps of the processing, and the output; b) Example of raw SNR data time series (input); c) Example of SNR detrended data time-series with ascending part and descending part.

residue. To do this, (Bilich, 2006) proposes a theoretical modelling of the direct signal and subtracting the modelled values from the time series  $SNR(t)$ . This method requires precise knowledge of the gain diagrams of the transmitter and receiver antenna, and since this information is complicated to obtain, other correction methods have been proposed. Larson et al. (2008) simply propose to subtract a low degree polynomial adjusted to the time series of the SNR (order 2 or 3). This method gives better results than the modelling method, and it is easier to implement. This is currently the method used in most studies on the subject.

Moreover, to eliminate the parabolic effects of the direct signal on the SNR records, we used a low-order polynomial fit as proposed by (Larson et al., 2010), the SNR multipath residuals  $SNR_m$  are used to compute the height of the water level (see Eq. IV.1):

$$SNR_m = \cos\left(\frac{4\pi h}{\Lambda} \sin(\varepsilon) + \psi_m\right) \quad (\text{IV.1})$$

where  $A$  is the amplitude and  $\psi_m$  is the phase offset.

#### IV.4.1.2 Discretization of the time series $SNR_m(t)$

The aim is to measure  $\tilde{f}(t)$ , the frequency of the oscillations of  $SNR_m$ , in order to deduce the variations of the antenna height  $h(t)$  based on Eq. II.33. The frequency  $\tilde{f}$  is not stationary, a moving window of the time series  $SNR_m(\sin(\theta))$  is necessary to determine its variations over time intervals. The choice of the length of the moving window is a critical parameter because it must meet contradictory requirements. The window must be large enough to accurately identify the fundamental frequency of the oscillations, but it must not be too wide for frequency variations to be almost constant over the time portion considered. Let  $\Delta(\sin(\theta))$  be the size of the moving window. To find the suited size  $\Delta(\sin(\theta))$  around each central value, it is necessary to have an estimate of the variations that  $SNR_m$  is likely to observe at any time. The method described by the flow chart in Fig. IV.3 was applied considering the following three parameters

as known by the user:

- $h_{min}(m)$ : the minimum height above the reflecting surface of the receiver during the measurement period.
- $h_{max}(m)$ : the maximum height above the reflecting surface of the receiver during the measurement period.
- $\dot{h}_{min}(m/s)$ : the absolute maximum vertical velocity of the reflecting surface.

The more precisely these values are known, the faster the determination of  $\tilde{f}$ . With the knowledge of these parameters, it is possible to calculate the minimum frequency  $\tilde{f}(min)$  and maximum frequency  $\tilde{f}(max)$  that can be observed at any given time, using Eq. II.33. The size of the moving window  $\Delta(\sin(\theta))$  will then be chosen based on the following two conditions:

$$\Delta(\sin(\theta)) \leq \frac{\rho \tilde{f}_{min}}{\Delta \tilde{f}_{max}} \quad (\text{IV.2})$$

$$\Delta(\sin(\theta)) > \frac{N_0}{\tilde{f}_{min}} \quad (\text{IV.3})$$

with  $\rho$  (in %) the maximum variations of  $\tilde{f}$  that is tolerated in the window and  $N_0$  is the minimum number of periods that one wishes to keep in the moving window for adjustment.  $\Delta \tilde{f}_{max}$  is the maximum variation of the frequency and it is obtained in the following way.

$$\Delta \tilde{f}_{max} = \left| \frac{2}{\lambda \dot{\theta} \cos(\theta)} \left( \dot{h}_{max} + \left| \frac{\dot{h}}{\cos^2(\theta)} \right| + \left| \frac{\dot{h} \ddot{\theta} \tan(\theta)}{\dot{\theta}^2} \right| \right) \right| \quad (\text{IV.4})$$

It is important to note that the size of the  $\Delta(\sin(\theta))$  window is not constant since each parameter on which it depends varies over time, so it will have to be re-estimated at each increment.

**IV.4.1.3 Determination of the frequency  $\tilde{f}$  of the multipath oscillations**

After the removal of the direct signal contribution using the polynomial approach defined by (Larson et al., 2008b), frequency  $\tilde{f}$  is estimated for each moving window using a Lomb Scargle periodogram (LSP):((Lomb, 1976; Scargle, 1982)). Knowing the fixed  $\tilde{f}_{min}$  and  $\tilde{f}_{max}$  values for each window, it is not necessary to consider the full frequency spectrum when calculating the LSP to determine the peak spectrum that corresponds to the main period in the window. I optimize in my thesis the duration of a session and the frequency of SNR acquisition for altimetry applications.

**IV.4.1.4 Determination of the height  $h$  of the antenna with respect to the reflection surface**

Once  $\tilde{f}(t)$  is determined for each satellite in view,  $h(t)$  is obtained by solving Eq. II.33 combine the measurements made by all GNSS satellites in view at a given moment, I used Least Square Method (LSM), called Roussel method, to simultaneously determine  $h$  and  $\dot{h}$  (Fig. IV.4). So, if we consider  $U = \frac{4\pi \tan(\theta)}{\lambda \dot{\theta}}$  and  $V = \frac{4\pi}{\lambda}$ , Eq. II.33 for a satellite  $i$  at a moment  $t$  is linear for  $h$  and  $\dot{h}$ :

$$\tilde{f}_i(t) = U_i \dot{h}(t) + V_i h(t) \quad (IV.5)$$

By combining all the satellites visible at time  $t$ , we obtain a linear system of equations:

$$\begin{pmatrix} \tilde{f}_1(t) = U_1 \dot{h}(t) + V_1 h(t) \\ \tilde{f}_2(t) = U_2 \dot{h}(t) + V_2 h(t) \\ \tilde{f}_3(t) = U_3 \dot{h}(t) + V_3 h(t) \\ \dots \end{pmatrix} \quad (IV.6)$$

or in matrix form:

$$\tilde{F} = U \dot{h}(t) + V h(t) = AX \quad (IV.7)$$

With the configuration matrix  $A = (UV)$ , and the vector containing the unknowns  $X = \begin{pmatrix} \dot{h}(t) \\ h(t) \end{pmatrix}$ . The least square solution can be expressed as:

$$X = (A^t A)^{-1} (A^t \tilde{F}) \tag{IV.8}$$

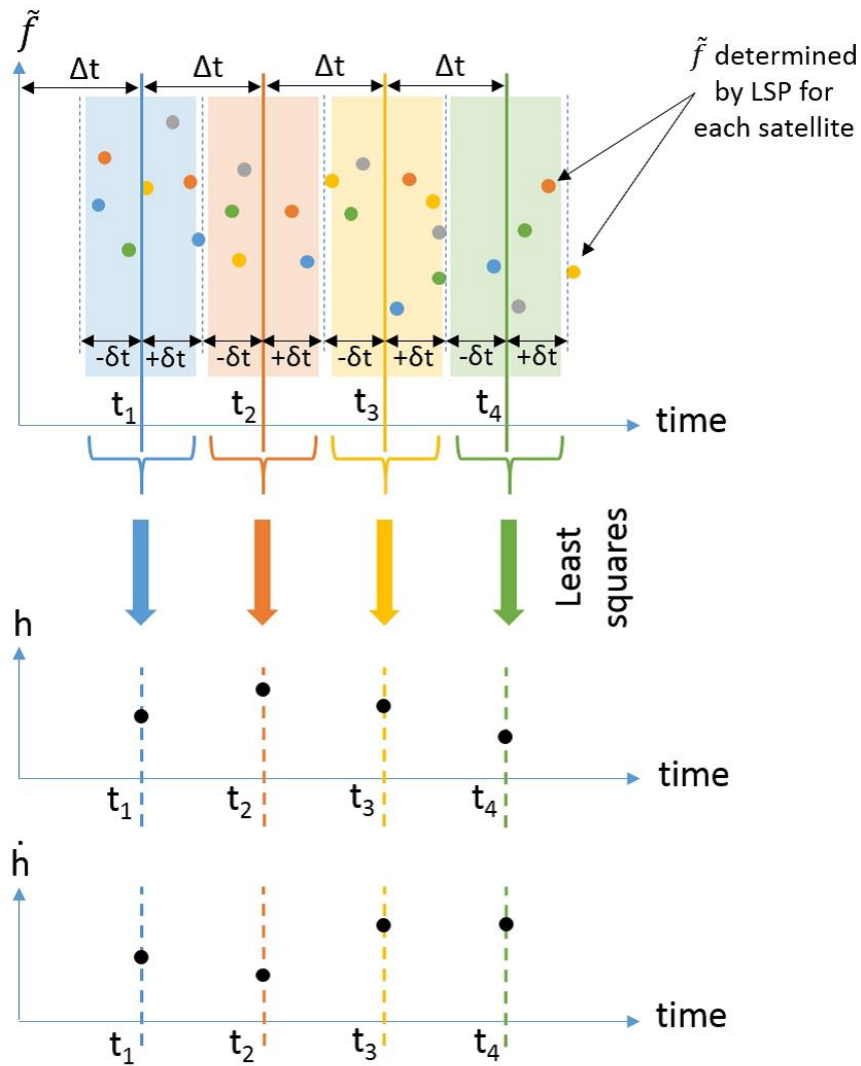


Figure IV.4 – Principle of the Least Squares inversion Method used to determine  $h$  and  $\dot{h}$  based on LSP estimates of  $f$ . For reasons of clarity, overlapping was not represented in this figure, even if in our case  $\delta t > \Delta t$ .

As shown in Fig. IV.4, there is an increment  $\Delta t$  between each estimate

## **Chapter IV. GNSS Reflectometry for detection of tide and extreme hydrological events: example of the Socoa (France), Mekong delta and Red River Delta (Vietnam)**

---

of  $h$  and a length of the moving window  $\delta t$ . The value  $\Delta t$  is chosen small as possible to have the best temporal resolution. Low value of  $\Delta t$  will simply cause oversampling. On the other hand, a value  $t$  must be chosen carefully. It must be as small as possible, in order to ensure the stability of  $h$  during the measurement time window, but it is also necessary to have sufficient observables/satellites (at least 2) in the equation system.

### **IV.4.2 Analysis of the GNSS-R-based SSH using SSA and CWT methods**

Singular spectrum analysis (SSA) is a technique of time series analysis by decomposing the original series into a sum of a small number of interpretable components such as trend, oscillatory components and noise ((Broomhead and King, 1986; Vautard et al., 1992)). It is based on the singular value decomposition of a specific matrix constructed upon the time series where an observed time series is unfolded into the column vectors of a Hankel structured matrix, known as a trajectory matrix. SSA is useful to model time series with complex cyclical patterns that increase over time. The SSA method is a powerful non-parametric technique to retrieve, without preconceived ideas, the main periodic signals.

The Continuous Wavelet Transform (CWT) is used to decompose a signal into wavelet coefficient. Wavelets are small oscillations that are highly localized in time. While the Fourier Transform decomposes a signal into infinite length sines and cosines, effectively losing all time-localization information, the CWT's basis functions are scaled and shifted versions of the time-localized mother wavelet. The CWT is used to construct a time-frequency representation of a signal that offers very good time and frequency localization. But the resulting wavelet coefficient map is more complex to analyse. For that reason we have decide to combine SSA and CWT analysis. These methods optimize the study of complex signals like the SSH time series derived from GNSS-R signals and they have enhanced the detection of secondary signals of weak amplitude, like the effect of

atmospheric pressure, generally blind by the main components of the tide.

#### IV.4.2.1 SSA method

SSA is based on the Principal Component Analysis (PCA) methods (Jolliffe, 1986), which the original data time series can be transformed into a feature time series by using a linear transformation (Vautard et al., 1992; Elsner and Tsonis., 1996; Allen and Smith, 1997; Ghil et al., 2001). The process consist of two main steps, which are summarized below:

- *Decomposition of the time series:* The decomposition takes a time series  $F = (f_0, \dots, f_{N-1})$ ,  $f_n \in \mathbb{R}$  of length  $N$  and comes up with an  $(M \times K)$  matrix. Parameter  $M$  ( $1 < M < N$ ) called the window length, and constructing the called trajectory matrix  $\mathbf{X} \in \mathbb{R}^{(M \times K)}$ ,  $K=N-M+1$ , taken portions of the original time series  $F$  as columns Ghil et al. (2001):  $F = (f_0, \dots, f_{N-1}) \rightarrow \mathbf{X} = [X_1 : \dots : X_k]$ ,  $X_j = (f_{j-1}, \dots, f_{j+M-2})^T$  The Singular Value Decomposition (SVD) of the  $\mathbf{X}$  matrix is applied, where  $j$ -th component of SVD is defined by the eigenvalues ( $\lambda_j$ ) and eigenvectors ( $U_j$ ) of the matrix  $\mathbf{X}\mathbf{X}^T$ :

$\mathbf{X} = \sum_{j=1}^d \sqrt{\lambda_j} U_j V_j^T$ ,  $V_j = \mathbf{X}^T U_j / \sqrt{\lambda_j}$ ,  $d = \max\{j: \lambda_j > 0\}$  The eigenvectors correspond to the Empirical Orthogonal Function (EOF) in SSA method, with the associated eigenvalues. The parameters  $(\sqrt{\lambda_j}, U_j, V_j)$  is  $j$ -th eigentriple, where  $\sqrt{\lambda_j}$  is the  $j$ -th singular value,  $U_j$  is the  $j$ -th left singular vector and  $V_j$  is the  $j$ -th right singular vector.

- *Reconstruction of the time series:* Reconstruction  $(M \times K)$  matrix of length  $N$  from the selected  $j$  components ( $j \subset \{1, \dots, M\}$ ) of the SVD. The result of the reconstruction stage is a time series additive component:

$X_j = \sum_{j \in J} \sqrt{\lambda_j} U_j V_j^T \rightarrow G = (g_0, \dots, g_{N-1})$  The subsequent reconstruction of a time series component ( $G$ ) as being applied to a matrix  $\mathbf{Y} = \{y_{ij}\}_{i=1}^M, j=1}^K$  (see details in (Golyandina et al., 2001)). Then

**Chapter IV. GNSS Reflectometry for detection of tide and extreme hydrological events: example of the Socoa (France), Mekong delta and Red River Delta (Vietnam)**

---

the elements of the time series  $G = (g_0, \dots, g_{N-1})$  calculated from the matrix  $\mathbf{Y}$  by averaging along cross-diagonals of matrix  $\mathbf{Y}^*$  as Eq. IV.9:

$$g_n = \begin{cases} \frac{1}{n+1} \sum_{m=1}^{n+1} y_{m,n-m+2}^* & 0 \leq n < M^* - 1, \\ \frac{1}{M^*} \sum_{m=1}^{M^*} y_{m,n-m+2}^* & M^* - 1 \leq n < K^*, \\ \frac{1}{N-n} \sum_{m=n-K^*+2}^{N-K^*+1} y_{m,n-m+2}^* & K^* \leq n < N \end{cases} \quad (\text{IV.9})$$

where  $M^* = \min\{M, K\}$ ,  $K^* = \max\{M, K\}$ ;  $\mathbf{Y}^* = \mathbf{Y}^T$  if  $M > K$ ;  $\mathbf{Y}^* = \mathbf{Y}$  if  $M \leq K$ .

**IV.4.2.2 Recover missing SSH derived from GNSS R data using SSA method**

Another interesting point of SSA is its possibility to reconstruct discontinuities and/or gaps in signal due to large storm effects, for example interruption of the electricity network. This section introduces the method of recovering missing data in a non-periodic time series using the SSA algorithm. In this algorithm, the data before and after the missing values are treated as two inseparable time series. SSA reconstructs missing data by using an iteratively inferred, smooth “signal” that captures coherent modes and removes the noise components. In this study, we have tested two cases of missing data in SSH time series. In the first case, assuming that the SSH based on GNSS-R signals from 22<sup>th</sup> February to 08<sup>th</sup> March missing 2 consecutive days of data (14.28%) during the storm. The time series is then recovered using the SSA method with different window size  $M$  of 2h, 6h, 12h, 24h, 48h, 72h and 96h, respectively (in Fig. IV.5). The test results (in Tab. IV.1) demonstrate that the accuracy of data recovery depends on the window size  $M$ . The larger the window size uses, the more accurate are the recovery data. The best results with highest correlation = 0.97 and smallest RMSE = 0.42 m, are obtained with for time window  $M = 96\text{h}$ .

In the second case, the size of the window  $M$  is fixed of 96h and the missing data increase from 1 day (7.14%), 2 days (14.28%), 3 days (21.42%), 4

TABLE IV.1 – Comparison of bias, RMSE and the correlation coefficient (R) between 2 days recovered data and *in-situ* tide gauge at the same period

| Window size M (h) | Bias (m) | RMSE (m) | R    |
|-------------------|----------|----------|------|
| 2                 | ----     | ----     | ---- |
| 6                 | -0.16    | 0.7      | 0.22 |
| 12                | -0.15    | 0.67     | 0.41 |
| 24                | -0.14    | 0.6      | 0.71 |
| 48                | -0.19    | 0.53     | 0.89 |
| 72                | -0.23    | 0.48     | 0.95 |
| 96                | -0.23    | 0.42     | 0.97 |

days (28.57%), 5 days (35.71%) and 6 days (42.86%), respectively (in Fig. IV.6). The results show that the lost data can be recovered but the accuracy is reduced (in Tab. IV.2). For the time series of 1 day removed values and a window size M of 96h, the recovery time series becomes almost stable is not any more affected by the number of removed values (RMSE of 0.28 m and R reach 0.99). However, the problem is more difficult in real time series because the irregularity can have in the data. The recovery of missing data in SSH time series is challenging if the missing data is more than 28.57%. Therefore, the accuracy of data recovery depends on the ratio between the sizes M and the number of consecutive missing data.

For the cases whose missing data are between 7% to 43% over the whole time series, the reconstructed component of the time series is calculated only when the percentage of missing data in the window size is less than 50%. In Tab. IV.2, we demonstrate the RMSEs and correlation of each experiment of different percentages of missing data. Obviously, if there are no missing data, the sum of first two RCs coincides with *in-situ* tide time series. If the percentage of missing data increases, the RMSE will become larger and the amplitude of the tide is quite difficult to recover even if the frequency is well defined. Even when the percentage of missing

**Chapter IV. GNSS Reflectometry for detection of tide and extreme hydrological events: example of the Socoa (France), Mekong delta and Red River Delta (Vietnam)**

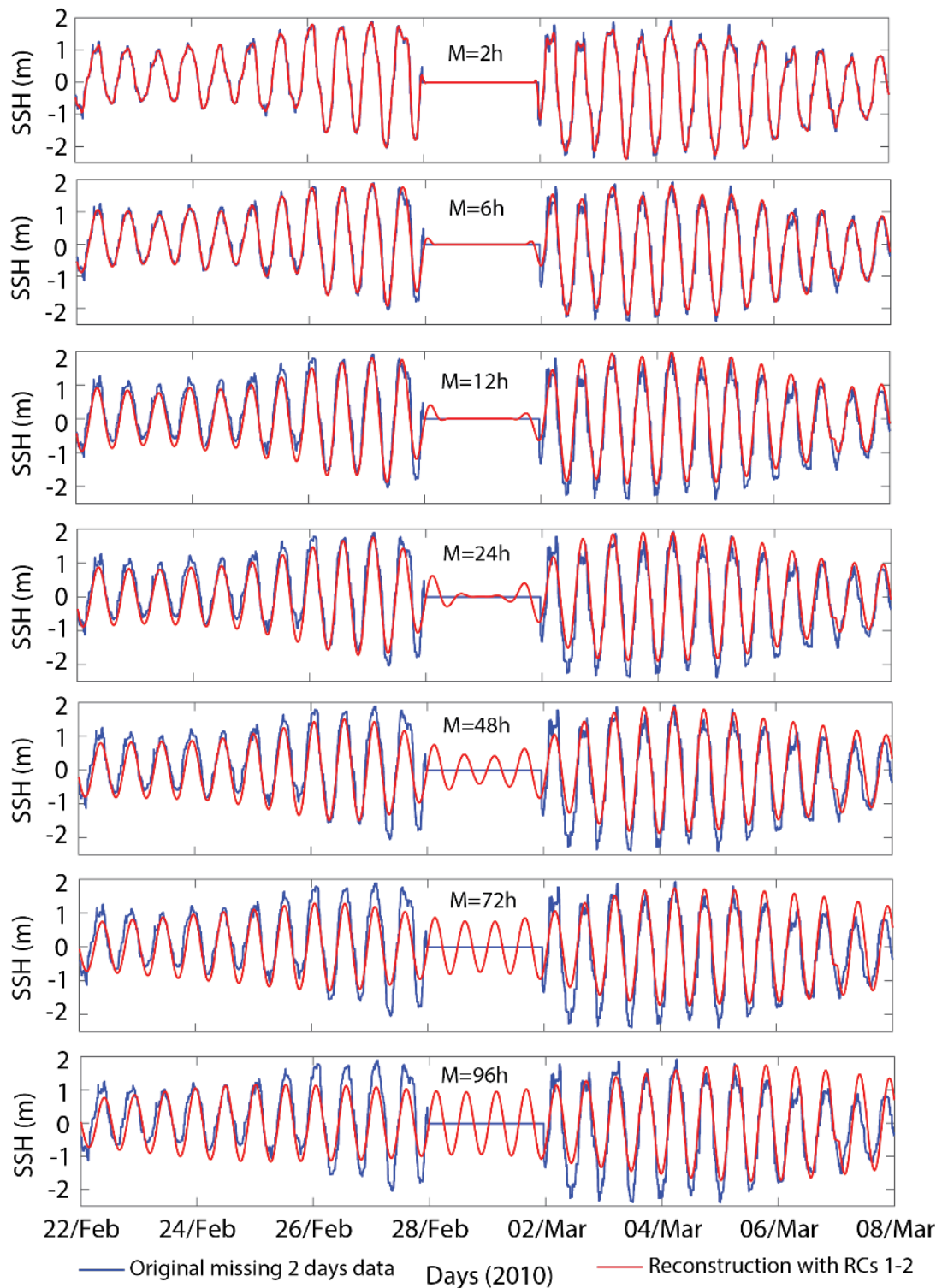


Figure IV.5 – Time series  $SSH_{GNSS}$  original lost two days of data during the storm and RCs using SSA method to reconstruct the tide components from 22<sup>th</sup> February to 08<sup>th</sup> March with the window size  $M$  of 2h, 6h, 12h, 24h, 48h, 72h and 96h, respectively.

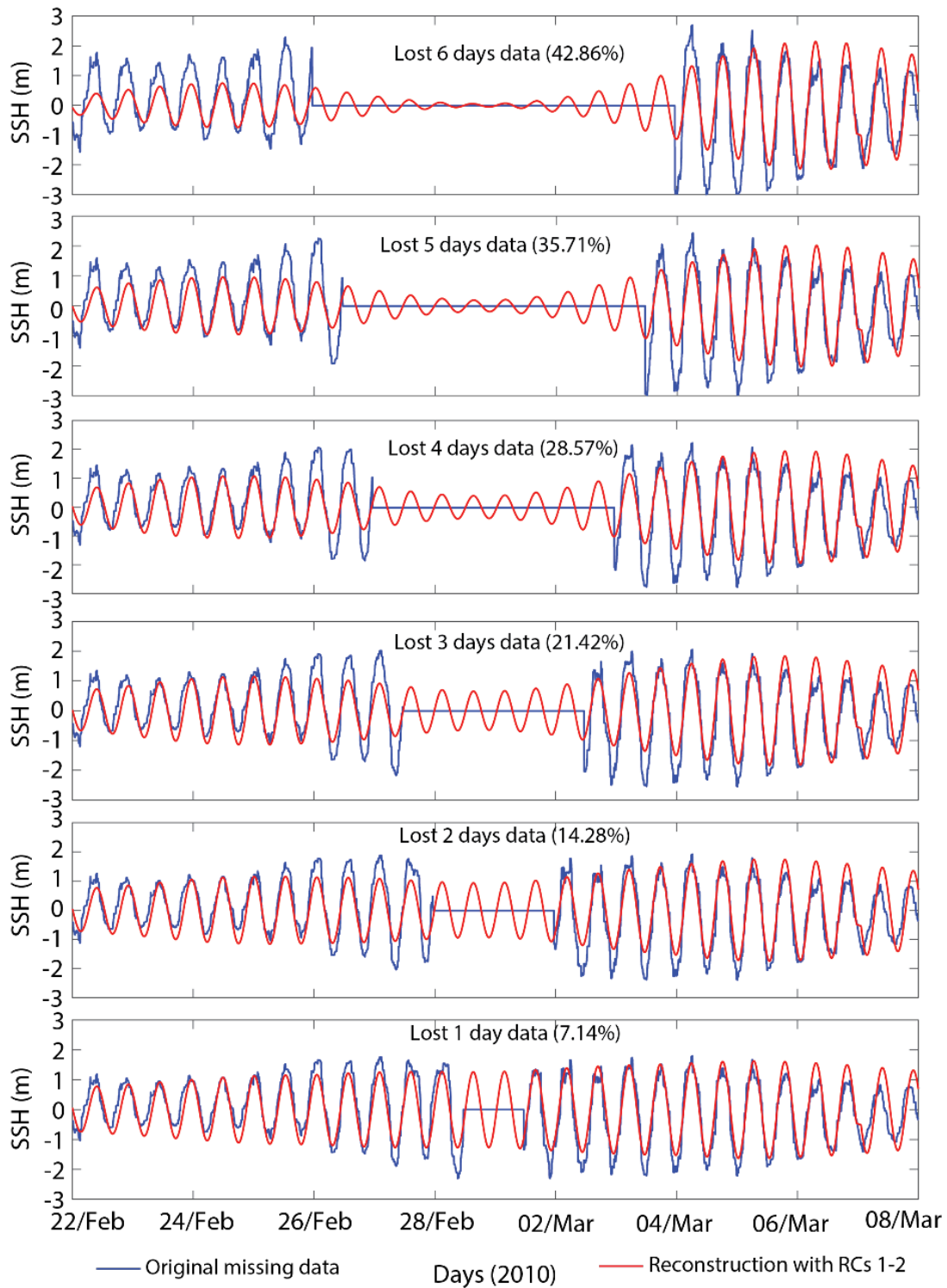


Figure IV.6 – Time series  $SSH_{GNSS}$  original from 22<sup>th</sup> February to 08<sup>th</sup> March lost 6 days, 5 days, 4 days, 3 days, 2 days and 1 day of data, respectively, and RCs using SSA method to reconstruct the tide components with the window size  $M$  of 96h.

**Chapter IV. GNSS Reflectometry for detection of tide and extreme hydrological events: example of the Socoa (France), Mekong delta and Red River Delta (Vietnam)**

TABLE IV.2 – Comparison of bias, RMSE and the correlation coefficient (R) between recovered data with the window size M of 96h and *in-situ* tide gauge at the same period

| Percentage of missing data (%) | Bias (m) | RMSE (m) | R    |
|--------------------------------|----------|----------|------|
| 7.14                           | -0.22    | 0.28     | 0.99 |
| 14.28                          | -0.23    | 0.42     | 0.97 |
| 21.42                          | -0.21    | 0.54     | 0.94 |
| 28.57                          | -0.2     | 0.61     | 0.84 |
| 35.71                          | -0.2     | 0.7      | 0.76 |
| 42.86                          | -0.21    | 0.77     | 0.69 |

data reaches 42.86%, the RMSE and correlation coefficient are 0.77 m and 0.69, respectively, but the tide amplitude is clearly underestimated. To conclude this technic is very interesting to reconstruct the missing data in terms of frequency but if the amplitude is a key parameter is a possible study the SSA cannot give good result even for short period of missing data.

**IV.4.2.3 CWT method**

A CWT is a function with zero mean and localized in frequency and time. The wavelet transform can be used to evaluate the existence and strength of line coupling between two signals in the many different frequencies (Gaillet et al., 1999; Grinsted et al., 2004; Garg et al., 2013). There are two types of wavelet transforms: the Continuous Wavelet Transform (CWT) and Discrete Wavelet Transform (DWT). Alternatively, the original time series can be reconstructed using CWT based on the inverse filter (Prokoph and Patterson, 2004). The reconstructed time series is the sum of the real part of the wavelet transform on all scales (Torrence and Compo, 1998):

$$x_n = \frac{\delta_j \delta_t^{1/2}}{C_\delta \psi_0(0)} \sum_{j=0}^J \frac{\Re\{W_n(S_j)\}}{S_j^{1/2}} \quad (\text{IV.10})$$

where  $\Re\{W_n(S_j)\}$  is the real part,  $J$  determines the largest scale, the factor  $\psi_0(0)$  is the wavelet function removes the energy scaling,  $S_j^{1/2}$  converts the wavelet transform to an energy density. The factor  $C_\delta$  comes from the reconstruction of a  $\delta$  function from its wavelet transform using the function  $\psi_0(\eta)$ . To derive  $C_\delta$  for a new wavelet function, assume a time series with a  $\delta$  function  $n = 0$ , given by  $x_n = \delta_{n0}$ . The construction in Eq. IV.10 then gives:

$$C_\delta = \frac{\delta_j \delta_t^{1/2}}{\psi_0(0)} \sum_{j=0}^J \frac{\Re\{W_n(S_j)\}}{S_j^{1/2}} \quad (\text{IV.11})$$

The  $C_\delta$  is a constant for each wavelet function.

## IV.5 The Socoa experiment

### IV.5.1 Characteristics of the Socoa study area

Saint Jean de Luz Bay is located in the east of the Bay of Biscay, along the French Atlantic coast, a few kilometers away from the Spain border (Fig. IV.7a). For several centuries, this place has been heavily affected by the strong storms and it was regularly flooded. In the middle of the 19<sup>th</sup> century, in order to protect the area from the ocean's tides, a breakwater was constructed. The study area divided into two parts separated by seawalls (the inside part and the outside part). The mean significant wave height in the outside part is 1.6 m and maximum wave height is 2.5 m (Abadie et al., 2005; Delpy et al., 2014).

The inside part of the bay is approximately 2 km long by 1 km wide. Thanks to the protection of the breakwaters, this part is almost unaffected by the coastal currents and waves (Platel, 2007), with a tidal range about 4.5 m at spring tides. The inside part receives freshwater inflows from two small rivers (Untxin and Nivelle rivers) (Fig. IV.7a). The study area is in a semi-diurnal macro-tidal environments well described in Pingree et al. (1986); New (1988).

## Chapter IV. GNSS Reflectometry for detection of tide and extreme hydrological events: example of the Socoa (France), Mekong delta and Red River Delta (Vietnam)

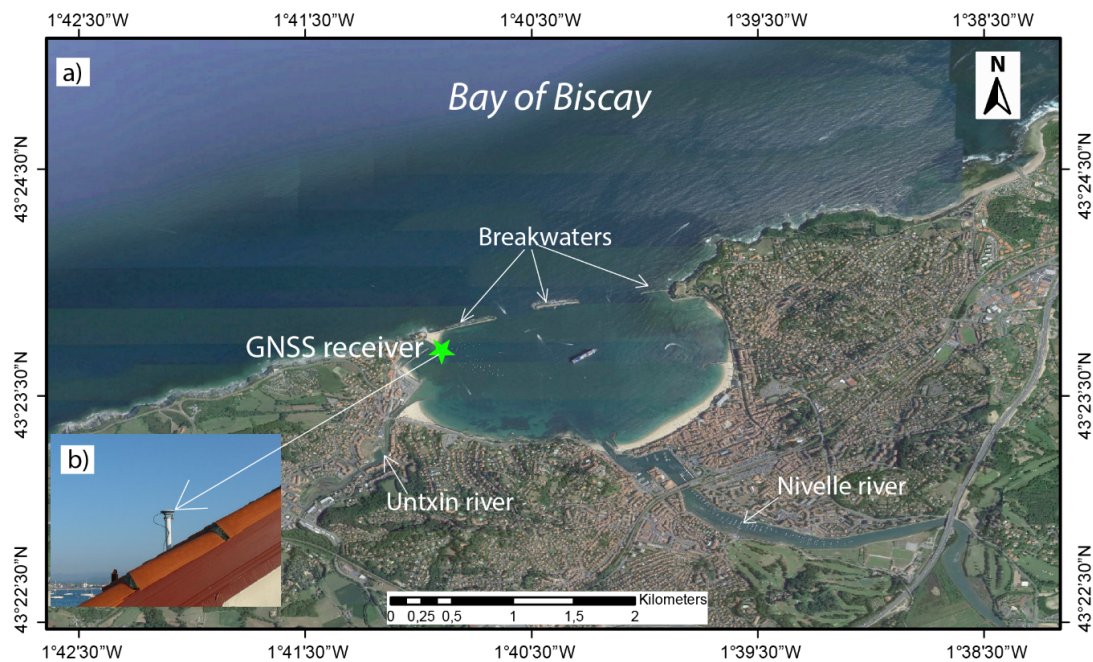


Figure IV.7 – a) Location of the GNSS receiver at the SCOA station ( $43^{\circ}23'42.83''\text{N}$ ,  $01^{\circ}40'54.05''\text{O}$ ); b) view of the antenna TRM55971.00 set up at 10.664 m above the sea surface (<http://rgp.ign.fr>).

### IV.5.2 Datasets

✓ The GNSS tide gauge data: The GNSS data from SCOA station are made available by Institut National de l'Information Géographique et Forestière (IGN). The GNSS data at the SCOA station were continuously from 2006 to present. At the SCOA GNSS station (Fig. IV.7b), consist of a Leica GR25 receiver and an antenna TRM55971.00 set up at 10.66 m above the sea surface, corresponds to the zero reference level of Marseille tide gauge (IGN1969). The data used were acquired at L1 frequency from GPS and GLONASS constellations operating at 1 sample per second. We proceeded the data acquired during 3 months from 01<sup>st</sup> January to 31<sup>th</sup> March 2010, before and after the storm Xynthia (between 27<sup>th</sup> February and 01<sup>st</sup> March 2010). The antenna height is constant and equal to 10.66 m during the entire acquisition period. In order to remove contamination of coastal topography on the reflection signals, an azimuth windows ranging from  $60^{\circ}$  to  $210^{\circ}$  was applied to estimate the SSH in the inside part of the

bay and an azimuth windows ranging from  $0^\circ$  to  $60^\circ$  and from  $330^\circ$  to  $360^\circ$  to estimate SSH in the outside part. Satellite elevation angles from  $1^\circ$  to  $25^\circ$  were considered to estimate SSH. The precise location of the specular reflection points on the reflecting surface and first Fresnel zone area was determined through direct modeling using GNSS Reflected Signals Simulations (GRSS) developed by Roussel et al. (Roussel et al., 2014). Figure IV.8 shows the locations of the specular reflection points corresponding to the location of the SCOA GNSS station on 1<sup>st</sup> March 2010 for both GPS and GLONASS satellites. In the inside part (green points), farthest reflection points are about 800 m for satellite elevations above  $1^\circ$ , and 15 m for satellite elevations of 25. For the outside part (violet points), the farthest reflection points are a bit more than 3.4 km away from the receiver for satellite elevations above  $0^\circ$ .

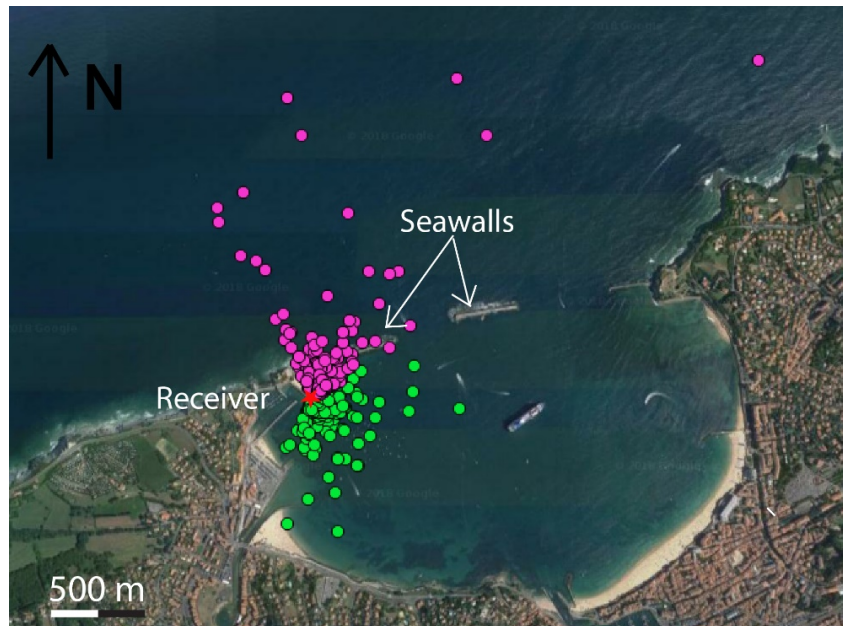


Figure IV.8 – Locations of the specular reflection points for the GNSS receiver installed at the SCOA station 1<sup>st</sup> March 2010. Only GPS and GLONASS satellites with elevation angles from  $0^\circ$  to  $25^\circ$  were considered for estimating SSH variations. Green points in the inside part, with azimuths from  $60^\circ$  to  $210^\circ$ . Pink points in the outside part, with azimuthal ranges  $0^\circ/60^\circ$  and  $330^\circ/360^\circ$ .

✓ *In-situ* tide gauge data: The SSH time series calculated from GNSS-R signals will be compared to the measurements recorded in the Socoa tide

**Chapter IV. GNSS Reflectometry for detection of tide and extreme hydrological events: example of the Socoa (France), Mekong delta and Red River Delta (Vietnam)**

---

gauge station from January to March 2010.

✓ Meteorological data (rainfall, wind speed and atmospheric pressure) measured at the temporal resolution of 1 hour between January and March 2010 at the Socoa station will be used to detect the Xynthia storm. They were made available by Infoclimat (<https://www.infoclimat.fr>). The atmospheric pressure was converted into inverted barometer effect ( $h_{atmos}$ ) using the following equation:

$$h_{atmos} = -\frac{P_{atm} - \bar{P}_{atm}}{\rho g} \quad (\text{IV.12})$$

where  $P_{atm}$  is the time varying mean of the global surface atmospheric pressure over the oceans;  $\rho = 1,020 \text{ gcm}^{-3}$  is density of seawater;  $g = 9,81 \text{ cms}^2$  is the mean acceleration of gravity (Wunsch and Stammer, 1997)

✓ Significant wave height (SWH) data over the study period were acquired by the directional wave buoy located ( $43^{\circ}31'56''\text{N}$ ;  $1^{\circ}36'54''\text{W}$ ).

### IV.5.3 SNR-based sea surface height variation estimates

In the inside part, the wave effect is reduced and in that case the vertical velocity of the moving surface is less than  $5 * 10^{-4} \text{ m/s}$  (threshold value define by (Larson et al., 2008b)), we used the same threshold value. When the velocity is upper than the threshold value we do not compute the height using Larson approximation (the static case is unusable) only the dynamic case is possible. The SNR-based SSH time series are computed using static SNR method (*i.e.* Larson method) in the inside part and the dynamic SNR method (*i.e.* Roussel method) in the outside part. The method described by the flow chart in Fig. IV.3, to determine  $h_{min}$  and  $h_{max}$  we choose to look the tide gauge database and we extract from this dataset the  $h_{min}$  and  $h_{max}$  during the highest tidal coefficient recorded, for security we include possible wave in the inside part more or less 1 m height. These value was set as inputs:  $h_{min} = 6.66 \text{ m}$ ,  $h_{max} = 14.66 \text{ m}$ , the height of the antenna above sea level being  $10.66 \text{ m}$  and  $\dot{h}_{max} = 5 * 10^{-4} \text{ m/s}$

as inputs. Comparison results between the  $SHH_{in-situ}$  and the  $SSH_{GNSS}$  time series (bias, root mean square RMSE and correlation coefficient R) are presented in Tab. IV.3a (inside part) and Tab. IV.3b (outside part). The time step of the moving window is defined at 5 min. But the tide gauge step is defined at 10 min so we resample the tide gauge data using least square method at 5 min to obtain coherent datasets. The  $SSH_{GNSS}$  time series calculated in three different cases, by considering separately: the GPS constellation/GLONASS constellation/ combined constellations.

TABLE IV.3 – Comparison between the  $SHH_{in-situ}$  gauges with the  $SSH_{GNSS}$  time series calculated with the GPS constellation/GLONASS constellation/combined constellations at the SCOA station from 01/01/2010 to 31/03/2010. (a) Outside part (dynamic case); (b) Inside part (static case).

|                         | N° of measures       | Bias (m)         | RMSE (m)       | R              |
|-------------------------|----------------------|------------------|----------------|----------------|
|                         | (GPS/GLO/both)       | (GPS/GLO/both)   | (GPS/GLO/both) | (GPS/GLO/both) |
| <b>(a) Inside part</b>  | 5 591/4 678/10 041   | 0.003/0.01/0.001 | 0.37/0.39/0.3  | 0.94/0.93/0.96 |
| <b>(b) Outside part</b> | 21 176/20 958/25 591 | 0.1/0.044/0.013  | 0.88/0.82/0.69 | 0.63/0.67/0.78 |

When considering either GPS or GLONASS constellation leads to a decrease of the correlation in the two part for the  $SSH_{GNSS}$  time series. Best results are obtained for inside part, the correlation coefficient reaches 0.96 for a RMSE of 0.3 m when using both satellite constellations. This shows that sea level based-on GNSS-R in case of unaffected by waves provides a reliable estimate of the tides. On the contrary, in the outside part, lower correlation coefficient is found when using both satellite constellations (R = 0.78). Although the number of SNR signals obtained in the outside part is higher than in the inside part (in Tab. IV.3) most of the reflection points are located in the open ocean, SNR signals in the outside part are influenced by waves. Moreover, in addition to the influence of components as tidal, the SNR signals in the outside part are also affected by noise. Although the elevation angle has been reduced ( $<25^\circ$ ), there is still some

reflection point located on the breakwater. The RMSE obtained in the outside part reach to 0.69 m when using both satellite constellations and is explained by the presence of waves that are detected by the SNR signals, but not by conventional tide gauges, which are equipped with dampers. Thanks to the seawalls, the inside part remains unaffected by the wave, GNSS-R SSH measured there by reflectometry is close to mean sea surface height measured by in-situ tide gauge.

#### **IV.5.4 Complementary between SSA and CWT method to extract the tides components in GNSS-R signals**

SSA was applied to decompose SSH time series in four RCs account for more than 95% of the explained variance. RC1 and RC2 accounted for 47.2% and 44.5% of the explained variance respectively, whereas RC3 and RC4 accounted for 2.7% and 1.0% respectively. We reconstruct the SSH time series using the first two RC modes and then evaluate the quality of reconstructed series by comparing with the in-situ tide gauge at the Socoa station. Similar, we have applied the wavelet analysis to analyze the time series SSH based on GNSS signals, which permits the identification of the main periodicities of tide in the time series. In order to extract the tide component in the GNSS-R signals, the SSH time series was reconstructed using the inverse continuous wavelet transform (iCWT).

The reconstruction of tide using SSA method and CWT method, the SSH based on GNSS signals were compared with the tide gauges records at Socoa station from January to March 2010 in terms of N (number of measurements), Bias, RMSE and R. Figure IV.9a present the comparison results for the SSH based on GNSS signals, sum of RC1 and RC2 using SSA method (Fig. IV.9b), the tide at period 12h using iCWT method (Fig. IV.9c) and Fig. IV.9d for the tide at period from 6h to 12h using iCWT method, respectively. The best results obtained from SSA method to reconstruct the tides with a bias of 0.003 m, RMSE of 0.16 m and R of 0.99. A good agreement observed from CWT method at 12h of period

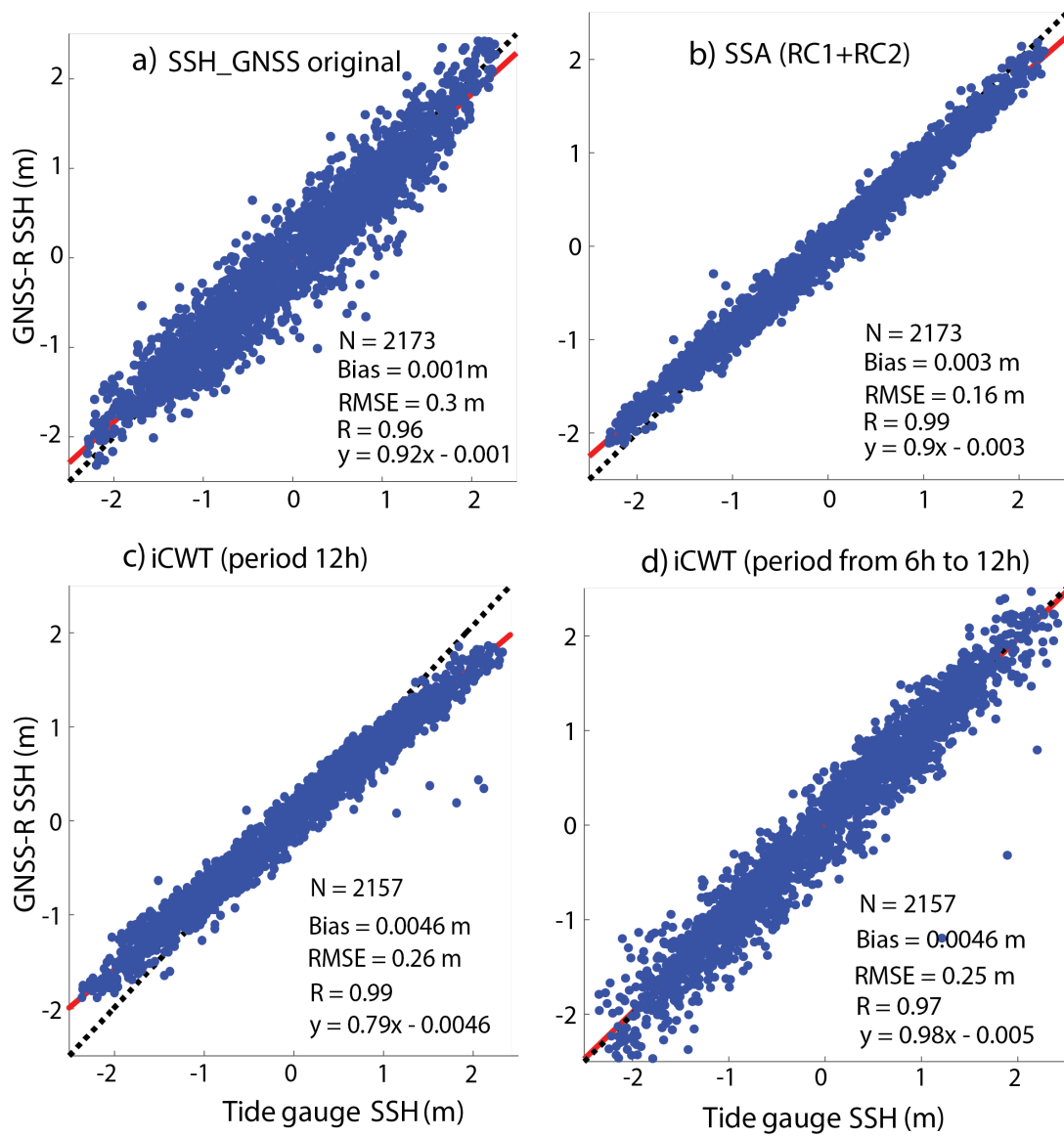


Figure IV.9 – Comparisons between in situ tide gauges and: a) SSH based GNSS data; b) sum of (RC1+RC2) using SSA method; c) inverse CWT at 12h frequency; d) inverse CWT from 6h to 12h frequencies.

and period from 6h to 12h. The results demonstrate that both of the SSA and CWT method reconstruct the tides similar to the tide gauge data.

#### **IV.5.5 Detection the Xynthia storm in the GNSS R signals using SSA and XWT method**

The Xynthia storm was an extraordinarily violent storm which hit in French from 26<sup>th</sup> February to 1<sup>st</sup> March, 2010. Although not directly affected to Socoa but it has caused strong winds and depression in the area. In order to detect the Xynthia storm, we used the RC3 component of the SSA method and XWT method. A surge is defined as the difference between observed and astronomical modeled tides at a specific location. This difference is due to meteorological phenomena like storms (Bode and A. Hardy, 1997; Olbert and Hartnett, 2010). The surge was identified by using T-Tide harmonic analysis software (Pawlowicz et al., 2002) as performed with the tide gauge records to separate the tide tides from the residual (in Fig. IV.10)

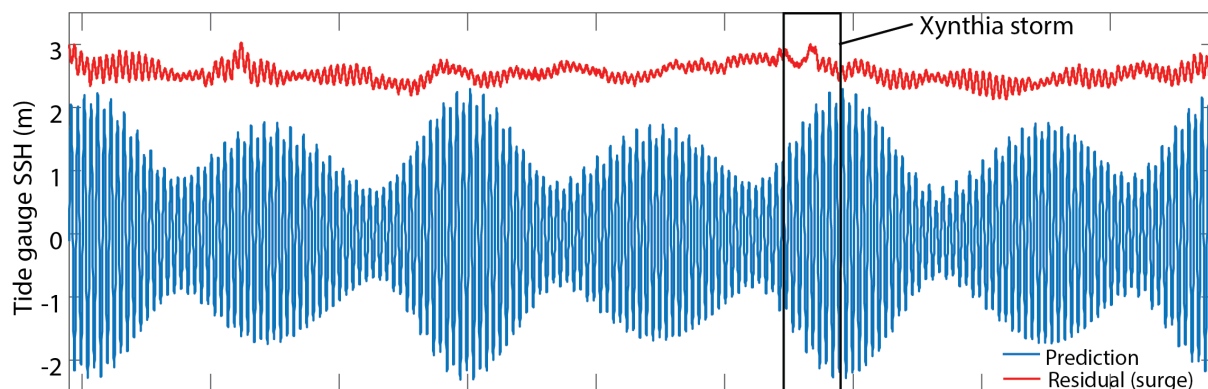


Figure IV.10 – Tide prediction time series (blue line) using T-Tide analysis Toolbox and residual (the surge) time series (red line) after removing of tidal signal for tide gauge data

Figure IV.11a and IV.11b show the time frequency maps of wavelet cross-correlation (XWT) and a liner correlation between RC3 and sum of the surge and  $h_{atmos}$  were performed. The combination of SSA and wavelet analysis (Fig. IV.11a) demonstrate a higher correlations were found over long time period. Very high correlations are observed between the two

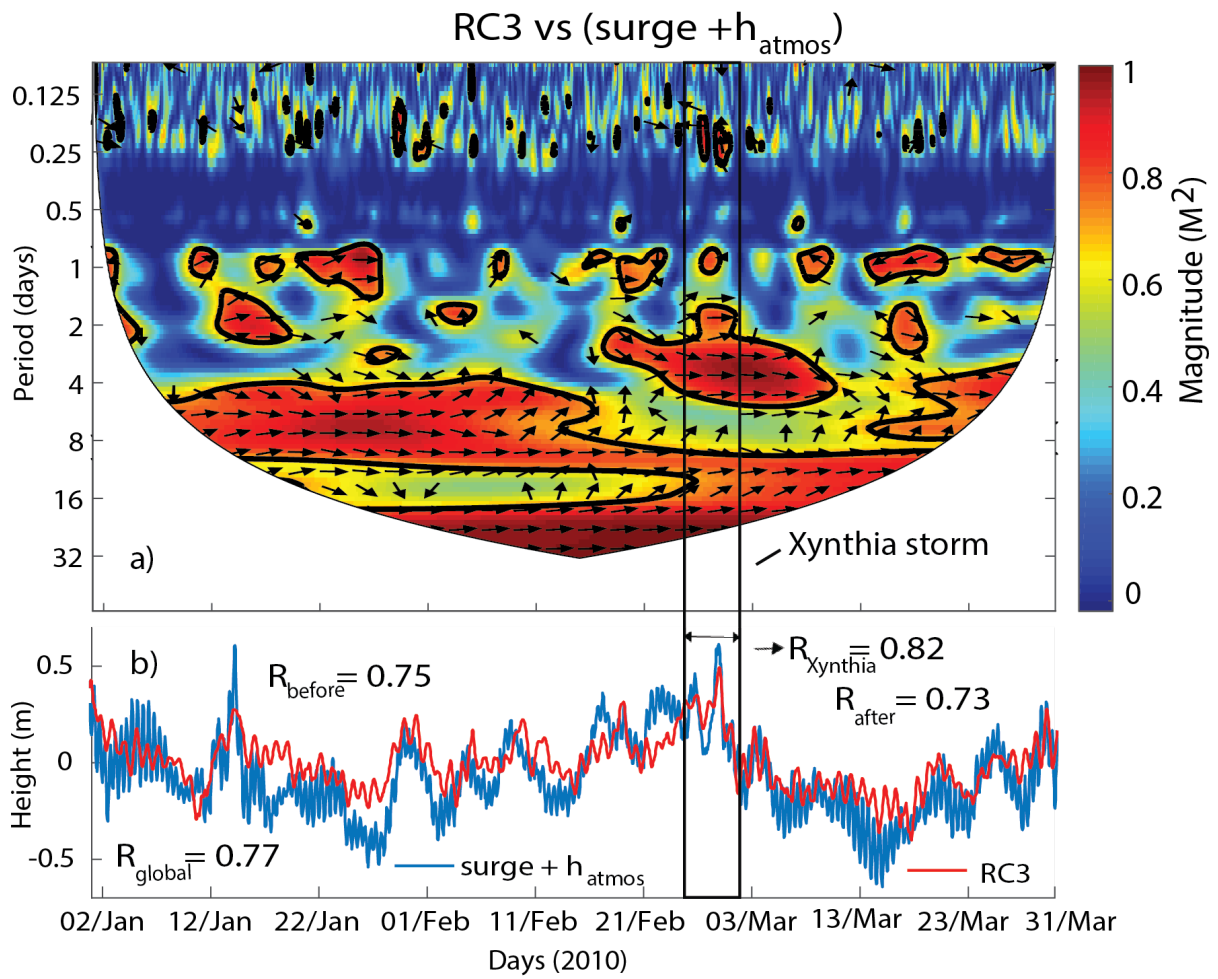


Figure IV.11 – a) XWT results for RC3 (SSA) and the surges and  $h_{atmos}$ ; b) Time series RC3 and the surges +  $h_{atmos}$  from January to March 2010 at Socoa.

## **Chapter IV. GNSS Reflectometry for detection of tide and extreme hydrological events: example of the Socoa (France), Mekong delta and Red River Delta (Vietnam)**

---

variables for periods higher than two weeks. High correlations were found on the periods 4-8 days before and after the Xynthia storm and 2-4 days during the Xynthia storm. High correlations are also found on smaller periods (from 4h to two days) during storm occurrences. The XWT confirms that the Xynthia storm was the more energetic event that occurred during the observation period. Temporal correlation between RC3 and the sum of the surge and of the IB exhibits larger values than the correlation with either the surge or the IB at all time scales (0.77 between January and March 2010, 0.75 before the storm, 0.82 during Xynthia, 0.73 after the storm for the sum of the surge and IB, the surge, IB respectively). As the surge and IB are strongly related, RC3 can be seen as the signature of the storm on the GNSS-R SSH signal. This can be explained by the fact that during storm, the GNSS-R signals are effected by atmospheric pressure and strong winds.

### **IV.6 The Mekong delta experiment (Vietnam)**

#### **IV.6.1 Characteristics of the Mekong delta area and experimental conditions**

The experiment site is located in Tran De port, Soc Trang province, Vietnam. This interesting site was chosen because of the competition between the hydrological regime (continental waters of Mekong River and tides (oceanic area) and the ocean tides, and, during the experiment, the presence of strong oceanic waves with an average speed of 0.4-0.5 m/s (Anthony et al., 2015; Hays, 2014). In winter, the flow direction has the same direction and under the influence of the north-east monsoon. Near the coast, flow orientation is more complex due to the influence of the estuaries and canals flowing into the sea. Coastal tide of the study area is semi-irregular, with a tidal amplitude in Hau river (Mekong River Delta) estuary at about 3 m (tides) and 1,80 m (low tide) (Le and Wyseure, 2013; Nguyen et al., 2012). Tidal amplitude decreases with the upstream distance. According

#### IV.6. The Mekong delta experiment (Vietnam)

to monitoring data in Vung Tau stations, the highest average tide peak of 443 cm (in months 10, 11) and the lowest is 58 cm in May, August. The highest tide feet - 24 cm (November), the lowest tide feet - 300 cm (June) (Nguyen and Ye, 2015).



Figure IV.12 – The GNSS receiver with a single antenna set up at about 30 m above water level, on the top of the Tran De water tower, Mekong Delta, Vietnam (Ha, 2018).

In order to monitor water level change in this area, Minh Cuong Ha (Fig. IV.12) and I installed a Leica GR25 receiver and an AR10 antenna on the top of Tran De water tower ( $106^{\circ}12'10.17''\text{E}$ ,  $9^{\circ}31'27.16''\text{N}$ ) at about 30 m above the mean sea surface (in Fig. IV.12). The Tran De water tower located in the Tran De port at 100 m from the Mekong River were acquired during one week from 23<sup>th</sup> to 30<sup>th</sup> August 2016.

The *in-situ* data used in this experiment consist in records of tide/river gauge from two hydrological stations over the period of acquisition: Tran De ( $106^{\circ}12'10.17''\text{E}$ ,  $9^{\circ}31'27.16''\text{N}$ ), Dai Ngai ( $106^{\circ}04'27.3''\text{E}$ ,  $9^{\circ}44'4.4''\text{N}$ ). The water level measurements are obtained at a 1h time sampling.

### **IV.6.2 Parameters for SNR signals analyzing**

The following two methods were tested:

- ✓ For the static case method (Larson method (Larson et al., 2013a)):  
 $\dot{h} \approx 0$ ,  $\tilde{f}$  is constant.
- ✓ For the dynamic case, we used the Roussel method (Roussel et al., 2015b): ( $\dot{h} \neq 0$ ,  $\tilde{f}(t)$  is proportional to the vertical antenna height velocity  $\dot{h}$ , the satellite elevation  $\varepsilon$  and its angular velocity  $\dot{\varepsilon}$ ). The input parameters chosen are:  $h_{min}= 26$  m,  $h_{max}= 34$  m and  $\dot{h}_{max}= 5*10^{-4}$  (mm/h).

Positions of the specular reflection points on the surface have been determined through direct modeling using GNSS reflected signal simulations (GRESS) developed by Roussel (Roussel et al., 2014). To remove the effect of the continent on the reflected signals, we used satellite angles  $\theta$  from  $0^\circ$  to  $25^\circ$  and make an azimuth mask from  $0^\circ$  to  $140^\circ$  which corresponds to the removal of continental reflections (Fig. IV.13).

### **IV.6.3 Comparison between the water level derived from GNSS-R and in-situ gauge records**

The water level height derived from SNR was compared to measurements obtained from a traditional Tran De tide gauge (located at 450 m from GNSS station) and a Dai Ngai river gauge (located at 26.7 km from GNSS station). The results in Tab. IV.4 shows that the water level obtained when combination of both GPS and GLONASS constellations is better than no combination. Good results obtained from two methods with correlation coefficient reaches 0.93 at Tran De station and reaches 0.85 at Dai Ngai station, respectively. The lower correlation obtained for the dynamic case, can be due to a quasi-static reflecting surface lowly affected by waves. Both method gives good results but the main difference is the number of solution computed: Larson gives accurate results but for a limited number of points located during quite constant period in terms of vertical surface

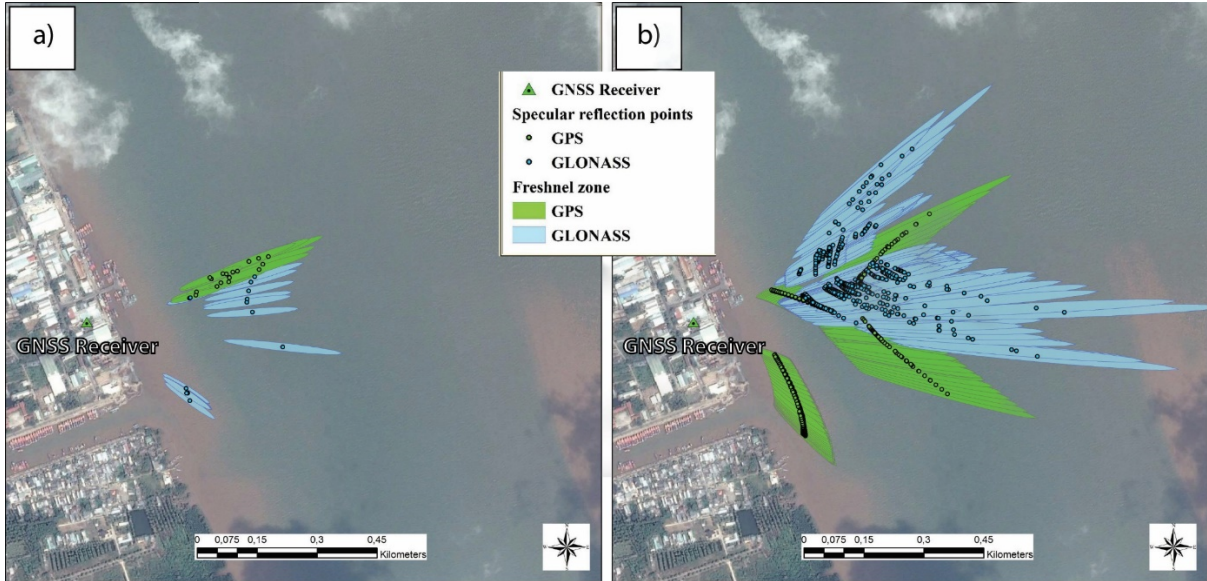


Figure IV.13 – Locations of the specular reflection points and Fresnel surface for a GNSS receiver on the top of the Tran De water tower from 23th to 30 August 2016 (all satellites with elevation angles from  $0^\circ$  to  $25^\circ$ ) (Ha, 2018): a) Simulation of SNR multipath using IPT method of Larson (Larson et al., 2008b); b) Simulation of SNR multipath using Roussel method (Roussel et al., 2015b).

velocity (maximum or minimum tide see Fig. IV.14 red circle) whereas LSM gives a larger number of a little bit less accurate solutions not only during maximum or minimum tides (red circles) but also during maximum vertical velocity (green ellipse). Time series variations of water level at Tran De station over 23 to 30 August 2016 are showed in Fig. IV.14.

## IV.7 Red River Delta (RRD) experiment

### IV.7.1 The study area and datasets

#### IV.7.1.1 Characteristics of the Red River Delta

The study area located in the East Sea shore and in the northern part of Vietnam, is characterized by a monsoon climate with a rainy season and dry season. The area of the RRD is approximately  $14,300 \text{ km}^2$ , entirely lying below three meters above sea level and much of it does not rise more than one meter above sea level (Luu et al., 2010). The RRD is

**Chapter IV. GNSS Reflectometry for detection of tide and extreme hydrological events: example of the Socoa (France), Mekong delta and Red River Delta (Vietnam)**

TABLE IV.4 – Comparison between the *in-situ* gauges with the raw SNR-based time series calculated with only the GPS constellation/GLONASS constellation/both constellations. a) In static case; b) In dynamic case.(Ha, 2018)

| <b>a) SNR Static case (method Larson)</b> |                            |                 |                 |                     |
|---|----------------------------|-----------------|-----------------|---------------------|
| <b>Hydrological station</b>               | <b>GNSS constellations</b> | <b>Bias (m)</b> | <b>RMSE (m)</b> | <b>Corr. Coeff.</b> |
| <b>Tran De station</b>                    | GPS                        | 0.08            | 0.32            | 0.92                |
|   | GLONASS                    | 0.01            | 0.52            | 0.83                |
|   | GPS+GLONASS                | 0.12            | 0.36            | 0.93                |
| <b>Dai Ngai station</b>                   | GPS                        | 0.09            | 0.41            | 0.78                |
|   | GLONASS                    | 0.04            | 0.57            | 0.67                |
|   | GPS+GLONASS                | 0.14            | 0.45            | 0.82                |
| <b>b) SNR Dynamic case (method LSM)</b>   |                            |                 |                 |                     |
| <b>Hydrological station</b>               | <b>GNSS constellations</b> | <b>Bias (m)</b> | <b>RMSE (m)</b> | <b>Corr. Coeff.</b> |
| <b>Tran De station</b>                    | GPS                        | 0.02            | 0.49            | 0.83                |
|   | GLONASS                    | 0.09            | 0.65            | 0.68                |
|   | GPS+GLONASS                | 0.13            | 0.5             | 0.85                |
| <b>Dai Ngai station</b>                   | GPS                        | 0.05            | 0.44            | 0.79                |
|   | GLONASS                    | 0.1             | 0.56            | 0.62                |
|   | GPS+GLONASS                | 0.14            | 0.44            | 0.81                |

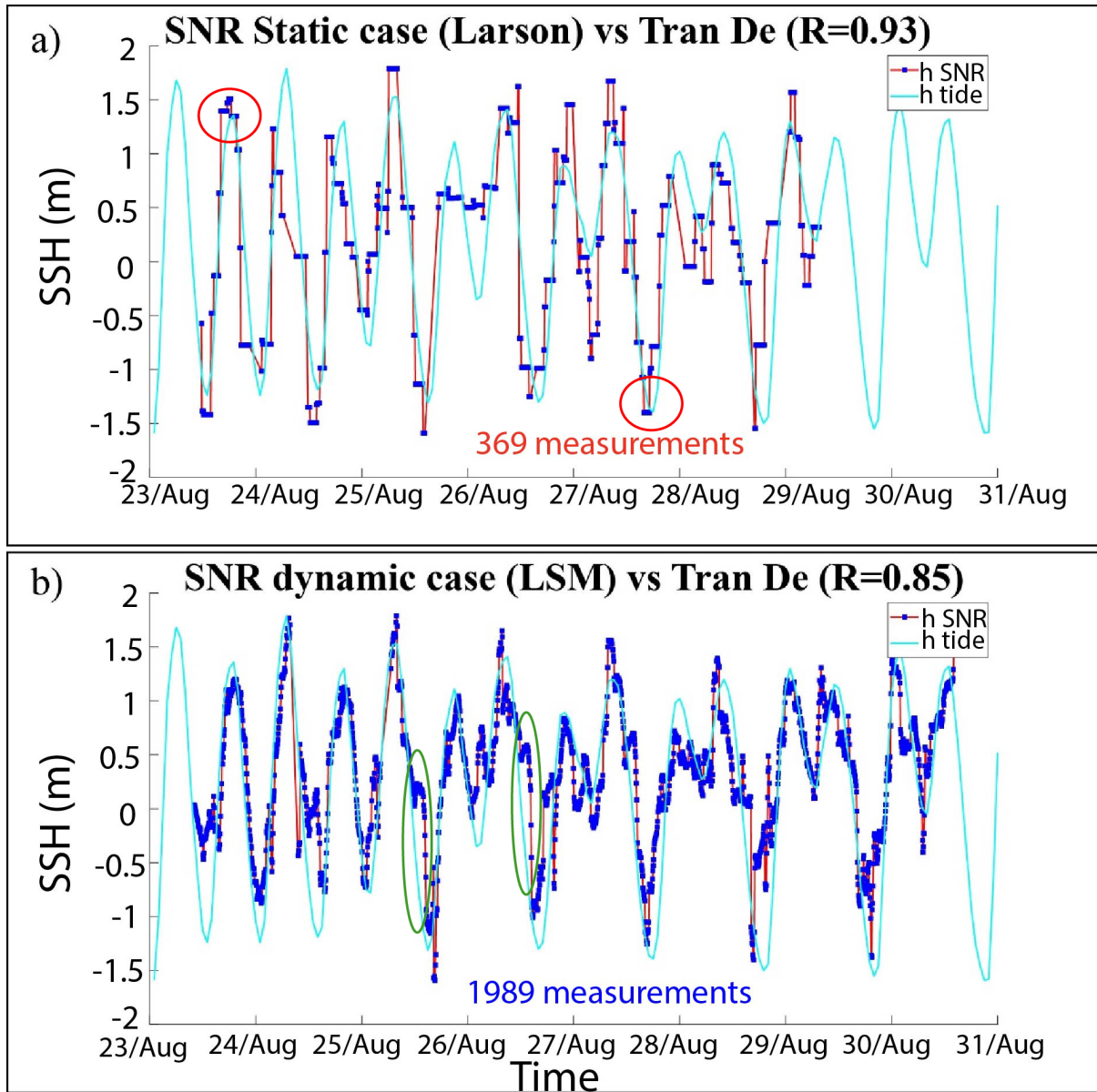


Figure IV.14 – Comparisons between water level height estimated from SNR measurements obtained with Larson method (a, 369 measurements), Roussel method (b, 1989 measurements) and Tran De tide gauge (cyan line), from 23<sup>th</sup> to 30<sup>th</sup> August 2016. modified from (Ha, 2018)

## **Chapter IV. GNSS Reflectometry for detection of tide and extreme hydrological events: example of the Socoa (France), Mekong delta and Red River Delta (Vietnam)**

---

limited landwards by the town of Son Tay in the north–west (150 km from the sea) and seawards by the coastline, which extends 360 km from Hai Phong province in the north-east to the Ninh Binh province in the south. This area includes an important coastal zone where mangroves contribute to ecosystem protection and biodiversity (Devienne, 2006; Krystian and Nguyen, 2005). The RRD has a very complex hydrological network and highly vulnerable to extreme events (Nguyen et al., 2014; Dang et al., 2005; Vreugdenhil et al., 2000). In fact, the area is regularly stricken by typhoons from June to October, causing widespread flooding and significant economic and social damage. In addition, heavy rainfall, salinization, flooding and drought are frequent hazards (Hansson and Ekenberg, 2000; Dang et al., 2005; Vreugdenhil et al., 2000).

### **IV.7.1.2 GNSS-R set-up**

A Leica GR25 receiver and an AR10 antenna were installed on the top of the old bridge abutment (21°02'44.04"N, 105°51'48.86"E) on the Red River in Hanoi, Vietnam (Fig. IV.15). GPS L1, L2 (S1C, S2W) and GLONASS L1 (S1C) frequencies were continuously acquired in rainy and windy conditions during the period of the Mirinae and Nida storms (Trinh and et al, 2016), from the 27<sup>th</sup> July to 12<sup>th</sup> August 2016 at a 1 Hz and 10 Hz frequency.

### **IV.7.1.3 River gauge data**

*In-situ* gauge is operated by Hydrological Meter, located at the same place of the experiment (Fig. IV.15), recorded from Hanoi Environmental Hydrology Station, National Centre for Hydro-meteorological Forecasting. The water level measurements are obtained at a 1h intervals and covers the period of the GNSS-R experiment. In the period of this campaign, the Mirinae and Nida storms caused heavy rainfall, large quantities of water from upstream (China) came to downstream (RRD) and released into the sea, the high water level recorded from hydrological station. There are lots

## IV.7. Red River Delta (RRD) experiment

of those oasis were totally flooded.

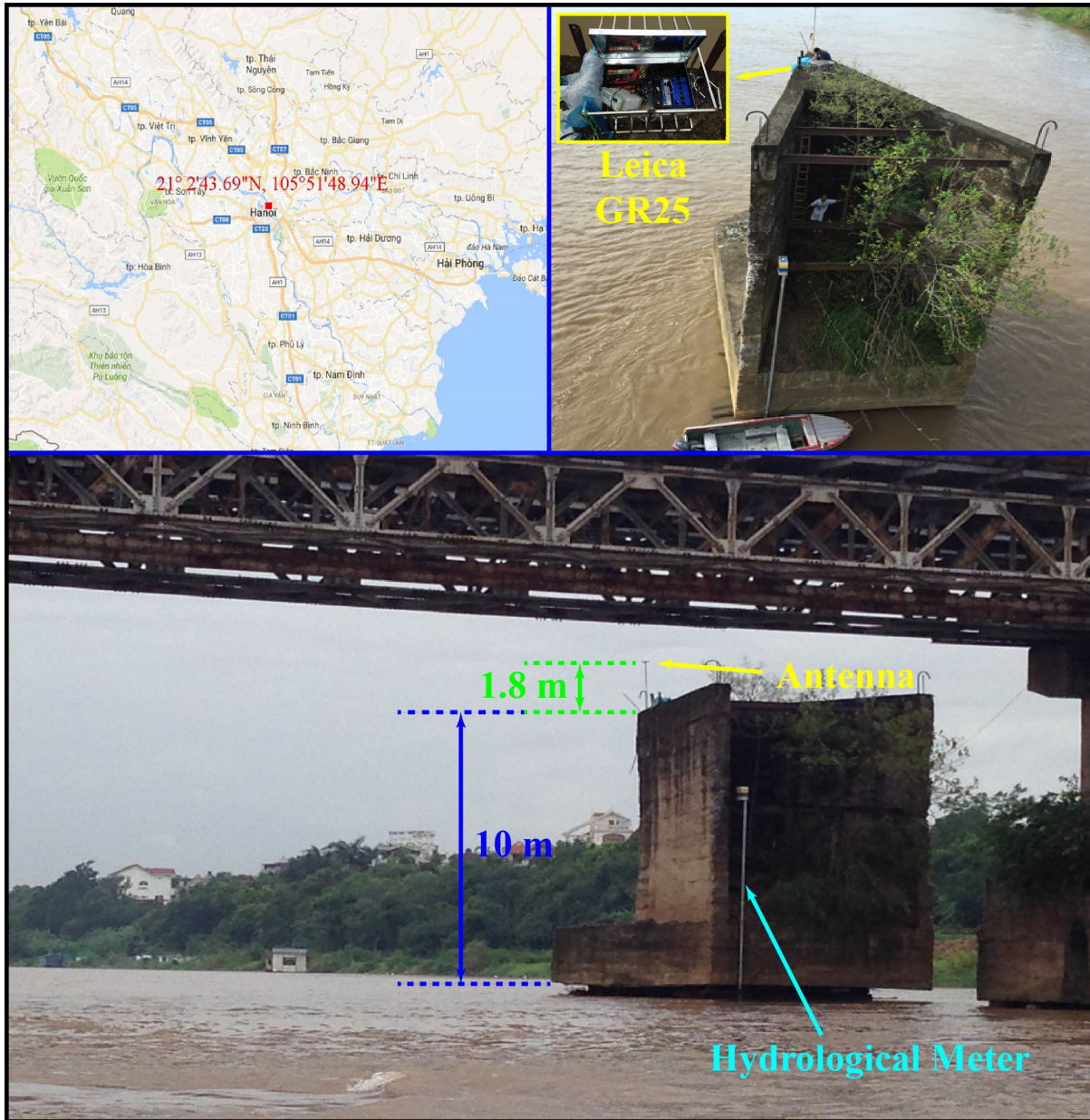


Figure IV.15 – The GNSS receiver with a single antenna installed on the top of the old bridge abutment ( $21^{\circ}2'44.04''N, 105^{\circ}51'48.86''E$ ) on the Red river in Hanoi, Vietnam from the 27<sup>th</sup> July to 12<sup>th</sup> August 2016. (Ha, 2018)

### IV.7.2 Parameters for SNR signals analyzing

The following two methods were used (the same method for Mekong Delta experiment):

Chapter IV. GNSS Reflectometry for detection of tide and extreme hydrological events: example of the Socoa (France), Mekong delta and Red River Delta (Vietnam)

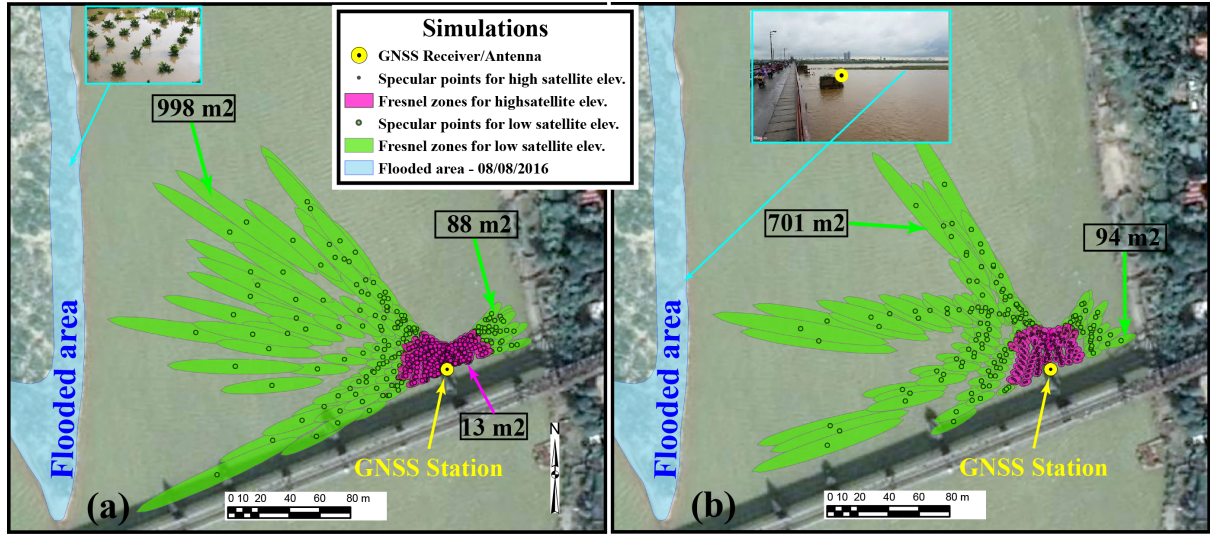


Figure IV.16 – Position of the GPS (a), GLONASS (b) specular reflection points and their first Fresnel surface for a GNSS receiver on Red River campaign. Simulations done the 08<sup>th</sup> of August 2016 with two range of satellite elevation angles  $\theta$ : High satellite elevation (in magenta; from  $30^\circ$  to  $70^\circ$ ) and low satellite elevation (in green:  $6^\circ$ - $30^\circ$  in the left side and  $18^\circ$ - $30^\circ$  in the right side). Sampling rate is equal to 15 mins (*i.e.*, satellites positions are actualized every 15 mins); the cyan area shows flooded area during the storm event. (Ha, 2018)

- ✓ For the static case method (Larson method (Larson et al., 2013a)):  $\dot{h} \approx 0$ ,  $\tilde{f}$  is constant.
- ✓ For the dynamic case, we used the Roussel method (Roussel et al., 2015b): ( $\dot{h} \neq 0$ ,  $\tilde{f}(t)$  is proportional to the vertical antenna height velocity  $\dot{h}$ , the satellite elevation  $\varepsilon$  and its angular velocity  $\dot{\varepsilon}$ ). The input parameters chosen are:  $h_{min} = 14$  m,  $h_{max} = 20$  m and  $\dot{h}_{max} = 5 \cdot 10^{-4}$  (mm/h).  $\dot{h}_{max}$  was chosen is approximately 3 times maximum water level fluctuations observed by Hanoi hydrological station ( $\approx 4$  m) during the flood period.

Due to the safety of the instruments and the location of the GNSS station placed within the same location as gauge stations, on the top of the old bridge abutment (Fig. IV.15), the SNR multipath signals obtained will be disturbed in the south direction of the GNSS antenna by the Long Bien bridge multipath. Therefore, positions of the reflection points on the surface and their Fresnel zones have been determined using GRESS with

azimuth mask from  $0^\circ$  to  $70^\circ$  (satellite elevation angles  $\theta$  limited from  $18^\circ$  to  $70^\circ$ ; North-East side of the antenna) and the azimuth from  $240^\circ$  to  $360^\circ$  with  $\theta$  limited from  $6^\circ$  to  $70^\circ$  in the North-West side of the antenna (Fig. IV.16). The maximum of the Fresnel zones measured  $\sim 1000 \text{ m}^2$  at the low satellite elevation and  $\sim 10 \text{ m}^2$  at the high satellite elevation.

### IV.7.3 Results

The Red river experiment is located far from the coast, so the water level is not influenced by tides and waves. In this site, the water level has calculated using two methods and two different ranges of satellite elevation. SSH were then compared with the water level recorded by the Hydrological station. The results show in Tab. IV.5, correlation coefficients obtained from both methods gives good results but the difference is in the number of solution computed: Larson gives accurate results but for a limited number of points whereas LSM gives large number of accurate solutions (Fig. IV.17). The high h estimated with high satellite elevation gives accuracy of  $\sim 10 \text{ cm}$  better than from low satellite elevation ( $6^\circ$ - $30^\circ$  in the left side and  $18^\circ$ - $30^\circ$  in the right side of the GNSS station).

The Nida storm, have been well recorded, one can see a delay of 48 hours for Nida between storms and GNSS-R level estimates due to the water transit time of the watershed (in Fig. IV.17).

In this study, I demonstrated that SNR data from GNSS-R receivers allows estimated the water level with an accuracy  $\sim 10\text{cm}$ . In the literature, the two methods (method Larson and method Roussel) are set down depending on the height variations of the GNSS-R antenna, if we no variations or very small ones that is to say we are the static case we used Larson method otherwise we are in the dynamic case and we used Roussel method.

**Chapter IV. GNSS Reflectometry for detection of tide and extreme hydrological events: example of the Socoa (France), Mekong delta and Red River Delta (Vietnam)**

TABLE IV.5 – Comparison between the *in-situ* gauges with the raw SNR-based time series calculated using different ranges of satellite elevation with only the GPS/GLONASS/GPS+GLONASS constellations. a) In static case and b) In dynamic case.

| Methods                       | GNSS constellation | Low elevation |          |             | High elevation |          |             |
|-------------------------------|--------------------|---------------|----------|-------------|----------------|----------|-------------|
|                               |                    | Bias (m)      | RMSE (m) | Corr. Coeff | Bias (m)       | RMSE (m) | Corr. Coeff |
| a) LARSON<br>(in static case) | GPS                | -0.15         | 0.24     | 0.93        | -0.01          | 0.13     | 0.96        |
|                               | GLONASS            | 0.2           | 0.25     | 0.95        | 0.03           | 0.1      | 0.98        |
|                               | GPS+ GLONASS       | -0.15         | 0.22     | 0.95        | -0.01          | 0.09     | 0.98        |
| b) LSM<br>(in dynamic case)   | GPS                | -0.26         | 0.32     | 0.93        | -0.07          | 0.16     | 0.94        |
|                               | GLONASS            | -0.25         | 0.38     | 0.87        | -0.11          | 0.13     | 0.99        |
|                               | GPS+ GLONASS       | -0.22         | 0.26     | 0.96        | -0.08          | 0.12     | 0.98        |

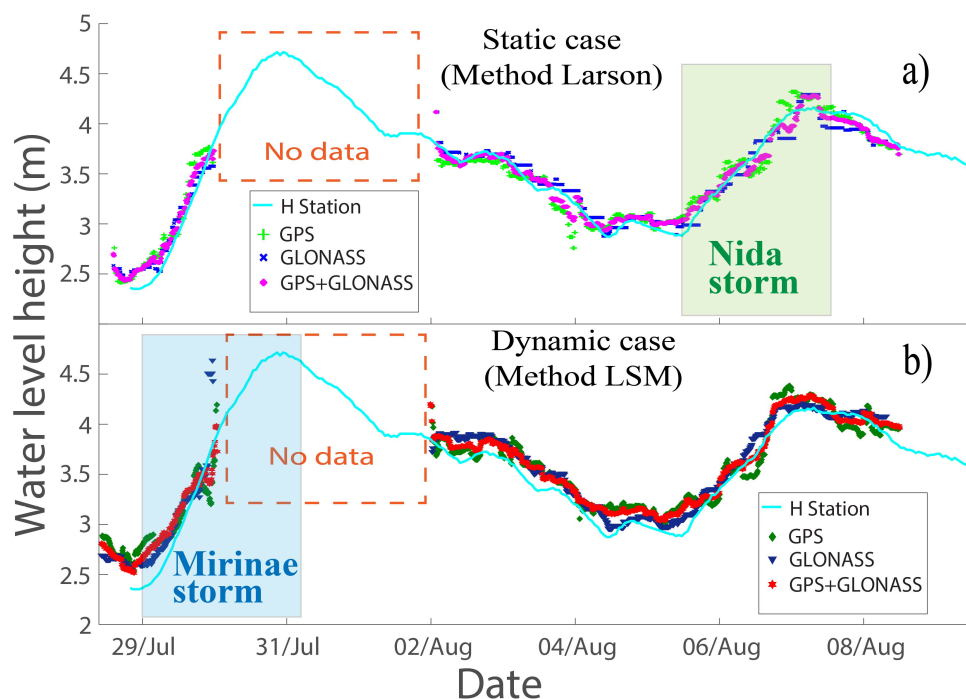


Figure IV.17 – Comparisons between heights estimated from SNR measurements obtained using methods LSM (a), method Larson (b) with only the GPS/GLONASS/GPS+GLONASS constellations versus height recorded from the hydrological station during the period of the Mirinae and Nida storms (from the 27<sup>th</sup> July to 12<sup>th</sup> August 2016)(Ha, 2018).

## IV.8 Conclusions and perspectives

In this chapter, it has been shown that it is possible to estimate SSH variations using a single geodetic antenna by simply analyzing the oscillations of the daily recorded SNR in complex environments such as the estuarine areas and coastal areas. The water level derived from SNR signal provides results of similar quality the classical gauges when using both GPS and GLONASS satellite. So it can allow evaluating the performances of GNSS-R for monitoring river changes. Therefore, GNSS reflectometry is a powerful alternative and a significant complement to current measurement techniques since it links the different spatial and temporal resolutions currently achieved by conventional tools (*i.e.*, spot and continuous measurements for a tide gauge, or covering a large area but low repeatability for conventional altimeters).

In the Socoa experiment, the Xynthia storm is also detected by using SSA and CWT method in the Socoa station. The comparisons made with tide gauge records from Socoa station showed that the SSA method extracts the tides and the major contributions with high accuracy by removing noise components. The accuracy of the tide estimates increased for the window size  $M$  greater than 6 h corresponding to cycle up and down of the tide. Analysis of the tidal using SSA with  $M = 12\text{h}$  gives two tide components whose peak periods correspond to the tidal period in the Saint Jean de Luz Bay (semi-diurnal (period of 6h) and diurnal tides (period of 12h)). The third reconstruction component (RC3) using the SSA method to detect the effects of atmospheric pressure in GNSS signals obtained a correlation coefficient  $R = 0.7$  compared with the atmospheric pressure data measured in the Socoa station. These results suggest that SSA is better than CWT method for the analysis of SSH time series to extract the main components in GNSS signals such as the tides and the effects of atmospheric pressure. Particularly, a correlation reach to 0.77 when using both the tide residual associated to surges and atmospheric pressure variation (see detail in the article in § IV.9).

#### **Chapter IV. GNSS Reflectometry for detection of tide and extreme hydrological events: example of the Socoa (France), Mekong delta and Red River Delta (Vietnam)**

---

In the Mekong river experiment, GNSS antenna was installed at the Tran De water tower (high 30 m), 100 m from the river. Comparisons with *in-situ* gauge data have a correlation coefficient of 0.92 with Larson method and 0.85 with LSM method. The results of Larson method are better than the LSM method can be explained by the reflecting surface is relatively static, less affected by waves. The water level derived from SNR signal provides results of similar quality the classical gauges when using both GPS and GLONASS satellite. So, it can allow evaluating the performances GNSS-R for monitoring river changes and the possibility to use this technique for calibration/validation of altimetry data (SARAL, Jason-2, 3, Sentinel-3A *etc.*). So, GNSS-R base on SNR analyzing is the promising tool for obtaining useful continuous and spatial measurements of river level. We obtain not only the river water level, but we can also retrieve the local slope of the water surface, and flooded areas. So, it can be used for detection of extreme hydrological events.

From the two studies in RRD and Mekong River Delta, we demonstrated that the SNR from GNSS-R receivers allows estimating the water level quite good accuracy  $\sim 10$  cm. Larson and Roussel methods can be applied not only in the coastal area (Roussel *et al.*, 2015b), but also for continental waters (river, lake, *etc.*) and even in the estuarine areas where has impacts of different characteristics such as hydrological regime, coastal oceanographic and so on. In the study, two methods are set down depending on the height variations of the GNSS-R antenna, if we have no variations or very small ones that is to say we are in the static case we used Larson method otherwise we are in the dynamic case and we used Roussel method. Both method gives good results but for a limited number of points whereas Roussel method gives a large number of accurate solutions. Multi-constellation increases the accuracy of the solutions and the number of computed points. The accuracy of GNSS-R, in many cases, is not obstacle for Red river or Mekong measurements because reference gauges record have water variations upper than 20 cm. The main storm *i.e.* Mirinae was not completely recorded due to the technical problem

**IV.9. Revised version of the article submitted at Remote Sensing, special issue  
“Remote Sensing of hydrological Extremes”:**

---

when Nida have been well recorded, one can see a delay of 48 hours for Nida between storms and GNSS-R answers due to the water transit time of the watershed.

**IV.9 Revised version of the article submitted at Remote Sensing, special issue “Remote Sensing of hydrological Extremes”:**

1 Article

## 2 Identifying 2010 Xynthia storm signature in 3 GNSS-R-based tide records

4 **Phuong Lan Vu**<sup>1</sup>, **Minh Cuong Ha**<sup>1</sup>, **Frédéric Frappart**<sup>2</sup>, **José Darrozes**<sup>1</sup>, **Guillaume Ramillien**<sup>1</sup>,  
5 **Grégory Dufrechou**<sup>1</sup>, **Pascal Gegout**<sup>1</sup>, **Denis Morichon**<sup>3</sup> and **Philippe Bonneton**<sup>4</sup>

6 <sup>1</sup> GET-GRGS, UMR 5563, CNRS/IRD/UPS, Observatoire Midi-Pyrénées, 14 Avenue Edouard Belin, 31400  
7 Toulouse, France; jose.darrozes@get.omp.eu (J.D.); Guillaume.Ramillien@get.omp.eu (G.R.);  
8 cuonghm.rsc@gmail.com;

9 <sup>2</sup> LEGOS-GRGS, UMR 5566, CNES/CNRS/IRD/UPS, Observatoire Midi-Pyrénées, 14 Avenue Edouard Belin,  
10 31400 Toulouse, France; frederic.frappart@legos.obs-mip.fr

11 <sup>3</sup> Université de Pau et des Pays de l'Adour, Laboratoire de Sciences Appliquées au Génie Civil et au Génie  
12 Côtier JE2519, Allée du parc Montaury, 64600 Anglet, France ; denis.morichon@univ-pau.fr

13 <sup>4</sup> Université Bordeaux 1, CNRS, UMR 5805 EPOC, Allée Geoffroy Saint-Hilaire – CS 50023, F-33615 Pessac,  
14 France ; philippe.bonneton@u-bordeaux.fr

15 \* Correspondence: phuonglan.vu@get.omp.eu; Tel.: +33-7-8232-1136

16 Received: date; Accepted: date; Published: date

17 **Abstract:** In this study, 3 months of records (January-March 2010) acquired by a geodetic GNSS  
18 station from the permanent network of RGP (Réseau GNSS Permanent), deployed by the French  
19 Geographic Institute (IGNF), located in Socoa, in the south of the Bay of Biscay, were used to  
20 determine the tide components and identify the signature of storms on the signal to noise ratio  
21 (SNR) during winter 2010. The Xynthia storm hit the French Atlantic coast on the 28<sup>th</sup> of February  
22 2010 causing large floods and damages from the Gironde to the Loire estuaries.

23 Blind separation of the tide components and of the storm signature was achieved using both a  
24 singular spectrum analysis (SSA) and a continuous wavelet transform (CWT). A correlation of  
25 0.98/0.97 and RMSE of 0.21/0.28 m between the tide gauge records of Socoa and our estimates of the  
26 sea surface height (SSH) using the SSA and the CWT respectively were found. Correlations of 0.76  
27 and 0.7 were also obtained between one of the mode from the SSA and atmospheric pressure from a  
28 meteorological station and a mode of the SSA. Particularly, a correlation reaches to 0.76 when using  
29 both the tide residual associated to surges and atmospheric pressure variation.

30 **Keywords:** GNSS; Singular Spectrum Analysis; Continuous Wavelet Transform; Tide gauge;  
31 Inverted barometer; Surge Storm  
32

### 33 1. Introduction

34 The sea level rise (SLR), caused by global warming, will impact low-lying coastal areas not only  
35 through inundation, but also as increase of storm surges repeatability and extreme astronomic tides  
36 will reach higher water levels [1, 2, 3]. Changes in climatic conditions are also likely to increase the  
37 elevation and the frequency of storm surges in various areas [4, 5, 6], causing a major threat to the  
38 increasing part of the world population living in coastal regions within a few meters above SL [7].

39 A surge is defined as the difference between observed and astronomical modeled tides at a  
40 specific location. This difference is due to meteorological phenomena like storms [8, 9]. When there

41 is a combination of high tide and storm events characterized by large rainfall, strong waves with  
42 important setup, surges can be responsible for inundation of coastal areas and damage of coastal  
43 facilities [10, 11].

44 If we consider the French case, this country has experienced many strong storms in the recent  
45 years, such as Oritia storm in 2000, Cyclone Kyrill in 2007, European tornado outbreak in 2008,  
46 Xynthia storm in 2010, Joachim winter storm in 2011, tidal surge Xavier in 2013, Darwin storm in  
47 2014, extratropical cyclone Zeus in 2017 and David storm in 2018. This series of extreme events put  
48 forward the urgent need for storm monitoring and early warning system along the French/European  
49 coasts. Geodetic GNSS stations located on top of cliffs can be used for this purpose. During the night  
50 of 27-28 February 2010, the Xynthia storm affected south western part of Europe mainly the Spanish  
51 and French coastal regions of Bay of Biscay, causing important damages, 59 casualties in Europe (47  
52 in France), and a large marine submersion [12, 13, 14, 15, 16] as in La Faute sur Mer area with 29  
53 casualties. Winds up to 160 km.h<sup>-1</sup> and pressure down from ~1000 to 977 hPa were recorded by  
54 meteorological stations during high spring tide were responsible for a huge storm surge along the  
55 coast of the Bay of Biscay [14, 17]. For example a surge of 1.53 m was recorded at La Rochelle tide  
56 gauge (8.01 m above the hydrographic zero). Such high tide level was never recorded since the  
57 set-up of this tide gauge in 1997. The surge was also greater than the largest recorded at Brest tide  
58 gauge (1.42 m) during the last 150 years [13]. For this reason, the densification of sensors and  
59 observations is crucial to establish a well-structured surveillance and warning system, to ensure the  
60 safety of populations. Currently, long-term monitoring is ensured by tide gauges that now used  
61 radar technique to measure the tides along the French coast. They are more and more co-located  
62 with either GNSS geodetic receivers or Doppler Orbitography and Radiopositioning Integrated by  
63 Satellite (DORIS) space geodesy system to separate changes in SSH from crustal motions (e.g.,  
64 Wöppelmann et al., 2006 [18]).

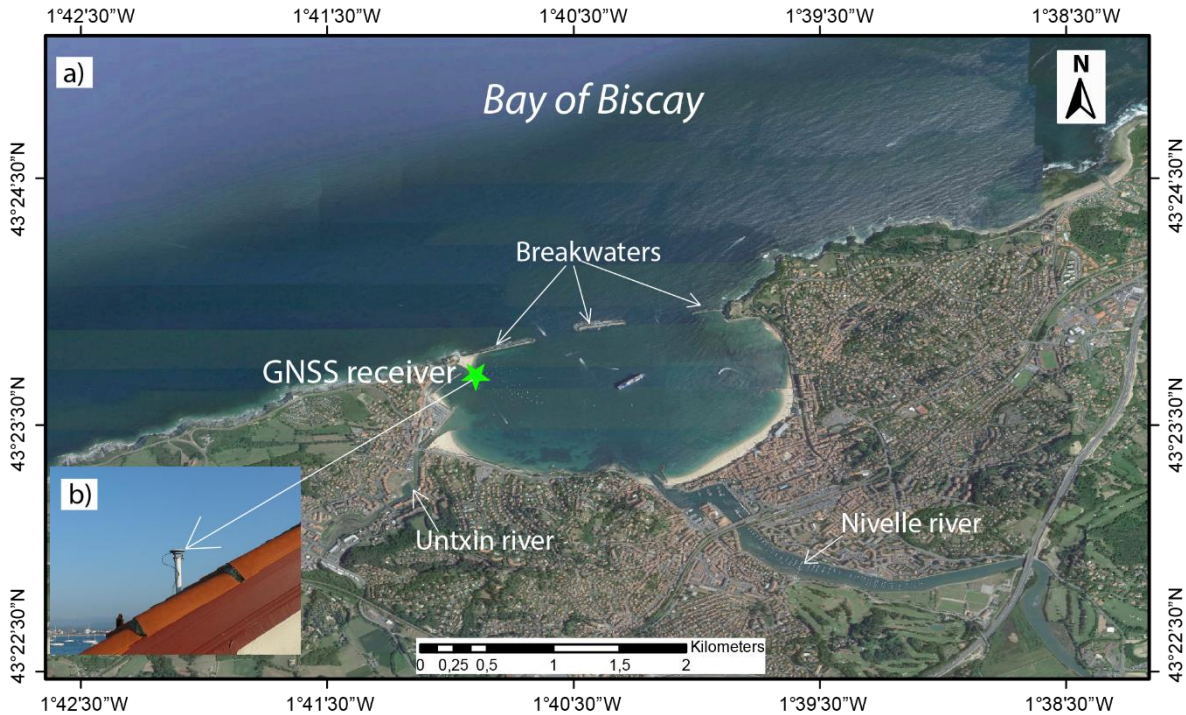
65 The Global Navigation Satellite Systems - reflectometry (GNSS-R) technique has demonstrated  
66 a strong potential for the monitoring of sea surface variations since the mid-90s based on waveform  
67 analysis [19, 20, 21]. Nowadays, for monthly to interannual monitoring, SSH variations are mostly  
68 derived the processing of the Signal-to-Noise Ratio (SNR) acquired by a geodetic GNSS receiver [22,  
69 23, 24, 25]. GNSS geodetic stations part of the national and international permanent GNSS networks  
70 and located in coastal areas can be used as “opportunistic” tide gauge according to Larson et al.  
71 (2013) when they record the SNR data. Contrary to classical tide gauges which are located in  
72 protected areas to dampen the effect of the waves on the signal, GNSS-R based time-series of Sea  
73 Surface Height (SSH) contains both the signatures of the tide and other information like the waves  
74 [26] as well as the surges signatures.

75 In this study, the SNR data records from the Socoa geodetic station (south west of France) were  
76 used to determine SSH variations from January to March 2010 in the Saint Jean de Luz Bay. Two  
77 methods (Singular Spectrum Analysis - SSA and Continuous Wavelet Transform – CWT) were  
78 applied to the SSH derived from SNR records to separate the tide signature from other geophysical  
79 signals. Comparisons were performed against the tide gauge records from the Socoa station. Non  
80 tidal signals were compared to surge estimates, pressure variations and waves to determine their  
81 nature. The potential of this technique, the choice of the location of the geodetic GNSS station, the  
82 choice of the statistical techniques are then discussed.

## 83 2. Study area

84 The analyses presented below were performed in the Bay of Saint de Luz, located in the east of  
85 the Bay of Biscay, along the French Atlantic coast, a few kilometers north from the Spanish border  
86 (Fig. 1a). For several centuries, this place has been strongly affected by powerful storms and has  
87 been regularly flooded. In the middle of the 19<sup>th</sup> century, in order to protect the area from the ocean’s  
88 tides, a breakwater was constructed. The study area is located between the breakwater and the  
89 coastline of the bay, call hereafter inside part, where wave effects are attenuated. The annual mean  
90 significant wave height in the inside part is 1.6 m with a maximum of 2.5 m [27, 28].

91 The inside part of the bay is approximately 2 km long by 1 km wide. Owing to the protection of  
 92 the breakwaters, this part is almost unaffected by the coastal currents and waves [29], with a tidal  
 93 range about 4.5 m at spring tides. The inside part receives also freshwater inflows from two small  
 94 rivers (Untxin and Nivelle rivers in Fig. 1a). The study area is in a semi-diurnal macro-tidal  
 95 environment [30, 31].



96

97 Figure 1: a) Location of the GNSS receiver at the SOCA station (43°23'42.83"N, 01°40'54.05"O); b)  
 98 view of the antenna TRM55971.00 set up on a roof, at 10.664 m above the sea surface (source:  
 99 <http://rgp.ign.fr>).

### 100 3. Datasets

#### 101 3.1. GNSS data

102 GNSS data, including SNR, have been continuously acquired since the 1<sup>st</sup> of April 2006 at a  
 103 frequency of 1 Hz using a Trimble NETR5 receiver (from 2009 until 2010) and a Trimble Zephyr  
 104 model 2 (TRM55971.00) geodetic antenna in Socoa (43°23'42.83"N, 01°40'54.05"W) at 10.66 m above  
 105 the mean sea surface (Fig. 1b). This station (SOCA) is part of RGP (Réseau GNSS Permanent -  
 106 <http://rgp.ign.fr>) from IGN (Institut National de l'Information Géographique et Forestière). In this  
 107 study, the data used were acquired at L1 frequency from GPS and GLONASS constellations between  
 108 1<sup>st</sup> of January to 31 March 2010.

#### 109 3.2. Tide gauge data

110 SSH records from the Socoa gauge station operated by the French REFMAR network  
 111 (<http://data.shom.fr/donnes/refmar/>) were used for comparison with SSH estimates, derived from  
 112 SNR technique, from January to March 2010. SSH measurements are available with a temporal  
 113 resolution of 10 minutes. The instrumental zero (of this tide gauge) is set to the hydrographic zero.  
 114 The Socoa tide gauge is located (43°23'42.86"N; 01°40'53.83"W) at the end of Socoa's breakwaters,  
 115 protecting it against wave effects, 5 m away from the GNSS station. The Socoa station is equipped  
 116 with a digital coastal tide gauge composed of an Optiwave 7300C sensor and a MARELTA  
 117 acquisition unit.

#### 118 3.3. Meteorological data

119 The Socoa meteorological station provides jourly estimates of rainfall, wind speed and  
 120 atmospheric pressure. Records from the period January - March 2010 were used in this study. They  
 121 were made available by Infoclimat (<https://www.infoclimat.fr>). The atmospheric pressure was  
 122 converted into inverted barometer effect ( $h_{atmos}$ ) using the following equation:

$$123 \quad h_{atmos} = - \frac{P_{atm} - \overline{P_{atm}}}{\rho g} \quad (1)$$

124 where  $P_{atm}$  is the time varying mean of the global surface atmospheric pressure over the  
 125 oceans;  $\rho = 1,020 \text{ gcm}^{-3}$  is density of seawater;  $g = 9,81 \text{ cms}^{-2}$  is the mean acceleration of gravity [32].

### 126 3.4. Significant wave height data

127 Significant wave height (SWH) data over the study period were acquired by the directional wave  
 128 buoy located (43°31'56"N; 1°36'54"W). SWH data are provided at the temporal resolution of 30  
 129 minutes by CANDHIS service from National swell off database from the Institute for maritime and  
 130 inland waterways (CETMEF-Brest)

## 131 4. Methods

132 SNR GNSS data were first inverted to derive water levels in the SCOA station using the  
 133 methodology developed by [22]. The resulting water levels were then analyzed using two spectral  
 134 methods i.e. SSA and CWT.

### 135 4.1. Inversion of the SNR data

136 GNSS-R is an opportunistic technique that provides information on the properties of the Earth  
 137 surface [33]. The inversion of the GNSS SNR can be used for the monitoring of SSH [24] using the  
 138 Interference Pattern Technique (IPT).

139 Following [34], the SNR quantity at any instant is described as:

$$140 \quad \text{SNR} = A_d^2 + A_m^2 + 2A_d A_m \cos \psi \quad (2)$$

141 where  $A_d$  and  $A_m$  are the amplitudes of the direct and reflected signals, respectively, and  $\varphi$  is  
 142 the phase difference between these two signals.

143 Assuming that  $A_m \ll A_d$ , thus SNR can be approximated by:

$$144 \quad \text{SNR} \approx A_d^2 + 2A_d A_m \cos \psi \quad (3)$$

145 The reflected signal perturbations are mainly visible for low satellite elevation angles [35] but  
 146 recent development demonstrate the possibility to use also high satellite elevation [26]. Assuming a  
 147 planar reflector which corresponds to the sea surface, the relative phase angle can be derived  
 148 geometrically from the path delay  $\delta$  of the reflected signal [36]:

$$149 \quad \psi = \frac{2\pi\delta}{\lambda} = \frac{4\pi h}{\lambda} \sin(\varepsilon) \quad (4)$$

150 where  $\lambda$  the signal wavelength,  $\varepsilon$  the satellite elevation and  $h$  the vertical distance between the  
 151 antenna phase centre and the reflecting surface. The frequency of the multipath oscillations can be  
 152 derived from (3) as proposed by [37] and improved by [22]:

$$153 \quad f_\psi = \frac{d\psi}{dt} = \frac{4\pi\dot{h}}{\lambda} \sin(\varepsilon) + \frac{4\pi h}{\lambda} \cos(\varepsilon) \dot{\varepsilon} \quad (5)$$

154  $\dot{h}$  ( $= \frac{dh}{dt}$ ) defines the vertical velocity and  $\dot{\varepsilon}$  ( $= \frac{d\varepsilon}{dt}$ ) defines the elevation angle velocity. Eq. (4) can  
 155 be simplified by making the following simple change of variable -  $x = \sin(\varepsilon)$ :

$$156 \quad \tilde{f} = \frac{d\psi}{dx} = \frac{4\pi}{\lambda} \left( \dot{h} \frac{\tan(\varepsilon)}{\varepsilon} + h \right) \quad (6)$$

157 where  $\tilde{f}$  is the frequency of the multipath oscillation.

158 - For the static case proposed by [24]:  $\dot{h} \approx 0$ , thus  $\tilde{f}$  is constant and directly proportional to the  
 159 receiver height above the reflecting surface.

160 - In the dynamic case,  $\dot{h} \neq 0$ , so the time series  $\tilde{f}(t)$  is proportional to the vertical antenna height  
 161 velocity  $\dot{h}$  and to the satellite elevation  $\varepsilon$  and its angular velocity  $\dot{\varepsilon}$ . Considering Eq. 5, only two  
 162 unknown quantities ( $h$  and  $\dot{h}$ ) have to be determined using the Least Square Method (LSM) [22]

163 In this study, we applied the approach proposed by [22] to the 1 Hz L2C SNR from GPS and  
 164 GLONASS satellites. The update interval was fixed to 10 minutes for height retrievals. A maximum

165 range of variations of  $\pm 4$  m from the elevation above mean sea surface (10.66 m) was considered for  
 166 the inversion algorithm. Due to the configuration of the site, all reflections from azimuth angles  
 167 between  $60$  and  $210^\circ$  were not taken into account to only keep the reflections occurring inside of the  
 168 bay. Besides, because of the presence of mask and multipath due to buildings and dikes, only  
 169 reflections from elevation angles ranging from  $1$  to  $25^\circ$  were considered.

#### 170 4.2. Analysis of the GNSS-R-based water levels

##### 171 4.2.1. Singular Spectrum Analysis

172 SSA is a principal component analysis in the time domain, used to extract statistical patterns  
 173 from short and noisy time-series without any a priori on the dynamics of the signal [38, 39].  
 174 Considering a signal  $x(t)$  composed of  $N$  samples taken in a window of size  $M$ , a lagged  
 175 autocorrelation matrix is obtained for a maximum lag  $M$  equals to the window size. The elements  
 176 ( $c_j$ ) of this matrix are defined as follows:

$$177 c_j = \frac{1}{N-j} \sum_{i=1}^{N-j} x(t_i)x(t_{i+j}) \text{ with } 0 \leq j \leq M-1 \quad (7)$$

178 where  $t_i$  and  $t_{i+1}$  are the sampling times.

179 Eigenvalues  $\lambda_k$  and eigenvectors  $E_j^k$  (also known as empirical orthogonal functions) of the  
 180 lagged autocorrelation matrix are determined and then sorted in descending order of the  
 181 eigenvalues. Following [39, 40], the  $k^{th}$  principal components among  $M$  is given by:

$$182 a^k(t_i) = \sum_{j=1}^M x(t_{i+j}) E_j^k \text{ with } 0 \leq i \leq N-M \quad (8)$$

183 The components of the original time-series analyzed using SSA can be reconstructed as follows:

$$184 x^k(t_i) = \frac{1}{M} \sum_{j=1}^M a(t_{i-j}) E_j^k \text{ with } M \leq i \leq N-M+1 \quad (9)$$

185 where  $x^k(t_i)$  is the  $k^{th}$  reconstructed components (RC) of the original times series.

186 In this study, the time series are decomposed into principal components (PCs) and then  
 187 reconstructed components (RCs) using a modified version of MATLAB algorithm [41].

##### 188 4.2.2. Continuous Wavelet Transform

189 The CWT of a signal  $x(t)$ , is defined as the sum over all time of the signal multiplied by scaled,  
 190 shifted versions of the wavelet function  $\psi(t)$  [42]:

$$191 C_x(a, \tau) = \int_{-\infty}^{+\infty} x(t) \psi_{a,\tau}^* dt ; \psi_{a,\tau}(t) = \frac{1}{a} \psi\left(\frac{t-\tau}{a}\right) \quad (10)$$

192 The results of the CWT are many wavelet coefficients  $C_x(a, \tau)$  where \* corresponds to the  
 193 conjugated complex. The two parameters  $a$  and  $\tau$  correspond respectively to the scale factor and the  
 194 temporal translation (shift). Afterward a wavelet spectrum  $W_X(a, \tau)$  is constructed according to the  
 195 relation below defined as the modulus of the wavelet coefficients [43]:

$$196 W_X(a, \tau) = C_X(a, \tau) C_X^*(a, \tau) = |C_X(a, \tau)|^2 \quad (11)$$

197 In order to investigate the relationship in time-scale space between two given signals, the cross  
 198 wavelet transform (XWT) is used. The XWT constructed from two CWTs exposes their common  
 199 power and provides further information concerning their relative phase. The wavelet cross spectrum  
 200  $W_{XY}(a, \tau)$  between two signals  $x(t)$  and  $y(t)$  is given by:

$$201 W_{XY}(a, \tau) = C_X(a, \tau) C_Y^*(a, \tau) \quad (12)$$

202 Where  $C_X(a, \tau)$  and  $C_Y^*(a, \tau)$  are respectively, the wavelet coefficient of  $x(t)$  and the conjugate  
 203 of the wavelet coefficient of  $y(t)$ .

204 In this study, wavelet analyzes were performed using a modified version of the cross wavelet  
 205 and wavelet coherence toolbox from [44].

## 206 5. Results

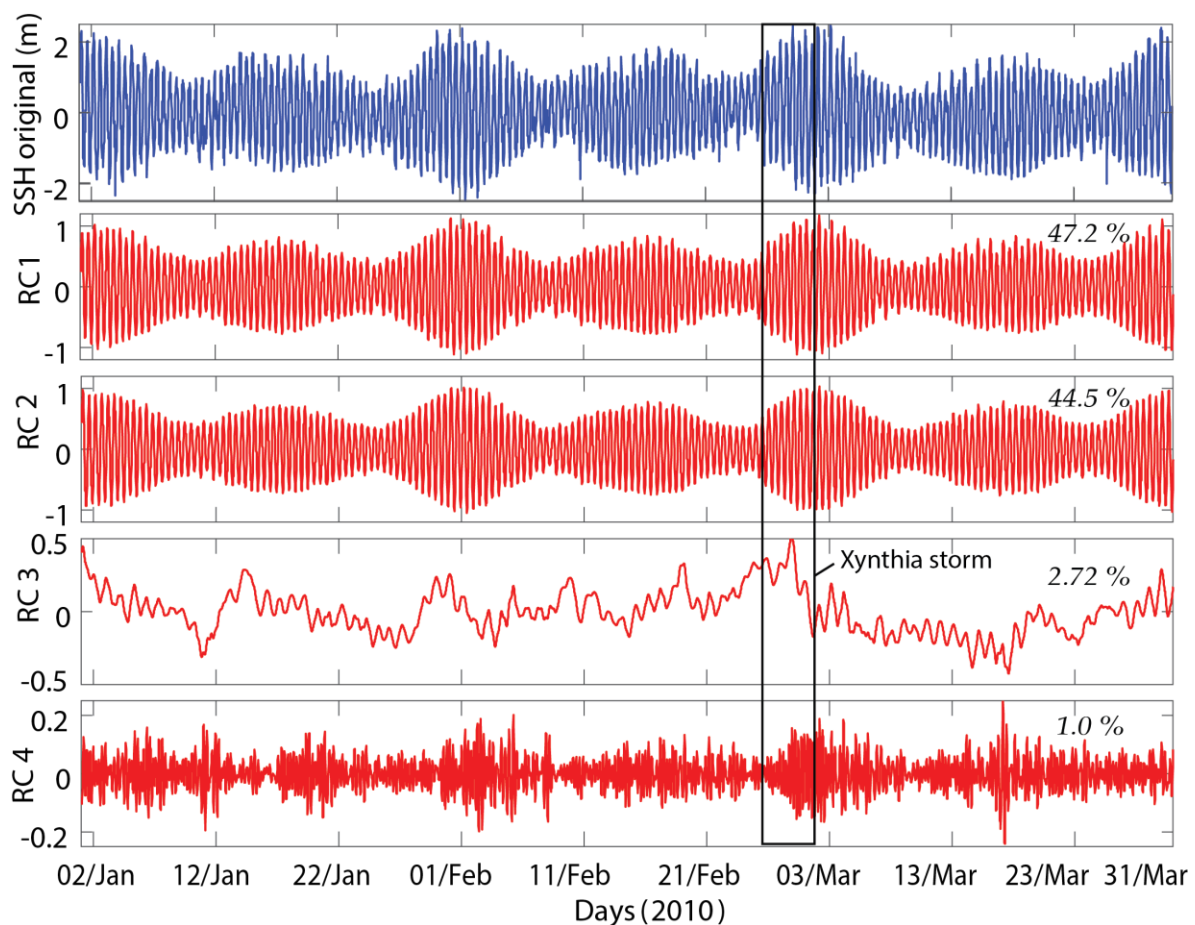
207 In this study, two statistical approaches were applied to blindly decompose GNSS-R-based time  
 208 series of SSH from Socoa: SSA and CWT. Our goal is to separate the major tide components from  
 209 other geophysical signals, including the signature of the extreme storm event as the Xynthia storm  
 210 occurred during the study period.

### 211 5.1. GNSS-R SSH time series analysis using the SSA method

212 The four first components (RC) of the SSA account for more than 95% of the explained variance.  
 213 Figure 2 presents GNSS-R SSH and the fourth first components of the SSA.

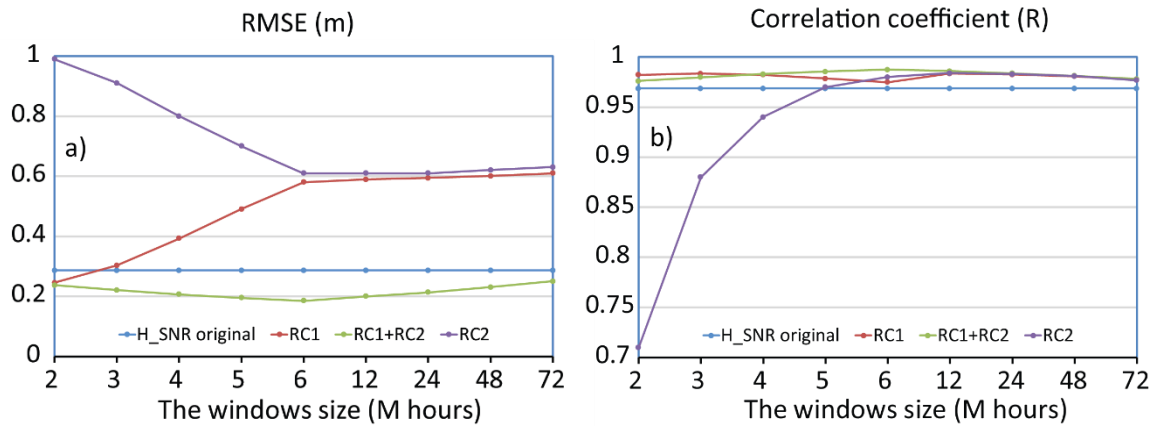
214 RC1 and RC2 accounted for 47.2% and 44.5% of the explained variance respectively, whereas  
 215 RC3 and RC4 accounted for 2.7% and 1.0% respectively. RC1 and RC2 exhibit oscillations of large  
 216 amplitude (between 2 and 4 m) of frequency lower ranging from less than a day to a quasi-monthly  
 217 modulation whereas RC3 and RC4 exhibit a less regular high frequency pattern of lower amplitude.  
 218 As the study area is a semi-diurnal macro-tidal environment [31, 45], the SSH is dominated by the  
 219 tides signal, the major RC modes represent the tides. Comparisons between the original GNSS-R  
 220 SSH, RC1, RC2 and sum of RC1 and RC2 modes and the tide gauge records at Socoa station were  
 221 performed. Their results are presented in terms of root mean square error RMSE (Fig. 3a) and  
 222 correlation coefficient R (Fig. 3b) for different window sizes  $M$ . A good agreement is generally  
 223 obtained for the original GNSS-R SSH, RC1, RC2 and sum of RC1 and RC2 modes and all the  
 224 window size. Nevertheless, it can be noticed that the agreement is lower with the tide gauge record  
 225 considering separately RC1 and RC2, especially visible for the RMSE (Fig. 3a) than considering the  
 226 GNSS-R SSH and the sum of RC1 and RC2 modes. But, higher correlations and lower RMSE are  
 227 observed for the sum of RC1 and RC2 modes than for GNSS-R SSH for all window sizes with an  
 228 optimum at 6 h ( $R=0.99$  and  $RMSE = 0.16$  m). Due to this very good agreement, RC1 and RC2 modes  
 229 correspond to the tide components of the GNSS-R SSH.

230



231

232 Figure 2: The GNSS-R SSH in Socoa and the four main components of its SSA decomposition  
 233 and its associated eigenvalues ( $\lambda$ ) expressed in % of the explained variance.

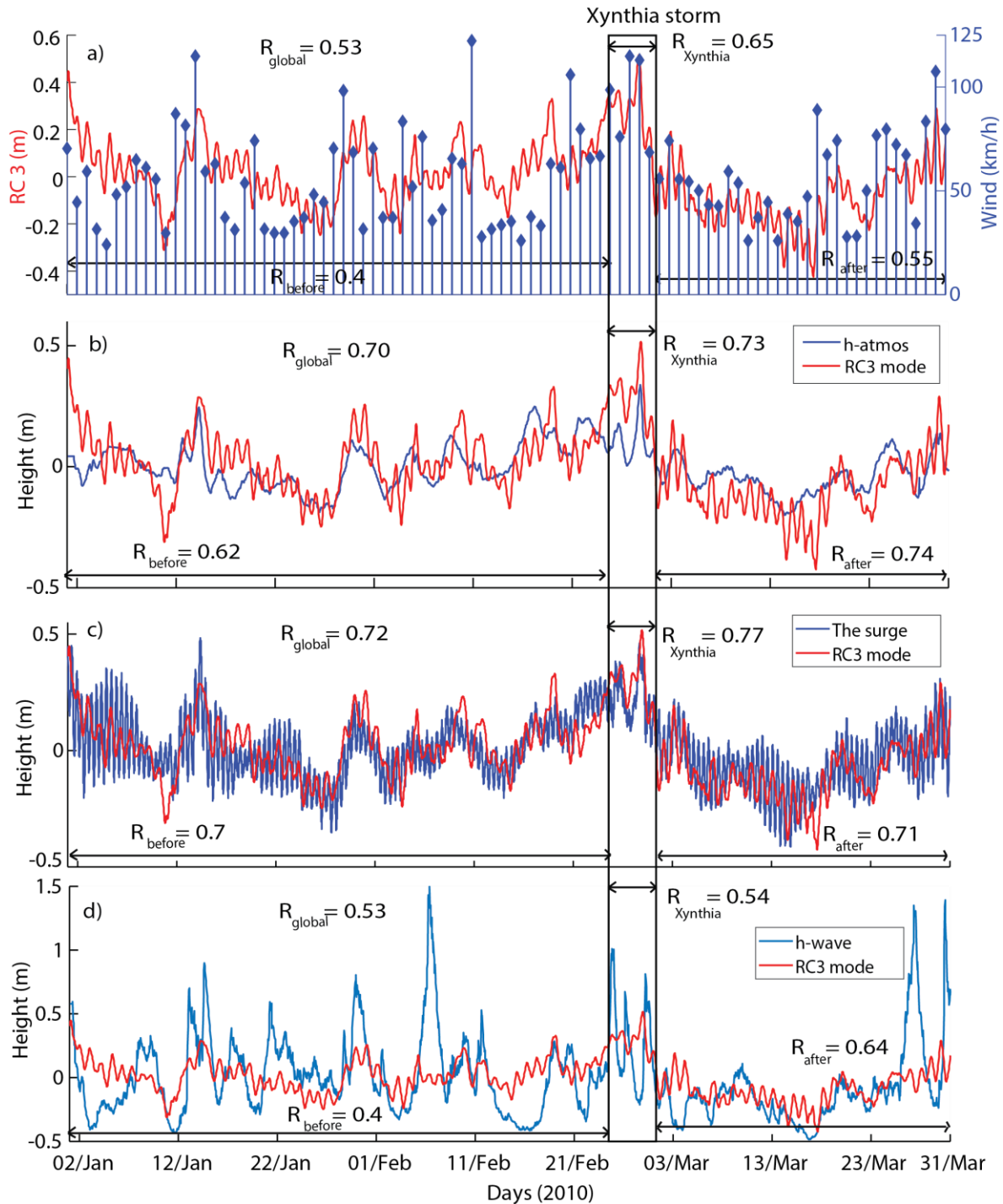


234

235 Figure 3: Impact of the time window size on the SSA results through comparisons with Socoa  
 236 tide gauge records in terms of RMSE (m) and correlation coefficient (R) (b). The blue line  
 237 corresponds to GNSS-R SSH, the red line to the 1<sup>st</sup> reconstruction mode (RC1), the purple line to  
 238 the 2<sup>nd</sup> reconstruction mode (RC2) and the green line to the sum of RC1+RC2.

239 During storms, SSH is significantly affected from other effects like atmospheric pressure (called  
 240 inverted barometer - IB), wind [46, 32], waves, which cause surges. The surge, determined from the  
 241 tide gauge records using T-Tide, the atmospheric pressure, converted into SSH ( $h_{atmos}$ ) using the  
 242 inverted barometer (IB) equation, and the wind speed (i.e. the latter two measured at the Socoa  
 243 weather station) were compared to the non-tidal component *i.e.* RC3 mode of the SSA. The result of  
 244 comparison between RC3 components with the wind speed is shown in Figure 4a,  $h_{atmos}$  in Figure  
 245 4b, the surge in Figure 4c and the SWH (measured at the Anglet buoy about 20 km away from the  
 246 Socoa station) in Figure 4d. A good agreement was found between RC3 and both the atmospheric  
 247 pressure ( $R=0.70$ ) and the surge ( $R=0.72$ ) over the whole study period. Low correlations with the  
 248 wind speed and SWH were obtained ( $R$  equals to 0.53 and 0.53 respectively). These low correlations  
 249 with the wind speed and SWH could appear surprising. But, in the inner part of the bay, the  
 250 presence of the dike is responsible for a large decrease of the wave amplitude caused by the wind. If  
 251 we focus our analysis on the 4 days of the Xynthia storm (from 27 February to 2 March 2010), the  
 252 correlation increases with three environmental variables considered here:  $R$  equals 0.73, 0.77 and  
 253 0.65 for  $h_{atmos}$ , the surge, and the wind speed respectively compared with periods before ( $R=0.62$ ,  
 254 0.70, 0.40 respectively) and after the storm ( $R=0.74$ , 0.71 and 0.55 respectively). On the contrary, a  
 255 better correlation between RC3 and SWH is found after ( $R=0.64$ ) than during ( $R=0.54$ ) Xynthia. The  
 256 larger correlation and more constant over time correlation obtained between the surge and the 3<sup>rd</sup>  
 257 reconstructed mode (RC3) of the SSA showed that RC3 and surge are strongly related. The increase  
 258 in correlation with the two other variables during the Xynthia storm event and also after can be  
 259 accounted for the large and long-term impact of the surge on the SSH.

260



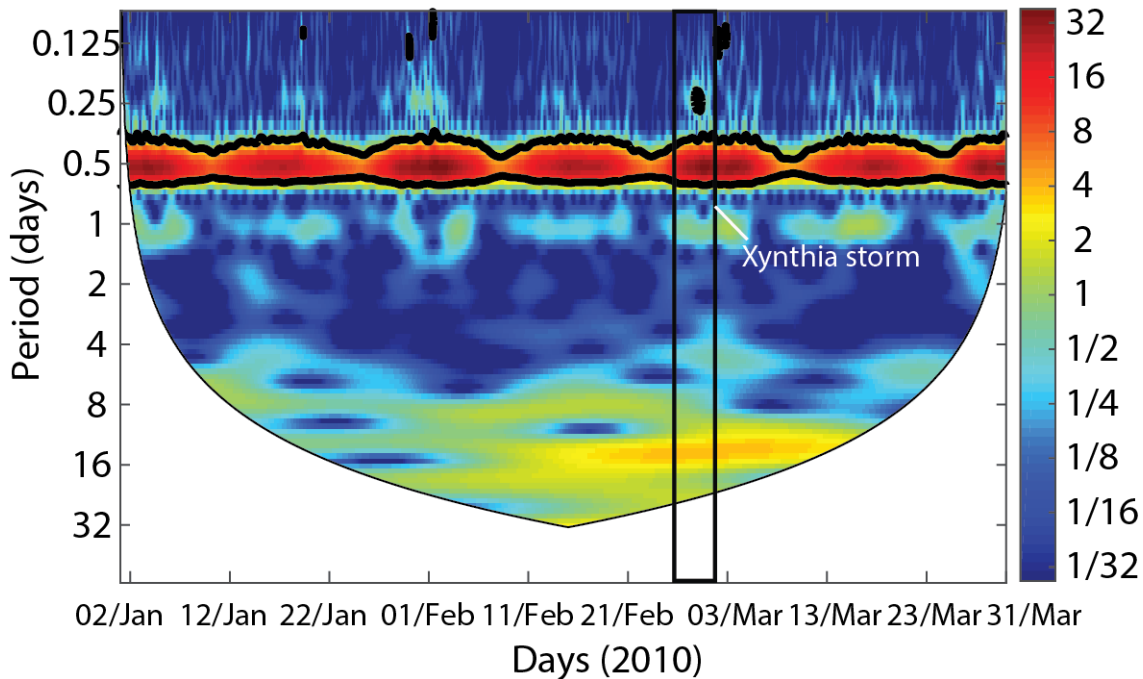
261

262 Figure 4: The GNSS-R SSH 3<sup>rd</sup> reconstruction mode (RC3) of the SSA (red) was compared to  
 263 different environmental variables (blue): the wind force (a), the IB effect (b), the surge (c), and the  
 264 SWH measured at the Anglet buoy about 20 km from Socoa station (d).

### 265 5.2. GNSS-R SSH time series analysis using CWT method

266 A continuous wavelet analysis was also applied to identify the period and temporalities of the  
 267 most energetic signals present in the time series of GNSS-R SSH from January to March 2010. The  
 268 time-frequency diagram of the CWT clearly exhibits large magnitude centered at the period of 12 h  
 269 during the whole study period (Figure 5). As for the SSA, the CWT provides a clear identification of  
 270 the main tide harmonics (semi-diurnal) present along the French Atlantic coast. A secondary  
 271 maximum, starting around the 21<sup>st</sup> of February and finishing around the 10<sup>th</sup> of March is also clearly  
 272 visible at a period of 16 days. This maximum corresponds to the low frequency of the Xynthia storm.

273 Another secondary maximum, well centered on the Xynthia storm, from the 26<sup>th</sup> of February to the  
 274 1<sup>st</sup> of March, has a period of 4 h- 8 h.



275

276 Figure 5: CWT of the GNSS-R SSH in Socoa from the 1<sup>st</sup> of January to the 31<sup>st</sup> of March 2010.

## 277 6. Discussion

### 278 6.1. The accidental tide gauge and more

279 Our results demonstrate the strong potential of the GNSS-R technique for the monitoring of the  
 280 coastal ocean. Larson et al. (2013) [37] earlier demonstrated that a GNSS geodetic station located  
 281 close to the shore can be used as an “accidental tide gauge”. In this study, we selected one of the  
 282 stations of the RGP located on the shore and obtained very accurate estimates of tides but also surge  
 283 in spite of the complex environment surrounding the station which caused perturbation of the signal  
 284 due to:

- 285 - the presence of several buildings, dikes, which mask part of the GNSS satellite and are  
 286 likely to cause parasite multipaths (more than one reflection),
- 287 - the presence of boats in the bay that are likely to also cause other parasite multipaths.

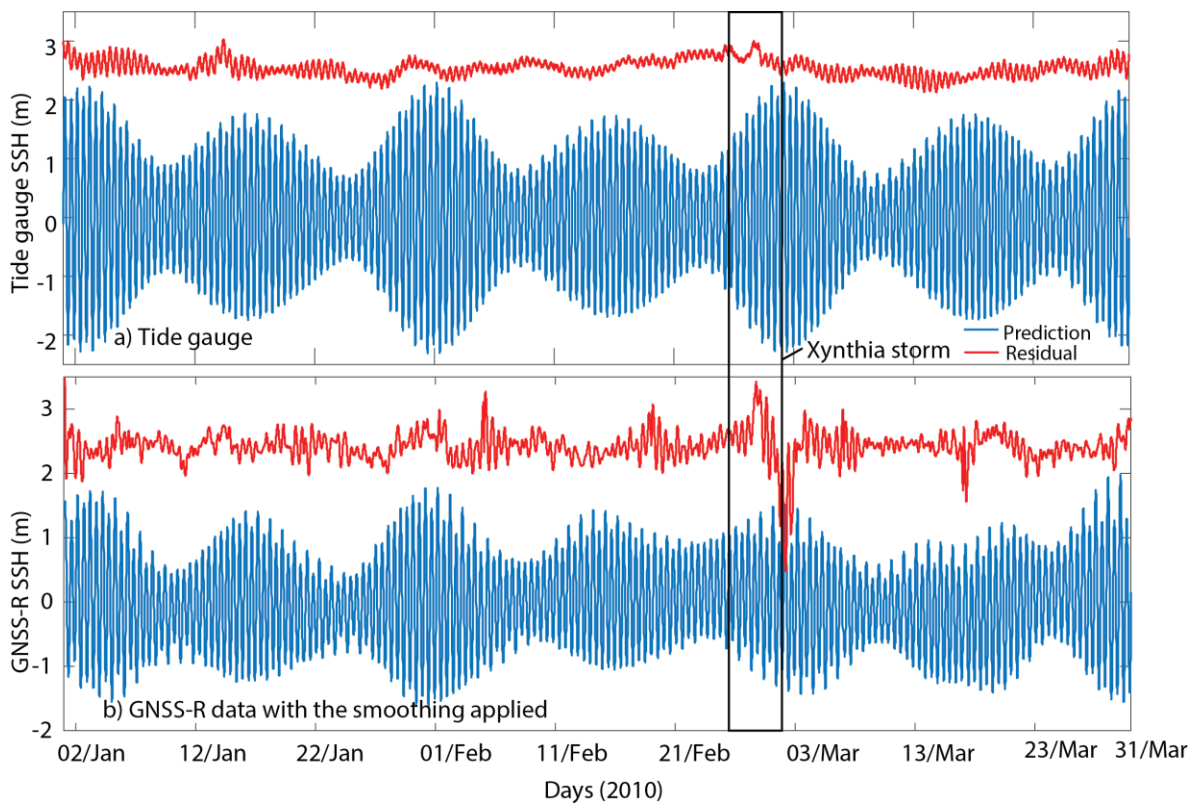
288 This means that:

- 289 - many other GNSS geodetic stations from permanent networks around the world can also be  
 290 used as accidental tide gauges to complement or improve the existing tide gauge networks,
- 291 - GNSS geodetic stations offer the opportunity to record other geophysical phenomena such  
 292 SWH (eg. Roussel et al., (2015) [22]) or surge or inverted barometer (this study).
- 293 - If located on a better environment as the top of a hill or a mast, better accuracy can be  
 294 reached (e.g. 0.12 m see [47]). The choice of the location and the altitude of deployment can  
 295 be facilitated by the use of dedicated softwares such as GNSS Reflected Signals Simulations  
 296 (GRESS) [48] or the GPS tool box [49] which provide simulation of the position of the  
 297 reflection points depending on the location of the GNSS geodetic station.

### 298 6.2. The choice of the SSA and CWT for separating tides from other geophysical parameters

299 One can wonder why not simply applying a harmonic analysis to the GNSS-R SSH such as  
 300 T-Tide harmonic analysis software [50] as performed with the tide gauge records to separate the tide

301 tides from the residual (Fig. 6a). When we applied T-Tide to the GNSS-R SSH, the signature of the  
 302 surge during Xynthia storm event is clearly visible. But the identification of the tides is less  
 303 satisfactory (presence of dissymetries) than when it is applied on the “wave protected” tide gauge  
 304 records (Fig. 6b). This is likely to be due to the larger complexity of the GNSS-R SSH that contains  
 305 the signature of different geophysical phenomena. Such dissymetries could be due to i) larger SWH  
 306 amplitudes at high tides than at low tides even if attenuated inside the bay, ii) the impact of the  
 307 Nivelle and Untxin river discharges on GNSS-R SSH that is composed of the reflections inside bay  
 308 and not punctual as the tide gauge. Other point, the tide gauge is far from these river outlets/mouths  
 309 and is less impacted by the river flows. On the contrary the use of the SSA or the CWT allows a blind  
 310 separation of the signal in different modes we were able to relate to geophysical signals, contrary to  
 311 the use of the harmonics analysis that allows a separation between the tides and a residual.



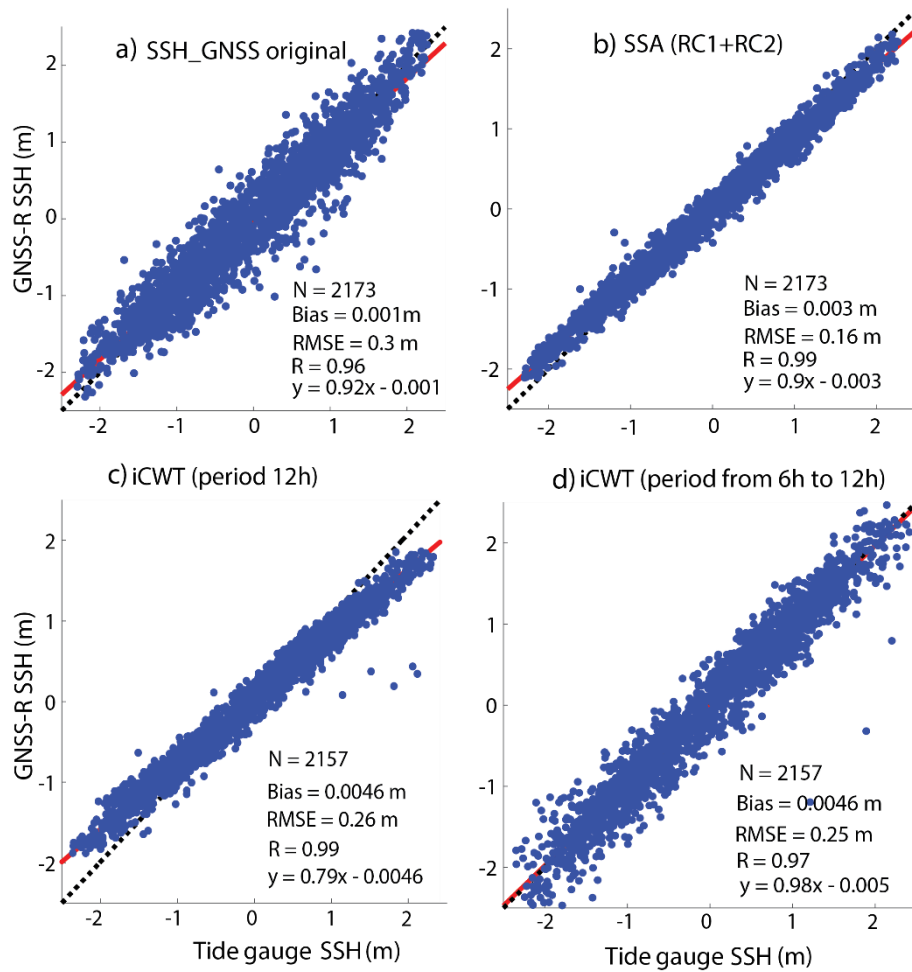
312

313 Figure 6: Tide prediction time series (blue line) using T-Tide analysis Toolbox and residual time  
 314 series (red line) after removing of tidal signal. a) For tide gauge data and b) GNSS-R SSH with the  
 315 smoothing applied.

316 6.3. The complementarity between SSA and inverse CWT (iCWT) to separate tides from other geophysical  
 317 signals

318 The GNSS-R SSH not only contains the tide components but also other geophysical signals.  
 319 Direct comparison with the tide gauge records gives quite good statistical results ( $R=0.96$  and  $RMSE$   
 320  $= 0.30$  m, see Table1 and Fig. 7a). Much better results is obtained using the two first reconstructed  
 321 modes of the SSA ( $R=0.99$  and  $RMSE = 0.16$  m, see Table1 and Fig. 7b). The use of the iCWT is more  
 322 complex. Only considering the main tide period (12h) of the iCWT, the reconstructed GNSS-R SSH is  
 323 less accurate ( $R=0.99$  but  $RMSE=0.26$  m) than the GNSS-R SSH from RC1 and RC2 and also exhibits a  
 324 slightly higher bias against the tide gauge records (bias=-0.005 m, see Table1 and Fig. 7c).  
 325 Considering a larger range of periods (6 to 12h) for the iCWT reconstructed GNSS-R SSH, improve  
 326 the slope of the regression  $\sim 1$  between tide gauge and GNSS-R SSH for a similar accuracy ( $R=0.97$   
 327 and  $RMSE=0.25$  m, see Table1 and Fig. 7d). SSA and iCWT are complementary tools for analyzing  
 328 the GNSS-R SSH estimates: the first one allows a good estimate of the tide and surge (Figs. 3, 4 and

329 7a) and the second is very useful to determine the typical time periods of the different phenomena  
 330 (Fig. 5) to relate them with their physical properties.



331  
 332 Figure 7: Comparisons between *in situ* tide gauges and: a) SSH based GNSS-R data; b) sum of  
 333 (RC1+RC2) using SSA method; c) inverse CWT at 12h frequency; d) inverse CWT from 6h to 12h  
 334 frequencies.

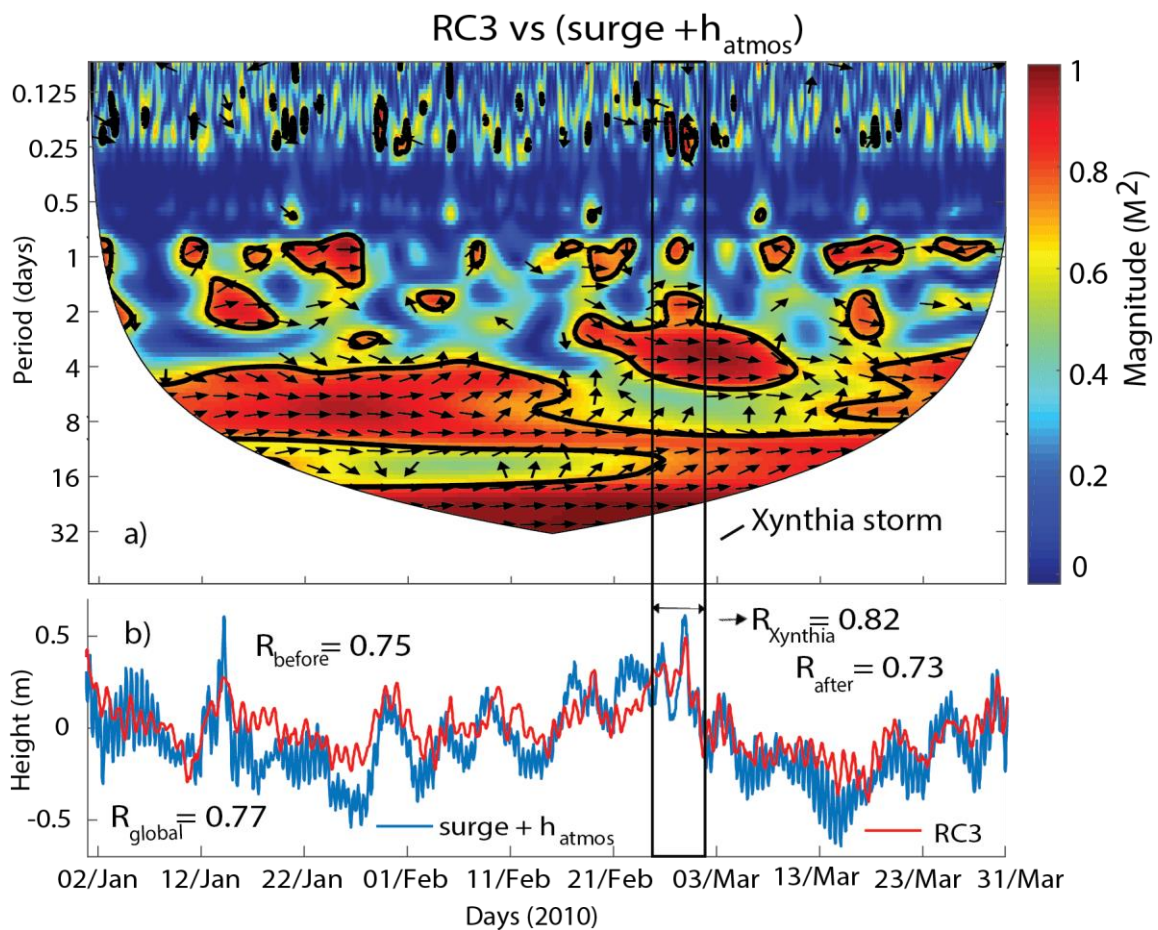
335 Table 1: Comparisons between in situ tide gauge records and GNSS-R SSH based data, sum of  
 336 (RC1+RC2) using SSA method, inverse CWT at 12h frequency, inverse CWT from 6h to 12h  
 337 frequencies (bias, RMSE and R).

|                     | Bias (m) | RMSE (m) | R    |
|---------------------|----------|----------|------|
| SSH GNSS-R          | 0.001    | 0.30     | 0.96 |
| RC1+RC2             | 0.003    | 0.16     | 0.99 |
| iCWT at 12h         | 0.005    | 0.26     | 0.99 |
| iCWT from 6h to 12h | 0.005    | 0.25     | 0.97 |

338 6.4. Is each SSA mode related to a single geophysical phenomena?

339 One can wonder if each SSA reconstructed mode can be attributed to a single and specific  
 340 geophysical phenomenon. The first two reconstructed modes were identified as the signature of  
 341 different tidal harmonics and their sum (RC1+RC2) was found to be in very good agreement with the  
 342 tide gauge records (R=0.99, Figs. 3 and 7b). But, RC3 was found to be in very good agreement with

343 the surge ( $R=0.72$ , Fig. 5c) but also with IB or  $h_{atmos}$  ( $R=0.70$ , Fig. 5b). A wavelet cross-correlation  
 344 (XWT) and a liner correlation between RC3 and the sum of the surge and  $h_{atmos}$  were performed  
 345 (Figs. 8a and b) respectively. Higher correlations were found over long time period. Very high  
 346 correlations are observed between the two variables for periods higher than two weeks. High  
 347 correlations were found on the periods 4-8 days before and after the Xynthia storm and 2-4 days  
 348 during the Xynthia storm. High correlations are also found on smaller periods (from 4h to two days)  
 349 during storm occurrences. The XWT confirms that the Xynthia storm was the more energetic event  
 350 that occurred during the observation period. Temporal correlation between RC3 and the sum of the  
 351 surge and of the IB exhibits larger values than the correlation with either the surge or the IB at all  
 352 time scales (0.77 against 0.72 and 0.70 between January and March 2010, 0.75 against 0.7 and 0.62  
 353 before the storm, 0.82 against 0.77 and 0.73 during Xynthia, 0.73 against 0.71 and 0.74 after the storm  
 354 for the sum of the surge and IB, the surge, IB respectively). As the surge and IB are strongly related,  
 355 RC3 can be seen as the signature of the storm on the GNSS-R SSH signal.



356

357 Figure 8: a) XWT for RC3 (SSA) and sum of the surge and  $h_{atmos}$ ; and b) Time series RC3 and the  
 358 surge +  $h_{atmos}$  from January to March 2010 at Socoa.

## 359 7. Conclusions

360 This study is the first convincing example of the use of GNSS-R technique to detect storm  
 361 signature on SSH through blind signal decomposition techniques as SSA and CWT. One of the mode  
 362 of the SSA decomposition was related to the temporal variations of the surge and atmospheric  
 363 fluctuations through IB ( $R=0.77$  for the study period when combining both effects). CWT allows to

364 identify the main periods of the different geophysical signals present in the GNSS-R SSH. A high (4h  
365 to 8h of period) and a low (4 and 16 days of period) frequencies were identified in the signature of  
366 the Xynthia event.

367 Our study confirms that GNSS-R approach is able to estimate SSH with almost a similar  
368 accuracy as the tide gauges ( $R=0.99$  and  $RMSE=0.16$  m on the three months of our study period)  
369 using the Socoa GNSS geodetic station from the RGP which is not located at any ideal location for  
370 SNR inversion (masks from surrounding buildings, presence of dikes and boats causing multipaths,  
371 proximity to two river mouths). Its main additional value was to demonstrate the ability of GNSS-R  
372 technique based on SNR inversion for storm detection. Our study shows that SSH monitoring would  
373 benefit from the use of the SNR records acquired by geodetic stations located along the coasts, and  
374 this secondary goal could be taken into consideration when permanent GNSS stations are installed  
375 close the shore.

376 In France, the RGP is one of the oldest permanent GNSS network in the world (late 90s) and has  
377 a dense coverage of the French metropolitan territory including the coastal areas. These long-term  
378 records could be used for long-term monitoring of the tides, but also of the wave setup and surges,  
379 and maybe, for studying sea level rise due to global warming. These “accidental” records could also  
380 present a growing interest in the context of global warming with the possible intensification of storm  
381 frequencies. Besides, as the newly installed geodetic stations now includes the acquisitions from the  
382 new constellations like GALILEO and BeiDou but also new signals as L5, E5 and E6 will increase the  
383 accuracy in the GNSS-R SSH retrievals.

384 If we consider only the very low incidence angles ( $0^{\circ}$ - $5^{\circ}$ ), the distance between the GNSS  
385 geodetic station and the farthest reflection points can reach several kilometers: 8 km for an antenna  
386 height of 60 m above the sea level and to  $\sim 28$  km for an antenna height of 250 m [48]. GNSS-R SSH  
387 could also be used for early warning in the case of huge storm and tsunami.

388  
389 **Acknowledgments:** This work was supported by Centre National de la Recherche Scientifique (CNRS) through  
390 the MISTRAL H2020 project and in the framework and by the Programme National de Télédétection Spatiale  
391 (PNTS, <http://www.insu.cnrs.fr/pnts>), grant n° PNTS-2017-05. Phuong-Lan Vu gratefully acknowledge the  
392 Vietnamese Government’s 911 project for funding during my thesis, without which the present study could not  
393 have been completed. We thank the French REFMAR network for providing us with the tide gauge records  
394 from Socoa station and the RGP (Réseau GNSS Permanent - <http://rgp.ign.fr/>) from IGN (Institut National de  
395 l’Information Géographique et Forestière) for providing the GNSS data at the SOCOA GNSS tide gauge station.  
396 We thank three anonymous Reviewers for their very helpful comments that helped us in improving the quality  
397 of the manuscript.

398 **Author Contributions:** All of the authors of the present work contributed to the discussion of the results, as  
399 well as the writing of the manuscript. Phuong-Lan Vu, Cuong Minh Ha, Frédéric Frappart, José Darrozes and  
400 Guillaume Ramillien designed the study, analyzed and discussed the preliminary results.

401 **Conflicts of Interest:** The authors declare no conflicts of interest.

402  
403  
404  
405  
406  
407  
408  
409

410

411 **References**

- 412 1. Cooper, M.J.P.; Beevers, M.D.; Oppenheimer, M. *The potential impacts of sea level rise on the coastal*  
413 *region of New Jersey, USA*; Climatic Change. **2008**; vol. 90, 475-492.
- 414 2. FitzGerald, D.M.; Fenster, M.S.; Argow, B.A.; Buynevich, I.V. *Coastal Impacts Due to Sea-Level*  
415 *Rise*; Annual Review of Earth and Planetary Sciences. **2008**; vol. 36, 601-647.
- 416 3. Kirshen, P.; Knee, K.; Ruth, M. *Climate change and coastal flooding in Metro Boston: impacts and*  
417 *adaptation strategies*. Climatic Change. **2008**. Doi: 10.1007/s10584-008-9398-9.
- 418 4. Karim, M.F.; Mimura, N. *Impacts of climate change and sea level rise on cyclonic storm surge floods in*  
419 *Bangladesh*. Global Environmental Change. **2008**; vol. 18, 490-500.
- 420 5. Bondesanf, M.; Castiglioni, G.B.; Elmis, C.; Pirazzolift, P.A.; Tomasin, A. *Coastal areas at risk from*  
421 *storm surges and sea level rise in northeastern Italy*. Journal of Coastal Research. **1995**; vol. 11, pp.  
422 1354-1379.
- 423 6. Tebaldi, C.; Strauss, B.H.; Zervas, C.E. *Modelling sea level rise impacts on storm surges along US*  
424 *coasts*. Environmental Research Letters. **2012**; vol. 7, doi:10.1088/1748-9326/7/1/014032.
- 425 7. McGranahan, G.; Balk, D.; Anderson, B. *The rising tide: assessing the risks of climate change and*  
426 *human settlements in low elevation coastal zones*. Environment and Urbanization. **2007**; vol. 7.
- 427 8. Bode, L.; Hardy, T.A. *Progress and recent developments in storm surge modeling*. Journal of  
428 Hydraulic Engineering. **1997**; vol. 123, pp. 315-331.
- 429 9. Olbert, A.L.; Hartnett, M. *Storms and surges in Irish coastal waters*. Ocean Modelling. **2010**; vol. 34,  
430 pp. 50-62.
- 431 10. McRobie, A.; Spencer, T.; Gerritsen, H. *The Big Flood: North Sea storm surge*. Philosophical  
432 Transactions of the Royal Society a: Mathematical, Physical and Engineering sciences. **2005**; vol.  
433 363; <https://doi.org/10.1098/rsta.2005.1567>.
- 434 11. De Zolt, S.; Lionello, P.; Nuhu, A.; Tomasin, A. *The disastrous storm of 4 November 1966 on Italy*.  
435 Natural Hazards and Earth System Sciences. **2006**; vol. 6, pp. 861-879.
- 436 12. Bertin, X.; Bruneau, N.; Breilh, J.F.; Fortunato, A.B.; Karpytchev, M. *Importance of wave age and*  
437 *resonance in storm surges: The case Xynthia, Bay of Biscay*. Ocean Modelling. **2012**; vol. 42, pp. 16-30.
- 438 13. Pineau-Guillou, L.; Lathuiliere, C.; Magne, R.; Louazel, S.; Corman, D.; Perherin, C. *Sea levels*  
439 *analysis and surge modelling during storm Xynthia*. European Journal of Environmental and Civil  
440 Engineering. **2012**; vol. 16, pp. 943-952.
- 441 14. Vinet, F.; Defosse, S.; Rey, T.; Boissier, L. *The production process of flooding risk in coastal area: the*  
442 *example of "Xynthia" areas*. Norois Environnement, aménagement, société. **2012**.
- 443 15. André, C.; Monfort, D.; Bouzit, M.; Vinchon, C. *Contribution of insurance data to cost assessment of*  
444 *coastal flood damage to residential buildings: insights gained from Johanna (2008) and Xynthia (2010)*  
445 *storm events*. Natural Hazards and Earth System Science. **2013**; vol. 13, pp. 2003-2012.
- 446 16. Genovese, E.; Przulski, V. *Storm surge disaster risk management: the Xynthia case study in France*.  
447 Journal of Risk Research. **2013**; vol. 16. DOI: 10.1080/13669877.2012.737826.
- 448 17. Przulski, V.; Hallegatte, S. *Gestion des risques naturels- Lecons de la tempête Xynthia*. **2014** ; HAL Id:  
449 hal-01079801.
- 450 18. Wöppelmann, G., Zerbini, S., and Marcos, M. *Tide gauges and Geodesy: a secular synergy illustrated*  
451 *by three present-day case studies*. Internal Geophysics (Geodesy). 2006; p. 980-991.
- 452 19. Martin-neira, M. *A Passive Reflectometry and Interferometry System (PARIS): Application to ocean*  
453 *altimetry*. ESA Journal. **1993**; pp. 331-355.
- 454 20. Martin-neira, M.; Caparrini, M.; Font-Rossello, J.; Lannelongue, S.; Vallmitjana, C.S. *The PARIS*  
455 *Concept: An Experimental Demonstration of Sea Surface Altimetry Using GPS Reflected Signals*. IEEE  
456 Transactions on Geoscience and Remote Sensing. **2001**; vol. 39. DOI: 10.1109/36.898676.
- 457 21. Lowe, S.T.; Zuffada, C.; Chao, Y.; Kroger, P.; Young, L.E.; LaBrecque, J.L. *5-cm-Precision aircraft*  
458 *ocean altimetry using GPS reflections*. Geophysical Research Letters. **2002**; vol. 29.
- 459 22. Roussel, N.; Ramillien, G.; Frappart, F.; Darrozes, J.; Gay, A.; Biancale, R.; Striebig, N.;  
460 Hanquiez, V.; Bertin, X.; Allain, D. *Sea level monitoring and sea state estimate using a single geodetic*  
461 *receiver*. Remote Sensing of Environment. **2015**; vol. 171, pp. 261-277.

- 462 23. Jeinking, J. *GNSS-SNR water level estimation using global optimization based on interval analysis*.  
463 *Journal of Geodetic Science*. **2016**; vol. 6, pp. 80-92.
- 464 24. Larson, K.M.; Löfgren, J.S.; Haas, R. *Coastal sea level measurements using a single geodetic GPS*  
465 *receiver*. *Advances in Space Research*. **2013**; vol. 51, pp. 1301-1310.
- 466 25. Lestarquit, L.; Peyrezabes, M.; Darrozes, J.; Motte, E. ; Roussel, N.; Wautelet, G.; Frappart, F.;  
467 Ramillien, G.; Biancale, R.; Zribi, M. *Reflectometry With an Open-Source Software GNSS Receiver:*  
468 *Use Case With Carrier Phase Altimetry*. *IEEE Journal of Selected Topics in Applied Earth*  
469 *Observations and Remote Sensing*. **2016**; vol. 9, pp. 4843-4853.
- 470 26. Roussel, N.; Frappart, F.; Ramillien, G.; Darrozes, J.; Baup, F. ; Lestarquit, L.; Ha, M.C. *Detection*  
471 *of soil moisture variations using gps and glonass snr data for elevation angles ranging from 2° to 70°*.  
472 *IEEE Journal of Selected Topics in Applied Earth Observations and Remote Sensing*. **2016**; vol. 9,  
473 pp. 4781–4794.
- 474 27. Abadie, S.; Butel, R.; Dupuis, H.; Brière, C. *Statistical parameters of waves on the south Aquitaine*  
475 *Coast*. *Comptes Rendus Geoscience*. **2005**; vol. 337, pp. 769-776.
- 476 28. Delpy, M.T.; Arduin, F.; Otheguy, P.; Jouon, A. *Effects of waves on coastal water dispersion in a*  
477 *small estuarine bay*. *Journal of Geophysical Research: Oceans*. **2014**; vol. 119, pp. 70-86.
- 478 29. Platel, J.P. *Atlas cartographique des phénomènes naturels et des caractéristiques physiques du littoral de la*  
479 *Cote Basque*. Rapport final, BRGM/RP-55262-FR. **2007**.
- 480 30. Pingree, R.D.; Mardell, G.T.; New, A.L. *Propagation of internal tides from the upper slopes of the Bay of*  
481 *Biscay*. *Nature*. **1986**; vol. 321, pp. 154-158.
- 482 31. New, A.L. *Internal tidal mixing in the Bay of Biscay*. *Deep Sea Research Part A. Oceanographic*  
483 *Research Papers*. **1988**; vol. 35, pp. 691-709.
- 484 32. Wunsch, C.; and Stammer, D. *Atmospheric loading and the oceanic “Inverted barometer” effect*.  
485 *Reviews of Geophysic*. **1997**. Vol. 35. Pages 79-107.
- 486 33. Motte, E.; Egido, A.; Roussel, N.; Boniface, K.; Frappart, F. *Applications of GNSS-R in continental*  
487 *hydrology*. *Land Surface Remote Sensing in Continental Hydrology*. **2016**; pp. 281-322.
- 488 34. Larson, K.M.; Small, E.E.; Gutmann, E.; Bilich, A.; Axelrad, P.; Braun, J. *Using GPS multipath to*  
489 *measure soil moisture fluctuations: initial results*. *GPS Solutions*.**2008**; vol. 12, p. 173–177.
- 490 35. Löfgren, J.S.; Haas, R.; Scherneck, H.G.; Bos, M.S. *Three months of local sea level derived from*  
491 *reflected: GNSS signals*. *Radio Science*. **2011**; vol. 46, pp. 1-10.
- 492 36. Bishop, G.J.; Klobuchar, J.A.; Doherty, P.H. *Multipath effects on the determination of absolute*  
493 *ionospheric time delay from GPS signals*. *Radio Science*. **1985**; vol. 20, pp. 388-396.
- 494 37. Larson, K.M et al. *The Accidental Tide Gauge: A GPS ReRflection Case study from Kachemak Bay,*  
495 *Alaska*. *IEEE Geosci. Remote Sens. Lett*. **2013b**. vol. 10, n° 15, pp. 1200-1204.
- 496 38. Broomhead, D.S.; King, G.P. *Extracting qualitative dynamics from experimental data*. *Physica D:*  
497 *Nonlinear Phenomena*. **1986**; vol. 20, pp. 217-236.
- 498 39. Vautard, R.; Yiou, P.; Ghil, M. *Singular-spectrum analysis: a toolkit for short, noisy, chaotic signals*.  
499 *Physica D: Nonlinear Phenomena*. **1992**; vol. 58, pp. 95–126.
- 500 40. Schoellhamer, D.H. *Singular spectrum analysis for time series with missing data*. *Geophysical*  
501 *Research Letters*. **2001**; vol. 28, pp. 3187–3190.
- 502 41. Claessen, D.; Groth A. *A beginner’s guide to SSA*. CERES, Ecole Normale Supérieure, Paris. **2002**.
- 503 42. Daubechies, I. *The Wavelet Transform, Time-Frequency Localization and Signal Analysis*. *IEEE*  
504 *Transactons on Information Theory*. **1990**; vol. 36, p. 961–1005.
- 505 43. Torrence, C.; Compo, G.P. *A Practical Guide to Wavelet Analysis*. *American Meteorological Society*.  
506 **1998**; vol. 79, pp. 61-78.
- 507 44. Grinsted, A.; Moore, J.C.; Jevrejeve, S. *Application of the cross wavelet transform and wavelet*  
508 *coherence to geophysical time series*. *Nonlinear Processes in Geophysics*. **2004**; vol. 11, pp. 561-566.
- 509 45. Pingree, R.D.; Le Cann, B. *Structure, strength, and seasonality of the slope current in the Bay of Biscay*  
510 *region*. *Journal of the Marine Biological Association of the United Kingdom*. **2009**; vol. 70, p.  
511 857–885.
- 512 46. Ponte, R.M. *Low-Frequency Sea Level Variability and the Inverted Barometer Effect*. *Journal of*  
513 *atmospheric and oceanic Technology*. **2006**; vol. 23. DOI: [10.1175/JTECH1864.1](https://doi.org/10.1175/JTECH1864.1).

- 514 47. Larson, K.M., Ray, R.D., and Williams, S.D. *A 10-Year Comparison of Water Levels Measured with a*  
515 *Geodetic GPS Receiver versus a Conventional Tide Gauge*. J. Atmos. Oceanic Technol. **2017**; vol. 34, p.  
516 295-307.
- 517 48. Roussel, N.; Frappart, F.; Ramillien, G.; Darrozes, J.; Desjardins, C.; Gegout, P.; Pérosanz, F.;  
518 Biancale, R. *Simulations of direct and reflected wave trajectories for ground-based GNSS-R experiments*.  
519 Geosci. Model Dev. **2014**; vol. 7, pp. 2261-2279.
- 520 49. Roesler, C., and Larson, K. M. *Software tools for GNSS interferometric reflectometry (GNSS-IR)*. GPS  
521 Solutions. **2018**; vol. 22, n° 13, p. 80.
- 522 50. Pawlowicz, R.; Beardsley, B.; Lentz, S. *Classical tidal harmonic analysis including error estimates in*  
523 *MATLAB using T\_TIDE*. Computers and Geosciences. **2002**; vol. 28, pp. 929-937.  
524

---

CHAPTER V

**Conclusion and perspectives**

---

## V.1 Conclusion

### In English:

Monitoring the sea level variations is essential to assess and warn the effects of climate change. *In situ* continuous measurements of these variations are often heterogeneous, localized and it corresponds generally to an expensive cost. On the other hand, remote sensing techniques, especially altimetry satellite, have long been conducted in the open ocean, along the coasts and in the continental water zones. In recent years, remote sensing space-based techniques have been used to study water stock variations in large river basins, providing spatio-temporal variations in inland water stocks, especially monitoring coastal dynamics (Chelton et al., 2001; Vignudelli et al., 2011; Frappart et al., 2015, 2017; Biancamaria et al., 2017). Despite a decrease in the accuracy when approaching the coast (Gommenginger et al., 2011; Obligis et al., 2011), radar altimetry measurements can be used for monitoring the sea surface height close to the shore. First of all, I have identified the limitations of altimetry in coastal areas where the waveform can also be a mix between coastal sea states, and land area answer. The errors due to the propagation delay and the land slope and/or roughness effects can also affect the recorded signal. In order to increase the number of valid data and their precision, an algorithm adapted to the radar echoes observed in the coastal area is used for the reprocessing. In chapter 3, I provide a thorough assessment of the performance of radar altimetry-based SSH for various missions (from ERS-2 to SARAL) during the period 1995-2015. The obtained SSH from satellite altimetry was then compared to the measurements at the in situ tide gauges. The results show that MLE-4 algorithm provided the most accurate estimates, especially for distances less than 10 km from the coast. The comparison statistics showed that the SARAL altimeter provides better results than other missions over the coastal area due to mainly at his weak ground footprint. The study also showed that model-based corrections of the ionosphere (GIM) and wet troposphere (ECMWF) delays

provide more realistic estimates close to the shore than the bi-frequency-based ionosphere and radiometer-based wet troposphere corrections that are generally used.

In addition to satellite altimetry data, we have also demonstrated/showed that the GNSS-R method can monitor sea level variations due to tides oceanic surges and it can, also be used to detect the extreme events and defined warning system for tsunami waves or surge storm before it reaches shore. In this study, we presented the Larson method (Larson et al., 2008a) and Roussel method (Roussel et al., 2015b) that used the SNR measurements, by inverse modelling, to retrieve sea height variations in three experiments (Red River, Mekong River Delta (Vietnam) and So-coa (France)). Our studies of Red River and Delta Mekong have shown that the  $SNR_m$  retrieve the water level with a good accuracy  $\sim 10$  cm. Our study confirms that GNSS-R approach is able to estimate SSH with a similar accuracy as the tide gauges, but also its main additional value is its ability for storm detection. For Red River, a Nida storm has been well recorded, and one can see a clear delay of 48 hours between Nida storm event and GNSS-R water level rise. This delay is due to the water transit time from the upstream watershed, where heavy rainfall occurs, to the downstream GNSS-R gauge station.

In addition, I also showed the example of the use of GNSS-R technique to detect the famous European storm, called Xynthia that occurred in winter 2010. This storm signature is clearly recorded on SSH, derived from GNSS SNR signal. Blind signal decomposition techniques as SSA and CWT highlight the sea level frequencies affected by this extreme event. Another fundamental point is that the SSA decomposition point out the interferences between temporal variations due to the oceanic surge and due to atmospheric fluctuations through IB ( $R=0.76$  for the study period when combining both effects). The last key point of SSA is its possibility to reconstruct discontinuities and/or gaps in signal due to large storm effects, e.g. electrical outages. I have used the SSA algorithm to recover missing data in a non-periodic time series. The results demonstrated that

the accuracy of data recovery depends on the window size  $M$ , larger  $M$  window size increase this accuracy, and the percentage of missing data, lower percentage ( $< 30\%$ ) improve the retrieval of the signal frequencies and amplitudes. The best results with correlation upper than 0.84 and RMSE lower than 0.65 m, are obtained with for time window  $M=96h$  and a percentage of missing data lower than 28.57%.

I present also a comparison between altimetry satellite and GNSS-R to monitor water height: the results showed that the SSH obtained from GNSS-R are better than those from altimetry satellite (*e.g.* the number of observation point and temporal resolution) but with a lowest special coverage illustrating the complementarity of both techniques. When using GNSS constellations, the farthest reflection points are located at a bit more than 8 km away from the receiver for satellite elevation above  $0^\circ$  and an antenna height of 60m (Roussel et al., 2014), but it can increase to  $\sim 28$  km for an antenna height of 250 m, so it can track storm from offshore but the time to issue a tsunami or a storm warning is short (only few ten minutes). Therefore, using GNSS-R technique is more advantageous than altimetry satellite to monitor sea level variations within 5 km from the coast. One can used GNSS-R technique to validate efficiently altimetry satellite, and for monitoring sea level rise which need long-term time series.

### **En français:**

La surveillance des variations du niveau de la mer est essentielle pour évaluer et prévenir les effets du changement climatique. Les mesures *in situ* continues de ces variations sont souvent hétérogènes, ponctuelles et présentent généralement à un coût élevé. A l’opposé, les techniques de télédétection, notamment l’altimétrie satellitaire, ont montré leur efficacité en haute mer, ceci avec une couverture mondiale, ce travail a mis en avant que l’on pouvait maintenant se rapprocher fortement des côtes. Ces dernières années, des techniques de télédétection spatiale ont aussi été utilisées pour étudier les variations des stocks d’eau dans les grands bassins fluviaux, fournissant des variations spatio-temporelles des stocks d’eaux continentaux en rapport avec la dynamique côtière (Chelton et al., 2001; Vignudelli et al., 2011; Frappart et al., 2015, 2017; Biancamaria et al., 2017). Malgré une diminution de la précision à l’approche de la côte (Gommenginger et al., 2011; Obligis et al., 2011), j’ai aussi identifié les limites de l’altimétrie dans les zones côtières où la forme d’onde est un mélange complexe entre les états de mer, les marées et la réponse des surfaces terrestres qui présente une pente topographique et/ou une rugosité qui peut fortement biaiser la mesure du niveau marin. Afin d’augmenter le nombre de données valides mais aussi leur précision, des algorithmes adaptés aux échos radar observés dans la zone côtière ont montré qu’ils étaient plus efficaces que les mesures effectuées à bord du satellite. Le chapitre 3 présente une évaluation approfondie des performances des systèmes SSH basés sur l’altimétrie radar pour diverses missions (d’ERS-2 à SARAL) au cours de la période 1995-2015. Le SSH obtenu à partir de l’altimétrie satellite a ensuite été comparée aux mesures effectuées au niveau des marégraphes *in situ*. Les résultats montrent que l’algorithme MLE-4 fournit les estimations les plus précises, en particulier près de la côte (distance < 10 km). Les données statistiques comparées ont montré que l’altimètre SARAL donne les meilleurs résultats sur la zone côtière en raison principalement de sa faible empreinte au sol. L’étude a également montré que les modèles de corrections du retard ionosphérique (GIM) et de la troposphère humide

(ECMWF) fournissent des estimations plus réalistes à proximité du rivage que les corrections obtenues à partir i) des radiomètres embarqués et ii) des mesures bi-fréquences effectuées à partir du satellite.

En plus des données altimétriques satellitaires, nous avons également démontré que nous pouvions utiliser une nouvelle méthode, le GNSS-R, qui permet de surveiller les variations du niveau de la mer, tout près des côtes. Variations qui sont dues aux marées océaniques et solides, aux surcotes marines mais également aux événements météorologiques extrêmes. Ce système devrait pouvoir être intégré aux systèmes d’alerte existant pour les tsunamis ou les surcotes liées aux tempêtes. Dans cette travail de recherche, j’ai présenté deux méthodes principales qui permettent d’inverser le signal SNR réfléchi des satellites GNSS pour obtenir la variation du niveau d’eau il s’agit de la méthode développée par (Larson et al., 2008a) et celle développée par (Roussel et al., 2015b). J’ai appliqué ces deux méthodes sur trois sites différents : i) le delta du fleuve Rouge (Vietnam), ii) le delta du Mékong (Vietnam), et iii) la baie de Socoa (France). Mes études au Vietnam ont montré que l’inversion du SNR réfléchi permet d’obtenir le niveau d’eau avec une bonne précision  $\sim 10$  cm. Sur le fleuve rouge, la tempête Nida a bien été enregistrée et on peut identifier et mesurer un net retard de 48 heures entre l’événement de tempête Nida et l’élévation du niveau d’eau GNSS-R en raison du temps de transit de l’eau du bassin versant amont, où les fortes pluies se produisent, et la station de mesure GNSS-R en aval. Sur Socoa, mon travail confirme que l’approche GNSS-R permet d’estimer le SSH avec une précision similaire à celle des marégraphes, mais que sa principale valeur ajoutée est sa capacité à détecter d’autres phénomènes comme les tempêtes.

Dans cette étude, j’ai également présenté l’exemple de l’utilisation de la technique GNSS-R pour détecter la fameuse tempête Xynthia survenue pendant l’hiver 2010. Cette signature de cette tempête est clairement enregistrée dans le SSH, dérivée du signal GNSS du SNR. Les techniques de décomposition de signaux telles que SSA et CWT mettent en évidence les fréquences du niveau de la mer affectées par cet événement extrême. Un

autre point fondamental est que la décomposition par SSA montre clairement les interférences entre les variations temporelles dues à la montée des vagues et celles dues aux fluctuations atmosphériques via IB ( $R=0,76$  pour la période étudiée en combinant les deux effets). Le dernier point clé de la SSA est sa possibilité de reconstituer des discontinuités du signal liées à aux effets des tempête, par ex. pannes électriques. J'ai utilisé l'algorithme SSA pour récupérer les données manquantes dans une série chronologique non périodique. Les résultats montrent que la qualité de la récupération des données dépend de la taille de la fenêtre  $M$  : plus la taille de la fenêtre  $M$  est grande, plus la récupération est efficace ; et plus le pourcentage de données manquantes est faible ( $< 30\%$ ) plus l'extraction des fréquences et des amplitudes du signal manquant sera efficace. Les meilleurs résultats sont obtenus, avec une corrélation supérieure à  $0,84$  et une RMSE inférieure à  $0,65$  m, pour une fenêtre temporelle  $M = 96$  h et un pourcentage de données manquantes inférieur à  $28,57\%$ .

J'ai aussi établi une comparaison entre le satellite altimétrique et le GNSS-R pour surveiller la hauteur d'eau : les résultats ont montré que les SSH obtenus à partir du GNSS-R sont meilleurs que ceux obtenus à partir du satellite altimétrique (*e.g.* le nombre de points d'observation et la résolution temporelle) par contre la couverture spatiale GNSS-R, à partir d'une station in situ, est nettement plus faible ce qui confirme la complémentarité de ces deux techniques. Lorsque l'on utilise des constellations GNSS, les points de réflexion les plus éloignés se trouvent à un peu plus de  $8$  km du récepteur pour une élévation du satellite proche de  $0^\circ$  et une hauteur d'antenne de  $60$  m (Roussel et al., 2014), mais la couverture peut atteindre  $\sim 28$  km pour une hauteur d'antenne de  $250$  m, ce qui permet de suivre l'arrivée d'une tempête avant qu'elle n'atteigne la côte. Cependant le temps nécessaire pour alerter sur l'arrivée d'un évènement extrême tel qu'un tsunami ou une tempête est assez court (quelques dix minutes seulement). L'utilisation de la technique GNSS-R est donc plus avantageuse que celle du satellite altimétrique pour surveiller les variations du niveau de la mer dans un rayon de  $5$  km de la côte. On peut aussi

l'utiliser pour valider les données altimétriques satellitaires ou bien faire des suivis temporels sur les évènements longs termes comme la montée du niveau marin lié au réchauffement climatique.

## V.2 Perspectives

### **In English:**

Satellite altimetry is an important measurement tool for coastal studies. With the launch of new SAR and interferometry missions, high accuracy and spatial coverage will be improved in the study of coastal areas. Put into orbit since April 2010, Cryostat 2 carries an altimeter equipped with a SAR and interferometric mode. The ground footprint of this altimeter will be about 10 times smaller than Envisat's, resulting in applications in coastal areas that would provide better spatial resolution and more accurate observations. The new altimeter also uses this SAR mode: Sentinel-3A launched in 2016 and Sentinel-3B launched in April 2018. Another project combining interferometric mode and the use of a Ka band: SWOT, scheduled to be launched in orbit in 2020, can complement traditional measurement data in coastal areas where it is very difficult to maintain or even acquire measurements.

We have seen that the GNSS-R, along with the recent development of different GNSS constellations, is and will be a fundamental tool for monitoring environmental phenomena. With the launch of TechDemoSat-1, the space segment opens up to reflectometry applications. With the launch of CYGNSS, <sup>3</sup>CAT-2 and the future establishment of a receiver on the international station, interest from scientists and private sector professionals is expected to increase, as these new vectors allow us to monitor storms, tsunamis, changes in droughts, rivers and ice, etc. These applications are now accessible through industrial receivers developed by young startups who saw the potential of GNSS-R technology and the numerous markets that they could conquer with it.

There are still many methodological and technical leaps to be made:

- Accuracy needs to be improved. Already, recent studies have shown that by using the signal phase, we could easily achieve altimetry precision to the centimeter (airborne tests in France ([Lestarquit et al., 2016](#)) and an accuracy of about 2– 3% ([Egido, 2013](#)) in terms of

volumetric water is already available. Can we, as in conventional GNSS, achieve superior quality information? This will include, as in conventional GNSS, better resolution of integer ambiguities, through improved antennas and an indispensable acquisition of all the constellations in dual-, or better, tri-frequency;

- The corollary of this increased flow of data acquired in real time and/or with a high sampling frequency (second or less) is that it will fill the bottleneck imposed by the transfer rate between the waveform acquisition system and storage systems. Currently, these systems allow us to track multiple satellites with multiple frequencies while retaining the shapes of waves as completely as possible (here, we mean GB/min). Another key problem for satellite solutions is the energy consumption: in fact, real-time systems use advanced processors which are highly energy-consuming;
- Finally, for  $\mu$ satellite (CubeSat) and/or RPAS platforms, the weight of the device and antennas and their miniaturization are also fundamental points to be improved.

### **En français:**

L'altimétrie par satellite est un outil important pour les études de la frange côtière. Avec le lancement de nouvelles missions SAR, la résolution spatiale et la couverture spatiale seront améliorées notamment dans les zones côtières. Avec la mise en orbite depuis avril 2010 de Cryostat 2, qui est équipé d'un altimètre radar (mode SAR et interférométrique) et dont la tache au sol est environ 10 fois plus petite que celle d'Envisat, il existe là aussi un outil adapté pour les applications en zone côtière. Le nouvel altimètre également en mode SAR du satellite Sentinel-3A lancé en 2016 et Sentinel-3B lancé en avril 2018 sera aussi un apport important pour la compréhension du domaine côtier. Un autre projet clé, associant le mode interférométrique et l'utilisation d'une bande Ka, est le projet SWOT qui permettra de compléter le dispositif des mesures traditionnelles; son lancement est prévu pour 2020.

Pour ce qui est de l'outil GNSS-R, nous avons vu qu'avec le développement récent de différentes constellations GNSS, il peut devenir un outil fondamental et pérenne pour la surveillance des phénomènes environnementaux. Avec le lancement de TechDemoSat-1, le segment spatial est maintenant ouvert aux applications de réflectométrie. Avec le lancement de CYGNSS, de 3CAT-2 et la mise en place future d'un récepteur sur la station internationale, l'intérêt des scientifiques et des professionnels du secteur privé devrait augmenter, ces nouveaux vecteurs nous permettant de surveiller les tempêtes, les tsunamis, les changements de sécheresse, les rivières et la glace, etc. Ces applications sont maintenant accessibles via des récepteurs industriels développés par de jeunes startups qui ont compris le potentiel de la technologie GNSS-R et les nombreux marchés qu'elles pourraient conquérir.

Il reste encore beaucoup à faire sur le plan méthodologique et technique:

- La précision des mesures environnementales doit être améliorée. Déjà, des études récentes ont montré qu'en utilisant la phase du signal, nous pouvons facilement obtenir une précision altimétrique centimétrique (essais en vol effectué en France ([Lestarquit et al., 2016](#))). Pouvons-nous, comme dans le GNSS conventionnel, obtenir des informations de qualité supérieure? Cela passera, comme pour le GNSS classique, par une meilleure résolution des ambiguïtés entières, grâce à des antennes améliorées et une acquisition indispensable de toutes les constellations en double. - ou mieux, tri-fréquence; Pour l'humidité des sols, une précision d'environ 2 à 3% sur les surfaces continentales est déjà disponible. Cependant, le suivi de ces paramètres présente de nombreux verrous qui devront être levés :
- Le corollaire de cet accroissement du flux de données acquises en temps réel ou à un pas d'échantillonnage temporel très élevé (à la seconde voir moins) est qu'il faudra combler le goulot d'étranglement imposé par le taux de transfert entre le système d'acquisition de formes d'ondes et les systèmes de stockage sur disques. Actuelle-

ment, ces systèmes nous permettent de suivre que quelques satellites avec plusieurs fréquences tout en conservant le plus possible la forme des ondes (nous parlons ici de Go/min). La consommation d'énergie est aussi un autre problème aux solutions satellitaires: en fait, les systèmes en temps réel utilisent des processeurs avancés avec un nombre croissant de corrélateurs qui consomment beaucoup d'énergie;

- Enfin, pour les plates-formes des  $\mu$ satellites (CubeSat) ou des drones, le poids de l'appareil et des antennes et leur miniaturisation sont également des points fondamentaux à améliorer.

# List of Figures

| No.  | Title  | Page No. |
|------|--|----------|
| I.1  | Principle of satellite altimetry ( <a href="#">Frappart et al., 2017</a> ) . . . .   | 16       |
| I.2  | Principle of the waveform analysis (CNES) . . . . .  | 17       |
| I.3  | Error budget for altimeter missions (©LEGOS/CNRS) . .  | 23       |
| I.4  | Theoretical ocean waveform from the Brown model ( <a href="#">Brown, 1977</a> ) and its characteristics (©AVISO/CNES) . . . . .  | 23       |
| I.5  | Typical waveform shapes over inland water (modified from ( <a href="#">Berry et al., 2005</a> )). . . . .  | 25       |
| I.6  | Perturbation of the radar waveform by the emerged lands within the altimeter footprint (© CLS). . . . .  | 26       |
| I.7  | Percentage of types echoes encountered in offshore environment (modified from ( <a href="#">Thibaut, 2008</a> )). . . . .  | 27       |
| I.8  | Schematic diagram of the OCOG algorithm ( <a href="#">Wingham et al., 1986</a> ). . . . .  | 31       |
| I.9  | Theoretical waveform sought by the Ice-2 algorithm ( <a href="#">Rémy et al., 1997</a> ) . . . . .   | 32       |
| I.10 | Schematic diagram of 5- $\beta$ parameter fitting method ( <a href="#">Martin et al., 1983</a> ) . . . . .   | 34       |
| I.11 | Delay-doppler isocontours on the ground supposed to be a perfect spherical surface (9 first isorange contours, and 14 isodoppler contours). The horizontal line is the trajectory of the satellite ( <a href="#">Frappart et al., 2017</a> ) . . . . . | 35       |
| I.12 | Schematic description of the slope error for an incline surface $\alpha$ (NASA). . . . .   | 41       |

|      |  |    |
|------|--|----|
| II.1 | Coverage density of the two oldest GNSS constellations: the US GPS system (orange) and the Soviet GLONASS system (green). However, there is a lack of coverage at the poles, this hole is more important for the GPS system than for the GLONASS system. On this representation are represented the different positions, during a day, of the set of satellites of each constellation, the time step between two positions is fifteen minutes. N.B.: the distance from Earth (blue sphere) to satellite is not to scale. . . . .             | 51 |
| II.2 | Structure of the modernized L-band GPS signals, the M-code is a new version of previous military P(Y) code. For Block IIR-M, IIF, and subsequent blocks, the $L_2C$ signal, scheduled to be the first of the modernized civil GPS signals. It will provide greater accuracy and robustness and faster signal acquisition than the current $L_1$ C/A-code signal. It is combination of C/A and two additional PRN ranging codes will be transmitted: $L_2$ Civil Moderate ( $L_2$ CM) code and the $L_2$ Civil Long ( $L_2$ CL) code. . . . . | 53 |
| II.3 | Multipath phenomenon on GNSS signals. $\varepsilon_i$ : angle of incidence. $\varepsilon_r$ : angle of reflection. Here we can see three different paths one with one reflection (left path) and the second one with 2 reflections (right path) and the last one, the center path corresponds to the direct path. To estimate SSH from GNSS signal, only one reflection (left path) is used. . . . .   | 67 |
| II.4 | Specular and diffuse reflection . . . . .  | 68 |
| II.5 | Glistening zone, decomposition of the reflective surface into multiple reflective facets. (Adapted from ( <a href="#">Shuanggen Jin, 2014</a> )). . . . .  | 71 |
| II.6 | Principle of the cGNSS-R. The receiver records the waveform of the direct and reflected signals and correlate them with local replicas generated by the receivers (modified from ( <a href="#">Kucwaj, 2016</a> )). . . . .  | 74 |

## List of Figures

---

|       |   |     |
|-------|---|-----|
| II.7  | Principle of iGNSS-R. The receiver records the reflected signal and correlates it with the direct signal by the receiver. D and R mean direct and reflected paths (modified from (Kucwaj, 2016)). . . . .   | 75  |
| II.8  | Principle of GNSS reflectometry with double antenna. $T$ : satellite/transmitter; $S$ : specular reflection point; $\varepsilon$ : satellite elevation; $\Delta\delta AB(t)$ : additional path covered by the reflected wave; $d$ : interdistance between the LHCP and RHCP antennas; and $h$ : height of the receiver above the reflecting surface (Roussel et al., 2014). . . . .   | 76  |
| II.9  | <i>In-situ</i> measurement scheme by the IPT method; a) geometry of the reflected multipath, position of the specular point that corresponds to the center of the first Fresnel surface (in blue); b) representation of the different polarizations recorded by an antenna "classic". . . . .   | 79  |
| II.10 | Waveforms depending on the type of scatter applied to a perfectly flat land surface (lake) and more or less rough ocean. For each profile, the blue curve shows the total waveform and the black curves show the individual reflections near the specular points, which are involved in the construction of the waveform. With $P_{spe}$ : specular point. On the maps, the path in blue corresponds to the path of the specular point. . . . . | 80  |
| II.11 | Geometry of a GNSS reflectometer with single antenna. . .   | 83  |
| II.12 | Phase diagram of the received GNSS signal illustrating the relationships between the phase (I) and quadrature (Q) components of the signal. . . . .   | 85  |
| IV.1  | Main permanent GNSS stations in Europe. With GNSS-R altimetry, coastal GNSS station are potential tide gauges (EUREF Permanent GNSS Network). . . . .   | 126 |

|   |     |
|---|-----|
| IV.2 Variations in the distance between the antenna and the specular reflection points (a) and the surface area of the first Fresnel surfaces (b) as a function of the elevation angle of the satellites and for different antenna heights.( <a href="#">Roussel et al., 2016</a> ) . . . . .   | 127 |
| IV.3 a) Processing flow chart of the data presenting the successive steps of the processing of SNR data to sea level variation time series: the input, the different steps of the processing, and the output; b) Example of raw SNR data time series (input); c) Example of SNR detrended data time-series with ascending part and descending part. . . . . | 132 |
| IV.4 Principle of the Least Squares inversion Method used to determine $h$ and $\dot{h}$ based on LSP estimates of $f$ . For reasons of clarity, overlapping was not represented in this figure, even if in our case $\delta t > \Delta t$ . . . . .  | 136 |
| IV.5 Time series $SSH_{GNSS}$ original lost two days of data during the storm and RCs using SSA method to reconstruct the tide components from 22 <sup>th</sup> February to 08 <sup>th</sup> March with the window size M of 2h, 6h, 12h, 24h, 48h, 72h and 96h, respectively. . . . .  | 141 |
| IV.6 Time series $SSH_{GNSS}$ original from 22 <sup>th</sup> February to 08 <sup>th</sup> March lost 6 days, 5 days, 4 days, 3 days, 2 days and 1 day of data, respectively, and RCs using SSA method to reconstruct the tide components with the window size M of 96h. . . . .   | 142 |
| IV.7 a) Location of the GNSS receiver at the SCOA station (43°23'42.83"N, 01°40'54.05"O); b) view of the antenna TRM55971.00 set up at 10.664 m above the sea surface ( <a href="http://rgp.ign.fr">http://rgp.ign.fr</a> ). . . . .  | 145 |

## List of Figures

---

|         |   |     |
|---------|---|-----|
| IV.8    | Locations of the specular reflection points for the GNSS receiver installed at the SCOA station 1 <sup>st</sup> March 2010. Only GPS and GLONASS satellites with elevation angles from 0° to 25° were considered for estimating SSH variations. Green points in the inside part, with azimuths from 60° to 210°. Pink points in the outside part, with azimuthal ranges 0°/60° and 330°/360° . . . . .    | 146 |
| IV.9    | Comparisons between in situ tide gauges and: a) SSH based GNSS data; b) sum of (RC1+RC2) using SSA method; c) inverse CWT at 12h frequency; d) inverse CWT from 6h to 12h frequencies. . . . .  | 150 |
| IV.10   | Tide prediction time series (blue line) using T-Tide analysis Toolbox and residual (the surge) time series (red line) after removing of tidal signal for tide gauge data . . . . .  | 151 |
| IV.11a) | XWT results for RC3 (SSA) and the surges and $h_{atmos}$ ; b) Time series RC3 and the surges + $h_{atmos}$ from January to March 2010 at Socoa. . . . .   | 152 |
| IV.12   | The GNSS receiver with a single antenna set up at about 30 m above water level, on the top of the Tran De water tower, Mekong Delta, Vietnam (Ha, 2018). . . . .  | 154 |
| IV.13   | Locations of the specular reflection points and Fresnel surface for a GNSS receiver on the top of the Tran De water tower from 23 <sup>th</sup> to 30 August 2016 (all satellites with elevation angles from 0° to 25°)(Ha, 2018): a) Simulation of SNR multipath using IPT method of Larson (Larson et al., 2008b); b) Simulation of SNR multipath using Roussel method (Roussel et al., 2015b). . . . . | 156 |
| IV.14   | Comparisons between water level height estimated from SNR measurements obtained with Larson method (a, 369 measurements), Roussel method (b, 1989 measurements) and Tran De tide gauge (cyan line), from 23 <sup>th</sup> to 30 <sup>th</sup> August 2016.modified from (Ha, 2018) . . . . .  | 158 |

|       |   |     |
|-------|---|-----|
| IV.15 | The GNSS receiver with a single antenna installed on the top of the old bridge abutment ( $21^{\circ}2'44.04''\text{N}$ , $105^{\circ}51'48.86''\text{E}$ ) on the Red river in Hanoi, Vietnam from the 27 <sup>th</sup> July to 12 <sup>th</sup> August 2016.(Ha, 2018) . . . . .  | 160 |
| IV.16 | Position of the GPS (a), GLONASS (b) specular reflection points and their first Fresnel surface for a GNSS receiver on Red River campaign. Simulations doe the 08 <sup>th</sup> of August 2016 with two range of satellite elevation angles $\theta$ : High satellite elevation (in magenta; from $30^{\circ}$ to $70^{\circ}$ ) and low satellite elevation (in green: $6^{\circ}$ - $30^{\circ}$ in the left side and $18^{\circ}$ - $30^{\circ}$ in the right side. Sampling rate is equal to 15 mins ( <i>i.e.</i> , satellites positions are actualized every 15 mins); the cyan area shows flooded area during the storm event.(Ha, 2018) | 161 |
| IV.17 | Comparisons between heights estimated from SNR measurements obtained using methods LSM (a), method Larson (b) with only the GPS/GLONASS/GPS+GLONASS constellations versus height recorded from the hydrological station during the period of the Mirinae and Nida storms (from the 27 <sup>th</sup> July to 12 <sup>th</sup> August 2016)(Ha, 2018). . . . .  | 163 |

# List of Tables

| No.  | Title  | Page No. |
|------|--|----------|
| I.1  | Main characteristics of the altimetry missions (Adapted from AVISO/CNES). . . . .  | 43       |
| II.1 | Characteristics of operational or most advanced GNSS constellations. The arrow indicates future developments. The set of GNSS frequency modulation codes is also presented: Binary Phase Shift Keying (BPSK: the most classic); Binary Offset Carrier (BOC); Multiplexed BOC (MBOC); Time Multiplexed BOC (TMBOC); Composite BOC (CBOC); Alternate BOC (AltBOC); Quadrature Phase Shift Keying (QPSK). Done on March 28, 2018, this table may therefore have evolved following the launches of the different satellites of the various constellations. . . . . | 58       |
| II.2 | Correspondence between channel number and sub-band for GLONASS $L_1$ and $L_2$ carrierse different satellites of the various constellations. . . . .   | 59       |
| IV.1 | Comparison of bias, RMSE and the correlation coefficient (R) between 2 days recovered data and <i>in-situ</i> tide gauge at the same period . . . . .  | 140      |
| IV.2 | Comparison of bias, RMSE and the correlation coefficient (R) between recovered data with the window size M of 96h and <i>in-situ</i> tide gauge at the same period . . . . .   | 143      |
| IV.3 | Comparison between the $SHH_{in-situ}$ gauges with the $SSH_{GNSS}$ time series calculated with the GPS constellation/GLONASS constellation/combined constellations at the SCOA station from 01/01/2010 to 31/03/2010. (a) Outside part (dynamic case); (b) Inside part (static case). . . . .   | 148      |

IV.4 Comparison between the *in-situ* gauges with the raw SNR-based time series calculated with only the GPS constellation/GLONASS constellation/both constellations. a) In static case; b) In dynamic case.([Ha, 2018](#)) . . . . . 157

IV.5 Comparison between the *in-situ* gauges with the raw SNR-based time series calculated using different ranges of satellite elevation with only the GPS/GLONASS/GPS+GLONASS constellations. a) In static case and b) In dynamic case. . . . . 163

# Bibliography

- Abadie, S., Butel, R., Dupuis, H., and Brière, C. (2005). Paramètres statistiques de la houle au large de la côte sud-aquitaine. *Comptes Rendus Geoscience*, 337(8):769 – 776.
- Allen, M. R. and Smith, L. A. (1997). Optimal filtering in singular spectrum analysis. *Physics Letters A*, 234(6):419 – 428.
- Alonso-Arroyo, A., Camps, A., Park, H., Pascual, D., Onrubia, R., and Martín, F. (2015). Retrieval of significant wave height and mean sea surface level using the gnss-r interference pattern technique: Results from a three-month field campaign. *IEEE Transactions on Geoscience and Remote Sensing*, 53(6):3198–3209.
- Amarouche, L., Thibaut, P., Zanife, O., Dumont, J., Vincent, P., and Steunou, N. (2004). Improving the jason-1 ground retracking to better account for attitude effects. *Marine Geodesy*, 27(1-2):171–197.
- Anderson, K. D. (2000). Determination of water level and tides using interferometric observations of gps signals. *Journal of Atmospheric and Oceanic Technology*, 17(8):1118–1127.
- Andréani, A. (2001). *Le GPS : une révolution - lack of GPS christopher columbus never found the Indies*. Number 160p. Sciences et Tec, Paris, jean jarry edition. Langue : Français.
- Anthony, E. J., Brunier, G., Besset, M., M.: Dussouillez, P. G., V-L., and Nguyen (2015). Linking rapid erosion of the mekong river delta to human activities. *Scientific reports*.
- Auber, J.-C., Bibaut, A., and Rigal, J.-M. (1994). Characterization of multipath on land and sea at gps frequencies," proceedings of the 7th international technical meeting of the satellite division of the institute of navigation. *Proceedings of the 7th International Technical Meeting of*

- the Satellite Division of The Institute of Navigation (ION GPS 1994) September 20 - 23, 1994 Salt Palace Convention Center Salt Lake City, UT*, pages 1155–1171.
- Azmani, M. (2010). *Fusion non-linéaire appliquée aux voies pilote et données du signal GPS L2C*. phdthesis, l'Université du Littoral Côte d'Opale, 50 rue Ferdinand Buisson – B.P. 719, 62228 Calais Cedex, France. ULCO 2010.30.
- Bamber, J. L. (1994). Ice sheet altimeter processing scheme. *International Journal of Remote Sensing*, 15(4):925–938.
- Beckmann, P. and Spizzichino, A. (1987). *The Scattering of Electromagnetic Waves from Rough Surfaces*. Artech House Radar Library.
- Berry, P. (2000). Topography from land radar altimeter data: Possibilities and restrictions. *Physics and Chemistry of the Earth, Part A: Solid Earth and Geodesy*, 25(1):81 – 88.
- Berry, P., Garwick, J., Freeman, J., and Mathers, E. L. (2005). Global inland water monitoring from multi-mission altimetry. *Geophysical Research Letters*, 32.
- Biancamaria, S., Frappart, F., Leleu, A.-S., Marieu, V., Blumstein, D., Desjonquères, J.-D., Boy, F., Sottolichio, A., and Valle-Levinson, A. (2017). Satellite radar altimetry water elevations performance over a 200m wide river: Evaluation over the garonne river. *Advances in Space Research*, 59(1):128 – 146.
- Bilich, A. (2006). Improving the precision and accuracy of geodetic gps: Applications to multipath and seismology.
- Bilich, A. and Larson, K. M. (2007). Mapping the gps multipath environment using the signal-to-noise ratio (snr). *Radio Science*, 42(6).
- Birol, F., Fuller, N., Lyard, F., Cancet, M., Niño, F., Delebecque, C., Fleury, S., Toub Blanc, F., Melet, A., Saraceno, M., and Leger, F. (2016).

## Bibliography

---

- Coastal applications from nadir altimetry: Example of the x-track regional products. *Advances in Space Research*, 59.
- Bishop, G. J., Klobuchar, J. A., and Doherty, P. H. (1985). Multipath effects on the determination of absolute ionospheric time delay from gps signals. *Radio Science*, 20(3):388–396.
- Blewitt, G., Altamimi, Z., Davis, J., Gross, R., Kuo, C.-Y., Lemoine, F. G., Moore, A. W., Neilan, R. E., Plag, H.-P., Rothacher, M., Shum, C. K., Sideris, M. G., Tregoning, P., and Zerbini, S. (2010). Geodetic observations and global reference frame contributions to understanding sea-level rise and variability.
- Bode, L. and A. Hardy, T. (1997). Progress and recent developments in storm surge modeling. *Journal of Hydraulic Engineering-asce - J HYDRAUL ENG-ASCE*, 123.
- Bondesan, M. (1995). Coastal areas at risk from storm surges and sea-level rise in northeastern italy. *Journal of Coastal Research*, 11:1354–1379.
- Brenner, A., Bindschadler, R., Zwally, H., and Thomas, R. H. (1983). Slope-induced errors in radar altimetry over continental ice sheets. *Journal of Geophysical Research*, 88:1617–1623.
- Brooks, R. L., Lockwood, D. W., and Lee, J. E. (1997). Land effects on topex radar altimeter measurements on pacific rim coastal zones. Technical report, Laboratory for Hydrospheric Processes, Wallops Flight Facility, NASA Goddard Space Flight Center, Wallops Island, VA 23337 USA.
- Broomhead, D. and King, G. P. (1986). Extracting qualitative dynamics from experimental data. *Physica D: Nonlinear Phenomena*, 20(2):217 – 236.
- Brown, G. (1977). The average impulse response of a rough surface and its applications. *IEEE Transactions on Antennas and Propagation*, 25(1):67–74.

- Callahan, P. S., E., and Rodriguez (2004). Retracking of jason-1 data. *Marine Geodesy*, 27.
- Camps, A., Caparrini, M., Sabia, R., and Ruffini, G. (2006). Sea surface salinity retrieval from space: Potential synergetic use of gnss-r signals to improve the sea state correction and application to the smos mission. In *2006 IEEE MicroRad*, pages 91–96.
- Camps, A., Pascual, D., Park, H., and Martín, F. (2012). Paris iod: Id-16a contribution to performance and error budgets. Technical report, ESA Project AO/1-6576/2010/F/WE – ID 51 GNSS-R-Feasibility Study (Phase A).
- Cardellach, E. (2001). *Sea Surface Determination Using GNSS Reflected Signals*. PhD thesis, Universitat Politecnica de Catalunya (UPC).
- Cardellach, E., Fabra, F., Rius, A., Pettinato, S., and D’Addio, S. (2012). Characterization of dry-snow sub-structure using gnss reflected signals. *Remote Sensing of Environment*, 124(0):122–134. 0034-4257.
- Cartwright, D. E. and Tayler, R. J. (1971). New Computations of the Tide-generating Potential. *Geophysical Journal International*, 23(1):45–73.
- Chelton, D. B., Ries, J. C., Haines, B. J., Fu, L.-L., and Callahan, P. S. (2001). Chapter 1 satellite altimetry. In Fu, L.-L. and Cazenave, A., editors, *Satellite Altimetry and Earth Sciences A Handbook of Techniques and Applications*, volume 69 of *International Geophysics*, pages 1 – ii. Academic Press.
- Chew, C., Small, E. E., and Larson, K. M. (2016). An algorithm for soil moisture estimation using gps-interferometric reflectometry for bare and vegetated soil. *GPS Solutions*, 20(3):525–537.
- Cooper, M. J. P., Beevers, M. D., and Oppenheimer, M. (2008). The potential impacts of sea level rise on the coastal region of new jersey, usa. *Climatic Change*, 90(4):475.

## Bibliography

---

- Creel, L. (2003). *Ripple Effects: Population and Coastal Regions*.
- Dang, Q.-T., Nguyen, S., T-P., and Nguyen (2005). Flood control for the red river. Technical report.
- Darrozés, J., Roussel, N., and Zribi, M. (2016). 7 - the reflected global navigation satellite system (gnss-r): from theory to practice. In Baghdadi, N. and Zribi, M., editors, *Microwave Remote Sensing of Land Surface*, pages 303 – 355. Elsevier.
- Davis, C. H. (1995). Growth of the greenland ice sheet: a performance assessment of altimeter retracking algorithms. *IEEE Transactions on Geoscience and Remote Sensing*, 33(5):1108–1116.
- Delpey, M., Ardhuin, F., Otheguy, P., and Jouon, A. (2014). Effects of waves on coastal water dispersion in a small estuarine bay. *Journal of Geophysical Research*, 119:70.
- Deng, X. and Featherstone, W. (2006). A coastal retracking system for satellite radar altimeter waveforms: Application to ers-2 around australia. *Journal of Geophysical Research*, 111.
- Devienne, S. (2006). *Red River Delta: Fifty Years of Change*. Agriculture in Southeast Asia.
- Dinardo, S., Lucas, B., and Benveniste, J. (2015). Sentinel-3 stm sar ocean retracking algorithm and samosa model. pages 5320–5323.
- Donlon, C., Berruti, B., Buongiorno, A., Ferreira, M. H., Féménias, P., Frerick, J., J., and Nieke (2012). The global monitoring for environment and security (gmes) sentinel-3 mission. *Remote Sensing of Environment*, 120:37–57.
- Dufréchéou, G. (2017). Aeromagnetic signature of an exhumed double dome system in the sw grenville province (canada). *Terra Nova*, 29.

- Duquenne, F., Botton, S., Peyret, F., Bétaille, D., and Willis, P. (2005). *GPS : Localisation et navigation par satellites*. Hermes Science Publications, 2nd edition revised and expanded edition. Langue : Français.
- Edden, C. A., D.E., and Cartwright (1973). Corrected tables of tidal harmonics. *Geophysical Journal*, 33:253–264.
- Egido, A. (2013). *GNSS Rectometry for Land Remote Sensing Applications*. phdthesis, Starlab Barcelona, Universitat Politècnica de Catalunya, Signal Theory and Communications Dpt., Barcelona.
- Egido, A., Paloscia, S., Motte, E., Guerriero, L., Pierdicca, N., Caparrini, M., Santi, E., Fontanelli, G., and Floury, N. (2014). Airborne gnss-r polarimetric measurements for soil moisture and above-ground biomass estimation. *IEEE Journal of Selected Topics in Applied Earth Observations and Remote Sensing*, 7(5):1522–1532.
- Elsner, J. B. and Tsonis., A. A. (1996). *Singular spectrum analysis : a new tool in time series analysis*. New York : Plenum Press.
- EPA (2017). <https://www.epa.gov/>.
- FitzGerald, D. M., Fenster, M. S., Argow, B. A., and Buynevich, I. V. (2008). Coastal impacts due to sea-level rise. *Annual Review of Earth and Planetary Sciences*, 36(1):601–647.
- Frappart, F., Blumstein, D., Cazenave, A., Ramillien, G., Birol, F., Morrow, R., and Rémy, F. (2017). *Satellite Altimetry: Principles and Applications in Earth Sciences*, pages 1–25. American Cancer Society.
- Frappart, F., Calmant, S., Cauhopé, M., Seyler, F., and Cazenave, A. (2006a). Preliminary results of envisat ra-2-derived water levels validation over the amazon basin. *Remote Sensing of Environment*, 100(2):252 – 264.
- Frappart, F., Do Minh, K., L’Hermitte, J., Cazenave, A., Ramillien, G., Le Toan, T., and Mognard, N. (2006b). Water volume change in the

## Bibliography

---

- lower mekong from satellite altimetry and imagery data. *Geophysical Journal International*, 167.
- Frappart, F., Papa, F., Marieu, V., Malbeteau, Y., Jordy, F., Calmant, S., Durand, F., and Bala, S. (2015). Preliminary assessment of saral/altika observations over the ganges-brahmaputra and irrawaddy rivers. *Marine Geodesy*, 38(sup1):568–580.
- Fu, L.-L., Chelton, D. B., and Zlotnicki, V. (1988). Satellite altimetry: Observing ocean variability from space. *Oceanography*, 1.
- Gaillot, P., Darrozes, J., and Bouchez, J.-L. (1999). Wavelet transform: a future of rock fabric analysis? *Journal of Structural Geology*, 21(11):1615 – 1621.
- Garg, A., Xu, D., and Blaber, A. (2013). Statistical validation of wavelet transform coherence method to assess the transfer of calf muscle activation to blood pressure during quiet standing. *Biomedical engineering online*, 12:132.
- Georgiadou, P. and Kleusberg, A. (1988). On carrier signal multipath effects in relative gps positioning. *Journal of Geodesy*, 13(3):172–179.
- Ghil, M., R. Allen, M., Dettinger, M., Ide, K., Kondrashov, D., Mann, M., Saunders, A., Tian, Y., and Varadi, F. (2001). Advanced spectral methods for climatic time series. *Reviews of Geophysics*, 40.
- Golyandina, N., Viktorovich Nekrutkin, V., and Zhigljavsky, A. (2001). Analysis of time series structure: Ssa and related techniques. *Monographs on Statistics and Applied Probability*, 90.
- Gommenginger, C., Thibaut, P., Fenoglio, L., Quartly, G., Deng, X., Gomez-Enri, J., Challenor, P., and Gao, Y. (2011). *Retracking altimeter waveforms near the coasts*, pages 61–101. Coastal Altimetry.

- Gouriou, T. (2012). *Changes in sea level components from tide gauge data since the end of the 18th century along the Charente-Maritime French Atlantic coast*. Theses, Université de La Rochelle.
- GPS-WORLD (2012). *Directions 2013: Plans set in motion for GPS*.
- Grimm, A. M. and Tedeschi, R. G. (2009). Enso and extreme rainfall events in south america. *Journal of Climate*, 22(7):1589–1609.
- Grinsted, A., C. Moore, J., and Jevrejeva, S. (2004). Application of cross wavelet transform and wavelet coherence to geophysical time series. *Non-linear Processes in Geophysics*, 11:561–566.
- Groves, P. D. (2008). *Principles of GNSS, Inertial, and Multisensor Integrated Navigation Systems*. Artech House, Hardcover, 518 pages.
- Guzkowska, M., Rapley, C., Ridley, J., Cudlip, W., M Birkett, C., and F Scott, R. (1990). Developments in inland water and land altimetry. Technical Report ESA CR 7839/88/F/FL, University College London, Mullard Space Science Laboratory.
- Ha, M. C. (2018). *Evolution of soil moisture and analysis of fluvial altimetry using GNSS-R*. PhD thesis, Université Toulouse III - Paul Sabatier.
- Hall, C. and Cordy, R. (1988). Multistatic scatterometry. In *In Proceedings of the IEEE International Geoscience and Remote Sensing Symposium*, Edinburgh, Scotland.
- Hannah, J. (2010). The difficulties in using tide gauges to monitor long-term sea level change.
- Hansson, K. and Ekenberg, L. (2000). Flood mitigation strategies for the red river delta.
- Harvey, C. (2015). Human impact on the oceans is growing — and climate change is the biggest culprit. *Climate and Environment*.

## Bibliography

---

- Haslett, S. (2008). *Coastal Systems*. London: Routledge, 2nd edition edition.
- Hayne, G. (1980). Radar altimeter mean return waveforms from near-normal-incidence ocean surface scattering. *IEEE Transactions on Antennas and Propagation*, 28(5):687–692.
- Hays, J. (2014). Mekong delta area of vietnam.
- Hofmann-Wellenhof, B., Lichtenegger, H., and Collins, J. (2001). *Global Positioning System - 2001 - Theory and Practice*. Springer, Vienna.
- Imel, D. (1995). Evaluation of the topex/poseidon dual-frequency ionosphere correction. *Journal of Geophysical Research Atmospheres*, 99.
- Jayles, C., Chauveau, J.-P., A., and Auriol (2015). Doris/diode: Real-time orbit determination performance on board saral/altika. *Marine Geodesy*, 38:233–248.
- Jolliffe, I. T. (1986). *Principal component analysis*. SpringerVerlag.
- Karim, M. F. and Mimura, N. (2008). Impacts of climate change and sea-level rise on cyclonic storm surge floods in bangladesh. *Global Environmental Change*, 18(3):490 – 500. Globalisation and Environmental Governance: Is Another World Possible?
- Kavak, A., Vogel, W. J., and Xu, G. (1998). Using gps to measure ground complex permittivity. *Electronics Letters*, 34(3):254–255.
- Keith Raney, R. (1998). Delay/doppler radar altimeter. *Geoscience and Remote Sensing, IEEE Transactions on*, 36:1578 – 1588.
- Keon, D., Pancake, C. M., and Yeh, H. (2015). Protecting our shorelines: Modeling the effects of tsunamis and storm waves. *Computer*, 48(11):23–32.

- Kirshen, P., Knee, K., and Ruth, M. (2008). Climate change and coastal flooding in metro boston: impacts and adaptation strategies. *Climatic Change*, 90(4):453–473.
- Krystian, P. and Nguyen, S. N. (2005). Experience and practices on flood control in vietnam. *Water International - WATER INT*, 30:114–122.
- Kucwaj, J.-C. (2016). *Étude et mise en oeuvre d’estimateurs pour l’altimétrie par réflectométrie GNSS. (Study and implementation of estimators for altimetry measurements by GNSS-reflectometry)*. PhD thesis, Université du Littoral Côte d’Opale.
- Kurtz, N., Galin, N., M., and Studinger (2014). An improved cryosat-2 sea ice freeboard retrieval algorithm through the use of waveform fitting. *The Cryosphere Discussions*, 8:1217–1237.
- Larson, K. M., Braun, J. J., Small, E. E., Zavorotny, V. U., Gutmann, E. D., and Bilich, A. L. (2010). Gps multipath and its relation to near-surface soil moisture content. *IEEE Journal of Selected Topics in Applied Earth Observations and Remote Sensing*, 3(1):91–99.
- Larson, K. M., Gutmann, E. D., Zavorotny, V. U., Braun, J. J., Williams, M. W., and Nievinski, F. G. (2009). Can we measure snow depth with gps receivers? *Geophysical Research Letters*, 36(17):n/a–n/a. L17502.
- Larson, K. M., Löfgren, J. S., and Haas, R. (2013a). Coastal sea level measurements using a single geodetic gps receiver. *Advances in Space Research*, 51(8):1301–1310. 0273-1177.
- Larson, K. M. and Nievinski, F. G. (2013). Gps snow sensing: results from the earthscope plate boundary observatory. *GPS Solutions*, 17(1):41–52.
- Larson, K. M., Ray, R. D., Nievinski, F. G., and Freymueller, J. T. (2013b). The accidental tide gauge: A gps reflection case study from kachemak bay, alaska. *IEEE Geoscience and Remote Sensing Letters*, 10(5):1200–1204.

## Bibliography

---

- Larson, K. M., Small, E. E., Gutmann, E., Bilich, A., Axelrad, P., and Braun, J. (2008a). Using gps multipath to measure soil moisture fluctuations: initial results. *GPS Solutions*, 12(3):173–177.
- Larson, K. M., Small, E. E., Gutmann, E. D., Bilich, A. L., Braun, J. J., and Zavorotny, V. U. (2008b). Use of gps receivers as a soil moisture network for water cycle studies. *Geophysical Research Letters*, 35(24):n/a–n/a. L24405.
- Le, T. A. and Wyseure, G. (2013). Water environmental governance in the mekong river delta, vietnam. *ResearchGate*.
- Lestarquit, L., Peyrezabes, M., Darrozes, J., Motte, E., Roussel, N., Wautelet, G., Frappart, F., Ramillien, G., Biancale, R., and Zribi, M. (2016). Reflectometry with an open-source software gnss receiver: Use case with carrier phase altimetry. *IEEE Journal of Selected Topics in Applied Earth Observations and Remote Sensing*, 9(10):4843–4853.
- Löfgren, J. S., Haas, R., Scherneck, H. ., and Bos, M. S. (2011). Three months of local sea level derived from reflected gnss signals. *Radio Science*, 46(06):1–12.
- Liu, Y., Kerkering, H., and Weisberg, R. H. (2015). Chapter 1 - introduction to coastal ocean observing systems. In Liu, Y., Kerkering, H., and Weisberg, R. H., editors, *Coastal Ocean Observing Systems*, pages 1 – 10. Academic Press, Boston.
- Löfgren, J. S. and Haas, R. (2014). Sea level measurements using multi-frequency gps and glonass observations. *EURASIP Journal on Advances in Signal Processing*, 2014(1):50.
- Lomb, N. R. (1976). Least-squares frequency analysis of unequally spaced data. *Astrophysics and Space Science*, 39:447–462.
- Luu, T. N. M., Garnier, J., Billen, G., Orange, D., Némery, J., Le, T. P. Q., Tran, H. T., and Le, L. A. (2010). Hydrological regime and water

- budget of the red river delta (northern vietnam). *Journal of Asian Earth Sciences*, 37(3):219 – 228.
- M Watson, R., I Griaznova, O., Long, C., and Holland, M. (2004). Increased sample capacity for genotyping and expression profiling by kinetic polymerase chain reaction. *Analytical biochemistry*, 329:58–67.
- MAJ, G., Rapley, C., and I M, M. (1986). Satellite altimeter measurements over land and inland water. In *Proceedings of IGARSS' 86 Symposiums, At Zurich*, volume ESA SP-254, pages 1563–1568.
- Marchan-Hernandez, J. F., Valencia, E., Rodriguez-Alvarez, N., Ramos-Perez, I., Bosch-Lluis, X., Camps, A., Eugenio, F., and Marcello, J. (2010). Sea-state determination using gnss-r data. *IEEE Geoscience and Remote Sensing Letters*, 7(4):621–625.
- Martin, T. V., Brenner, A. C., Zwally, H. J., R., and Bindschadler (1983). Analysis and retracking of continental ice sheet radar altimeter waveforms. *Journal of Geophysical Research*, 88:1608–1616.
- Martin-Neira, M. (1993). A passive reflectometry and interferometry system (paris): Application to ocean altimetry. *ESA Journal*, 17:331–355.
- Martin-neira, M., Colmenarejo, P., Ruffini, G., and Serra, C. (2002). Altimetry precision of 1 cm over a pond using the wide-lane carrier phase of gps reflected signals. *Canadian Journal of Remote Sensing*, 28:394–403.
- McGranahan, G., Balk, D., and Anderson, B. (2007). The rising tide: assessing the risks of climate change and human settlements in low elevation coastal zones. *Environment and Urbanization*, 19(1):17–37.
- Mimura, N. (2013). Sea-level rise caused by climate change and its implications for society. *Proceedings of the Japan Academy, Ser. B, Physical and Biological Sciences*, pages 281–301.
- Motte, E., Egido, A., Roussel, N., Boniface, K., and Frappart, F. (2016). 9 - applications of gnss-r in continental hydrology. In Baghdadi, N.

## Bibliography

---

- and Zribi, M., editors, *Land Surface Remote Sensing in Continental Hydrology*, pages 281 – 322. Elsevier.
- New, A. (1988). Internal tidal mixing in the bay of biscay. *Deep Sea Research Part A. Oceanographic Research Papers*, 35(5):691 – 709.
- Nguyen, N. H., Delgado, J. M., Vo, K. T., Le, M. H., Merz, B., Bárdossy, A., and Apel, H. (2012). Floodplain hydrology of the mekong delta, vietnam. *Hydrological Processes*, 26:674–686.
- Nguyen, Q. C. and Ye, F. (2015). Study and evaluation on sustainable industrial development in the mekong delta of vietnam. *Journal of Cleaner Production*, 86:389–402.
- Nguyen, T.-T., Kawamura, A., Tong, T.-N., Nakagawa, N., Amaguchi, H., R., and Jr, J. (2014). Hydrogeochemical characteristics of groundwater from the two main aquifers in the red river delta, vietnam. *Journal of Asian Earth Sciences*, 93:180–192.
- Obligis, E., Desportes, C., Eymard, L., J. Fernandes, M., Lazaro, C., and Nunes, A. (2011). *Tropospheric Corrections for Coastal Altimetry*, pages 147–176.
- Olbert, A. and Hartnett, M. (2010). Storms and surges in irish coastal waters. *Ocean Modelling*, 34:50–62.
- Pawlowicz, R., Beardsley, B., and Lentz, S. (2002). Classical tidal harmonic analysis with error analysis in matlab using *tide.Computers&Geosciences*, 28 : 929 – 937.
- Pingree, R., T. MARDELL, G., and L. New, A. (1986). Propagation of internal tides from the upper slopes of the bay of biscay. *Nature*, 321.
- Platel, J. P. (2007). Atlas cartographique des phénomènes naturels et des caractéristiques physiques du littoral de la cote basque. Technical report.

- Prokoph, A. and Patterson, R. T. (2004). *From Depth Scale to Time Scale: Transforming Sediment Image Color Data into a High-Resolution Time Series*, pages 143–164. Springer Netherlands, Dordrecht.
- Raven, P., NORGAARD, R., PADOCH, C., PANAYOTOU, T., RANDALL, A., ROBINSON, M., J., and RODMAN (1992). Conserving biodiversity: A research agenda for development agencies. Technical report.
- Ray, C., Martin-Puig, C., Clarizia, M., Ruffini, G., Dinardo, S., Gommenginger, C., and Benveniste, J. (2015). Sar altimeter backscattered waveform model. *Geoscience and Remote Sensing, IEEE Transactions on*, 53:911–919.
- Rémy, F., B., and Legrésy (1997). Surface characteristics of the antarctic ice sheet and altimetric observations. *Journal of Glaciology*, page 265–275.
- Rodriguez, E. (1988). Altimetry for non-gaussian oceans - height biases and estimation of parameters. *J. geophys. Res.*, 93,.
- Rodriguez, E. and Chapman, B. (1989). Extracting ocean surface information from altimeter returns - the deconvolution method. *Journal of Geophysical Research*, 94.
- Rodriguez, E. and Martin, J. (1995). Assessment of the topex altimeter performance using waveform retracking. *Journal of Geophysical Research Atmospheres*, 99.
- Roussel, N., Frappart, F., Ramillien, G., Darrozes, J., Baup, F., and Ha, C. (2015a). Detection of soil moisture content changes by using a single geodetic antenna: The case of an agricultural plot. In *2015 IEEE International Geoscience and Remote Sensing Symposium (IGARSS)*, pages 2008–2011.
- Roussel, N., Frappart, F., Ramillien, G., Darrozes, J., Baup, F., Lestarcquit, L., and Ha, M. C. (2016). Detection of soil moisture variations using gps and glonass snr data for elevation angles ranging from 2° to

## Bibliography

---

- 70°. *IEEE Journal of Selected Topics in Applied Earth Observations and Remote Sensing*, 9(10):4781–4794.
- Roussel, N., Frappart, F., Ramillien, G., Desjardins, C., Gegout, P., Pérosanz, F., and Biancale, R. (2014). Simulations of direct and reflected waves trajectories for in situ gnss-r experiments. *Geoscientific Model Development Discussions*, 7:1001–1062.
- Roussel, N., Ramillien, G., Frappart, F., Darrozes, J., Gay, A., Biancale, R., Striebig, N., Hanquiez, V., Bertin, X., and Allain, D. (2015b). Sea level monitoring and sea state estimate using a single geodetic receiver. *Remote Sensing of Environment*, 171(Supplement C):261 – 277.
- Ruf, C., Keihm, S., Subramanya, B., and Janssen, M. (1995). Topex/poseidon microwave radiometer performance and in-flight calibration. *Journal of Geophysical Research Atmospheres*, 99.
- Scargle, J. D. (1982). Studies in astronomical time series analysis. ii - statistical aspects of spectral analysis of unevenly spaced data. *Astrophysical Journal*, 263:835–853.
- Scharroo, R. and Smith, W. (2010). A global positioning system - based climatology for the total electron content in the ionosphere. *Journal of Geophysical Research*, 115.
- Sešek, A. and Trontelj, J. (2013). Measurement system for sea wave monitoring. In *MIDEM 2013, At Kranjska Gora, Slovenija*.
- Senior, C. A., Jones, R. G., Lowe, J. A., Durman, C. F., D., and Hudson (2002). Predictions of extreme precipitation and sea-level rise under climate change. *Philos Trans A Math Phys Eng Sci*, pages 1301–1311.
- Shuanggen Jin, Estel Cardellach, F. X. (2014). *GNSS Remote Sensing. Theory, Methods and Applications*. Springer.
- Stammer, D., A., and Cazenave (2017). *Satellite Altimetry Over Oceans and Land Surfaces*. Boca Raton.

- Stosius, R., G. B., Helm, A., Hoechner, A., and J. W. (2010). Simulation of space-borne tsunami detection using gnss-reflectometry applied to tsunamis in the indian ocean. *Natural Hazards and Earth System Sciences*, 10.
- Strub, P. and James, C. (2002). The 1997-1998 oceanic el niño signal along the southeast and northeast pacific boundaries - an altimetric view. *Progress In Oceanography*, 54:439–458.
- Sutour, C., Émilie Darrin, Giremus, A., and Pereira, V. (2012). Étude d’une nouvelle modélisation des erreurs de multitrajets en navigation gps. Rapport de projet, Université Bordeaux 1 - Sciences Technologies.
- Tebaldi, C., Strauss, B. H., and Zervas, C. E. (2012). Modelling sea level rise impacts on storm surges along us coasts. In *Environ. Res. Lett*, volume 7.
- Thibaut, P. (2008). Rapport sur la classification des formes d’onde dans pistach. Technical report, Recherche Collecte Localisation.
- Thibaut, P., Poisson, J. C., Bronner, E., and Picot, N. (2010). Relative performance of the mle3 and mle4 retracking algorithms on jason-2 altimeter waveforms. *Marine Geodesy*, 33(sup1):317–335.
- Torrence, C. and Compo, G. P. (1998). A practical guide to wavelet analysis. *Bulletin of the American Meteorological Society*, 79(1):61–78.
- Trenberth, K. E. and Hoar, T. J. (1996). The 1990–1995 el niño-southern oscillation event: Longest on record. *Geophysical Research Letters*, 23(1):57–60.
- Trenberth, K. E. and Olson, J. G. (1988). An Evaluation and Intercomparison of Global Analyses from the National Meteorological Center and the European Centre for Medium Range Weather Forecasts. *Bulletin of the American Meteorological Society*, 69:1047–1056.
- Treuhaft, R. N., Lowe, S. T., Zuffada, C., and Chao, Y. (2001). 2-cm gps altimetry over crater lake. *Geophysical Research Letters*, 28(23):4343–4346.

## Bibliography

---

- Trinh, T.-T. and et al (2016). <https://vietnamnews.vn/society>.
- Vautard, R., Yiou, P., and Ghil, M. (1992). Singular-spectrum analysis: A toolkit for short, noisy chaotic signals. *Physica D: Nonlinear Phenomena*, 58(1):95 – 126.
- Verron, J., Sengenès, P., Lambin, J., Noubel, J., Steunou, N., A., and Guilot (2015). The saral/altika altimetry satellite mission. *Marine Geodesy*, 38:2–21.
- Vignudelli, S., Kostianoy, A. G., Cipollini, P., and Benveniste, J. (2011). *Coastal Altimetry*. Springer, Berlin, Heidelberg.
- Vreugdenhil, C. B., N, H.-T., and Phan (2000). Flood risk for the red river delta. International European - Asian Workshop, Ecosystem & Flood.
- Vu, P. L., Frappart, F., Darrozes, J., Marieu, V., Blarel, F., Ramillien, G., Bonnefond, P., and Birol., F. (2018). Multi-satellite altimeter validation along the french atlantic coast in the southern bay of biscay from ers-2 to saral. *Remote Sensing*, 10(1).
- Wahr, J. M. (1985). Deformation induced by polar motion. *Journal of Geophysical Research*, 90.
- Wahr, J. M. and et al. (1981). Body tides on an elliptical, rotating, elastic and oceanless earth. *Geophysical Journal International*, 64:677–703.
- Ward, P. W. (2005). *Understanding GPS: Principles and Applications*, chapter 5 Satellite Signal Acquisition Tracking and Data Demodulation, pages 153–243. Artech House.
- Wingham, D., Francis, C., Baker, S., Bouzinac, C., Brockley, D., Cullen, R., de Chateau-Thierry, P., Laxon, S., Mallow, U., Mavrocordatos, C., Phalippou, L., Ratier, G., Rey, L., Rostan, F., Viau, P., and Wallis, D. (2006). Cryosat: A mission to determine the fluctuations in earth’s land and marine ice fields. *Advances in Space Research*, 37(4):841 – 871. Natural Hazards and Oceanographic Processes from Satellite Data.

- Wingham, D., Rapley, C., and H D, G. (1986). New techniques in satellite altimeter tracking systems.
- Wolters, E. (2017). Monitoring global sea level using satellite data.
- Woodworth, P. and Smith, D. (2003). A one year comparison of radar and bubbler tide gauges at liverpool. *International Hydrographic Review*, 4:42–49.
- WOPPELMANN, G. (1997). *Tide gauge geodetic fixing in a global reference system with space geodetic techniques*. Theses, Observatoire de Paris.
- Wunsch, C. and Stammer, D. (1997). Atmospheric loading and the oceanic "inverted barometer" effect. *Reviews of Geophysics - REV GEOPHYS*, 35:79–107.

## Bibliography

---